UNIVERSITÀ DELLA
CALABRIA

Dipartimento di Ingegneria Informatica, Modellistica, Elettronica e Sistemistica

Dottorato di Ricerca in
Ingegneria Civile e Industriale

XXXIV CICLO

DEM-CFD simulation of fluid-particle flow in carrier-based Dry Powder Inhalers for pharmaceutical applications

Settore Scientifico Disciplinare ING/IND-26

Coordinatore: Ch.mo Prof. Enrico Conte
Firma ______________________________

Conte Enrico
07.12.2022
16:58:06
GMT+01:00

Supervisore: Ch.mo Prof. Francesco Paolo Di Maio
Firma ____________________

Firmato digitalmente da Di Maio Francesco Paolo
C=IT

Co-supervisore: Ch.mo Prof. Alberto Di Renzo
Firma ____________________

Di Renzo Alberto
06.12.2022 09:12:03
GMT+01:00

Dottoranda: Ing. Francesca Orsola Alfano
Firma ____________________

FRANCESCA
ORSOLA ALFANO
05.12.2022
17:31:41
GMT+00:00

Abstract

Dry powder inhalers (DPI) are medical devices specifically engineered to ensure maximum and effective delivery of active pharmaceutical ingredients (API) in powder form upon inhalation by a patient.

In this work, highly challenging CFD–DEM simulations are utilized to deterministically track the motion of both carrier and API particles in dry powder formulations along their flow from the dose cup through the exit of a swirl-flow-based dry powder inhaler.

To achieve this purpose, a combination of different solutions is adopted: a sufficiently small time-step is coupled to scaled contact/adhesive interaction parameters; grid-based contact detection and fluid-to-particle and particle-to-fluid interpolation of the gas-solid interaction variables, i.e. gas velocity and voidage and drag force; a rolling friction model to allow for appropriate adhesion behaviour of the particles.

Single phase air-flow, coupled air-carrier particle flow and coupled air-carrier-API particles are characterized in the device for different typical inhalation conditions. The aim is to investigate and gain detailed insight on all stages of the particles' lift-up, aero-dispersion, de-aggregation, inter-particle and particle-wall collisions across the scales from few micron sized API powders to a commercial sized device.

Thanks to a 4-way coupled CFD–DEM model, inertial, collisional, rotational and inter-particle adhesion effects can be taken into account in modelling the coupled air and particle dynamics.

Contents

List of Figures vii

List of Tables xx

Nomenclature xxiii

1 Literature review **1**
- 1.1 Dry Powder Inhalers . . . 1
  - 1.1.1 Commercially available formulations . . . 4
  - 1.1.2 DPI design . . . 5
  - 1.1.3 Efficiency of DPI . . . 7
- 1.2 High dosage DPI . . . 8
- 1.3 Experimental analysis . . . 11
  - 1.3.1 Cascade impactors . . . 12
  - 1.3.2 Laser diffraction techniques . . . 13
  - 1.3.3 Image analysis techniques . . . 13
- 1.4 Modelling of DPI . . . 14
  - 1.4.1 Modelling of the fluid phase . . . 14
  - 1.4.2 Modelling of the solid phase . . . 15
  - 1.4.3 Multiphase simulations . . . 16
- 1.5 Research objective . . . 17
- 1.6 Thesis layout . . . 18

2 CFD-DEM approach **19**
- 2.1 Modelling of the fluid phase . . . 19
  - 2.1.1 Governing equations . . . 20
  - 2.1.2 Turbulence . . . 21
    - 2.1.2.1 Reynolds Averaged Navier Stokes . . . 24
    - 2.1.2.2 Eddy Viscosity Models . . . 25
    - 2.1.2.3 Reynolds Stress Transport (RST) models . . . 26
    - 2.1.2.4 Large Eddy Simulation . . . 26
  - 2.1.3 Numerical approach . . . 28
- 2.2 Modelling of the solid phase . . . 29
  - 2.2.1 Governing equations . . . 30

- 2.2.2 Modelling of contact forces 30
  - 2.2.2.1 Linear spring dashpot model 32
  - 2.2.2.2 Hertz-Mindlin no-slip model 34
- 2.2.3 Contact torque and rolling resistance 35
- 2.2.4 Time integration 35
- 2.2.5 Neighbour search algorithm 38

2.3 Fluid–solid coupling 39
- 2.3.1 Interpolation algorithms 41
- 2.3.2 CFD-DEM algorithm 43

2.4 Fluid forces on particles 44
- 2.4.1 Drag force 44
  - 2.4.1.1 Ergun 45
  - 2.4.1.2 Wen and Yu 45
  - 2.4.1.3 Di Felice 46
  - 2.4.1.4 Gidaspow 46
  - 2.4.1.5 Gidaspow-blend 46
  - 2.4.1.6 Drag models for polydisperse systems 47
- 2.4.2 Pressure gradient force 47
- 2.4.3 Lift force 47
  - 2.4.3.1 Saffman lift force 48
  - 2.4.3.2 Magnus lift force 49
- 2.4.4 Fluid torque 50

2.5 Modelling of cohesive systems 51
- 2.5.1 Johnson-Kendall-Roberts model 52
  - 2.5.1.1 Dimensionless JKR model 53
- 2.5.2 Polynomial approximation of JKR model 54
- 2.5.3 Simplified models 55
  - 2.5.3.1 Linear cohesion model (sjkr) 56
  - 2.5.3.2 Constant force model (VDW) 57

3 Materials and methods 59

3.1 Simulation software 59
- 3.1.1 MFIX 59
- 3.1.2 Other softwares 61
  - 3.1.2.1 OpenFOAM 62
  - 3.1.2.2 LIGGGHTS 62

3.2 Post-processing tools 62
- 3.2.1 VTK files 62
- 3.2.2 ParaView 63
- 3.2.3 MATLAB 64

3.3 Geometry and computational grid 65
- 3.3.1 Swirl-based Dry Powder Inhaler 65
  - 3.3.1.1 Geometry 65
  - 3.3.1.2 Mesh 66

3.3.1.3 Grid independence study 68
3.3.2 Cyclohaler 74
3.3.2.1 Inhaler geometry and mesh 75
3.3.2.2 Capsule geometry 76

4 Design and modelling of a DPI 77
4.1 Simulation parameters and set-up 77
4.2 Single phase air flow field 78
4.3 Motion of carrier particles 80
4.4 Model validation 82
4.5 Analysis of carrier particle trajectories 86
4.6 Carrier particle velocity field 88
4.7 Effect of different parameters on powder dispersion 89
4.7.1 Inlet flowrate 89
4.7.2 Particle size and rolling friction 90
4.7.3 Restitution coefficient 91
4.7.4 CFD–DEM coupling approach 92
4.7.5 Variable inhalation profile 94
4.7.6 Cohesion 99
4.7.6.1 Particle emission as a function of cohesiveness 99
4.7.6.2 Comparison between SJKR and VDW cohesion models 101
4.8 Carrier-wall collisions 103

5 Introduction of API particles 106
5.1 Deaggregation due to particle-wall collisions 106
5.1.1 Simulation parameters and set-up 106
5.1.2 Escape velocity 109
5.1.3 Influence of DEM parameters 110
5.1.4 The role of rolling friction 111
5.1.4.1 Conversion of translational energy 114
5.2 Analytical model for escape velocity 116
5.2.1 South pole detachment 117
5.2.2 Equatorial detachment 117
5.2.3 South emisphere detachment 118
5.2.4 Calculation of cohesion energy 119
5.2.4.1 SJKR model 120
5.2.4.2 JKR model 120
5.2.4.3 VDW model 121
5.2.5 Model validation with DEM simulations 122
5.2.6 Model application to carrier-wall impact 122
5.2.7 Effect of the cohesion model on escape velocity 123
5.3 Can a single carrier-wall impact promote complete API deaggregation? 125

6 Simulation of carrier-API systems 126

- 6.1 API - carrier configuration 126
  - 6.1.1 Definition of dosage 127
  - 6.1.2 Fast calculation of number of particles in each phase . 129
- 6.2 Positioning of API particles 130
  - 6.2.1 Kissing number 130
  - 6.2.2 3D configuration 131
- 6.3 Simulation parameters and set-up 133
- 6.4 Dispersion of API particles 134
- 6.5 Comparison with experiments 136
- 6.6 API deaggregation 138
- 6.7 Effect of different parameters on deaggregation 140
  - 6.7.1 Inlet flowrate 140
  - 6.7.2 Cohesion model 140
  - 6.7.3 Weight dosage 141
  - 6.7.4 Drag model 145
- 6.8 Variable inhalation profile 147

7 Capsule-based DPI 152

- 7.1 CFD modelling of the Cyclohaler 152
  - 7.1.1 Simulation setup 152
  - 7.1.2 Fluid flow 153
  - 7.1.3 Model validation 155
  - 7.1.4 Comparison with constant flowrate 155
  - 7.1.5 Comparison of turbulence models 156
  - 7.1.6 Lagrangian tracking 158
    - 7.1.6.1 Powder emission 159
    - 7.1.6.2 Collision statistics 161
- 7.2 DEM simulation of the motion of particles in the capsule . . 163
  - 7.2.1 Rotating motion of the capsule 164
  - 7.2.2 Modelling strategy 165
  - 7.2.3 Collision between the capsule and the inhaler 167
  - 7.2.4 DEM parameters 167
  - 7.2.5 Rotation motion only, free flowing particles 168
  - 7.2.6 Rotation motion only, cohesive particles 172
  - 7.2.7 Rotation and shaking motion, cohesive particles . . . 173
  - 7.2.8 Characterization of powder emission 173
  - 7.2.9 Carrier-wall collisions 177
  - 7.2.10 Simulation with both carrier and API particles 180

8 High dosage systems 184

- 8.1 Single carrier particle covered 184
  - 8.1.1 Simulation parameters and setup 185
  - 8.1.2 Particle dispersion 186

- 8.1.3 Evolution of an API agglomerate 186
- 8.1.4 Effect of inlet flowrate and particle diameter 189
- 8.1.5 Effect of lift forces and PCF drag model 191
  - 8.1.5.1 API detachment from the carrier 193
- 8.1.6 Effect of fluid torque 194
- 8.1.7 Effect of turbulence 198
- 8.2 Multiple carrier particles covered 199
  - 8.2.1 Simulation parameters and setup 199
  - 8.2.2 Dispersion as a function of particle location 204
  - 8.2.3 API-Carrier deaggregation 208
  - 8.2.4 Deaggregation of API clusters 209
  - 8.2.5 Re-agglomeration phenomena 214
  - 8.2.6 Comparison between two different blends 216

9 Conclusions 220
- 9.1 Design and modelling of a DPI 220
- 9.2 Introduction of API particles 222
- 9.3 Simulation of carrier-API systems 223
- 9.4 Capsule-based DPI 223
- 9.5 High dosage systems 225
- 9.6 Future work 226

Bibliography 228

List of Figures

1.1 Deep lung deposition of particles with aerodynamic diameters of 1 to 5 μm (green). Generally, particles > 5 μm (red) impact on the oropharynx, while the bulk of particles <1 μm (yellow) is exhaled (Zillen et al., 2021). 2
1.2 Schematics of dry powder inhaler (DPI) dispersion mechanisms. (Zheng et al., 2021) 3
1.3 Flow rate versus device resistance for several commercial DPI. Points are at a 4 kPa pressure drop. Lines are also presented for pressure drops of 2 and 6 kPa (Clark et al., 2020). 7
1.4 The relationship between dose emission from a DPI and the patient's inhalation (Clark et al., 2020). 7
1.5 API particles placed on a a) spherical polystyrene carrier ($\approx 200\mu$m) (Young et al., 2011) and b) tomahawk lactose carrier ($\approx 200\mu$m) (Dickhoff et al., 2003). c) API particles trapped in crevices of an irregular, non spherical surface (Young et al., 2005) 9
1.6 Theoretical blend structure and influence on fine particle dose and fraction as a function of drug-carrier loading. (I) High adhesion site filling (adhesion >> aerosol energy), (II) filling of intermediate sites (adhesion ≈ aerosol energy, (III) region of constant aerosol performance (adhesion << aerosol energy), (IV) transition stage between monolayer/multilayer particulate system and (V) multi-layer particle formation and formulation segregation. (Young et al., 2011) 10
1.7 Stages of the NGI (Marple et al., 2004). 12
1.8 Calculated velocity profile (a) and turbulence scale (b) of an Aerolizer using RANS with $k - \varepsilon$ SST turbulence model (Coates et al., 2004). 14
1.9 Detachment of API particles due to carrier-wall collision (Ariane et al., 2018). 15
1.10 Impact of adhesive units with lactose fines and lactose carrier. (Sarangi et al., 2021) 16

2.1 Different representations of the particle treatment: (a) unresolved surface method ($\Delta x \gg D$) and (b) resolved surface method ($\Delta x \ll D$)). Adapted from Norouzi et al. (2016). . . 20
2.2 Submerged turbulent jet. Credits: C. Fukushima and J. Westerweel, Technical University of Delft, The Netherlands, CC BY 3.0 `<https://creativecommons.org/licenses/by/3.0>`, via Wikimedia Commons. 22
2.3 Different resolved turbulence scales and velocity fluctuations in a turbulent flow (Norouzi et al., 2016). 23
2.4 a) Configuration for the 2D contact between a sphere and a wall and b) definition of the tangential displacement (Di Renzo and Di Maio, 2004). 32
2.5 Schematic of the spring-dashpot system used to model particle contact forces in normal and tangential direction. 33
2.6 Schematics of one-way and four-way coupling strategies. Adapted from Norouzi et al. (2016). 39
2.7 DEM interpolation schemes (NETL Multiphase Flow Science Team, 2020): a) centroid method, b) Divided Particle Volume Method, c) interpolation based on the staggered grid. 41
2.8 2-D schematic of a staggered grid scheme used for discretizing the gas-phase field (Garg et al., 2012). 42
2.9 Framework of explicit coupling in the CFD-DEM model (Norouzi et al., 2016). 43
2.10 Drag force as a function of void fraction for different drag models. $d = 100$ μm, $\rho_f = 1.2$ kg/m^3, $|\vec{w}_i| = 5$ m/s and $\mu_f = 1.8 \cdot 10^{-5}$ Pa $\cdot$s 45
2.11 Steps of the drag model in polydisperse systems according to CDD model (Cello et al., 2010). 48
2.12 Illustration of slip-shear force on a particle in a non-uniform flow field (Norouzi et al., 2016). 49
2.13 Illustration of the Magnus lift force (Norouzi et al., 2016). . . 50
2.14 Variation in pressure p as a function of the distance h between two surfaces caused by the sum of the attractive and repulsive van der Waals forces (Marshall and Li, 2014). 51
2.15 Tabor number as a function of particle radius ($E = 0.2$ GPa, $r =$ 1-200 μm, $\gamma = 0.04$ J/m^2, $z_{in} = 0.165$ nm) 52
2.16 Force-displacement relationship with JKR and Hertz models. 53
2.17 Force-displacement relationship with JKR model in dimensionless variables 54
2.18 Force-displacement relationship for JKR model and polynomial JKR model. 55

2.19 Contact area between two particles ($R_1 = 5$ μm, $R_2 = 100$ μm) as a function of normal overlap for three different formulation of SJKR cohesion model. Overlap value are normalized by dividing for the radius of the smaller particle, while contact area values are normalized by dividing for the surface area of the smaller particle. 57
2.20 Cohesive force as a function of inter-particle distance in VDW model. 58

3.1 Geometry of the system. Side view, top view and 3D transparent representation. In the last one, blue arrows denote the two air inlets and the air outlet from the top of the exit duct; the red part represents the particles filling the hemispherical dose cup. 66
3.2 Mesh obtained with Cartesian grid cut-cell technique. The insert shows the application of the cartesian cut-cell technique to adapt the grid to the geometry, for the numerical solution of the gas flow. The grid size is 250 μm, giving rise to a total of ∼135k cells. 67
3.3 Resistance coefficient (R) obtained with grids S_1, S_2, S_3. . . . 69
3.4 Side-view pressure field for grids S_0 (Δx=182 μm), S_1 (Δx=250 μm), S_2 (Δx=333 μm). Gas flowrate is 60 L/min. 71
3.5 Side-view gas velocity magnitude for grids S_0 (Δx=182 μm), S_1 (Δx=250 μm), S_2 (Δx=333 μm). Gas flowrate is 60 L/min. 71
3.6 Tangential velocity profiles for grids S_0, S_1, S_2 a) in the swirl chamber and b) in the mouthpiece. c) Locations in the device from where profiles were extracted. Gas flowrate is 60 l/min. 72
3.7 Number of carrier particles (150 μm diameter) in the device as a function of time for 500 ms of simulation. At the beginning of the simulation there are 3422 particles in the system. Gas flowrate is 60 L/min. 72
3.8 Snapshots of particle positions at 10, 50, 100, 500 ms for three grid sizes. a) 10 ms, b) 50 ms, c) 100 ms, d) 500 ms. 73
3.9 x-coordinate of particle ID1934 for grids S_0, S_1, S_2. 74
3.10 Geometry of the Cyclohaler. 75
3.11 Mesh used in CFD simulations: a) full inhaler, c) wall resolution near the outlet section. 76
3.12 Capsule geometry. 76

4.1 Velocity field of the fluid flow inside the device at 60 l/s inlet flowrate: a) horizontal component of velocity (v_z) profiles at different vertical coordinates, b) side view and c) top view of the gas velocity magnitude, d) streamlines. 79

4.2 Particle positions represented by spheres coloured based on the velocity magnitude during the simulation: a) 0 ms, b) 5 ms, c) 8 ms, d) 15 ms, e) 100 ms, f) 500 ms. 60 L/min gas flowrate. 81
4.3 Cumulative percentage of particles that leave the device as a function of time. (60 L/min, 150 micron particles). The three stages indicated in the figure are described and commented in the accompanying text. 82
4.4 a) Map of the axial velocity in the present work and cross-section heights B, C and D corresponding to the profiles shown in parts b and c. b) Tangential velocity profiles reported in Ponzini et al. (2021) at the different cross-sections. c) Corresponding tangential velocity profiles obtained in the present work. 83
4.5 Cup emptying, top view. Flow-rate = 60 L/min, rise time 0.3 s for experimental data (top), constant flowrate profile for simulation results (bottom). The red arrows point to the cup (dashed circle) and the powder in the initial position. a) Start; b) 5 ms (after dose-protector opening); c) 10 ms; d) 15 ms. Reprinted from Pasquali et al. (2015) with permission from Elsevier. 84
4.6 Dispersion in the swirl chamber, side view. Flow-rate = 100 L/min, square wave profile. a) 1ms; b) 10 ms; c) 20 ms; d) 40 ms; e) 70 ms; f) 100 ms. 85
4.7 Exit velocity of carrier particles in simulations as a function of residence time. Scatter plot and smooth moving average using 50 points (LOWESS method). 86
4.8 Trajectories of particles G, R, B. a) Side view and b) top view. 87
4.9 x-coordinate as a function of time for the three selected particles: a) G, b) R, c) B. 87
4.10 Relationship between residence time and d_0. Particles are colored according to the final value of vertical component of velocity. The points representing particles R, G and B are marked. a) Definition of d_0, b) residence time plot. 88
4.11 Average value over all carrier particles of the radial (v_r), tangential (v_θ) and vertical velocity (v_y) (a) and angular velocity (b) as a function of time. Air flowrate: 60 L/min, 150 micron particles. 89
4.12 Cumulative percentage of particles that leave the device as a function of time for simulations with 3 different inlet flowrate: 40 L/min, 60 L/min, 100 L/min. 150 μm particles. 90
4.13 Cumulative percentage of particles that leave the device as a function of time for simulations with 2 different diameters with and without rolling friction (RF). 60 L/min gas flowrate. 90

4.14 Average tangential velocity (a) and number of particles (b) in the swirl chamber for simulations with and without rolling friction. 200 micron particles, 60 L/min inlet gas flowrate. . . 91
4.15 a) Cumulative percentage of particles that leave the device as a function of time and b) mean tangential velocity over time for simulations with different coefficient of restitution. 200 μm particles, 60 L/min inlet flowrate. 92
4.16 Particle position during the simulations with 1-way and 4-way coupling. 93
4.17 Gas pressure (a,b) and gas velocity magnitude (c,d) at 3 ms with 1-way and 4-way coupling. 94
4.18 Mean y-component of the drag F_d, buoyancy F_b and total force F_{tot} acting on the particles with 1-way and 4-way coupling in the first 20 ms of simulation. 60 L/min, 200 μm particles. 95
4.19 Inspiratory profiles obtained from asthmatic patients inhaling twice through the NEXThaler®. Profiles corresponding to the 10th, 50th and 90th percentile of the Peak Inspiratory Flow (PIF). Extracted from the data published in Buttini et al. (2016b). 95
4.20 Particle arrangement in the inhaler with constant flowrate profile (step, 60 L/min) and realistic profile (P50): a) 10 ms, b) 40 ms, c) 80 ms, d) 200 ms. 96
4.21 Cumulative percentage of particles that leave the device as a function of time with constant inlet flowrate (step, 60 L/min) and realistic inhalation profile (P50). 97
4.22 Fluid streamlines coloured according to velocity magnitude for simulation with constant flowrate (step, 60 L/min) and realistic inhalation profile (P50) at a) 5 ms, b) 10 ms, c) 20 ms. 98
4.23 Force comparison with increasing values of the cohesion parameter, k. 100
4.24 Powder emission from the inhaler for simulations increasing level of cohesive forces between carrier particles. 100
4.25 Comparison between the cohesive force calculated by SJKR and the short-range contribution of the VDW model as a function of the overlap between two particles. The dashed line shows the normal elastic force calculated with the Hertz model 101
4.26 Emitted fraction as a function of the cohesion model used. The reference pull off force is $2{\cdot}10^{-5}$ N. 102
4.27 a) Particle arrangement in the swirl chamber after 50 ms with and without p-w interactions, b) Percentage of particles exiting the system with free flowing particles, p-p interactions and p-p and p-w interactions. 103

4.28 Location of carrier-wall collision events in the first 10 ms of simulation. Points are coloured according to impact velocity. 40 L/min, 200 μm particles, no rolling friction. 104
4.29 Particle-wall impact velocity as a function of y coordinate. All the impacts that occur in the first 50 ms of simulation are reported. The points are colored based on the time at which the impact occurs. 40 L/min, 200 μm particles, no rolling friction. 105
4.30 Number of particle-wall impacts as a function of time. (40 L/min, 200 μm particles, no rolling friction). 105

5.1 System with 2 particles and a wall used in the simulations. . 107
5.2 Cohesion energy density, k, as a function of the Bond number (Bo). 109
5.3 Escape velocity as a function of coefficient of restitution (e) and static friction coefficient (μ_s). 111
5.4 Carrier and API velocity profiles during wall collision and particle position after impact (at $t = 1.6\tau_c$) in three cases: a) detachment of API particle, b) no detachment of API particle without rolling friction, c) no detachment of API particle with rolling friction. Velocity values are normalized with the initial velocity of the carrier particle, time values are normalized with collision duration. The yellow area indicates when the carrier particle is in contact with the wall. 112
5.5 Evolution of a) overlap, b) angular velocity and c) relative velocity of the API particle (with respect to the carrier) during detachment with and without rolling friction (RF). 113
5.6 Particle on a wall. 114
5.7 API particle in south pole position 117
5.8 API particle in equatorial position 118
5.9 API particle attached in a generical position in the south emisphere 119
5.10 Cohesion energy with the three cohesion models VDW, JKR, SJKR. 119
5.11 Normal force vs overlap according to VDW cohesion model. . 121
5.12 Comparison between analytical model for the escape velocity (Equation 5.31) and DEM simulations with MFIX (SJKR cohesion model). 122
5.13 Escape velocity as a function of Bond number calculated by the macroscopic analytical model and compared to DEM simulations. 123
5.14 Escape velocity as a function of angle for different cohesion models. 124

5.15 Escape velocity of particles in equatorial position as a function of API diameter and adhesion force. The dashed line shows the typical carrier-wall impact velocity in the swirl chamber. 125

6.1 API and carrier 126
6.2 Illustration of the definition of the surface coverage. 128
6.3 Weight dosage, ε_w, as a function of surface coverage, α, for different values of the size ratio, r_d. The considered density ratio (r_ρ) is 1. 128
6.4 Small circles (pink) around a large circle (grey). r is the radius of the small circles, R is the radius of the large circle. a is the apothem of the regular polygon inscribed in the circumference with radius $R + r$. 131
6.5 Generation of the coated carrier particles by random positioning of fine particles (purple) on the surface of coarser ones (grey) for a size ratio $r_d = 20$ and density ratio $r_\rho = 1$. API w/w loadings of 1% (a), 5% (b), 10% (c) and 13% (d). 133
6.6 a) Initial configuration of 1585 coated carrier particles with 1% API dosage (w/w%). Each carrier particle has an average of 86 API particles stuck on the surface. b) Configuration after DEM gravity settling with the API particles repositioned. 135
6.7 Position of carrier (yellow) and API (blue) particles during the simulation: a) 3 ms, b) 7 ms, c) 10 ms, d) 15 ms. API particles are shown with an enlarged size to improve visibility. 60 L/min gas flowrate. 135
6.8 Percentage of emitted particles and average number of API particles attached to a carrier particle as a function of time (gas flowrate 60 L/min). 136
6.9 API emission in simulations and experiments with a 40 L/min inlet gas flowrate and 1% w/w API. a) Normalized fluorescence intensity, b) cumulative percentage of emitted API particles. 137
6.10 Initial lifting of API particles. API particles are shown with an enlarged size to improve visibility. 138
6.11 Average forces (hydrodynamic and contact/adhesive) exerted on carrier particles in the first 8 ms (a) and on API particles during the first 3 ms of simulation (b) with an inlet gas flowrate of 60 L/min. 139
6.12 Emitted fraction of API particles (a) and mean number of API particles on a carrier (b) for different inlet flowrates. . . 140
6.13 Position of particles in the simulations with VDW and SJKR cohesion model at a) 2 ms, b) 4 ms, c) 6 ms. Inlet gas flowrate is 40 L/min. API particles enlarged 4 times to improve visibility. 142

6.14 a) Particles exiting the system and b) number of API particles in contact with a carrier for simulations with VDW and SJKR cohesion model. Inlet gas flowrate is 40 L/min. 143
6.15 Initial position of particles in the simulation with 5% API dosage (w/w). 143
6.16 Position of particles in the simulations with 1% and 5% weight dosage of API particles at a) 2 ms, b) 4 ms, c) 6 ms. Inlet gas flowrate is 40 L/min, cohesion model is SJKR. API particles enlarged 4 times to improve visibility. 144
6.17 Application of agglomerate detection algorithm near the outlet section. a) Percentage of API particle fully deaggregated (i.e., not in contact with any other particle), b) number of API particles in aggregate form. Inlet gas flowrate is 40 L/min. . 145
6.18 Comparison between the positions of the particles after 2 ms from the activation of the air flow obtained with the monodisperse (Gidaspow-blend) and polydisperse (PCF) drag model. 146
6.19 Time evolution of the average drag force acting on API (a) and carrier (b) particles using the polydisperse (PCF) or monodisperse (no PCF) model. 146
6.20 Percentage of emitted API particles (a) and average number of API particles adhering to the carrier as a function of time as the drag model varies, polydisperse (PCF) and monodisperse (no PCF). 147
6.21 Snapshots of particle position at different times: a) 20 ms, b) 30 ms, c) 40 ms, d) 50 ms, e) 70 ms, f) 100 ms. Enlarged API to improve visibility. Gravity is directed in $-z$ axis. 148
6.22 Mean number of API particles adhered on a carrier a) and mean Bond number (ratio between cohesive force and weight) for simulations with step (60 L/min) and P50 inhalation profiles. 149
6.23 Snapshots near mouthpiece exit for simulations with constant flowrate profile, 60 L/min (step) and variable inhalation profile (P50) at times t_{25}, t_{50}, t_{75}, t_{100}. t_x = time at which the emitted fraction of the API particles is $x\%$. 150
6.24 Percentage of API particles near the outlet section fully deaggregated. 150

7.1 Inhalation profile for the Cyclohaler calculated according to Byron et al. (2014). 153
7.2 Fluid streamlines coloured according to gas velocity magnitude at different time instants. 154
7.3 Comparison between simulation and experiments. 155
7.4 Resistance coefficient of the Cyclohaler as a function of time for variable inhalation profile and constant flowrate. 155

7.5 Vertical slice of gas velocity for simulations with a) $LES-WALE$ turbulence model and b) $k-\varepsilon$ turbulence model. Inlet flowrate is 60 L/min. 156
7.6 Gas velocity above the grid for simulations with a) $LES-WALE$ turbulence model and b) $k-\varepsilon$ turbulence model. Inlet flowrate is 60 L/min. 157
7.7 Gas velocity in the swirl chamber for simulations with a) $LES-WALE$ turbulence model and b) $k-\varepsilon$ turbulence model. Inlet flowrate is 60 L/min. 157
7.8 Gas velocity near the outlet section for simulations with a) $LES-WALE$ turbulence model and b) $k-\varepsilon$ turbulence model. Inlet flowrate is 60 L/min. 158
7.9 Particle properties used in Lagrangian tracking simulations and initial position of particles in the capsule holder. 159
7.10 Trajectory of a particle in the first 95 ms (simulation F100). . 160
7.11 Direction of particle velocity at the beginning of the simulation (simulation T100). 161
7.12 Emitted fraction of particles for the three simulations. 161
7.13 Location of all particle-wall collision events that occurred in 500 ms for F100 simulation (frozen flow, 100 μm particles). Points are coloured according to impact velocity. 162
7.14 Deaggregation estimate according to the sub-scale wall collision detachment model by Ariane et al. (2018). 163
7.15 a) Angular velocity profile assumed for the capsule, b) number of complete rotations of the capsule as a function of time. . . 165
7.16 Gravitational acceleration components as a function of time . 165
7.17 Capsule oscillating motion 167
7.18 a) Initial position of the particles in the capsule and rotation direction b) position of the filled capsule inside the Cyclohaler inhaler. 169
7.19 Position of particles in the capsule at a) 0.1 s, b) 0.2 s, c) 0.3 s, d) 0.5 s, e) 2.0 s, f) 2.4 s. 170
7.20 Emitted mass (left axis) along with angular velocity profile . 170
7.21 Mean fictitious forces (Centrifugal, Euler, Coriolis) acting on particles as a function of time. Weight force is reported as well. 171
7.22 Mean fictitious forces (centrifugal, Euler, Coriolis) and weight force at the beginning (a) and end (b) of the simulation. . . . 171
7.23 a) Capsule filled with 25 mg of 200 micron particles, b) capsule filled with 25 mg of 100 micron particles, c) emitted mass 172
7.24 Emitted mass for free-flowing particles (FF-R) and cohesive particles (C-R). 173
7.25 Position of particles in the capsule at a) 0.1 s, b) 0.2 s, c) 0.3 s, d) 0.5 s, e) 2.0 s, f) 2.4 s. 174

7.26 Configuration after 150 ms a) without cohesion, b) with cohesion. 174
7.27 a) Comparison between the centrifugal acceleration and the acceleration due to vibrations. Values are divided by g (gravitational acceleration); b) direction of capsule rotation (up) and capsule shaking (down). 175
7.28 Position of particles in the capsule at a) 0.1 s, b) 0.2 s, c) 0.3 s, d) 0.5 s (C-RS simulation). 175
7.29 Emission profiles: free-flowing (FF-R), cohesive (C-R), cohesive and shaking (C-RS). 176
7.30 Emitted fraction in C-RS simulation and with the logistic model. 176
7.31 Scatter plot of residence time as a function of initial z coordinate. Points are coloured according to the magnitude of the exit velocity. 177
7.32 a) Exit locations and exit velocity direction, b) exit velocity magnitude. 178
7.33 Number of carrier-wall collision as a function of time for the three simulations. 178
7.34 Scatter plot of impact velocity events for the C-RS simulation. Points are coloured according to the shaking frequency of the capsule. 179
7.35 Collision map for two simulations: a) free-flowing particles, rotating motion only (FF-R) and b) cohesive particles, rotation and shaking motions (C-RS). Points are coloured according to the initial axial position (z_0) of the colliding particle. . 179
7.36 Initial position of particles inside the capsule. The magnification shows the real size of particles. 180
7.37 Position of carrier (grey) and API (magenta) particles in the capsule at a) 0.05 s, b) 0.10 s, c) 0.15 s, d) 0.20 s, e) 0.25 s, f) 0.3 s. API particles are enlarged 10 times to improved visibility. 181
7.38 Total number of API particles in contact with the walls of the capsule. The different colours of the background indicate the different shaking frequencies. 182
7.39 Emitted fraction of API and carrier 182
7.40 Particles exiting from one of the capsule's holes at a) 0.18 s, b) 0.22 s, b) 0.28 s. 182
7.41 a) Mean number of API adhered on a carrier particle, b) percentage of carrier particles fully deaggregated inside the capsule. The different colours of the background indicate the different shaking frequencies. 183

8.1 Initial configurations: a) 10 μm API particles, b) 5 μm API particles. 185

8.2 Covered carrier particle placed on top of the filled cup (a). Configuration of the API particles before (b) and after (c) gravity settling. 187
8.3 Deagglomeration of 10 micron API particles at a) 1.2 ms, b) 1.4 ms, c) 1.7 ms, d) 1.8 ms. 60 L/min gas flowrate. 188
8.4 Dynamic evolution of the first API agglomerate hitting the wall. 188
8.5 Tangential velocity of API particle in an API agglomerate . . 189
8.6 Drag force as a function of particle diameter and voidage degree according to Gidaspow-blend drag model for a relative gas-solid velocity of a) 5 m/s, b) 10 m/s. 189
8.7 Collision duration of a particle-wall impact as a function of normal impact velocity for particles having 5 and 10 micron (mechanical properties reported in Table 8.1, Hertz contact model). 190
8.8 Mean drag force (a), number of API particles on a carrier and percentage of deaggregated API particles (b) for simulations with 40 L/min and 60 L/min inlet flowrate and with 5 and 10 micron API particles. 191
8.9 Powder emission for a) carrier and b) API particles in the three simulations: GIdaspow, CDD, CDD+lift. 192
8.10 Position of the API particles in the three simulations: a) Gidaspow, b) CDD, c) CDD + lift 192
8.11 Average vertical position of the particles over time for the three simulations. a) API, b) carrier. 192
8.12 Comparison between drag, lift, Magnus, pressure gradient forces. a) Direction of forces just before detachment from the carrier (1 ms), b) modulus of forces on API particles during the simulation. Gravity force is $\approx 10^{-3}$ nN. 193
8.13 Detachment of the API from the carrier for the three simulations: a) Gidaspow, b) CDD, b) CDD + lift. 194
8.14 Carrier covered just before the first impact with the wall for the three simulations: a) Gidaspow, b) CDD, b) CDD + lift. 194
8.15 API agglomerates obtained from the simulation in the CDD + lift case. After the impact with the wall, fragmentation takes place. 195
8.16 Average size of API agglomerates as a function of time in the three simulations. 195
8.17 Mean angular velocity with and without fluid torque on carrier (a) and API (b) particles. 196
8.18 Fluid vorticity in the upper part of the swirl chamber ($t = 0.02s$). 197
8.19 Estimate on the effect of fluid torque on (a) a carrier particle ($D = 200\mu m$) and (b) a API particle ($D = 5\mu m$). 197

8.20 Position of carrier particles (grey), API particles (magenta) and fluid streamlines in the swirl chamber for simulations with and without LES-WALE turbulence modelling at a) 1 ms, b) 3 ms, c) 5 ms. API particles are shown with an enlarged size to improve visibility. 60 L/min gas flowrate. 200
8.21 Position of carrier particles (grey), API particles (magenta) and fluid streamlines in the whole inhaler for simulations with and without LES-WALE turbulence modelling at 20 ms. API particles are shown with an enlarged size to improve visibility. 60 L/min gas flowrate 201
8.22 API particles in simulations with and without LES turbulence coloured according to their residence time. Particles in grey are still in the inhaler after 20 ms. 60 L/min gas flowrate. . . 201
8.23 Initial position of API particles in the cup. a) View from the top, b) view from the bottom, c) side view. 202
8.24 Steps to create the initial API-carrier configuration with 10% of API particles (5 μm): a) two ordered layers, b) particles deleted to reach desired dosage, c) configuration after packing. 203
8.25 Scanning electron microscopy images of (a) low (carrier:drug=85:1) and (b) high (carrier:drug=5:1) dosage carrier-drug blends with a 230 μm spherical carrier particle (Young et al., 2011) compared to configuration used in the simulations: c) lower dosage (5%), d) higher dosage (10%). 204
8.26 Particle position inside the inhaler during the simulation at different times: a) 1.5 ms, b) 2 ms, c) 3 ms, d) 5 ms, e) 6 ms, f) 10 ms, g) 12 ms, h) 20 ms, i) 50 ms. 205
8.27 Trajectories of selected API particles (10 % dosage): a) B, b) G, c) R, d) Y. 207
8.28 Number of R, G, B, Y, API in the system in the simulation with a) 5% dosage and b) 10 % dosage. 207
8.29 Number of API particles adhered on a carrier particle for simulations with a) 5% dosage and b) 10 % dosage. 209
8.30 Deaggregation of carrier particle B at a) 25%, b) 50%, c) 75% and d) 100 % of deaggregated API. Simulation with 5% and 10% API dosage per carrier particle covered. 210
8.31 Deaggregation of carrier particle G at a) 25%, b) 50%, c) 75% and d) 100 % of deaggregated API. Simulation with 5% and 10% API dosage per carrier particle covered. 210
8.32 Deaggregation of carrier particle R at a) 25%, b) 50%, c) 75% and d) 100 % of deaggregated API. Simulation with 5% and 10% API dosage per carrier particle covered. 211
8.33 Deaggregation of carrier particle Y at a) 25%, b) 50%, c) 75% and d) 100% of deaggregated API. Simulation with 5% and 10% API dosage per carrier particle covered. 211

8.34 Examples of cluster observed between 5 and 10 ms. 10% dosage. Particles are coloured according to the carrier particle they were initially attached to (red, R; blue, B; green, G; yellow, Y). 212
8.35 Percentage of API particles fully deaggregated for simulations with different weight dosage. 213
8.36 Maximum number of API particles in a cluster for simulations with a) 5% dosage and b) 10 % dosage. 214
8.37 Number of distinct clusters for simulations with a) 5% dosage and b) 10 % dosage. 214
8.38 Two examples of re-agglomerated API particles on carrier located near the ceiling of the swirl chamber. The weight dosage is 10%, 20 ms after the start of the simulation. 215
8.39 API particles moving in the bottom of the swirl chamber after 20 ms. a) 5% weight dosage, b) 10 % weight dosage. 215
8.40 Close up of API particles moving in the bottom of the swirl chamber after 20 ms. a) 5% weight dosage, b) 10 % weight dosage. 216
8.41 Deaggregation stages of API particles from carrier particle G in the salbutamol-lactose system. a) Detachment of the external layers due to fluid dynamic forces; b) configuration before first carrier-wall impact; c) configuration after first carrier-wall impact; d) configuration before second carrier-wall impact; e) configuration after second carrier-wall impact; f) configuration right before emission from the inhaler. . . . 217
8.42 State of the API particles emitted from the inhaler in the first 20 ms for the three simulations considered: budesonide (BUD), 5% dosage; budesonide, 10% dosage; salbutamol (SAL), 10% dosage. 218

List of Tables

1.1 Examples of commercially available dry powder carrier formulation with corresponding drug:carrier weight ratios. The slash indicates that there are two active ingredients. The dosage is reported for each. If different dosages are available on the market, they are indicated with a comma. Adapted from Yeung et al. (2018a). 4

3.1 Domain division, dimensions and number of cells for the three different grids (S_1, S_2, S_3). 68
3.2 Solution obtained with the three different grids. 69
3.3 Results of the validation procedure for the resistance coefficient, R. 70
3.4 Parameters of grid S_0. 70
3.5 Number of rotations in the swirl chamber and average rotation period for particle ID1934. 74

4.1 Properties of the gas phase and the CFD model. 78
4.2 Physical and DEM model properties used in simulations of carrier particles. 78
4.3 Three particles selected from the simulation. 86

5.1 Physical and mechanical properties used in the simulations. 107
5.2 Equilibrium overlap and cohesion energy density for different values of the Bond number. 109
5.3 Escape velocity as a function of Bond number with and without rolling friction. 110
5.4 Escape velocity as a function of the DEM timestep used in the simulations. 110
5.5 Cohesion parameters for VDW and JKR model by considering $Bo = 500$. 124

6.1 Weight dosage ($\varepsilon_w\%$), number of API particles (N_A) and surface coverage (α) for the API-carrier configurations shown in Figure 6.5. 133

6.2 Physical and DEM model properties used in simulations of carrier and API particles. 134
6.3 Exit percentiles of API particles with step and P50 inhalation profiles. t_x = time at which the emitted fraction of the API particles is $x\%$. All times are expressed in milliseconds (ms). 149

7.1 Percentage of particles that exit the system from outlet section and inlet section for the three Lagrangian tracking simulations: 100 μm particles, frozen flow (F100); 50 μm particles, frozen flow (F50); 100 μm particles, transient flow (T100). . 160
7.2 Angular acceleration, initial angular velocity and initial angle for the two traits. 164
7.3 Capsule-wall collision frequency considered in the simulations 167
7.4 DEM simulation parameters 168
7.5 Cohesion parameters and reference pull-off force value 169
7.6 Collision statistics. 179

8.1 Physical and mechanical properties used in the simulations. . 185
8.2 Cohesive/adhesive interaction force and surface energy density. 186
8.3 Characteristics of the first carrier-wall impact for the coated particle: instant and normal impact velocity. 194
8.4 Characteristics of the first API-wall impact in simulations with and without fluid torque. 5 micron, 60 L/min flowrate, CDD polydisperse drag model, Saffman and Magnus forces included. 198
8.5 Percentage of emitted API particles for each API phase; fine particle dose (FPD) and fine particle fraction (FPF) at 20 ms 208
8.6 Percentiles of detachment times of API particles. t_x = time at which the detached fraction of the API particles is $x\%$. All times are expressed in ms. 210

Nomenclature

Acronims

AFM	Atomic Force Microscope
API	Active Pharmaceutical Ingredient
CAB	Cohesive-adhesive balance
CAD	Computer Aided Design
CFD	Computational Fluid Dynamics
COPD	Chronic Obstructive Pulmonary Disease
DEM	Discrete Element Modeling
DPI	Dry Powder Inhalers
DPM	Discrete Particle Method
ED	Emitted Dose
FPD	Fine Particle Dose
FPF	Fine Particle Fraction
LD	Loaded Dose
LES	Large Eddy Simulations
LSD	Linear Spring Dashpot
PIFR	Peak Inspiration Flowrate
PIV	Particle Image Velocimetry
pMDI	Pressurized Metered-Dose Inhalers
RANS	Reynolds Averaged Navier-Stokes equations
RF	Rolling Friction

SEM	Scanning Electron Microscope
STL	Standard Triangle Language or STereo Lithography interface format

Greek letters

ν	Poisson coefficient	
τ_c	Contact time	s
θ	Angle	rad
α	Surface coverage	
δ	Displacement, overlap	m
η	Damping coefficient	
γ	Surface energy	$\mathrm{J/m^2}$
μ_f	Fluid viscosity	$\mathrm{Pa \cdot s}$
μ_r	Rolling friction coefficient	
μ_s	Sliding friction coefficient	
μ_T	Tabor number	
μ_t	Subgrid scale turbulent viscosity	$\mathrm{m^2/s}$
ω	Particle angular velocity	rad
ρ	Density	$\mathrm{kg/m^3}$
ε	Voidage degree	
ε_w	Dosage by weight	

Latin letters

ΔP	Pressure drop	kPa
Δp	Pressure gradient	kPa
$\vec{u}$	Gas velocity	m/s
$\vec{v}$	Particle velocity	m/s
$\vec{w}$	Particle-fluid relative velocity	m/s
A	Hamaker constant	J
a	Radius of the contact area	m

A_{cont}	Contact area	m^2
C_{ou}	Courant number	
d	Particle diameter	µm
e	Coefficient of restitution	
E_{eq}	Equivalent Young modulus	GPa
F	Force	N
g	Gravitational constant	$\mathrm{m/s}^2$
G_{eq}	Equivalent shear modulus	GPa
I	Moment of inertia	$\mathrm{kg} \cdot \mathrm{m}^2$
k	Cohesion energy density	$\mathrm{J/m}^3$
k_n	Normal spring stiffness	N/m
k_t	Tangential spring stiffness	N/m
m	Particle mass	g
M_w	Molecular weight	g/mol
m_{eq}	Equivalent mass	g
N_{part}	Number of particles	
Q	Volumetric inhalation flowrate	L/min
R	Internal resistance of a DPI	$\mathrm{kPa}^{0.5} \cdot \mathrm{min/L}$
r	Particle radius	µm
r_d	Size ratio	
r_ρ	Density ratio	
R_{eq}	Equivalent radius	m
R_{gas}	Ideal gas constant	$\mathrm{J/(mol \cdot K)}$
r_N	Number ratio	
T	Torque	$\mathrm{N \cdot m}$
t	Time	s
T_r	Rolling resistance	$\mathrm{N \cdot m}$

T_ω	Fluid torque	$\mathrm{N \cdot m}$
U_g	Gas velocity magnitude	m/s
V_p	Particle volume	m^3
V_{cell}	Cell volume	m^3
z_{in}	Cutoff distance for cohesion forces	µm
Re_p	Reynolds number for a particle in a fluid	
Re_R	Particle rotational Reynolds number	
Re_S	Particle shear Reynolds number	

Subscripts

θ	Tangential component in cartesian coordinates
b	Pressure gradient contributions
c	Contact contributions
coh	Cohesive contributions
d	Drag contributions
f	Relative to the fluid
i	Relative to i-th particle/fluid cell
j	Relative to j-th particle/fluid cell
n	Normal impact velocity or overlap components
p	Relative to the particle
r	Radial component in cylindrical coordinates
t	Tangential impact velocity or overlap components
x	Longitudinal component in cartesian coordinates
y	Vertical or axial component
z	Trasversal component in cartesian coordinates

Chapter 1

Literature review

1.1 Dry Powder Inhalers

Dry powder inhalers (DPI) are medical devices specifically engineered to ensure maximum and effective delivery of active pharmaceutical ingredients (API) in powder form upon inhalation by a patient. They are commonly applied for the treatment of respiratory diseases, such as asthma and chronic obstructive pulmonary disease (COPD), but several other solutions are under development, e.g. for antituberculosis and anticancer drugs, antibiotics (Hoppentocht et al., 2014) and vaccines, including SARS-CoV-2 (Rashid et al., 2021).

The advantages of DPI compared to other inhalation therapies (such as Pressurized metered-dose inhalers, pMDI) are: absence of propellants, quick drug administration, ease of use, no coordination required, multi-dose devices available (Berkenfeld et al., 2015; Hoppentocht et al., 2014). Also, the activation of the aerodispersion process by the patient's breath facilitates the powder uptake through the respiratory system (Islam and Gladki, 2008), allowing the fine drug particles to reach the lung terminations without the complications due to the barrier protections along the inspiratory ducts. For these reasons, these devices have attracted a growing interest in the last years, so much effort is being devoted to their most efficient design and the optimal corresponding powder formulation.

The dry powder formulations are either drug-based (carrier-free), characterized by the agglomeration of fine particles, or carrier-based, with micronized drug particles attached to coarse lactose carriers (Zheng et al., 2021).

The fine API is designed to be respirable (1-5 μm diameter), in order to reach the lower lung airways, and resulting highly cohesive. Particles larger than 5 μm generally impact on the oropharynx and are subsequently swallowed, while particles smaller than 1 μm do not deposit at all and tend to be exhaled (Figure 1.1).

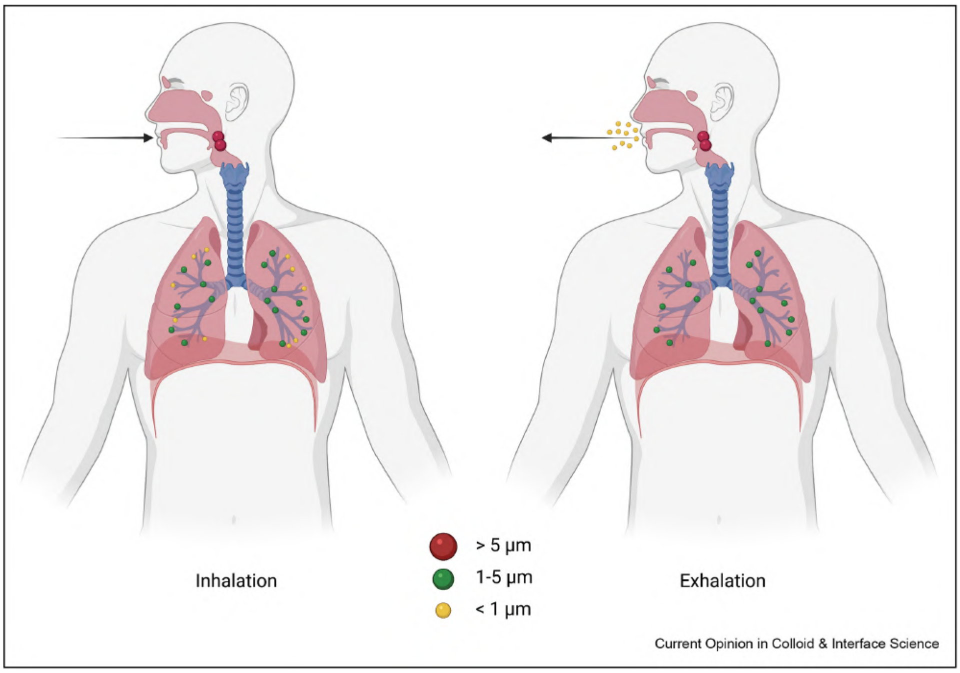

Figure 1.1: Deep lung deposition of particles with aerodynamic diameters of 1 to 5 μm (green). Generally, particles > 5 μm (red) impact on the oropharynx, while the bulk of particles <1 μm (yellow) is exhaled (Zillen et al., 2021).

To improve manufacturability and flow properties, carrier-based formulations are used, in which the API is adhered to coarser carrier particles (50-200 μm). The DPI is then designed to promote the dose aerodispersion and the subsequent "aerosolization", i.e., detachment of the API during inhalation. Microscopically, the delivery process is governed by the local interaction between the air flow dynamics caused by the patient's inhalation and the solids' geometrical, physical, and surface properties (de Boer et al., 2017).

Overall, the powder dispersion process in a DPI is highly complex and involves several intertwined physical mechanisms: hydrodynamic dispersion, including acceleration, turbulence, irregular flow, swirling, particle rotational motion and collisions with the device walls (Kou et al., 2016).

The delivery of the powdered medication is solely based on the interaction between the patient's inspiratory flow and the internal resistance of the dispenser, which is characterized by a complex and tortuous geometry. Microscopically, the resulting delivery process is governed by the local interaction between the hydrodynamics and the solids' geometrical, physical and surface properties, including the possible presence of different and interacting solid phases.

Figure 1.2 shows a schematic illustration of the dispersion mechanisms involved in a DPI. When the patient inhales, the following phenomena might occur:

- the agglomerate breaks up or detaches due to flow-related forces (shear fluidization, turbulence);
- the particle/agglomerate collides with other particles/agglomerates, causing it to break up or a drastic change of movement;
- the particle/agglomerate impacts on the device wall, breaks up into smaller pieces that are entrained back to the air flow or captured by the wall;
- the particle/agglomerate reattaches to another particle/agglomerate to form a new agglomerate.

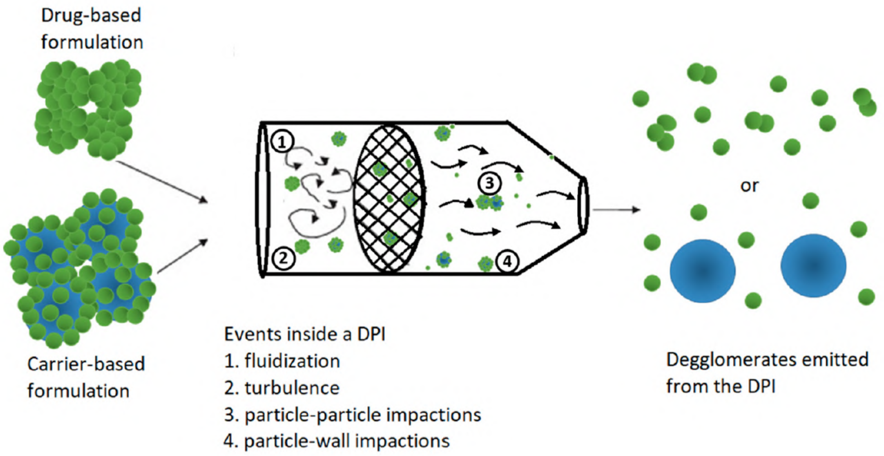

Figure 1.2: Schematics of dry powder inhaler (DPI) dispersion mechanisms. (Zheng et al., 2021)

The first events lead to particle de-agglomeration, whereas the last one is known as particle re-agglomeration, a phenomenon often overlooked in DPI design (Zheng et al., 2021).

The complex interaction between air flow, particle motion and adhesion/cohesion forces among API and carrier particles requires a very careful formulation and manufacture along with an optimal device geometry and flow configuration. The understanding of these factors and the ability to manipulate them is crucial to the achievement of the desired drug delivery (van Wachem et al., 2017; Begat et al., 2004b; Zhou et al., 2013).

1.1.1 Commercially available formulations

Examples of commercially available dry powder carrier formulation for asthma and COPD are reported in Table 1.1.

Product	**Company**	**API**	**Dose content (μg)**	**Total mass (mg)**	**API:carrier (w/w)**
Anoro Ellipta	GlaxoSmithKline	Umeclinidium/Vilanterol	74.2/40	12.5	unknown
Breo Ellipta	GlaxoSmithKline	Fluticasone/Vilanterol	100, 200/25	12.5	1:100
Brimica Genuair	Menarini	Aclinidium/Formoterol	400/12	11	1:27
Foradile Aerolizer	Novartis	Formoterol	12	25	1:2083
Fostair NEXThaler	Chiesi	Beclomethasone/Formoterol	100/6	10	1:94
Seebri Breezhaler	Novartis	Glycopyrronium	63	23.6	1:375
Seretide Accuhaler	GlaxoSmithKline	Fluticasone/Salmeterol	100,250,500/50	Up to 12.5	unknown
Spiriva	Boehringer Inglheim	Tiotropium	22.5	5.5	1:244

Table 1.1: Examples of commercially available dry powder carrier formulation with corresponding drug:carrier weight ratios. The slash indicates that there are two active ingredients. The dosage is reported for each. If different dosages are available on the market, they are indicated with a comma. Adapted from Yeung et al. (2018a).

The majority of pulmonary drugs on the market fall into one of three therapeutic categories (Telko and Hickey, 2005):

- β_2 agonists, such as salbutamol (short-acting β_2 agonist), formoterol (long-acting β_2 agonist) and vilanterol (ultra long-acting β_2 agonist), which cause bronchodilation by relaxing the airway smooth muscles and help to control asthma or COPD symptoms;
- Corticosteroids, such as budesonide, fluticasone and beclomethasone, with an anti-inflammatory effect;
- Anticholinergics, such as tiotropium, glycopyrronium, umeclidinium and aclidinium, which act as muscle relaxants in the lungs and help individuals breathe more easily.

The carrier material is usually lactose, but other sugars such as mannitol or glucose are used as well (Kaialy et al., 2010; Pilcer and Amighi, 2010). Mannitol is also used to treat cystic fibrosis; inhalation of mannitol as a dry powder changes the viscoelastic properties of airway secretions, contributing to an increased mucociliary and cough clearance of retained secretions (Flume et al., 2015).

Excipients are often added to the dry powder formulation. It has been shown that lactose fines increase the performance of the inhaler (Yeung et al., 2018b), favouring API detachment from the carrier and deagglomeration phenomena. The fines either occupy carrier surface areas of high adhesion or they tend to co-agglomerate with the drug particles on the carrier surface. Supporting evidence exists for both mechanisms but also contradicting conclusions can be found in literature (de Boer et al., 2012). Lactose blends are by far the most common and have been in use since the

1960s (Clark et al., 2020), but other sugars, such as mannitol or trehalose, are also used as excipients. Aminoacids such as leucine are used as well, due to their surface-active properties that change surface composition and morphology of the resulting particles (Zillen et al., 2021).

Other attempts to improve dispersion of lactose carrier based formulations are modulation of the carrier particle rugosity, for example by surface smoothing in a high-shear mixer, and reduction of the interparticulate bonds between drug and carrier particles with the use of force control agents (FCAs), like magnesium stearate. The first DPI containing such FCAs are NEXThaler® from Chiesi and Breezhaler® from Novartis (Hoppentocht et al., 2014).

1.1.2 DPI design

The design of a DPI is complex as there are multiple components that need to be considered for efficient aerosol dispersion and enhanced performance of a formulation. There is ongoing research into DPI devices either through optimisation of current marketed devices or via development of novel devices (Yeung et al., 2018a).

DPI can be categorised into two fundamental inhaler designs:

- single-dose capsule DPI;
- multidose DPI.

Capsule-based devices, such as Cyclohaler®, Aerolizer®, RS01® and Handihaler®, are single unit-dose DPI equipped with a capsule containing powder formulation that is placed into a capsule chamber. A piercing mechanism allows the formulation to be aerosolised by using inspired air to generate an air flow and turbulence for aerosol dispersion. Even though considered an older technology, capsule-based inhalers are still widely used, as they offer a very good performance with carrier-based formulations thanks to the spinning motion of the capsule (Martinelli et al., 2015; Buttini et al., 2018).

Multidose DPI are a second generation technology. They are already loaded with multiple doses of the medication, and thus do not require reloading after each use. Two different type of multidose DPI are available (Laube et al., 2011):

- premetered factory dispensed doses, which are packaged inside blisters (such as Diskus®);
- reservoir-based devices, in which a bulk of the formulation is stored in a large powder reservoir and the single dose is metered by the patient before inhalation. Examples of such inhalers are Turbuhaler® or Novolizer®.

Newer generation of reservoir-based inhalers are NEXThaler® (Chiesi) and Genuair® (AstraZeneca). The NEXThaler® contains 120 doses and has the addition of a breath actuated mechanism (BAM), dispensing individual doses of approximately 10 mg of carrier formulation into a dosing chamber which is covered by a plastic sleeve dose protector. The Genuair® inhaler device was developed from the Novolizer®, but does not require reservoir cartridge loading and is disposable (Yeung et al., 2018a).

While the inhaler designs differ, the varying formulations within them all require the patient to supply the energy to fluidize the powder, dispense it from the inhaler during inhalation, and disperse the formulation sufficiently well so that the drug component of the aerosol can penetrate and deposit in the lungs.

To achieve this dispensing and dispersing, the formulations have been developed in conjunction with design elements of the inhalers, such as swirl chambers, grids, and orifices. These design elements, which differ between DPI, present varying degrees of airflow resistance and result in DPI with differing pressure drop/flow rate characteristics. In general, the flow rate though a DPI (Q) is proportional to the square root of the pressure drop (ΔP) the patient develops across it:

$$\sqrt{\Delta P} = Q \cdot R \tag{1.1}$$

The constant of proportionality is termed the device resistance, R.

Figure 1.3 presents flow rate resistance curves for a variety of inhalers, covering a range of pressure drops that are typically achievable by patients (2 - 6 kPa). Patients inhale faster through low-resistance devices and slower through high-resistance devices because the pressure drops they generate tend to be similar.

Powder dispersion generally improves as pressure drops and inhaled flow rates increase, because the increased energy supply disperses the powder more effectively. At the same time, oropharyngeal filtering, which removes drug in the upper respiratory tract, increases with increasing flow rates due to inertial impaction (Clark et al., 2020).

The resistance coefficient is usually referred to the maximum flowrate during inhalation, i.e., the peak inspiration flowrate (PIFR). However, the time taken to achieve the PIFR can also be important (Clark et al., 2020). Some powder inhalers deliver their dose rapidly following the start of an inhalation, and a major fraction of the dose can be delivered before the patient reaches the PIFR. Figure 1.4 shows the relationship between dose emission from a DPI and the patient's inhalation. It can be seen that the flow acceleration is particularly important and plays a major role in pulmonary drug delivery.

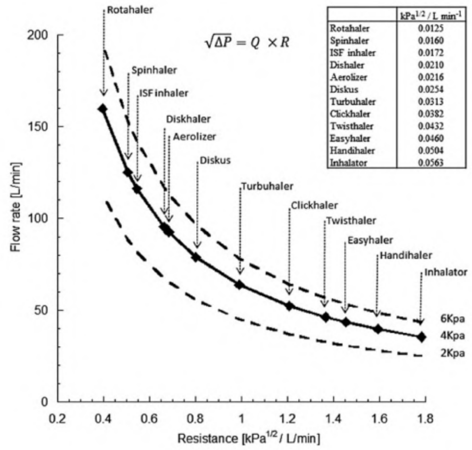

	kPa$^{1/2}$ / L min^{-1}
Rotahaler	0.0125
Spinhaler	0.0160
ISF inhaler	0.0172
Dishaler	0.0210
Aerolizer	0.0216
Diskus	0.0254
Turbuhaler	0.0313
Clickhaler	0.0382
Twisthaler	0.0432
Easyhaler	0.0460
Handihaler	0.0504
Inhalator	0.0563

Figure 1.3: Flow rate versus device resistance for several commercial DPI. Points are at a 4 kPa pressure drop. Lines are also presented for pressure drops of 2 and 6 kPa (Clark et al., 2020).

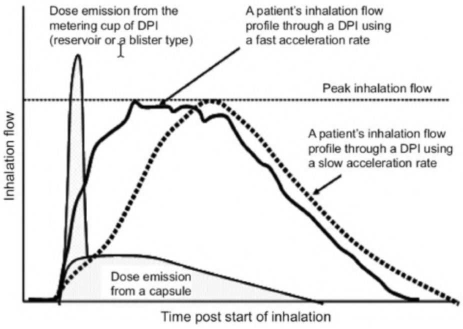

Figure 1.4: The relationship between dose emission from a DPI and the patient's inhalation (Clark et al., 2020).

1.1.3 Efficiency of DPI

For an ideal DPI, a number of characteristics are important for device reliability, clinical efficacy and patient acceptance (Islam and Gladki, 2008).

Pulmonary drug administration will only result in an effective and safe therapy when the inhaler is able to reproducibly deliver a high fine particle dose to the site of action in the respiratory tract (Hoppentocht et al., 2014).

The efficiency of DPI is generally defined and characterized by the following experimentally measurable macroscopic parameters (Young et al., 2005):

- the loaded dose (LD) is the total mass of fine drug powder initially placed in the inhaler;
- the emitted dose (ED) is the total mass of powder that has left the

inhaler;

- the fine particle dose (FPD) is the mass of respirable particles that have left inhaler, i.e., with a diameter smaller than a cutoff diameter (typically in the range of 5 μm);
- the fine particle fraction (FPF) is the ratio between fine particle dose and fines initially present in the inhaler (LD);

A higher FPF correlates with a more efficient deaggregation and a reduced oropharyngeal deposition. Of course, a high FPF device is a high efficiency device, as more API reaches the lower airways and API waste is minimized.

The oropharyngeal deposition can be predicted from the inertial parameter, defined as: d_pQ^2, with d_p being the particle diameter (μm) and Q the fluid flowrate (cm^3/s). The higher the inertial parameter, the higher the oropharyngeal deposition (Coates et al., 2005a).

The FPF is correlated to the inhaler resistance, R. Inhalers with more powerful dispersion principles tend to have higher resistances (Hoppentocht et al., 2014). However, devices with higher resistance need a higher inspiratory force by the patients to achieve the desired air flow. This could be difficult for patients with severe asthma and for children and infants. Therefore, a balance between these two factors is necessary to achieve the desired therapeutic effect from DPI formulations (Islam and Gladki, 2008).

Due to the poorly understood microscopic dynamics, experimental results show that the average efficiency of DPI (i.e., the FPF) is relatively low, usually ranging from 20% to 40% (Sommerfeld et al., 2019).

1.2 High dosage DPI

The development and use of DPI has originally been focused on diseases like asthma and COPD. The pulmonary route for these applications is particularly convenient as it provides a rapid, direct access to the site of action which translates into immediate effectiveness of the treatment (Hoppentocht et al., 2014).

In recent years, it has been observed that the administration of drug by inhalation may have other applications. Pulmonary drug delivery seems to be a promising alternative to conventional drug administration routes for vaccines, anti-virals and antibiotics, that can be used for the treatment of cystic fibrosis, diabetes, tuberculosis, influenza, lung cancer, lung infections, COVID-19 (Scherließ and Etschmann, 2018; Yeung et al., 2018b; Hickey and da Rocha, 2019; Rashid et al., 2021). Most of these applications require the delivery of high doses of active pharmaceutical ingredients, in the range of milligrams (Yeung et al., 2018a). For comparison, the highest API dosage

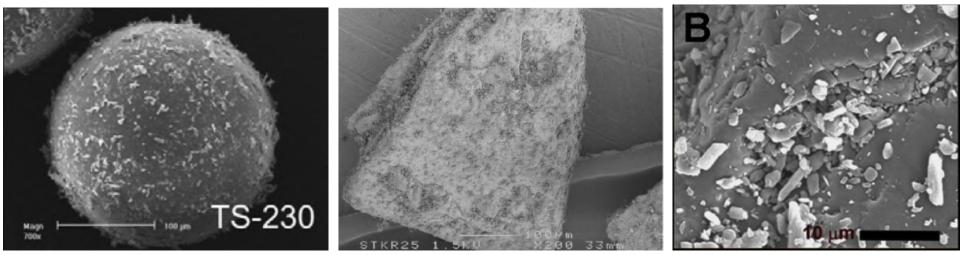

(a) **(b)** **(c)**

Figure 1.5: API particles placed on a a) spherical polystyrene carrier ($\approx 200\mu$m) (Young et al., 2011) and b) tomahawk lactose carrier ($\approx 200\mu$m) (Dickhoff et al., 2003). c) API particles trapped in crevices of an irregular, non spherical surface (Young et al., 2005)

for asthma treatment product available in the market is 550 μg (see e.g. Table 1.1). The fact that pressurised Metered Dose Inhalers (pMDI) are only able to deliver a maximum of 500 μg API in a single shot, make Dry Powder Inhalers (DPI) the first choice in high dose formulation (Scherließ and Etschmann, 2018).

High drug contents may increase the influence of the physico-chemical drug properties on the behaviour of the powder formulation during inhalation (Hoppentocht et al., 2014). The fine API particles are subjected to strong van Der Waals forces (Begat et al., 2004a), liquid bridge interactions (Di Renzo et al., 2020), triboelectric charging phenomena (Zafar et al., 2018), with poor flowability properties (Finlay, 2001). These systems have generally low performances, and are highly sensitive to changes in morphology, dose, carrier (Young et al., 2005).

Figure 1.5 show SEM images of carrier particles with a similar size but different shape and morphology: spherical polystyrene (Figure 8.25b) and tomahawk lactose (Figure 1.5b and 1.5c)

Carrier particles such as crystallised tomahawk lactose (Figure 1.5b) are characterized by a heterogeneous surface, containing pits and crevices, where API particles can be trapped, as shown in Figure 1.5c. This irregular surface will have regions of high adhesion, where the API will preferably adhere; these regions are usually referred to as "active sites" (Young et al., 2011).

The theory of active sites is illustrated in Figure 1.6. If the adhesion force is greater than the energy due to inhalation, particles will remain adhered to the surface. Subsequently, at low drug loadings the aerosolised drug concentration will remain low. As the drug loading increases, the higher adhesion sites are preferentially filled followed by lower adhesion regions, resulting in a relative increase in aerosolised drug dose. These two potential mixing effects may be referred to as Type I and II regions. As the drug loading is increased, it is envisaged that many of the remaining areas on

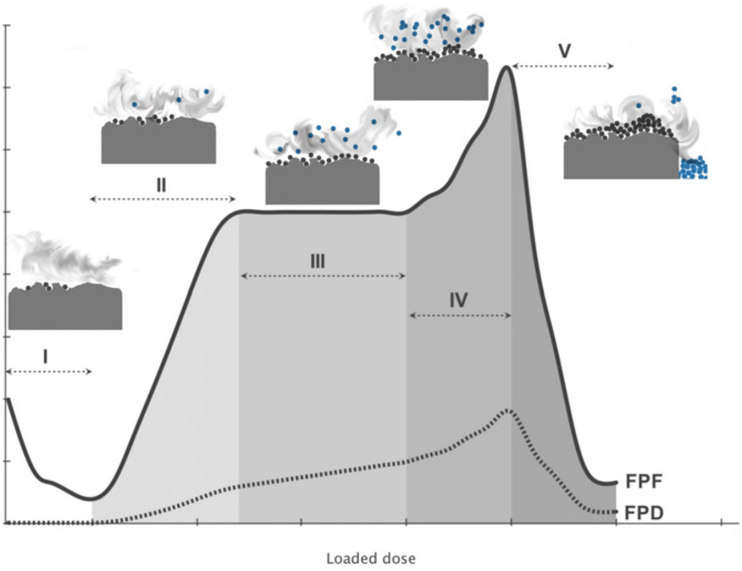

Figure 1.6: Theoretical blend structure and influence on fine particle dose and fraction as a function of drug-carrier loading. (I) High adhesion site filling (adhesion >> aerosol energy), (II) filling of intermediate sites (adhesion ≈ aerosol energy, (III) region of constant aerosol performance (adhesion << aerosol energy), (IV) transition stage between monolayer/multilayer particulate system and (V) multi-layer particle formation and formulation segregation. (Young et al., 2011)

the carrier surface will have significantly lower adhesion forces and constant aerosol performance will be reached (Type III regions) where increased drug loading will result in a concurrent increase in aerosolised dose and constant aerosolised fraction, with a corresponding plateau in aerosol performance. As the drug loading is increased further it would be likely that multiple agglomerate systems are formed, as the available space on the carrier will approach a monolayer. As this Type IV region occurs, a further increase in performance would be expected to be observed since the ”effective” mass of the attached drug particles is increased due to multiplet formation. Finally, at very high drug loadings (Type V) the formulation begins to fail due to mass agglomeration and formulation segregation.

The transition from low to high dosages requires therefore changes in the powder formulation and in the dispersion process. This can either be obtained through a device specifically designed to deliver high powder doses (Claus et al., 2014), modifications of existing inhalers or by particle engineering techniques to obtain well dispersible powders. Some examples are the addition of excipients, the reduction of the size of the carrier, the reduction of roughness and surface irregularities of the carrier (Yeung et al., 2018a).

Dickhoff et al. (2003) carried out experiments on a lactose-budesonide blend at different drug dosages (0.4 - 6 % w/w) and evaluated the residual drug on the carrier. They found that the percentage of API residual on the carrier increases with dosage if the flow rate is 30 L/min. An opposite trend, however, is observed for higher flowrates, suggesting that changes in the balance between adhesion and separation forces during inhalation involves different phenomena for high-dose systems. Yeung et al. (2018b) evaluated the dispersion of micronized beclomethasone dipropionate (BDP) in a ternary blend. They observed the formation of increase in the total cohesive force with increasing BDP concentration, which lead to an increased number of large agglomerates after inhalation.

A linear increase of the fine particle dose with loaded dose was found by Young et al. (2011), who considered spherical polystyrene carrier particles covered with salbutamol. The linear trend, however, is not confirmed at a drug:carrier ratio higher than 1:10, for which aggregation phenomena of the API make the blend not homogeneous.

Young et al. (2005) carried out experiments with a lactose-salbutamol blend in the Cyclohaler, by considering different dosages. They observed the presence of a critical adhesion limit at high dosages, above which the formation of multi-layer particle aggregates and segregation phenomena occur.

The results obtained experimentally are often conflicting. Moreover, the mechanism of drug particle liberation is still not clear as it is difficult to obtain detailed information on microscopic scale phenomena with a macroscopic experimental approach.

1.3 Experimental analysis

The performance of DPI is usually evaluated *in vitro*, using specific characterization apparatuses that reproduce human airways with the aim to quantify properties such as dose uniformity, emitted powder mass and fine particle fraction.

Different methods are available for collecting data ”outside” of the inhaler:

- Air flow rate and pressure drop profile can be recorded at the inlet and outlet sections with flowmeters and pressure transducers;
- Particle and droplet emission time and size distribution can be measured at the device outlet, optically or via cascade impactors;
- Temperature and the shape of aerosol plumes can be imaged with fast thermo-cameras.

On the other hand, measuring what happens inside DPI devices is definitely more complex. X-ray-based methods are used to image fast phenomena, such as the initial lift of carrier particles, but quantitative data are quite difficult to obtain (Benassi and Cottini, 2021).

1.3.1 Cascade impactors

Cascade impactors are the most widely used instruments for sizing aerosols; they are recommended by regulatory authorities including the United States Pharmacopeia, European Pharmacopoeia and Chinese Pharmacopoeia (Zhang et al., 2020).

Cascade impactors contain several stages, with orifices of decreasing size. A cut-off diameter is associated with each stage of the impactor. When the aerosol is drawn through the impactor, the particles deposit on different stages, based on their inertia. After each run, the impactor is disassembled and the mass of particles deposited on each stage is determined, mostly via analytical methods (Telko and Hickey, 2005).

Some of the commonly used cascade impactors are:

- Twin stage impinger;
- Multistage impinger;
- Electrical Low Pressure Impactor (ELPI);
- Next Generation Impactor (NGI, Copley Scientific Ltd., Nottingham, UK), shown in Figure 1.7;
- Andersen Cascade Impactor (ACI, Copley Scientific Ltd.).

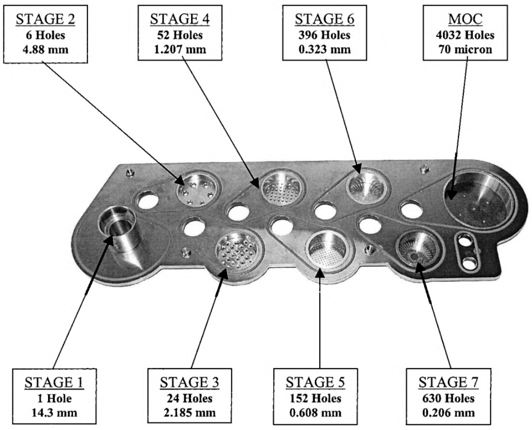

Figure 1.7: Stages of the NGI (Marple et al., 2004).

One of the advantages of these techniques is that they directly measure aerodynamic size (Telko and Hickey, 2005). However, cascade impactor experiments are time-consuming and laborious due to complicated experimental operations and the subsequent quantification of APIs, which can take several days or even weeks (Zhang et al., 2020).

1.3.2 Laser diffraction techniques

Laser diffraction techniques are widely used in formulation development to determine particle size distribution of granular material. The operating principle is based on the fact that different size particles diffract the light at different angles (Telko and Hickey, 2005).

Inhaler adapters have been specially designed to allow the integration of laser diffraction instruments with dry powder inhalers, aiming at detecting the particle sizes of inhaled aerosols.

Zhang et al. (2020) modified a Sympatec HELOS by integrating an inhaler device, artificial throat and preseparator. The setup was employed to investigate the dispersion and fluidization processes of DPI. The artificial throat was used to simulate the direction changes of air flow, and the preseparator was applied to mimic bronchi bifurcation. Such applications are promising as they represent a novel approach for real-time monitoring pulmonary delivery process of DPI transportation and detachment processes.

1.3.3 Image analysis techniques

Powerful optical techniques are today available for image analysis and measurements. Such techniques have recently been applied to DPI, to gain useful insights in the mechanism of powder fluidisation and subsequent drug release into the complex air stream within DPI.

Particle Image Velocimetry (PIV) has been used to obtain instantaneous velocity measurements of the fluid flow in DPI (Dos Reis et al., 2021; Pasquali et al., 2015; Fletcher et al., 2021). The fluid is seeded with tracer particles which, being sufficiently small, faithfully follow the flow dynamics. The fluid with entrained particles is illuminated so that particles are visible. The motion of the seeding particles is used to calculate the velocity field of the flow being studied.

High-speed photography measurements have been applied to study carrier motion (Pasquali et al., 2015; Merusi et al., 2018), capsule movement (Benque and Khinast, 2019) and API-carrier detachment phenomena (Kou et al., 2016) in specially designed transparent DPI.

While light-scattering and imaging methods are very useful in the characterization of raw materials (e.g., drug particles or excipient particles), cascade impaction is more useful in determining the fine-particle fraction, so it is a better measure of the performance of the formulation. The different methods complement each other (Telko and Hickey, 2005).

1.4 Modelling of DPI

In helping the development of increasingly efficient and effective devices, numerical simulation tools can be a valuable ally, owing to their ability to reproduce the local air-particle flow with good accuracy.

1.4.1 Modelling of the fluid phase

Computational Fluid Dynamics (CFD) is widely used in the design of different types of inhalation devices and to determine aerodynamic paths and turbulent flow effects (Wong et al., 2012; Ruzycki et al., 2013; Milenkovic et al., 2013). CFD studies have become popular thanks to the availability of commercial softwares that offer a wide range of fluid dynamic models.

Due to the complex geometry of the DPI flow passage and the relatively high flow rate, the problem is normally considered to be turbulent, which is characterised by the presence of a wide range of time and length scales in the flow field. Capturing all the turbulent time and length scales requires very fine spatial and temporal discretization, making most computation attempts impractical even with the powerful computational resources available today. For DPI applications, the turbulence is normally not resolved directly but relying on RANS turbulence models (Zheng et al., 2021; Sommerfeld et al., 2019).

Coates et al. (2004) carried out some of the earliest simulation work on DPI. The flow field in the Aerolizer has been studied through RANS equations and $k-\varepsilon$ SST turbulence model, as shown in Figure 1.8.

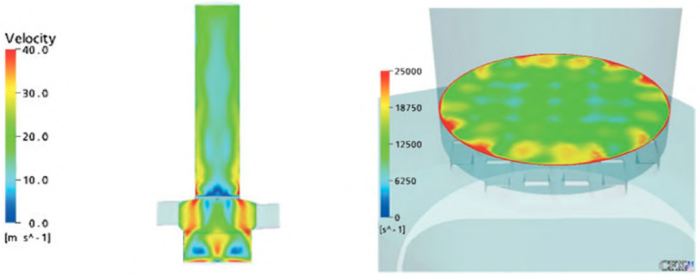

(a) (b)

Figure 1.8: Calculated velocity profile (a) and turbulence scale (b) of an Aerolizer using RANS with $k-\varepsilon$ SST turbulence model (Coates et al., 2004).

Due to the limitations of RANS, simulations might not be capturing all details of the swirling flow generated in the devices.

More recent studies use more refined turbulence models, such as Reynold Stress Model or LES approach (van Wachem et al., 2017; Milenkovic et al., 2013; Tong et al., 2010). However, Milenkovic et al. (2013) found that although significant turbulence non-homogeneity and anisotropy were shown in the flow field, only some local differences in the secondary flow prediction were observed between LES and $k-\omega$ SST model.

A higher detail can be obtained using LBM (Lattice-Boltzmann Method), which has been used to study fluid stresses acting on API and carrier particles (Cui et al., 2014; Cui and Sommerfeld, 2015, 2018).

1.4.2 Modelling of the solid phase

The motion of the powder inside the DPI is often modeled in a Lagrangian way (Sommerfeld and Schmalfuß, 2016; Coates et al., 2005a; Milenkovic et al., 2014, 2017); particles are considered as point-masses and tracked in post-processing, after the stationary fluid field is solved. Collisions between solid particles are binary and instantaneous. Such approach is computationally expensive for the fluid phase but requires relatively limited effort to track the particles along the motion. However, it is limited to dilute systems of fine particles, for which particle inertial effects, rotational motion and collisions can be neglected or largely simplified without sacrificing accuracy.

DEM (Discrete Element Method, Cundall and Strack (1979)) is also a valide alternative, since it allows multiple particle contact and takes into account solid deformations for a detailed study of impacts and contact forces between solid bodies (Ariane et al., 2018; Cui and Sommerfeld, 2019; Yang et al., 2015a).

DEM has been used to build micro-scale models that can be incorporated in macro-scale simulation of prototype inhalers (van Wachem et al., 2017; Tong et al., 2015a).

Ariane et al. (2018) developed a simple model based on DEM to estimate how much API is detached from a carrier after a wall collision, as shown in Figure 1.9.

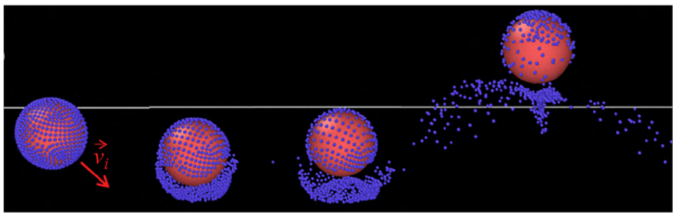

Figure 1.9: Detachment of API particles due to carrier-wall collision (Ariane et al., 2018).

Their model is based on the calculation of the dispersion ratio, i.e., the

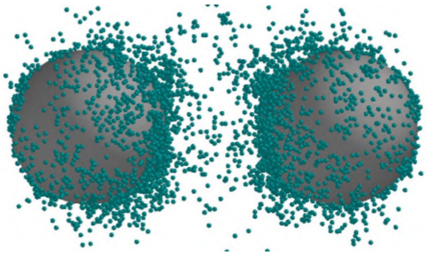

Figure 1.10: Impact of adhesive units with lactose fines and lactose carrier. (Sarangi et al., 2021)

ratio between the "detachment" area and the total surface area of the carrier particle, which is a function of impact angle and impact velocity.

Sarangi et al. (2021) studied deaggregation of API particles by carrier-carrier impact (Figure 1.10), analyzing the effect of the size of the carrier particle.

Tamadondar and Rasmuson (2020) analysed the dispersion of API particles due to collisions considering carrier particles with different roughness levels.

1.4.3 Multiphase simulations

DEM can be coupled with CFD technique for multiphase simulations. The detailed treatment of particle-particle and particle-wall contacts and the possibility to study dense system with a 4-way coupling approach has attracted a considerable interest in the recent years (Sommerfeld et al., 2019; Tong et al., 2015b; Yang et al., 2015b).

The CFD–DEM technique in the study of DPI has been applied to study the formation and breakdown of agglomerates (Tong et al., 2009) or to evaluate the mechanisms of aggregation and deaggregation of active principle particles adhered on carrier particles (Tong et al., 2017; Nguyen et al., 2018).

Tong et al. (2016) investigated the behaviour of agglomerate-agglomerate collision based on a combined computational fluid dynamics (CFD) and discrete element method (DEM) approach, aiming to develop better understanding of the underlying the mechanisms of loose drug agglomerates aerosolisation in DPI.

Benque and Khinast (2019, 2021, 2022) carried out CFD-DEM simulations on a capsule-inhaler system, highlighting the importance of the inhalation profile generated by the patient and the dominant role of capsule-wall collisions, which help to break up particle clusters and allow an easier powder discharge from the capsule.

Recently, careful CFD–DEM simulations have proved effective in reproducing the flow of air and relatively large (i.e. carrier) particles in a commercial DPI geometry (Ponzini et al., 2021). In aiming to achieve quantitative and predictive simulations of DPI, the authors employed an implicit approach where only the carrier particles are simulated, while fine API particles are treated as a continuum phase diluted in air. This approach allows for the simulation of a realistic powder concentration, even though requiring a huge effort in the parametrisation of the API release from carrier particles (Benassi and Cottini, 2021).

Despite the efforts in building linked multi-scale models where simulations of particle-scale systems are used to develop a model to be used in a four-way CFD–DEM simulation at the device scale (see e.g. van Wachem et al. (2017)), the study of the API-carrier phenomena occurring in the entire inhaler with the CFD-DEM approach is still a little explored topic (Zhao et al., 2022; Tong et al., 2017; Benassi and Cottini, 2021). Whilst the direct simulation of the fine API solid phase in combination with the coarse carrier is particularly rich of information on the details of the fines' deaggregation process, it poses severe limitations associated with the microscopic size of the API particles (<5 μm), which requires the use of an extremely small timestep and a consequent substantial increase of the computational resources required, especially considering that millions of particles need to be simulated. There are also difficulties related to the size of the Eulerian computational cells, which in the non-resolved CFD–DEM coupling must be large enough to contain at least one of the coarse particles.

Despite these limitations, it is worth evaluating the feasibility of a direct study of the coupled carrier-API motion, in order to gain a better understanding of the factors involved in such dispersion and API aerosolization process.

1.5 Research objective

In this work, highly challenging CFD–DEM simulations are utilized to deterministically track the motion of both carrier and API particles in dry powder formulations along their flow from the dose cup through the exit of a swirl-flow-based Dry Powder Inhaler.

To achieve this purpose, a combination of different solutions is progressively adopted: a sufficiently small time-step is coupled to scaled contact/adhesive interaction parameters; grid-based contact detection and fluid-to-particle and particle-to-fluid interpolation of the gas-solid interaction variables, i.e. gas velocity and voidage and drag force; specific models for fluid-solid interactions; a rolling friction model to allow for appropriate adhesion behaviour of the particles.

Single phase air-flow, coupled air-carrier particle flow and coupled air-carrier-API particles will be characterized for different typical inhalation conditions and in two different inhaler configurations. The aim is to investigate and gain detailed insight on all stages of the particles' lift-up, aerodispersion, de-aggregation, inter-particle and particle-wall collisions across the scales from few micron sized API powders to a commercial sized device. Thanks to a 4-way coupled CFD–DEM model, inertial, collisional, rotational and inter-particle adhesion effects can be taken into account in modelling the coupled air and particle dynamics.

1.6 Thesis layout

Chapter 1 introduces the peculiarity and challenges of Dry Powder Inhalers and reviews the current research. The objectives and the thesis layout are presented.

In Chapter 2, the CFD-DEM approach is presented, along with the physical models used.

In Chapter 3, the softwares used for simulations and post-processing are summarized. The geometries and computational grids used throughout the work are described as well.

In Chapter 4, the design and modelling of a swirl-based DPI is presented. The fluid flow and carrier particle motion are characterized and effect of different parameters on powder dispersion is evaluated.

In Chapter 5, API particles are introduced in the simulation by considering a single coated carrier particle first. The detachment of API due to carrier-wall collision is analysed with a specific focus on cohesive models. A simple analytical model to relate impact velocity and API detachment is developed.

In Chapter 6, API particles are introduced in the full simulations of the swirl-based inhaler and API deaggregation and emission is analysed as a function of different parameters.

In Chapter 7, the analysis of a commercially available capsule-based DPI is performed through accurate CFD simulations with Lagrangian tracking of carrier particles. The influence of the motion of the capsule on powder dispersion is evaluated with DEM simulations of both carrier and API particles.

In Chapter 8, the delivery process of high dosage formulations from dry powder inhalers is studied by considering selected carrier particles coated with 5% and 10% (w/w) of a 5 μm API. The deaggregation process is studied in detail and an analysis of the most appropriate fluid-solid interaction models is presented. API deaggregation and emission stages are also characterized as a function of the initial dosage and particle position.

Chapter 2

CFD-DEM approach

To model fluid-particle flows, Euler-Euler and Euler-Lagrange approaches are used as most common combinations. In the Euler-Euler approach, both fluid and solid phases are considered as continuum phases, while the Euler-Lagrange approach considers a combination of computational fluid dynamics (CFD) and the discrete element method (DEM), referred as CFD-DEM.

Two different formulations are available for CFD-DEM technique. If the size of the fluid cells is much smaller than the particles, the approach is referred to as resolved CFD-DEM. If, on the other hand, the size of fluid cells is larger than particle size, the approach is referred to as unresolved surface CFD-DEM. The two formulations are shown in Figure 2.1

In the resolved CFD-DEM, fluid flow is fully resolved over the entire surface of particles and detailed profiles of fluid fields are obtained around all particles. These profiles are then integrated to obtain the total hydrodynamic forces acting on individual particles. Since the computational cost of solving the fluid phase equations over the entire grid cells is high, this treatment is only feasible for systems containing no more than a few hundred particles.

In the unresolved CFD-DEM, systems containing thousands or even millions of particles can be studied. The coupling between solid phase at particle scale and fluid phase at fluid cell scale is done via drag force and with empirical or theoretical correlations developed for the flow across a single particle or an assembly of particles. However, the effect of the presence of particles on local changes of flow profile inside the fluid cell is neglected.

2.1 Modelling of the fluid phase

The resolution of the fluid phase using computational fluid dynamics, CFD, starts from the assumption that the fluid is a continuous medium.

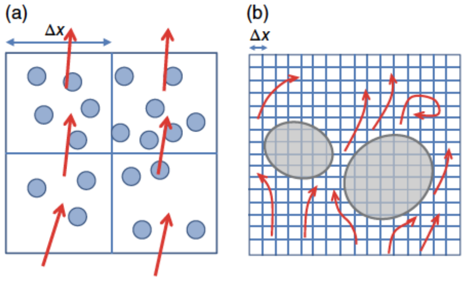

Figure 2.1: Different representations of the particle treatment: (a) unresolved surface method ($\Delta x \gg D$) and (b) resolved surface method ($\Delta x \ll D$)). Adapted from Norouzi et al. (2016).

2.1.1 Governing equations

The equations solved in CFD are the Navier-Stokes equations (Batchelor, 2000), the mathematical formalization of three conservation principles (also referred to as balance equations):

- mass conservation principle;
- momentum conservation principle;
- energy conservation principle

The mass conservation principle, or continuity equation, is expressed by the following:

$$\frac{\partial \rho_f}{\partial t} + \nabla \cdot (\rho_f \vec{u}) = 0 \tag{2.1}$$

where ρ_f is the gas density, and $\vec{u}$ the velocity vector.

The momentum equation is expressed by:

$$\frac{\partial}{\partial t}(\rho_f \vec{u}) + \nabla \cdot (\rho_f \vec{u} \times \vec{u}) = -\nabla p - \nabla \cdot \hat{\tau} + \rho_f \vec{g} \tag{2.2}$$

where $\vec{g}$ is the gravity acceleration vector, p is the hydrostatic pressure, and $\hat{\tau}$ is the stress tensor. If the fluid is Newtonian (i.e., viscosity constant with the rate of deformation) and Stokesian (i.e., advective inertial forces small compared with viscous forces), the stress tensor is expressed by (van der Hoef et al., 2008):

$$\hat{\tau} = -\left(\lambda - \frac{2}{3}\mu_f\right)(\nabla \cdot \vec{u})\hat{I} + \mu_f(\nabla \vec{u} + (\nabla \vec{u})^T) \tag{2.3}$$

with λ and μ_f being the coefficients of bulk and shear viscosity, respectively, and $\hat{I}$ the unit tensor.

A gas flow can be defined as incompressible when its volume is not easily modifiable with the application of pressure. This condition can be verified using the Mach number, defined as the ratio between the velocity of the flow and the velocity of sound in the medium. A Mach number less than 0.3 identifies the flow as incompressible, and consequently, since the volume can be assumed to be constant, the density is constant:

$$\rho_f = \rho_{f0} \tag{2.4}$$

where ρ_{f0} is a constant.

For higher Mach numbers, the density is a function of pressure: $\rho_f = \rho_f(P)$. The simplest and the most used correlation is the ideal gas law:

$$\rho_f = \frac{p\ M_w}{R_{gas}\ T_k} \tag{2.5}$$

where p is the pressure, M_w the fluid molecular weight, R_{gas} is the ideal gas constant and T_k the absolute temperature.

On the other hand, at high pressure and low temperature, the behavior of real gases deviates from the prediction of the ideal gas equation. This change of behavior results from the molecules of the gas taking up a significant portion of the total volume as the gas density increases. In addition, intermolecular attractive forces become increasingly important. The van der Waals equation is given by:

$$\left(p + a_{vdw}\ \rho_f^2\right)(1/\rho_f - b) = R_{gas}T_k \tag{2.6}$$

van der Waals introduced the constant b, the "co-volume" of the particles, and the constant a_{vdw}, a measure of the attractive forces. There parameters are evaluated based on the experimental observation. Similar modifications using terms with temperature and pressure dependencies can be used in case the fluids are near the phase change (Redlich-Kwong, Soave-Redlich-Kwong, Modified Soave-Redlich-Kwong).

If incompressible flow condition is verified, the equations become:

$$\nabla \cdot \vec{u} = 0 \tag{2.7}$$

$$\frac{\partial}{\partial t}\vec{u} + (\vec{u} \cdot \nabla)\vec{u} = -\frac{1}{\rho_f}\nabla \mathrm{p} + \frac{\mu_f}{\rho_f}\nabla^2\vec{u} + \rho_f\vec{g} \tag{2.8}$$

2.1.2 Turbulence

A fundamental dimensionless number in the field of fluid dynamics is the Reynolds number, which is the ratio between fluid's inertia and viscous damping in a fluid flow.

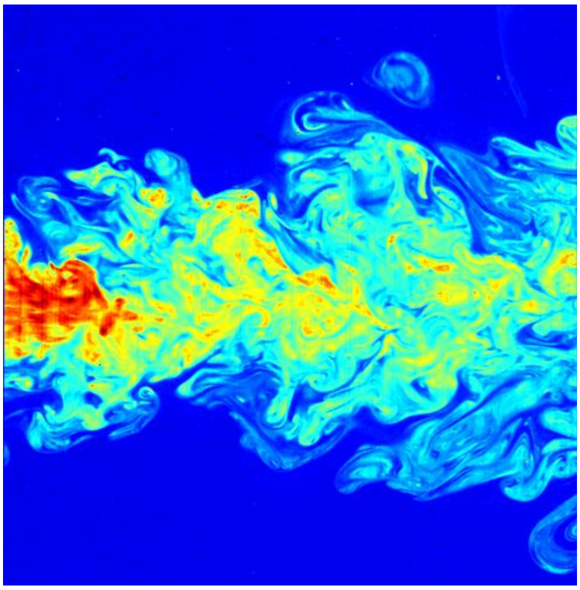

Figure 2.2: Submerged turbulent jet. Credits: C. Fukushima and J. Westerweel, Technical University of Delft, The Netherlands, CC BY 3.0 `<https://creativecommons.org/licenses/by/3.0>`, via Wikimedia Commons.

Reynolds number is defined as:

$$Re = \frac{\rho_f U L}{\mu_f} \tag{2.9}$$

where ρ_f is the density of the fluid, U is a characteristic velocity of the fluid with respect to a reference object, L is a characteristic flow length scale, μ_f is the dynamic viscosity of the fluid.

At low Reynolds numbers, i.e., at relatively low velocities and spatial scales, the equations of fluid motion for a viscous fluid have steady-state solutions. The fluid can be imagined as constituted by layers sliding over each other without mixing and its motion can be represented with good accuracy by a two-dimensional approach, such as in the Couette or pipe flow (Wilcox, 2006). This type of motion, controlled by viscous diffusion of vorticity and momentum, is referred to as laminar and can be observed experimentally and in nature.

At larger Reynolds numbers, the fluid's inertia becomes predominant compared to viscous diffusion. In observing a waterfall or smoke exiting from a chimney (see e.g. Figure 2.2), the flow appears to be anisotropus, inherently three-dimensional, unsteady, irregular, chaotic, characterized by apparently random vortexes and eddies (Pope, 2000). Such motion is referred to as turbulent flow.

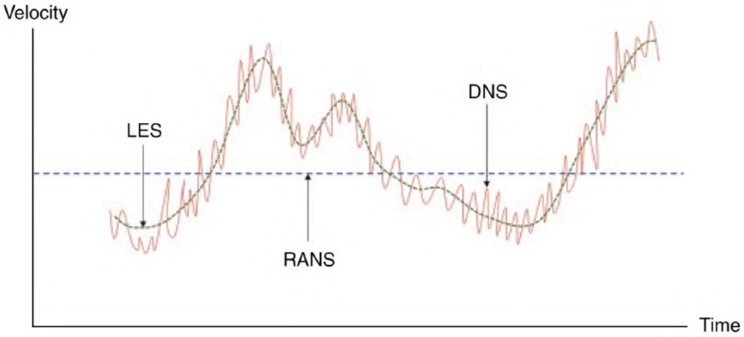

Figure 2.3: Different resolved turbulence scales and velocity fluctuations in a turbulent flow (Norouzi et al., 2016).

In the turbulent flow regime, the motion appears characterized by a deterministic chaos: if we were able to obtain the analytical exact solution to the Navier-Stokes equations, it would be possible to determine the velocity and pressure field at each time instant, both in the present and in the future. However, even a small error would lead the solution to diverge consistently. Since the strong non-linearity present in the Navier-Stokes equations requires a numerical approach, the solutions is always affected by numerical and/or truncation errors, and a mathematical model to predict the effect of turbulence must be employed.

The formal basic theory of turbulence was obtained through a statistical approach by Kolmogorov (1941). In the process of turbulent mixing, the energy is transmitted to the fluid in swirling structures comparable to the characteristic size of the system, for example, the size of the hydraulic diameter of the utilized duct. Once produced, the vortices of maximum size will not be able to dissipate their kinetic energy directly into heat, but they will produce vortices of smaller and smaller size, up to a scale in which viscous dissipation will prevail; the characteristic scale at which the dissipation of kinetic energy occurs is called the Kolmogorov scale.

Different approaches to solve the Navier-Stokes equations have been developed in the last century, differing in accuracy and computational load (Wilcox, 2006):

- Direct Numerical Simulation (DNS): this is the conceptually simplest approach, as space and time are discretized with grids with a characteristic dimension smaller than the smaller vortex. This is the approach that produces the most accurate results but has an extremely large computational cost. For industrial applications it is therefore too expensive, it is used principally in the study of the most fundamental aspects of turbulence at low Reynolds numbers.

- Reynolds Averaged Navier-Stokes (RANS): these methods assume that turbulent motion can be described as an average motion plus its fluctuation over time. The quantities of the Navier-Stokes equations are averaged over a certain time interval; by doing so, the calculation times are considerably reduced as the scales of the mean motion are considerably greater than those of the turbulent motion. Examples of RANS turbulence models are: Spalart-Allmaras, $k-\omega$, $k-\varepsilon$, and RST models, which add a variety of additional equations to bring closure to the Navier-Stokes equations.

- Large Eddy Simulation (LES): this approach consists in numerically evaluating the behaviour of the largest turbulent scales and appropriately modeling the smaller scales. It offers more accurate results than RANS and at the same time has a significantly lower computational cost compared to DNS, which is why it is a rapidly developing method.

An exemplary diagram of the resolution of velocity fluctuations obtained with the three approaches is shown in Figure 2.3. While RANS resolves integral scales, LES resolves only the largest scales, and DNS resolves all scales.

2.1.2.1 Reynolds Averaged Navier Stokes

To obtain the Reynolds-Averaged Navier-Stokes equations, each solution variable in the instantaneous Navier-Stokes equations is decomposed into its mean, or averaged, value and its fluctuating component. The averaging process may be thought of as time-averaging for steady-state situations and ensemble averaging for repeatable transient situations. Inserting the decomposed solution variables into the Navier-Stokes equations results in equations for the mean quantities. The mean mass and momentum transport equations can be written as:

$$\frac{\partial}{\partial t}\rho_f + \nabla \cdot (\rho_f \bar{u}) = \ 0 \tag{2.10}$$

$$\frac{\partial}{\partial t}(\rho_f \bar{u}) + \ \nabla \cdot (\rho_f \bar{u} \ \times \ \bar{u}) = -\nabla \cdot \bar{p}\ \hat{I} + \nabla \cdot (\bar{\tau} + \hat{\tau}_{rans}) + \rho_f \vec{g} \tag{2.11}$$

where the over signed variables are averaged.

These equations are essentially identical to the original Navier-Stokes equations, except that an additional term now appears in the momentum equation. This additional term is the stress tensor, which has the following definition:

$$\hat{\tau}_{rans} = -\rho_f \hat{R} + \frac{2}{3}\rho_f k \hat{I} \tag{2.12}$$

where $\hat{R}$ is the Reynolds stress term:

$$\hat{R} = \begin{pmatrix} \bar{u'_i u'_i} & \bar{u'_i u'_j} & \bar{u'_i u'_k} \\ \bar{u'_i u'_j} & \bar{u'_j u'_j} & \bar{u'_j u'_k} \\ \bar{u'_i u'_k} & \bar{u'_j u'_k} & \bar{u'_k u'_k} \end{pmatrix} \tag{2.13}$$

and k is the turbulent kinetic energy, defined to be half the trace of the Reynolds stress tensor.

The Reynolds stress term needs to be modelled to provide "closure" to the RANS equations, i.e., to obtain equations where only the mean velocity and pressure appear. The closure problem is solved by introducing additional equations, according to a RANS turbulence model.

RANS turbulence models can be catalogued in four main categories (Wilcox, 2006), depending on the number of additional equations introduced:

- Algebraic (Zero-Equation) models (e.g., mixing length model)
- One equation models (e.g., Spalart-Allmaras);
- Two equations (e.g, $k - \varepsilon$, $k - \omega$);
- Reynolds Stress Transport Models.

2.1.2.2 Eddy Viscosity Models

Eddy viscosity models are based on the analogy between the molecular gradient-diffusion process and turbulent motion and are based on the Boussinesq approximation (Pope, 2000). The turbulent stresses are related to the mean flow by introducing the concept of "eddy viscosity". The turbulent stresses are calculated as:

$$- \bar{u'_i u'_j} = 2\mu_t S_{ij} - \frac{2}{3} k \delta_{ij} \tag{2.14}$$

where:

- μ_t is the turbulence eddy viscosity;
- $S_{ij} = \left(\frac{\partial \bar{v}_i}{\partial x_j} + \frac{\partial \bar{v}_j}{\partial x_i} \right)$ is the mean rate of strain tensor;
- k is the turbulent kinetic energy
- δ_{ij} is the Kroneker delta.

The eddy viscosity models solve additional transport equations for scalar quantities that enable the turbulent viscosity to be derived. Most one-equation and two-equation RANS turbulence models are eddy viscosity models.

2.1.2.3 Reynolds Stress Transport (RST) models

The Boussinesq approximation, i.e., the assumption that the stress tensor is linearly proportional to the mean strain rate, does not consider the anisotropy of turbulence.

Reynolds Stress Transport (RST) models can take turbulence anisotropy by directly solving transport equations for each component of the Reynolds stress tensor, $\hat{R}$ (Equation 2.13). They have the potential to predict complex flows more accurately than eddy viscosity models because the transport equations for the Reynolds stresses naturally account for the effects of turbulence anisotropy, streamline curvature, swirl rotation and high strain rates.

2.1.2.4 Large Eddy Simulation

Large Eddy Simulation (LES) is a transient technique in which large scales of turbulence are resolved directly anywhere in the flow domain, while small-scale motions are modeled. One justification for the LES technique is that by modeling only part of the entire turbulence scale and explicitly solving the rest, the error in the turbulence modeling assumptions is not so consequential. Furthermore, it is assumed that the smaller eddies are self-similar and therefore admit simpler and above all universal modeling. The disadvantage of the approach is the computational expense, which, although lower than the direct numerical simulation, is higher than in the RANS methods. While the RANS equations are obtained by means of an averaging process, the equations solved for LES are obtained by means of a spatial filtering. The spatial filtering defines the maximum size of the directly solved fluid dynamic structures and removes the smaller eddies, reducing the range of scales that must be resolved.

The filter applied in LES can be either implicit or explicit. In the explicit filtering a filter, such as box or Gaussian, is applied directly to the discretized Navier-Stokes equations. The filtering of the generic instantaneous flow variable $f\,(t,x)$:

$$\widetilde{f}(t,x) = \iiint_{-\infty}^{+\infty} G\left(x-x',\Delta\right) f\left(t,x'\right) dx' \tag{2.15}$$

where $G\,(x-x',\Delta)$ is the applied filter with a width $\Delta = (\Delta_x \Delta_y \Delta_z)^{\frac{1}{3}}$.

In the implicit filtering the computational grid behaves as LES low-pass filter. Taking full advantage of the numerical grid resolution is generally less computational expensive (Berselli, 2005). Inserting the decomposed solution variables into the Navier-Stokes equations results in equations for the filtered quantities. The filtered mass, momentum, and energy transport equations can be written as:

$$\frac{\partial}{\partial t}\rho_f + \nabla\cdot(\rho_f \widetilde{u}) = \ 0 \tag{2.16}$$

$$\frac{\partial}{\partial t}(\rho_f \widetilde{u}) + \nabla \cdot (\rho_f \widetilde{u} \times \widetilde{u}) = -\nabla \widetilde{p} + \nabla \cdot (\widetilde{\tau} + \hat{\tau}_{LES}) + \rho_f \vec{g} \tag{2.17}$$

where the over signed variables are filtered.

The filtered equations look identical to the corresponding RANS equations. Now the new tensor, $\hat{\tau}_{LES}$, represents the subgrid scale stresses that result from the interaction between the larger, resolved eddies and the smaller, unresolved eddies and are modelled using the Boussinesq approximation as follows:

$$\hat{\tau}_{LES} = 2\mu_t \hat{S} - \frac{2}{3}(\mu_t \nabla \cdot \widetilde{u}) \tag{2.18}$$

where $\hat{S}$ is the strain rate tensor and evaluated from the velocity $\widetilde{u}$.

The sub-grid scale turbulent viscosity, μ_t, must be modelled to close the problem. Three subgrid scale models are available in literature:

- The Smagorinsky Subgrid Scale model provides the following mixing-length type formula for the subgrid scale viscosity (Smagorinsky, 1963):

  $$\mu_t = \rho_f \Delta^2 |\hat{S}| \tag{2.19}$$

  where Δ is the length scale or grid filter width and $\hat{S}$ is the strain rate tensor and evaluated from the velocity $\widetilde{u}$.

- Dynamic Smagorinsky Subgrid Scale model (Germano et al., 1991): the calculation of the turbulent viscosity follows the same equation as the previous model (Equation 2.19), but the length scale, Δ, is evaluated dynamically as a function of a number of test-filtered variables:

  $$\Delta = C_s V^{\frac{1}{3}} \tag{2.20}$$

  where C_s is a constant of the model and V is the cell volume.

- The Wall-Adapting Local-Eddy viscosity (WALE) Subgrid Scale model: it is a more modern subgrid scale model that uses a novel form of the velocity gradient tensor in its formulation (Nicoud and Ducros, 1999). Similar to the Smagorinsky Subgrid Scale model, it suffers from the limitation that the model coefficient is not universal.

  The WALE Subgrid Scale model provides the following mixing-length type formula for the subgrid scale viscosity:

  $$\mu_t = \rho_f \Delta^2 S_w \tag{2.21}$$

The length scale Δ is evaluated dynamically as a function of a number of test-filtered variables, according to the following:

$$\Delta = \begin{cases} \min\left(C_w V^{\frac{1}{3}}, kd\right) & \text{if length scale is applied} \\ C_w V^{\frac{1}{3}} & \text{if length scale is not applied} \end{cases} \tag{2.22}$$

where C_w is a constant of the model and V is the cell volume, k is the von Karman constant. The deformation parameter S_w is defined as:

$$S_w = \frac{S_d : S_d^{\frac{3}{2}}}{S_d : S_d^{\frac{5}{4}} + S : S^{\frac{5}{2}}} \tag{2.23}$$

where S is the strain rate tensor and evaluated from the velocity $\widetilde{u}$. The tensor S_d is defined as:

$$S_d = \frac{1}{2}\left[\nabla u \cdot \nabla u + \left(\nabla u \cdot \nabla u\right)^T\right] - \frac{1}{2} tr\left(\nabla u \cdot \nabla u\ \right)\hat{I} \tag{2.24}$$

2.1.3 Numerical approach

Equations 2.1 and 2.2 are solved via finite-difference, finite-element, or finite-volume methods on a Eulerian grid.

The Eulerian grid, or mesh, can be structured or unstructured. A structured mesh is characterized by regular connectivity that can be expressed as a two or three dimensional array. Every grid point is uniquely individuated by indexes, expressing them as a two-dimensional or three-dimensional arrays. This restricts the element choice to quadrilaterals in 2D or hexahedra in 3D. The regularity of the connectivity requires limited memory storage since neighborhood relationships are defined by the storage arrangement.

Depending on the discretization, the Eulerian grid can be "body fitted" or "cartesian". If the points of the mesh overlap the boundaries of physical space, the mesh is called "body fitting". This allows greater precision of the results at the edges of the domain but increases the computational cost of its generation. On the other hand, in a cartesian grid, the elements of the mesh are parallel to the coordinate axes of the system, which allows a simpler discretization of the physical space and gives advantages in the numerical resolution of the fluxes of modeling equations. However, the discretization at the edges can be coarser, for example, if there are very sharp curves or angles.

If the simulation is unsteady, the equations need to be integrated in time. The fluid time step for integration, Δt_f, needs to be sufficiently small to ensure stability. The Courant - Friedrichs - Lewy condition suggests to choose a fluid timestep that ensures a Courant number, C_{ou}, smaller than 1:

$$C_{ou} = \frac{u \cdot \Delta t_f}{\Delta x} < 1 \tag{2.25}$$

where u is the magnitude of the velocity and Δx the length interval.

The momentum equation (Equation 2.2) cannot be solved directly to obtain the gas velocity, u, since the pressure gradient is indirectly determined by the continuity equation. Since the indirect specification of the pressure gradient is computationally not convenient, a predictor - corrector procedure for solving coupled mass and momentum equations of fluid phase is employed in this step (Patankar, 1981). For example, the SIMPLE (Semi-Implicit Method for Pressure-Linked Equation) or PISO (Pressure implicit with splitting operator) algorithms can be used for this purpose.

The solution loop of the SIMPLE algorithm is as follows:

- Set the initial conditions and begin the iteration loop;
- Solve the momentum equation using the available pressure field (momentum-predictor step);
- Solve the pressure-correction equation (pressure correction step);
- Apply under-relaxation (relaxation step) and update mass fluxes;
- Correct the velocity field using the new pressure field and mass fluxes (momentum-corrector step).

If the velocity components and the pressure are calculated for the same grid points, some physically unrealistic fields arise as solutions, so a staggered grid finite volume scheme is usually considered when dealing with the Eulerian representation of the gas-phase (Patankar, 1981): the scalar properties, fluid pressure, and fluid volume fraction are determined at the center of each fluid cell, while velocities and forces are obtained at the faces of the fluid cell. A standard first order upwind or higher order schemes (second order upwind, QUICK, SUPERBEE, etc.) may be used to discretize the convective terms, while the divergence and gradient terms are calculated using the semi-finite difference in the selected staggered grid (Norouzi et al., 2016).

2.2 Modelling of the solid phase

The modelling of the solid phase is based on the Distint Element Method (DEM), a modelling approach first introduced by Cundall and Strack (1979) for granular systems. The idea behind this technique is both intuitive and effective: each solid object inside the system is tracked individually and its trajectory is calculated in detail, by numerically integrating Newton's 2^{nd} law of motion. This approach is Lagrangian, as the system is considered as a set of discrete entities and the equations are solved following the point of view of each of them.

2.2.1 Governing equations

In the DEM approach, particles are individually tracked along their deterministic motion in the device, as resulting from the calculation of all forces acting on them.

The position ($\vec{x}_i$), linear ($\vec{v}_i$) and angular velocities of the i^{th} particle evolve according to Newton's 2^{nd} law of motion:

$$\frac{d\vec{x}_i}{dt} = \vec{v}_i \tag{2.26}$$

$$m_i \frac{d\vec{v}_i}{dt} = \vec{F}_T = \sum_{j=i}^{N_C} \vec{F}_{c,ij} + \vec{F}_{coh,ij} + \vec{F}_{d,i} + \vec{F}_{b,i} + \vec{F}_{l,i} + \vec{F}_{g,i} \tag{2.27}$$

$$I_i \frac{d\vec{\omega}_i}{dt} = \vec{T}_T = \sum_{j=i}^{N_C} \vec{T}_{c,ij} + \vec{T}_r \tag{2.28}$$

where $\vec{F}_T$ is the net sum of all the forces acting on the i^{th} particle: contact, cohesive, drag, pressure gradient, lift and gravitational forces, respectively; $\vec{T}_T$ is the sum of all torques acting on the i^{th} particle: contact torque and rolling resistance.

The calculation of all the terms included in the sum will be discussed below.

2.2.2 Modelling of contact forces

In discrete element modelling, two formulations are available to describe the interactions between bodies: hard-sphere approach and soft-sphere approach.

The hard-sphere approach assumes that particles are rigid, non-deformable bodies, and collisions are binary and instantaneous. The motion of billiard balls on a pool table is a good example of a system that could be modelled according to the hard sphere approach: each sphere travels freely until the next collision occurs and the trajectory of two colliding objects can be accurately established by impulse equations, since the duration of the impact is extremely short compared to other time-scales. This approach is often referred to as Discrete Particle Method (DPM) (Sommerfeld et al., 2019), it is numerically efficient and particularly suitable for dilute systems.

On the other hand, a system like a heap of flour could hardly be simulated with this method. Each grain of flour is surrounded by many other grains (multiple simultaneous collisions) and every interaction is quite complex, with cohesive and electrostatic forces involved. For such systems, the soft-sphere approach works best, as it assumes that particles are deformable bodies and their interactions are dynamic processes.

In the soft-sphere approach, the collisions are not instantaneous, but evolve in time according to force-displacement laws in a displacement-driven manner: the contact forces depend on the actual normal and tangential displacement, which are evaluated in terms of the relative position and orientation of the two bodies involved in the collision (Di Renzo and Di Maio, 2004).

To define the normal and tangential displacements, the 2D case of a circular particle (radius r) colliding with a flat wall (Figure 2.4a) can be considered. The particle approaches the wall with initial translational velocity v_0 and initial rotational velocity ω_0. In a generic instant during the collision, the normal displacement, δ_n, is defined as the difference between the particle radius and the distance between the center of the particle and the wall; δ_n is often referred to as "normal overlap" as it is the interpenetration between the particle and the wall surface:

$$\delta_n = r - y \tag{2.29}$$

The definition of the tangential displacement δ_t (analogously referred to as "tangential overlap") is less trivial. It can be interpreted as the difference between the translational displacement of the particle on the wall surface $(x - x_0)$ and the distance travelled by rolling (Di Renzo and Di Maio, 2004), as shown in Figure 2.4b:

$$\delta_t = [x - x_0] - [(\theta - \theta_0) \cdot (-r)] \tag{2.30}$$

Most DEM codes calculate the tangential overlap from the tangential relative velocity, v_t, at the contact point (Norouzi et al., 2016). For a physical contact starting at time t_0, the tangential overlap at time t is given by:

$$\delta_t = \int_{t_0}^{t} v_t dt \tag{2.31}$$

The solution of integral is numerically obtained with a discrete approach, by calculating the incremental tangential overlap ($v_t dt$) and adding it to the tangential overlap of previous time step, $\delta_{t,0}$:

$$\delta_t \approx v_t dt + \delta_{t,0} \tag{2.32}$$

The tangential overlap of each collision needs to be saved at each time step, as the previous value is required in Equation 2.32 to calculate the new value.

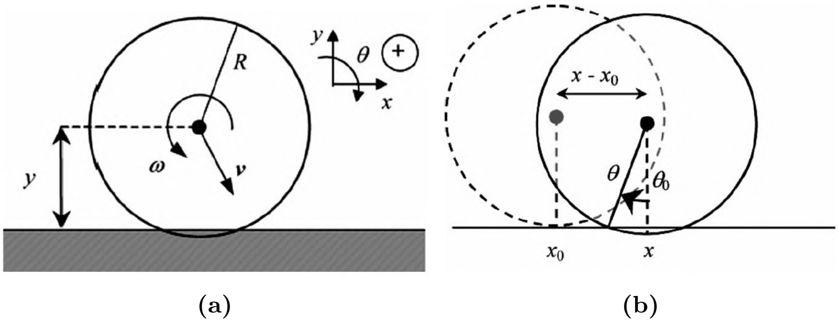

Figure 2.4: a) Configuration for the 2D contact between a sphere and a wall and b) definition of the tangential displacement (Di Renzo and Di Maio, 2004).

The calculation of the contact force as a function of normal and tangential overlap depends on the contact model employed. Different contact models have been developed and applied for DEM simulations. Two models will be presented below: the Linear-Spring-Dashpot model (LSD) and the Hertz-Mindlin no-slip model (H-MDns). The aforementioned contact models are viscoelastic models (i.e. do not take into account plastic deformation) suitable for free-flowing materials that do not experience attractive van der Waals forces. The introduction of adhesive and cohesive interactions in the contact model will be discussed later (section 2.5).

2.2.2.1 Linear spring dashpot model

The linear spring-dashpot model (LSD) was introduced by Cundall and Strack (1979). The overlap between two contacting bodies is represented as a combination of linear mechanical elements arranged in series or parallel both in normal and tangential direction. A schematic of the contact between two particles (i and j) is shown in Figure 2.5.

In normal direction, the collision force between particle i and j consists of an elastic contribution (spring) and a viscous contribution (dashpot), as in the classical formulation of the Kelvin-Voigt model for viscoelastic materials. The spring models a Hookean elastic solid (i.e., force/stress proportional to deformation), while the dashpot takes into account the dissipation of kinetic energy by considering the constituting equation of a Newtonian fluid (i.e., force/stress proportional to velocity). The left side of Figure 2.5 shows the contact in normal direction with a RC circuit analogy: the contact force corresponds to the current, while the deformation corresponds to the voltage. As the two mechanical elements are in parallel, the total contact force in normal direction between particles i and j is the sum of the elastic and viscous force:

$$F_{c,ij}^{(n)} = -(k_n\delta_n + \eta_n v_n) = -(k_n\delta_n + \eta_n \frac{d\delta_n}{dt}) \tag{2.33}$$

where δ_n is the normal overlap (eq. 2.29), k_n is the normal spring stiffness of the linear spring, η_n is the normal damping coefficient and v_n is the component of the relative velocity between colliding particles in normal direction. The normal spring stiffness, k_n, can be estimated from the mechanical properties of the materials, like Young modulus and Poisson coefficient (see e.g. Di Renzo and Di Maio (2004)), while the damping coefficient, η_n, is usually calculated from the normal coefficient of restitution e_n (Di Renzo et al., 2021), i.e. the ratio between the rebound velocity (velocity after collision) and the impact velocity (velocity before collision). The relationship between the normal coefficient of restitution and the damping coefficient is the following:

$$\eta_n = \frac{-2\ln e_n\sqrt{mk_n}}{\sqrt{(\ln e_n)^2 + \pi^2}} \tag{2.34}$$

where m is the mass of the particle.

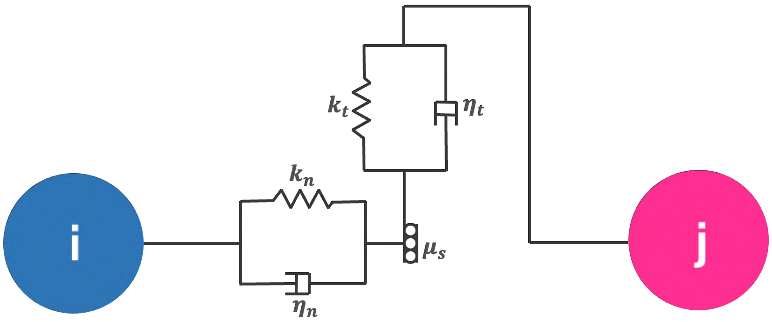

Figure 2.5: Schematic of the spring-dashpot system used to model particle contact forces in normal and tangential direction.

The force in tangential direction can be expressed in a similar fashion, as shown in the right side of Figure 2.5:

$$F_{c,ij}^{(t)} = -(k_t\delta_t + \eta_t v_t) \tag{2.35}$$

where δ_t is the tangential overlap (eq. 2.32), k_t is the tangential spring stiffness, η_t is the tangential damping coefficient and v_t is the component of the relative velocity between colliding particles in tangential direction. However, in tangential direction sliding can occur (represented by the slider in Figure 2.5). Assuming valid Coulomb's friction law, if at any time during contact $F_{c,ij}^{(t)} \geq \mu_s F_{c,ij}^{(n)}$, with μ_s being the static friction coefficient, sliding occurs and the value of Coulomb's limit is used for the tangential force (Garg et al., 2012):

$$F_{c,ij}^{(t)} = -\min\left(\mu_s F_{c,ij}^{(t)}, k_t\delta_t + \eta_t v_t\right) \tag{2.36}$$

The tangential spring stiffness, k_t, is usually set to two-fifths of the normal stiffness, while the tangential damping coefficient, η_t, can be taken to be half of the normal damping coefficient (Garg et al., 2012).

Given its simplicity and relatively straightforward implementation, the LSD model is one of the most popular contact models in DEM codes (Norouzi et al., 2016).

2.2.2.2 Hertz-Mindlin no-slip model

A more accurate representation of the contact problem can be obtained by considering the Hertz-Mindlin no-slip model, first introduced by Tsuji et al. (1993). The elastic theory of Hertz (Hertz, 1882) is used for the normal contact problem, while the no-slip solution developed by Mindlin and Deresiewicz (1953) is used for the tangential contact.

The normal ($F_{c,ij}^{(n)}$) and tangential ($F_{c,ij}^{(t)}$) contact forces allow for the elastic-frictional interaction and also include a dissipative term ensuring constant coefficient of restitution, similar to the LSD model. However, the functional force-displacement relationship is non-linear:

$$F_{c,ij}^{(n)} = -\frac{4}{3}E_{eq}\sqrt{R_{eq}}\delta_n^{\frac{3}{2}} - \eta_n^H \delta_n^{\frac{1}{4}} v_n \tag{2.37}$$

$$F_{c,ij}^{(t)} = -\min\left(\mu_s F_{c,ij}^{(n)}, 8G_{eq}\sqrt{R_{eq}}\delta_n^{\frac{1}{2}}\delta_t + \eta_t^H \delta_n^{\frac{1}{4}} v_t\right) \tag{2.38}$$

where δ represents the (normal and tangential) displacement between the contacting particles, v their relative velocity at the contact point, η^H the damping coefficients (again related to the restitution coefficient, see e.g. Di Renzo et al. (2021)), μ_s the slider friction coefficient. R_{eq}, E_{eq} and G_{eq} are the equivalent properties (radius, Young modulus and shear modulus) of the contact between particles i and j:

$$R_{eq} = \left(\frac{1}{R_i} + \frac{1}{R_j}\right)^{-1} \tag{2.39}$$

$$E_{eq} = \left(\frac{1-\nu_i^2}{E_i} + \frac{1-\nu_j^2}{E_j}\right)^{-1} \tag{2.40}$$

$$G_{eq} = \left(\frac{1-\nu_i}{G_i} + \frac{1-\nu_j}{G_j}\right)^{-1} \tag{2.41}$$

where ν is the Poisson's ratio of the material. The same relationships can be applied for a collision of a sphere i with a wall j, if an infinite radius R_j is assumed for the wall ($R_{eq} = R_i$).

2.2.3 Contact torque and rolling resistance

Contacts in the tangential directions cause the relative rotation of the two colliding objects. The rotational torque acting on particle i due to the tangential contact with particle j (first term in Equation 2.28) is defined as:

$$\vec{T}_{c,ij} = \vec{R}_i \times \vec{F}^{(t)}_{c,ij} \tag{2.42}$$

where $\vec{F}^{(t)}_{c,ij}$ is the tangential contact force and $\vec{R}_i$ is the vector from the centre of particle i to the contact point.

If the only term in Equation 2.28 was the sum of the rotational torque contributions, a particle that undergoes a tangential impact would start rolling indefinitely. This is not what happens in real systems, as particles experience a rolling resistance arising from different sources, such as asymmetry of the contact pressure distribution, micro-slip and friction on the contact surface, plastic deformations around the contact area, etc. (Norouzi et al., 2016).

To include these effects in DEM simulations, a rolling resistance torque or rolling friction opposing the rotation of particles can be added in Equation 2.28. One of the most common rolling resistance models is the Constant Directional Torque model (CDT, Ai et al. (2011)). The rolling resistance torque, T_r, is calculated as follows:

$$\vec{T}_r = -\mu_r R_{eq} F^{(n)}_{c,ij} \frac{\vec{\omega}_i - \vec{\omega}_j}{|\vec{\omega}_i - \vec{\omega}_j|}. \tag{2.43}$$

in which μ_r is the user-defined rolling friction coefficient, $F^{(n)}_{c,ij}$ is the normal contact force between objects i and j, ω_i and ω_j are the angular velocities of objects i and j, and R_{eq} is the equivalent radius.

Rolling friction is also used to model shape-like effects in DEM simulations. Since simulating the real shape of particles is computationally expensive, the introduction of a rolling resistance model can be a useful strategy to obtain a simulated model that behaves similarly to the real system (Wensrich and Katterfeld, 2012).

2.2.4 Time integration

Equations 2.26, 2.27 and 2.28 can be integrated in time with an explicit 1^{st} order scheme. Given the values of position, velocity and angular velocity of the particles at time t, their value at time $t + \Delta t$ can be calculated as:

$$\vec{x}(t + \Delta t) = \vec{x}(t) + \vec{v}(t + \Delta t) \cdot \Delta t \tag{2.44}$$

$$\vec{v}(t + \Delta t) = \vec{v}(t) + \frac{\vec{F}_{tot}(t)}{m} \cdot \Delta t \tag{2.45}$$

$$\vec{\omega}(t+\Delta t) = \vec{\omega}(t) + \frac{\vec{T}}{I} \cdot \Delta t \tag{2.46}$$

The choice of the integration step (timestep, Δt) plays a key role. A too high value can cause system instability while a too low timestep increases the calculation load of the simulation with a corresponding increase in the time needed to complete it. In the latter case, the computational load could be so high to make the simulation infeasible.

The approach to select an appropriate Δt for the solid phase usually starts from the definition of a threshold value, a critical timestep for the system to be simulated: τ_C. The solid phase timestep is then chosen as a fraction of τ_C. Usually a fraction ranging from 1/10 to 1/50 is chosen, based on experience and on the system considered.

As already shown in the previous section, the linear spring-dashpot contact model (LSD) represents the normal elastic contact between two bodies with a spring. As first proposed by Cundall and Strack (1979), the period of oscillation of a mass m connected to a spring with elastic costant k_n can be taken as critical time interval, $\tau_C = 2\pi\sqrt{m/k_n}$.

It can be noticed that the critical timestep is inversely proportional to the square root of the spring stiffness: $\tau_C \propto k_n^{-0.5}$. Therefore, by reducing k_n, a higher timestep can be selected, meaning that the simulation can be completed in a shorter time. This is the most common and effective speed-up procedure used in DEM simulations; Tsuji et al. (1993) proved that in the CFD-DEM simulation of fluidized beds, the value of k_n does not have a strong influence on the results. Di Renzo and Di Maio (2004) showed that a smaller k_n gives the same normal and tangential velocity profiles with the LSD model. However, the reduction of k_n cannot be extreme, otherwise considering too soft particles would lead to largely unrealistic overlaps.

The critical timestep is also proportional to the square root of the mass and, as a consequence, increases with the diameter of the particle: $\tau_C \propto d^{1.5}$. Therefore, a smaller timestep needs to be selected for smaller particles. Another speed-up technique for DEM simulations is coarse-graining, which substitutes the actual particles by a reduced number of bigger, representative elements (”parcels” or ”grains”) according to appropriate scaling parameters (Di Renzo et al., 2021).

By considering also the dissipative term of the normal force (dashpot), a more accurate estimate of the critical timestep is given by the total duration of the contact (Garg et al., 2012):

$$\tau_C = \frac{\pi}{\sqrt{\frac{k_n}{m_{eq}} - \frac{1}{4}\left(\frac{\eta_n}{m_{eq}}\right)^2}} \tag{2.47}$$

where k_n is the spring elastic normal constant, η_n the damping coefficient, m_{eq} the armonic mean of the masses of the two objects i and j involved in the collision:

$$m_{eq} = \left(\frac{1}{m_i} + \frac{1}{m_j}\right)^{-1} \tag{2.48}$$

A different value of τ_C is calculated for particle-particle contact and particle-wall contact. The minimum value needs to be chosen as critical timestep.

If Hertzian contact model is used, Equation 2.47 is not accurate as the force-displacement relationship is non-linear. Some authors suggest to use the Rayleigh wave speed to calculate the critical time step for non-linear contact models:

$$\tau_{C,R} = \frac{\pi R}{0.1631\nu + 0.8766}\sqrt{\frac{\rho}{G}} \tag{2.49}$$

with ρ particle density, R particle radius, G shear modulus, ν Poisson's ratio. This approach considers the time taken for a Rayleigh wave to pass a sphere in a single time increment (Otsubo et al., 2017).

The critical timestep for the Hertzian model can still be selected by considering the actual contact duration, as reported by Di Renzo and Di Maio (2004). However, τ_C will be now dependent on the impact velocity, $v_{n,0}$:

$$\tau_C = \frac{4\Gamma\left(\frac{2}{5}\right)\sqrt{\pi}C^2 R_{eq}}{5\Gamma\left(\frac{9}{10}\right)v_{n,0}} \tag{2.50}$$

where $\Gamma(x)$ is the gamma function:

$$\Gamma(x) = \int_0^{+\infty} t^{x-1}e^{-t}dt \tag{2.51}$$

and C is given by:

$$C = \left(\frac{15 m_{eq} v_{n,0}^2}{16 E_{eq} R_{eq}^3}\right)^{0.2} \tag{2.52}$$

If an estimate of the maximum impact velocity $v_{n,0}$ is available, Equation 2.50 guarantees an appropriate choice of the critical timestep.

Higher order integration schemes are also available in most DEM codes, such as Adam-Bashfort (Garg et al., 2012) or velocity-Verlet integration schemes (Kloss et al., 2012). These methods are conditionally stable, meaning that the integration timestep needs to be selected carefully in order to have numerical stability.

Higher order schemes are computationally more expensive than the first order scheme. Since the timestep usually selected in DEM simulation is small, the first-order time scheme is a reasonable choice, as it is faster and has less memory requirements (Garg et al., 2012). The main drawback of the first order scheme is the fact that it can suffer from poor energy conservation. However, energy conservation is not a crucial issue in gas-solid systems due to the presence of non-conservative forces such as the interphase drag force (van der Hoef et al., 2008) .

2.2.5 Neighbour search algorithm

One of the most important components in the DEM method is the neighbour search algorithm, needed to indicate to the software which particles could be affected by contact with the particle of interest. If the software has to evaluate the interactions between all the possible pairs of particles, the computational load is $O(N^2)$ (with N equal to the total number of particles), making the simulation unfeasible for dense systems.

To reduce the computational load, a grid based neighbour search is usually performed. The simulation domain is discretized in cube cells and the particles are identified by the computational cell in which their center is located. The algorithm considers as potential neighbors the particles that are in the same cell as the particle of interest and in the 26 adjacent cells. The search algorithm comes called every $N_{s,n}$ iterations of DEM, a parameter usually set to 20-50. Using this approach, the software needs to perform a second check on the distance travelled by the particles: if a particle travels a distance higher than its radius during the $N_{s,n}$ iterations, then the neighbor search algorithm is called earlier. Since the dynamics of the system is not known a priori, this second test is critical and ensures that the system does not become unstable due to large particle overlaps which might occur if a high value for $N_{s,n}$ is specified (Garg et al., 2012).

After determining the potential neighbors, the software must determine the "effective" neighbors. Two particles of radius R_i e R_j that are in position $\vec{x}_i$ e $\vec{x}_j$ are considered neighbours if they satisfy the following condition:

$$|\vec{x}_i - \vec{x}_j| < K_{fac}(R_i + R_j) \tag{2.53}$$

The K_{fac} parameter is user-defined and is a value greater than or equal to 1. By choosing $K_{fac} = 1$, only the particles that touch or overlap are considered neighbours; this choice leads to a high calculation load, as the software has to call up the neighbor search algorithm very frequently to be sure not to lose any contact. As K_{fac} increases, the number of potential neighbors increases and the neighbour search algorithm can be called less frequently. However, if K_{fac} is too high, the particle may have a very large number of neighbors, with the risk of having to build arrays with a size greater than the maximum allowed size. A value ranging from 1.2 to 2 is usually a good compromise between computational load and memory requirements (Garg et al., 2012).

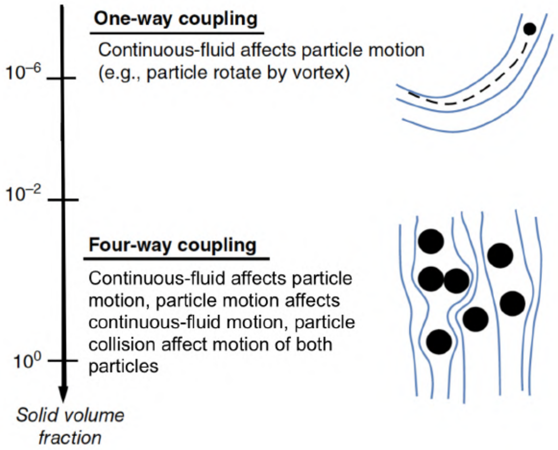

Figure 2.6: Schematics of one-way and four-way coupling strategies. Adapted from Norouzi et al. (2016).

2.3 Fluid–solid coupling

In the previous sections, the CFD and DEM technique have been presented as tools to simulate fluid and granular systems, respectively. The motion of fluid phase is described by Navier-Stokes equations, while the motion of discrete particles is described by Newton's second law of motion.

The CFD-DEM technique combines the two approaches. Given that the technique is applied to a multiphase system, the phase coupling is a basic yet fundamental concept. Coupling can occur through exchange of momentum (e.g., interaction forces between phases), energy, and mass (e.g., evaporation) among phases. In isothermal, non-reacting systems, momentum coupling is the main topic of interest.

Depending on the particle operating condition and volume fraction of particles in the flow, different coupling strategies can be used. The two most common approaches are shown in Figure 2.6.

The one-way coupling approach is suitable for dilute systems where the motion of particles is mostly affected by the fluid flow. Equations 2.1 and 2.2 can be solved independently from the solid phase equations, as the effect of the solid phase on the fluid flow is not included in the calculation.

The four-way coupling approach is needed in denser systems, where the effect of the solid phase on the fluid is relevant and particle-particle collisions are frequent. Examples of such systems are fluidized beds (Di Renzo et al., 2008) and high-load cyclones (Napolitano et al., 2022). With this approach, collision forces should be calculated for each contact between the discrete elements (according to the approach already presented in Section 2.2.2), and the effect of the solid phase on the motion of the fluid has to be included in Equations 2.1 and 2.2.

In unresolved four-way CFD-DEM coupling, the solid particles do not exclude volume for the gas phase in a natural way. This has to be incorporated artificially in the conservation in Equations 2.1 and 2.2, by introducing the void fraction, ε, which is the ratio between the volume occupied by the fluid and the total volume of the cell. The total fluid-solid interaction force, $\vec{F}_{f\to s}$, needs to be taken into account as well.

According to these two considerations, mass and momentum conservation equations for the fluid phase (Equations 2.1 and 2.2 in pure CFD) could be written as follows:

$$\frac{\partial \varepsilon \rho_f}{\partial t} + \nabla \cdot (\varepsilon \rho_f \vec{u}) = 0 \tag{2.54}$$

$$\frac{\partial \varepsilon \rho_f \vec{u}}{\partial t} + \nabla \cdot (\varepsilon \rho_f \vec{u}\vec{u}) = -\nabla p - \nabla \cdot \hat{\tau} + \varepsilon \rho_f \vec{g} - \vec{F}_{f\to s} \tag{2.55}$$

The momentum conservation (Equation 2.55) is usually written in a different, more convenient form (van der Hoef et al., 2008). The total fluid-solid interaction force, $\vec{F}_{f\to s}$, can be decomposed into two contributions:

$$\vec{F}_{f\to s} = \vec{F}_{fp} + \vec{F}_{st} \tag{2.56}$$

The first contribution, $\vec{F}_{fp}$, usually referred to as interphase momentum transfer, takes into account the drag and lift forces and is defined as:

$$\vec{F}_{fp} = \frac{1}{V_{cell}} \sum_{i=1}^{k_v} \left(\vec{F}_{d,i} + \vec{F}_{l,i} \right) \tag{2.57}$$

with V_{cell} the volume of the fluid cell, k_v the number of particle in the fluid cell of interest, $\vec{F}_{d,i}$ and $\vec{F}_{l,i}$ the drag and lift forces acting on particle i, respectively.

The second contribution, $\vec{F}_{st}$, takes into account the force due to the fluid stress tensor:

$$\vec{F}_{st} = -\frac{1}{V_{cell}} \sum_{i=1}^{k_v} (V_i \nabla p + V_i \nabla \cdot \hat{\tau}) \tag{2.58}$$

with V_i being the volume of particle i and k_v the number of particle in the fluid cell of interest.

Given that:

$$\frac{1}{V_{cell}} \sum_{i=1}^{k_v} V_i = 1 - \varepsilon \tag{2.59}$$

equation 2.58 can be written as:

$$\vec{F}_{st} = -(1-\varepsilon)(\nabla p + \nabla \cdot \hat{\tau}) \tag{2.60}$$

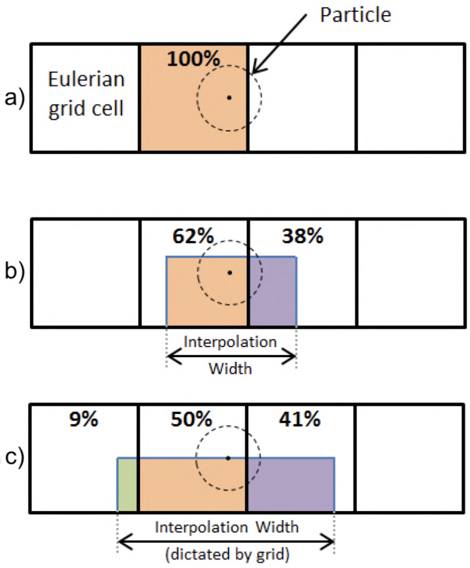

Figure 2.7: DEM interpolation schemes (NETL Multiphase Flow Science Team, 2020): a) centroid method, b) Divided Particle Volume Method, c) interpolation based on the staggered grid.

By substituting the decomposition in Equation 2.2 (Norouzi et al., 2016), the momentum conservation equation can be finally written as:

$$\frac{\partial \varepsilon \rho_f \vec{u}}{\partial t} + \nabla \cdot (\varepsilon \rho_f \vec{u}\vec{u}) = -\varepsilon \nabla p - \varepsilon \nabla \cdot \hat{\tau} + \varepsilon \rho_f \vec{g} - \vec{F}_{fp} \tag{2.61}$$

This formulation for the momentum conservation equation is known as "Model A" (Gidaspow, 1994).

The effect of the fluid on the particles is taken into account by adding the drag, lift and pressure gradient forces in the total force, as already shown in Equation 2.27. The specific formulations of the fluid-solid force contributions in the DEM part of the code will be discussed later in the chapter.

2.3.1 Interpolation algorithms

In the CFD-DEM model, the solid phase information is available at the particle scale while the fluid phase information is available at the fluid cell scale. Therefore, a special attention is required when particle scale information is used to calculate a fluid cell property and vice versa.

Let us consider the case of the fluid volume fraction, ε. This property appears in mass and momentum conservation equations and is used in the fluid-particles interaction force formulas.

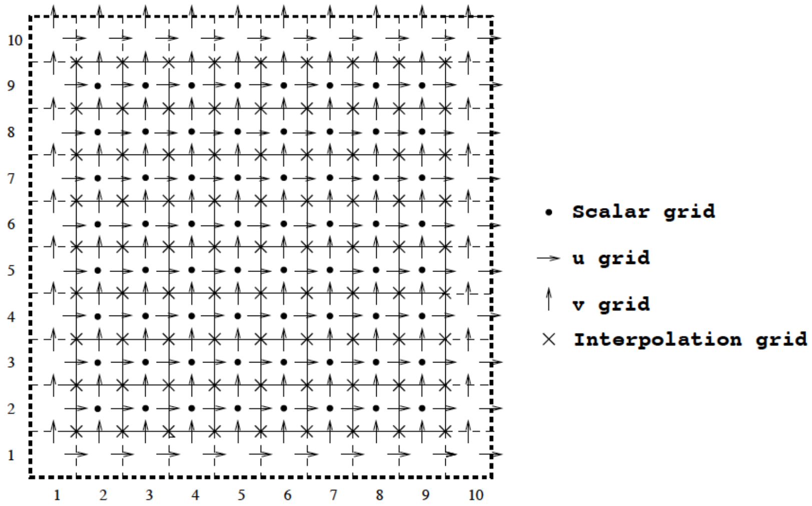

Figure 2.8: 2-D schematic of a staggered grid scheme used for discretizing the gas-phase field (Garg et al., 2012).

To determine the the void fraction in a specific cell, three different approaches may be followed, shown in Figure 2.7.

The first one, known as centroid method, does not use any interpolation strategy. The void fraction is calculated as the sum of the volume of the particles whose centres are located in a CFD cell (Figure 2.7a). This approach might lead to an artificially inhomogenous volume fraction field, especially if the particle size approaches the size of the fluid cells (Kloss et al., 2012).

The second approach (Figure 2.7b) is known as Divided Particle Method Square Filter. The information is interpolated to/from particle position using a square filter of a user-defined size. The smoothing prevents abrupt changes in the porosity (ε), avoids the possibility of ε being close to zero and reduces the porosity standard deviation (Volk and Ghia, 2018).

The third approach (Figure 2.7c), described by Garg et al. (2012), is a smoothing approach based on the size of the Eulerian grid. It is based on the definition of an interpolation grid, on whose nodes all the fluid-solid quantities are calculated. This approach is particularly advantageous for the interpolation of the gas-velocity components at particle location, since all the components of the gas-phase velocity are referred to the same interpolation grid. The same strategies can in fact be followed to map an Eulerian property (such as gas velocity) to a particle location.

An example of such scheme is presented in Figure 2.8. The solid dots represent the scalar grid where scalar quantities are computed (pressure field, void fraction, etc.), while the arrows show the components of the velocity field (u and v here), each of them having their own grid. The points indicated by "×" compose the interpolation grid.

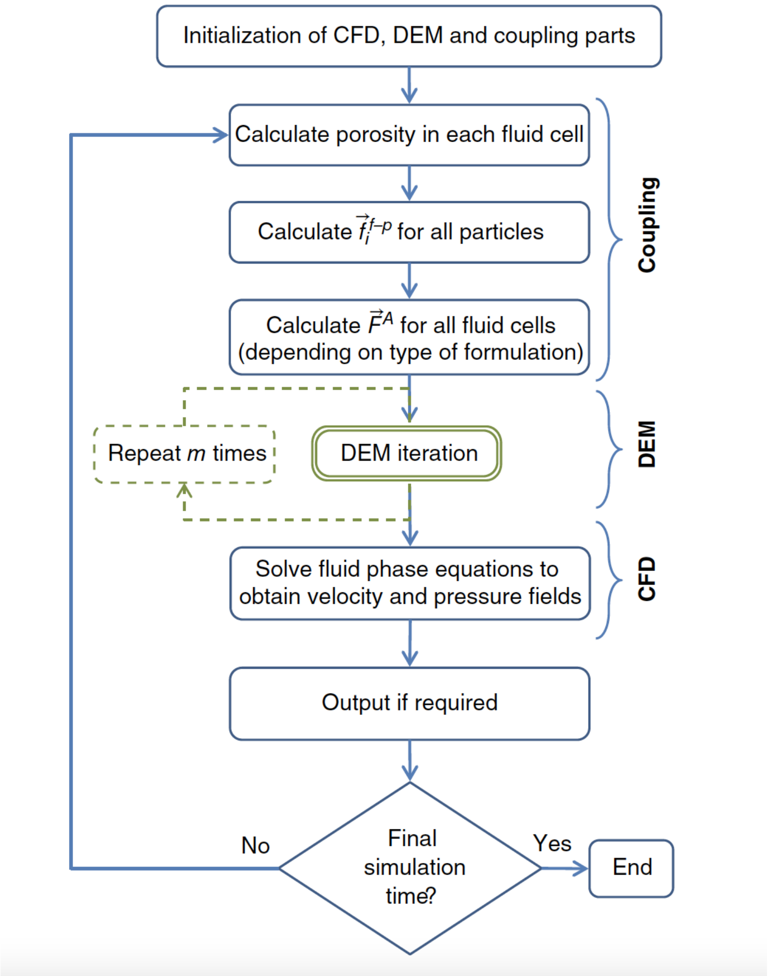

Figure 2.9: Framework of explicit coupling in the CFD-DEM model (Norouzi et al., 2016).

2.3.2 CFD-DEM algorithm

Figure 2.9 shows the general framework of coupling in the unresolved CFD-DEM model, as reported by Norouzi et al. (2016).

The simulation starts with the inizialization of all the components in the simulation: DEM, CFD and coupling.

The void fraction is each fluid cells is then calculated based on particle location, mesh structure and interpolation strategy.

The velocity of particles, the velocity of the fluid, as well as the pressure and stress tensor at the current fluid time step, are then used to calculate the fluid-particle interaction force acting on each particle, $\vec{f}_i^{f-p}$.

The corresponding volumetric fluid-particle interaction force is calculated in each fluid cell ($\vec{F}^A$).

The next step is the iteration loop of the DEM part of the code. The time step for integrating the equation of motion of particles is Δt_p and iteration loop of DEM is repeated m times (where m here is the ratio between the fluid timestep, Δt_f, and the solid timestep, Δt_p, usually smaller than Δt_f). After the DEM loop is completed, the new position and translational and rotational velocities of all particles in the next fluid time step are obtained .

The fluid phase equations can then be solved to obtain velocity and pressure fields.

The results of calculations are velocity and pressure fields of the fluid phase and position and velocity of all particles in the next time step.

The procedure is repeated until the end time of the simulation is reached.

2.4 Fluid forces on particles

In all fluid-particle flows, drag, lift and pressure gradient forces play a key role in the movement of particles. An accurate calculation of these force contributions is important for an accurate, realistic simulation of multiphase flows.

2.4.1 Drag force

The drag coefficient of an isolated smooth sphere moving in a fluid has been extensively studied for many years now (Bird et al., 2007), with different correlations available. These correlations, however, are not directly applicable in CFD-DEM problems: the drag force on a particle moving in a dense bed is strongly influenced by the surrounding particles.

The drag force is proportional to the relative velocity between the i-th solid particle and the local mean velocity of the surrounding fluid, $\vec{w}_i$:

$$\vec{F}_d = \sum K_{gs} \vec{w}_i \tag{2.62}$$

where K_{gs} is the interfacial momentum exchange between the two phases.

The intensity of the force depends on the amount of solid in the fluid cell and on the flow condition. The quantity of solid is defined through the void fraction (or volume fraction or porosity) ε, i.e., the ratio between the volume of the fluid and the total volume. The fluid motion regime (e.g. laminar or turbulent) is defined by the Reynolds number. In unresolved CFD-DEM codes, the Reynolds number for a particle in a fluid is expressed as a function of the void fraction:

$$Re_p = \frac{d|\vec{w}_i|\rho_f \varepsilon}{\mu_f} \tag{2.63}$$

where d is the particle diameter, $\vec{w}_i$ is the particle-fluid relative velocity, ρ_f and μ_f are the fluid density and viscosity, respectively.

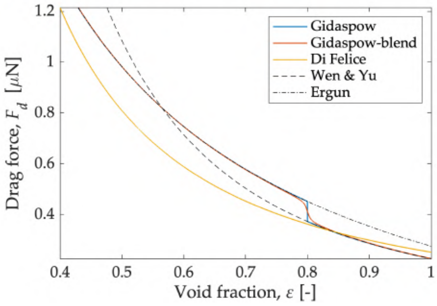

Figure 2.10: Drag force as a function of void fraction for different drag models. d = 100 μm, $\rho_f = 1.2$ kg/m^3, $|\vec{w}_i| = 5$ m/s and $\mu_f = 1.8 \cdot 10^{-5}$ Pa ·s

The calculation of K_{gs} depends on the drag model used. Some of the existing and widely used drag models will be listed. The presented models are expressed according to the "Model A" formulation.

A comparison between the presented drag models is reported in Figure 2.10. The curves have been obtained considering a 100 μm particle in air ($\rho_f = 1.2$ kg/m^3, $\mu_f = 1.8 \cdot 10^{-5}$ Pa ·s), moving with a relative velocity of 5 m/s.

2.4.1.1 Ergun

The Ergun model (Ergun, 1952) is a formulation of the drag force suitable for dense systems. It is the combination of Carman-Kozeny (viscous flow, low Reynolds) and Burke-Plummer (high Reynolds flow) equations, and associates the drag force to the pressure drop in a porous medium.

The interfacial momentum exchange is given by:

$$K_{gs,E} = 150 \frac{\mu_f (1-\varepsilon)}{\varepsilon d^2} + 1.75 \frac{\rho_f (|\vec{w}_i|}{d} V_p \tag{2.64}$$

2.4.1.2 Wen and Yu

The Wen and Yu drag model (Wen and Yu, 1966) is suitable for diluted systems. It has been derived from experimental data on settling velocity presented by Richardson and Zaki (1997).

The interfacial momentum exchange is given by:

$$K_{gs,WY} = 0.75 \cdot C_d \cdot |\vec{w}_i| \cdot \rho \cdot \varepsilon \cdot \frac{\varepsilon^{-2.65}}{d} V_p \tag{2.65}$$

where d is the particle diameter, V_p is the particle volume and c_D is the drag coefficient for a spherical particle:

$$C_d = \begin{cases} \frac{24}{Re_p}(1 + 0.15 Re_p^{0.687}) & \text{if } Re_p \leq 1000. \\ 0.44 & \text{if } Re_p > 1000. \end{cases} \tag{2.66}$$

2.4.1.3 Di Felice

Di Felice drag model (Di Felice, 1994) has a similar formulation to the Wen and Yu drag model, with an interfacial momentum exchange expressed by:

$$K_{gs,DF} = 0.75 \cdot C_d \cdot |\vec{w}_i| \cdot \rho \cdot \varepsilon \cdot \frac{\varepsilon^{-(\chi-1)}}{d} V_p \tag{2.67}$$

where:

$$\chi = 3.7 - 0.65 \cdot e^{-0.5 \cdot (1.5 - log10(Re_p))^2} \tag{2.68}$$

and:

$$C_d = \left(0.63 + \frac{4.8}{\sqrt{Re_p}}\right)^2 \tag{2.69}$$

The fact that the void degree exponent in equation 2.67 is itself a function of the Reynolds number, makes Di Felice drag model applicable over a wider range than the Wen and Yu model.

2.4.1.4 Gidaspow

Gidaspow drag model (Gidaspow, 1994) is a combination of Wen and Yu (Equation 2.65) and Ergun (Equation 2.64) drag models. The Wen and Yu equation is used if the system is dilute, while the Ergun equation is used if the system is dense:

$$K_{gs,G} = \begin{cases} K_{gs,WY} & \text{if } \varepsilon > 0.8. \\ K_{gs,E} & \text{if } \varepsilon \leq 0.8. \end{cases} \tag{2.70}$$

Due to combination of the two models, a good representation for both diluted and dense systems can be obtained. However, a noticeable "switch" at $\varepsilon = 0.8$ occurs due to the transition, as visible in Figure 2.10.

2.4.1.5 Gidaspow-blend

The Gidaspow-blend model is similar to the Gidaspow model, using Wen and Yu equation for dilute systems and Ergun equation for dense system. However, the combination of the two models occurs through a smoothed average function of the void fraction, ε (Garg et al., 2012). The interfacial momentum exchange is given by:

$$K_{gs,GB} = (1 - \phi_{gs}) \cdot K_{gs,E} + \phi_{gs} \cdot K_{gs,WY} \tag{2.71}$$

with:

$$\phi_{gs} = \frac{\tan^{-1}[150 \cdot 1.75(\varepsilon - 0.8)]}{\pi} + 0.5 \tag{2.72}$$

2.4.1.6 Drag models for polydisperse systems

The expression of the drag forces presented so far are derived for monodisperse systems, but are often applied to calculate the drag also in polydisperse systems. In the classic formulation for the drag force, the only variable that takes into account the effects of the surrounding particles on the drag force acting on a specific particle is the void fraction, ε. In a polydisperse system, however, the same void fraction could be obtained with countless particle distributions, and each of them would give rise to the same force on the particle if the monodisperse approach is followed. In some cases it is therefore necessary to take into account the polydispersion by introducing a few more elements in the drag force model.

Different models dealing with the presence of polydisperse particles are available in literature (Beetstra et al., 2007; Holloway et al., 2010; Cello et al., 2010; Rong et al., 2014). Their general form is:

$$F_{d,i} = \gamma_i \overline{F_d} \tag{2.73}$$

where $\overline{F_d}$ is evaluated with monodisperse models and the repartition coefficient, γ_i distributes such average force across the different particle size classes. It it itself a function of the flow conditions (Re_p and ε) and the local polydispersion index, y_i:

$$y_i = \frac{D_i}{\overline{D}} \tag{2.74}$$

in which $\overline{D} = \left(\sum_k \frac{x_k}{D_k}\right)^{-1}$ is the Sauter mean diameter, and x_k is the volume fraction of the particle size class.

The steps to calculate the drag force according to Cello - Di Renzo - Di Maio model (CDD, Cello et al. (2010)) are shown in Figure 2.11. Compared to the other polydisperse drag models available in literature, it has the advantage of being computationally efficient and applicable in a wide range of Reynolds number, void fraction and polydispersion index.

2.4.2 Pressure gradient force

The pressure gradient force, also known as generalized buoyancy, is defined as the product between the particle volume, V_p, and the gradient of the averaged pressure, ∇p:

$$F_b = -V_p \nabla p \tag{2.75}$$

2.4.3 Lift force

Lift force is generally normal to the relative motion of fluid and particle and is due to particle rotation and fluid shear stress. This force involves the

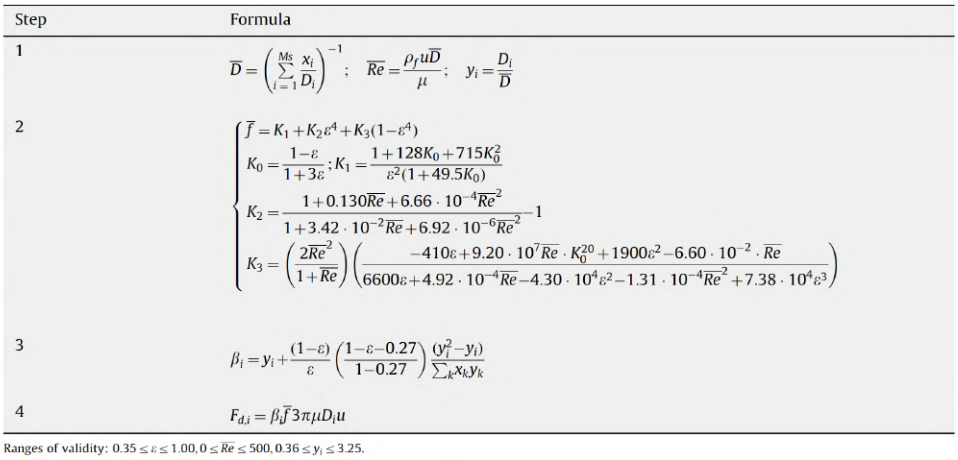

Step	Formula
1	$\overline{D}=\left(\sum_{i=1}^{Ms}\frac{x_i}{D_i}\right)^{-1};\quad \overline{Re}=\frac{\rho_f u\overline{D}}{\mu};\quad y_i=\frac{D_i}{\overline{D}}$
2	$\begin{cases}\overline{f}=K_1+K_2\varepsilon^4+K_3(1-\varepsilon^4)\\ K_0=\frac{1-\varepsilon}{1+3\varepsilon};K_1=\frac{1+128K_0+715K_0^2}{\varepsilon^2(1+49.5K_0)}\\ K_2=\frac{1+0.130\overline{Re}+6.66\cdot10^{-4}\overline{Re}^2}{1+3.42\cdot10^{-2}\overline{Re}+6.92\cdot10^{-6}\overline{Re}^2}-1\\ K_3=\left(\frac{2\overline{Re}^2}{1+\overline{Re}}\right)\left(\frac{-410\varepsilon+9.20\cdot10^7\overline{Re}\cdot K_0^{20}+1900\varepsilon^2-6.60\cdot10^{-2}\cdot\overline{Re}}{6600\varepsilon+4.92\cdot10^{-4}\overline{Re}-4.30\cdot10^4\varepsilon^2-1.31\cdot10^{-4}\overline{Re}^2+7.38\cdot10^4\varepsilon^3}\right)\end{cases}$
3	$\beta_i=y_i+\frac{(1-\varepsilon)}{\varepsilon}\left(\frac{1-\varepsilon-0.27}{1-0.27}\right)\frac{(y_i^2-y_i)}{\sum_k x_k y_k}$
4	$F_{d,i}=\beta_i\overline{f}3\pi\mu D_i u$

Ranges of validity: $0.35 \le \varepsilon \le 1.00, 0 \le \overline{Re} \le 500, 0.36 \le y_i \le 3.25$.

Figure 2.11: Steps of the drag model in polydisperse systems according to CDD model (Cello et al., 2010).

shear-dependent Saffman lift force, caused by the fluid velocity gradient, and the rotational-dependent Magnus lift force, imposed by particle contact and rebound from a surface (Norouzi et al., 2016).

2.4.3.1 Saffman lift force

The Saffman lift force, or slip-shear lift force, is experienced by particles moving in a shear layer (Figure 2.12). The uneven distribution of velocity around the particle causes an uneven pressure distribution, which results in a lift force acting on the particles in the direction of growth of the slip velocity.

It is expressed by the following:

$$F_{LS} = \frac{\rho_f}{2}\frac{\pi}{4}d^3 C_{LS}\left(\vec{w}_i \times \vec{\omega}_f\right) \tag{2.76}$$

where d is the particle diameter, $\vec{w}_i$ is the particle-fluid relative velocity, $\vec{\omega}_f$ is the curl of velocity vector and C_{LS} is the Saffman lift coefficient.

The curl of velocity vector (or vorticity) is defined by:

$$\vec{\omega}_f = \nabla \times \vec{u}_f = \begin{pmatrix} \frac{\partial u_z}{\partial y} - \frac{\partial u_y}{\partial z} \\ \frac{\partial u_x}{\partial z} - \frac{\partial u_z}{\partial x} \\ \frac{\partial u_y}{\partial x} - \frac{\partial u_x}{\partial y} \end{pmatrix} \tag{2.77}$$

The Saffman lift coefficient, C_{LS}, is calculated as follows:

$$\beta = 0.5\frac{Re_S}{Re_p} = 0.5\frac{d|\vec{\omega}_f|}{|\vec{w}_i|} \tag{2.78}$$

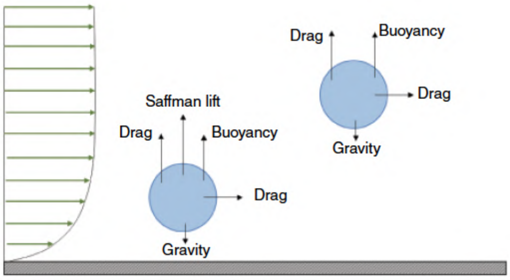

Figure 2.12: Illustration of slip-shear force on a particle in a non-uniform flow field (Norouzi et al., 2016).

$$f(Re_p, Re_S) = \begin{cases} (1 - 0.3314\beta^{0.5}) \exp\left(-\frac{Re_p}{10}\right) + 0.3314\beta^{0.5} & Re_p \leq 40 \\ 0.0524(\beta Re_p)^{0.5} & Re_p > 40. \end{cases} \tag{2.79}$$

$$C_{LS} = \frac{4.1126}{Re_S^{0.5}} f\left(Re_p,\ Re_S\right) \tag{2.80}$$

Re_p is the particle Reynolds number (Equation 2.63) and Re_S is the particle shear Reynolds number:

$$Re_S = \frac{\rho_f d^2 |\vec{\omega}_f|}{\mu_f} \tag{2.81}$$

2.4.3.2 Magnus lift force

If the particle rotates with high angular velocity (for example due to repeated collisions with a wall), the flow field of the fluid around it deforms, giving rise to a transverse lift force. The Magnus lift force is caused by asymmetric pressure distribution around the particle due to velocity difference between bottom and top of the particle.

It can be calculated as:

$$F_{LR} = \frac{\rho_f}{2} \frac{\pi}{4} d^2 \; C_{LR} \, |\vec{w}_i| \, \frac{\vec{\omega}_r \times \vec{w}_i}{|\vec{\omega}_r|} \tag{2.82}$$

where $\vec{\omega}_r$ is the relative rotation between the fluid ($\vec{\omega}_f$, vorticity) and the particle ($\vec{\omega}_p$):

$$\vec{\omega}_r = \frac{1}{2}\vec{\omega}_f - \vec{\omega}_i \tag{2.83}$$

and C_{LR} is the Magnus lift coefficient, which can be calculated as:

$$C_{LR} = 0.45 + \left(\frac{Re_R}{Re_p} - 0.45\right) \exp\left(-0.05684 \cdot Re_R^{0.4} \cdot Re_p^{0.3}\right) \tag{2.84}$$

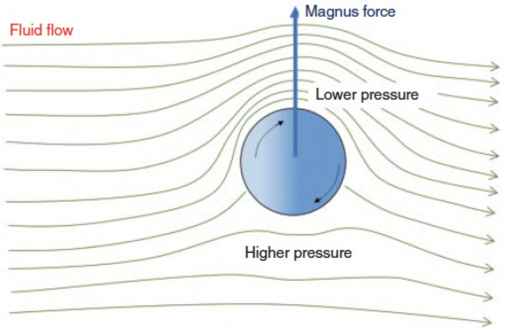

Figure 2.13: Illustration of the Magnus lift force (Norouzi et al., 2016).

The above formula is valid for $Re_p < 140$.

Re_R is the particle rotational Reynolds number, given by:

$$Re_R = \frac{\rho_f d^2 |\vec{\omega}_r|}{\mu_f} \tag{2.85}$$

2.4.4 Fluid torque

Fluid torque, or rotation drag, incorporates the drag on a rotating particle from the surrounding fluid and expresses the rotational resistance due to inertia of fluid (Sommerfeld, 2008).

It depends on the difference in angular velocity between the particle and the surrounding fluid ($\vec{\omega}_r$) and can be calculated from the following:

$$\vec{T}_\omega = 2.01 d^3 \mu_f \vec{\omega}_r (1 + 0.201\sqrt{Re_R}) \tag{2.86}$$

valid for $20 < Re_R < 1000$. The such calculated torque is added on the right hand side of Equation 2.28.

In a 4-way coupled approach, the effect of the particle on the motion of the fluid phase is taken into account through force-coupling. Similarly, a torque-coupling might be considered as well if the effect of the fluid torque on the solid phase is taken into account.

Andersson et al. (2012) proposed a torque-coupling scheme based on the introduction of a particle stress tensor into the Navier-Stokes equation for momentum conservation (Equation 2.61), which is proportional to the rotational slip velocity.

The particle stress tensor is defined as:

$$\vec{T}_{ij}^P = \frac{1}{V_{cell}} \sum_{l=1}^{n_P} \epsilon_{mij} \vec{N}_m \tag{2.87}$$

where ϵ_{mij} is the Levi-Civita permutation tensor, V_{cell} the control volume (e.g., a grid cell), $\vec{N}_m$ is the torque vector, composed by the torques exerted from the fluid on each particle. The summation is carried out over all n_p particles in the volume V_{cell}.

2.5 Modelling of cohesive systems

The powders used in the pharmaceutical field are in almost all cases particles with poor flowability properties. It is therefore necessary to introduce in the simulation a model that can take into account the adhesion and cohesion forces between particles. To establish the most suitable model for cohesive forces for the system in question, reference can be made to the Tabor number, μ_T, a dimensionless group that compares cohesive force and contact force (Marshall and Li, 2014). μ_T is defined by the following equation:

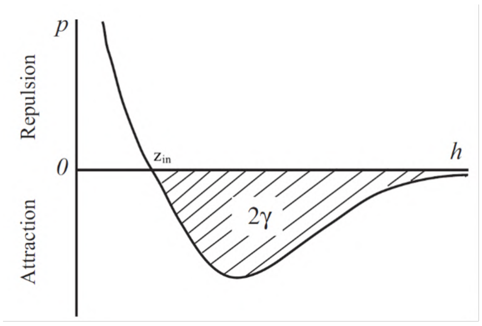

Figure 2.14: Variation in pressure p as a function of the distance h between two surfaces caused by the sum of the attractive and repulsive van der Waals forces (Marshall and Li, 2014).

$$\mu_T = \left(\frac{4r\gamma^2}{E^2 z_{in}^3} \right)^{1/3} \tag{2.88}$$

where z_{in} is the cut-off distance and γ is the surface energy density. The meaning of z_{in} and γ is illustrated in Figure 2.14. z_{in} is the distance between two particles in the vacuum at which the attractive and repulsive - steric - van der Waals forces are equal, while γ is defined as half the work (per unit area) required to separate two surfaces that are initially at distance h.

For weak van der Waals-type interactions between two surfaces at distance z_{in}, the surface energy density is a function of the Hamaker constant, A, according to the following:

$$\gamma = \frac{A}{24\pi z_{in}^2} \tag{2.89}$$

Typical values of the Hamaker constant for ceramic and organic materials in air range from $5 \cdot 10^{-20}$ J to $10 \cdot 10^{-20}$ J and the use of a cutoff distance

$z_{in} = 0.165$ nm is suggested (Marshall and Li, 2014). From these values, the calculated surface energy from Equation 2.89 is about $\gamma = 0.04$ J/m^2.

Figure 2.15 shows the Tabor number, μ_T, as a function of particle radius, calculated from Equation 2.88. The calculated values are higher than 1, even for the smallest diameter considered (1 μm).

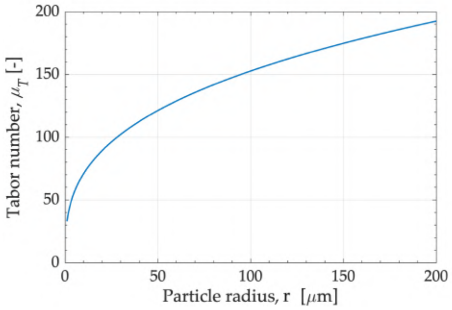

Figure 2.15: Tabor number as a function of particle radius ($E = 0.2$ GPa, $r =$ 1-200 μm, $\gamma = 0.04$ J/m^2, $z_{in} = 0.165$ nm)

For $\mu_T \gg 1$, the order of magnitude of the adhesive force is much lower than that of the elastic deformation. The model to refer to in such cases is the Johnson-Kendall-Roberts elastic contact model, commonly known as the JKR model (Johnson et al., 1971).

2.5.1 Johnson-Kendall-Roberts model

The basis of the JKR model is the hypothesis that adhesive-type interactions occur only within the "flattened" region of the surfaces of the colliding particles, or in the contact region. In this way the adhesion interaction between two particles is approximated by the adhesion force between two parallel flat surfaces. Since the deformation of the particles is caused by the force acting between them, which is in turn influenced by the deformation of the particles, the interaction between two adhesive particles of micrometric size is a highly non-linear process. It follows that the cohesion and collision forces between particles cannot simply be summed, but a specific model for the contact forces between particles is required that includes the combination of elastic and adhesive effects. The normal contact force is a function of the normal overlap, δ_n and the cohesion surface energy, γ:

$$F_{el,JKR} = 4\sqrt{\pi\gamma E_{eq}}a^{3/2} - \frac{4E_{eq}}{3R_{eq}}a^3 \tag{2.90}$$

$$\delta_n = \frac{a^2}{R_{eq}} - \sqrt{\frac{4\pi\gamma a}{E_{eq}}} \tag{2.91}$$

where a is the radius of the contact area.

According to JKR contact model, the cohesive interaction acts also at negative overlaps during the detachment phase, when the two objects would no longer touch. This is due to the deformation caused by the cohesive force during the impact, which holds the surfaces together up to a maximum of attractive (negative) force called pull-off force. In order for the particles to detach, the force that separates them must exceed this force and the nominal distance between the particles (between the spheres considered undeformed) must exceed the overlap corresponding to the pull-off force. The force-displacement plot of the JKR model, described by Equations 2.90 and 2.91, is shown in Figure 2.16 (red curve) in comparison with the curve of the Hertz contact model. When two particles approach each other, the contact is formed when the two surfaces touch, i.e. when $\delta_n = 0$ (point O in Figure 2.16). An attractive interaction force starts pulling the two particles closer, increasing the overlap until the equilibrium value is reached, at which $F_{el,JKR} = 0$ (point E in in Figure 2.16). In the unloading phase, when the two particles detach, the same path from equilibrium (E) to zero (O) overlap is followed, but then the attractive force will continue to increase in magnitude until it reaches the pull-off force value (point P in Figure 2.16). The contact will break if a critical value of the overlap is reached (point C in Figure 2.16), after which the attractive force will suddenly drop to zero. The full JKR model thus provides an attractive force that acts also when particles are not physically in contact, but only in the unloading phase. This hysteretic process makes the DEM implementation of the model more complex.

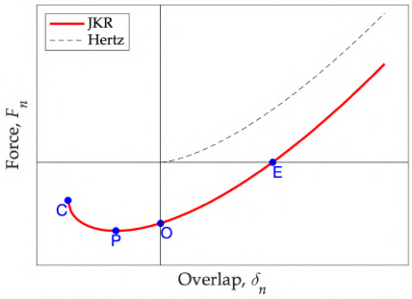

Figure 2.16: Force-displacement relationship with JKR and Hertz models.

2.5.1.1 Dimensionless JKR model

The JKR model can be expressed in a dimensionless form by expressing the variables as a function of the equilibrium (E) and pull-off (P) points in the graph (Figure 2.16). The pull-off force F_P, the value of the force beyond which the detachment takes place, is given by:

$$F_P = -3\pi\gamma R_{eq} \tag{2.92}$$

The point E is the point at which the force is zero ($F_{el,JKR} = 0$), so there is an equilibrium between the cohesive contribution and the elastic contribution. The value of the radius of the contact area (a_E) and of the overlap (δ_E) at this point are given by:

$$a_E = \left(9\pi\gamma\frac{R_{eq}^2}{E_{eq}}\right)^{\frac{1}{3}} \tag{2.93}$$

$$\delta_E = \left(\frac{\pi\gamma\sqrt{3R_{eq}}}{E_{eq}}\right)^{\frac{2}{3}} \tag{2.94}$$

If $a^* = a/a_E$, $\delta^* = \delta/\delta_E$, and $F^* = F/F_p$, the functional relationships of the JKR model can be expressed by:

$$\delta^* = \left(3a^{*2} - 2\sqrt{a^*}\right) \tag{2.95}$$

$$F^* = 4\left(-a^{*3} + a^{*1.5}\right) \tag{2.96}$$

The dimensionless force-displacement graph for the JKR model is shown in 2.17, along with the coordinates of the points of interest.

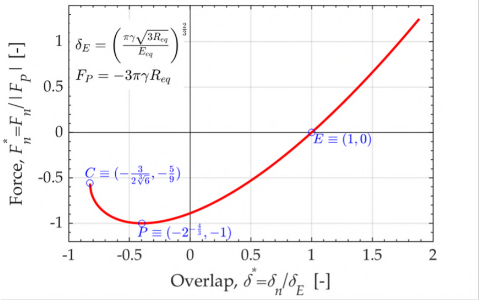

Figure 2.17: Force-displacement relationship with JKR model in dimensionless variables

2.5.2 Polynomial approximation of JKR model

The JKR model can be expressed by a slightly less expensive version from the computational point of view, using polynomial approximations. The comparison between the full JKR model and the polynomial approximation is shown in Figure 2.18, where the normal force as a function of the overlap is reported for both models. The trait of the negative overlap model has been approximated with a parabola having the vertex in F_p and passing through $\left(0,\ \frac{4}{9}\sqrt{3}F_p\right)$. The segment of the positive overlap model (therefore in contact) is the vertical translation of a value equal to $\frac{4}{9}\sqrt{3}F_p$ of the curve that represents the Hertz elastic normal force model. The translation is done in such a way as to have the same equilibrium overlap value, δ_E. As in the full JKR model, the difference between the loading phase and the unloading phase is taken into account, so that a reasonable approximation of the phenomenon can be obtained, as shown in Figure 2.18. The advantage is not having to solve dynamically a fourth degree equation to obtain the force as a function of the overlap (see e.g. Parteli et al. (2014)).

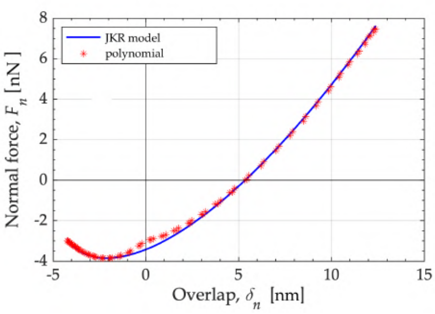

Figure 2.18: Force-displacement relationship for JKR model and polynomial JKR model.

The equation of the considered polynomial JKR model is:

$$F = \begin{cases} \frac{4}{3}E_{eq}\sqrt{R_{eq}}\delta^{1.5} - \frac{4}{9}\sqrt{3}\cdot F_p, & \delta \geq 0 \\ a\delta^2 + b\delta + c, & \delta < 0. \end{cases} \tag{2.97}$$

where:

$$\begin{cases} a = 2^{\frac{8}{3}}\left(\frac{4}{9}\sqrt{3} - 1\right)\frac{F_p}{\delta_E^2} \\ b = 2^{\frac{7}{3}}\left(\frac{4}{9}\sqrt{3} - 1\right)\frac{F_p}{\delta_E} \\ c = \ \frac{4}{9}\sqrt{3}\cdot F_p \end{cases} \tag{2.98}$$

The values of coefficients a, b and c can be determined at the beginning of the simulation as they depend only on the properties of the particles (radius, Young's modulus, surface energy density, see Equations 2.94 and 2.92).

2.5.3 Simplified models

The complexity of the model, its hysteretical trend and the computational burden associated with the non-linearity of the equations of the JKR model has led to the development of simplified cohesion models.

2.5.3.1 Linear cohesion model (sjkr)

The linear cohesion model, also referred to as *simplified JKR* or *sjkr* (Kloss et al., 2012), modifies Hertz-Mindlin contact by adding a normal cohesion force proportional to the contact area, A_{cont}:

$$F_{coh} = kA_{cont} \tag{2.99}$$

where k is the cohesion energy density, with the dimensions of an energy per unit volume (J/m^3). The calculated force acts only when $A_{cont} > 0$, and therefore when the two bodies are in contact; in the case of two spheres, when the distance between their centers is less than the sum of the radii.

The contact area can be calculated according to Hertz contact theory from the following:

$$A_{cont} = \pi R_{eq} \delta_n \tag{2.100}$$

where R_{eq} is the equivalent radius and δ_n is the normal overlap. This formulation is used in the software EDEM (Solutions, 2014).

The software LIGGGHTS calculates the contact area with two different formulations (DCS Computing, 2016). The first formulation (*sjkr1*) is based on geometrical considerations:

$$A_{cont} = \frac{\pi}{4} \frac{(-d+r+R)(-d+r-R)(-d-r+R)(d+r+R)}{d^2} \tag{2.101}$$

with d, r and R being the distance between the centers of the two spheres, the radius of the first sphere, the radius of the second sphere, respectively.

The second formulation (*sjkr2*) is expressed as follows:

$$A_{cont} = 2\pi R_{eq}(2\delta_n) \tag{2.102}$$

A comparison between the contact area calculated with the three different formulations is shown in Figure 2.19. Given the difference in the calculation of the contact area, the three formulations give different macroscopic results for the same cohesion energy density (Ramírez-Aragón et al., 2018).

The force calculated by Equation 5.1 is added to the Hertzian normal elastic contact force, as they act in opposite direction. The total elastic force acting in normal direction is thus given by:

$$F_{el,sjkr} = kA_{cont} - \frac{4}{3} E_{eq} \sqrt{R_{eq}} \delta_n^{1.5} \tag{2.103}$$

An equilibrium overlap value, for which $F_{el,sjkr} = 0$, exists with this cohesion model. It corresponds to the condition in which the cohesive, attractive force is perfectly balanced by the repulsive elastic force. By considering the formulation of contact area expressed by Equation 2.100, the equilibrium overlap is given by:

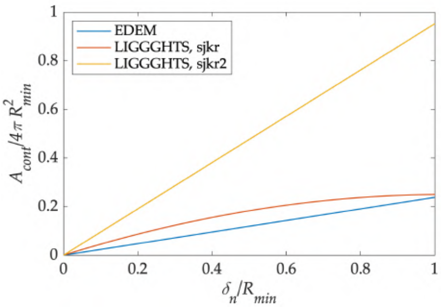

Figure 2.19: Contact area between two particles ($R_1 = 5\ \mu$m, $R_2 = 100\ \mu$m) as a function of normal overlap for three different formulation of SJKR cohesion model. Overlap value are normalized by dividing for the radius of the smaller particle, while contact area values are normalized by dividing for the surface area of the smaller particle.

$$\delta_{eq} = R_{eq}\left(\frac{3}{4}\pi k \frac{1}{E_{eq}}\right)^2 \tag{2.104}$$

2.5.3.2 Constant force model (VDW)

The interparticle cohesion model proposed by Galvin and Benyahia (2014) is implemented in the MFIX software and is referred to as "VDW" model. It is based on Hamaker's approximation of the van Der Waals interparticle attractive force by summing all pairwise combinations of corresponding intermolecular attraction forces between the two bodies in a vacuum.

The cohesive/adhesive force between the like or dissimilar particles, respectively, and with the walls are accounted for using a combination of a van der Waals force model between distant particles and constant surface energy model for particles in contact:

$$F_{coh} = \begin{cases} 0 & z > z_{out} \\ \frac{A \cdot 2R_{eq}}{12z^2} & z_{in} < z \leq z_{out} \\ 2\pi\gamma(2R_{eq}) & z \leq z_{in} \end{cases} \tag{2.105}$$

z is the distance between the surfaces of the two particles involved, R_{eq} is the equivalent radius, A is the Hamaker constant, z_{in} and z_{out} are the inner and outer cutoff, respectively, and γ is the surface energy, calculated from Equation 2.89.

The inner cutoff prevents the force from tending to infinity and the outer cutoff limits the number of interactions considered by excluding sufficiently distant particles. Typical values for the inner and outer cutoff are $z_{in} = 0.165$ nm and $z_{out} = 6$ nm according to Marshall and Li (2014).

The third expression of Equation 2.105 is applied when the particles are in contact (or at a distance lower that z_{in}) and it is analogous to the Bradley relationship (Greenwood, 1997), adding a constant force contribution to the Hertzian load. The second expression of Equation 2.105 is a simplified formula for the Hamaker/van der Waals force, valid when z is much smaller than the particle radii, according to Gu et al. (2016). As it is applied when 0.165 nm $< z \leq 6$ nm, the assumption is reasonable. The trend of the cohesive force as a function of the interparticle distance according to the VDW model is shown in Figure 2.20.

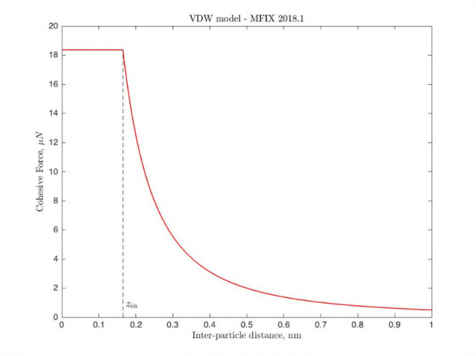

Figure 2.20: Cohesive force as a function of inter-particle distance in VDW model.

The model implemented in MFIX can also taken into account surface asperities, by appropriately reducing the adhesive/cohesive force based on a correction term which takes into account the radius of the asperity (Galvin and Benyahia, 2014). Equation 2.105 is written without taking this term into account, as in the present work it is assumed that surfaces are smooth.

Chapter 3

Materials and methods

In this Chapter, the software used for the simulations will be described. Moreover, the geometry and the numerical grid of the two DPI considered in the present work will be presented and analysed.

3.1 Simulation software

3.1.1 MFIX

An extended version of the open-source code MFIX-DEM (Garg et al., 2012) (version 18.1.5) with some modifications is used to solve the governing equations for the fluid and particle phases.

MFIX (Multiphase Flow with Interphase eXchanges) (NETL Multiphase Flow Science Team, 2020) is an open-source software that allows the modeling and simulation of multiphase systems of engineering interest. The MFIX code was developed by the National Energy Technology Laboratory of the US Department of Energy, is written in FORTRAN and has the following capabilities: multiphase flow, multiple types of particles, three-dimensional Cartesian or cylindrical coordinate systems, uniform or non-uniform cartesian grids, energy balances, and balances of gas and solid species. The theoretical basis and the numerical implementation of the MFIX software are described in Syamlal et al. (1993, 1998).

The software was initially developed to be run in bash shell, through the definition of a textual, input data sheet containing the keywords specified in the guide and the subsequent run from the command line in serial or parallel (through MPI protocol). A Graphical User Interface (GUI) has been introduced in the latest versions (NETL Multiphase Flow Science Team, 2020). The command line version of the code has been used in the present work.

The software allows to import and create geometry for the domain interpretation. The basic version allows to import geometries through textual STL files, with the graphical version the possibility of creating new ones has been added. The meshing operation leads to the creation of Cartesian, structured, staggered meshes.

MFIX provides a suite of models that treat the carrier phase (typically the gas phase) and disperse phase (typically the solids phase) with different approaches:

- MFIX-TFM (two-fluid model) is a Eulerian-Eulerian model in which the fluid and solids as evaluated as continuous phases.
- MFIX-DEM (Discrete Element Model) is a Eulerian-Lagrangian model that treats the fluid phase as a continuum and models the individual particles of the solid phase.
- MFIX-PIC (Multiphase Particle in Cell) is another Eulerian-Lagrangian model that represents the fluid as a continuum while a "parcel" is used to represent groups of real particles with similar physical characteristics.

The CFD model implemented in MFIX is a finite volume implementation which uses a staggered grid and a SIMPLE-type iterative pressure-velocity coupling with an automatic time-step adjustment to reduce the runtime. Gas can be modelled as laminar or turbulent (mixing length and $k-\varepsilon$ model available), incompressible or compressible, by defining the fluid density as constant or through the ideal gas law.

MFIX-DEM has been used in the present work. The Discrete Element Method (DEM) model for the solid allows a simulation of large numbers of interacting discrete objects, with the resolution of the particle equation of motion.

The initial position of the discrete particles can be defined by different seeding options. By defining the coordinates and volume of an "initial solids" region, particles will be placed in a cubical, ordered arrangement fulfilling the prescribed void fraction. Initial particle data can also be read from a text file containing coordinates, velocity, density, diameter, phase ID.

The soft-sphere collision models LSD (Equation 2.33) and Hertian (Equation 2.37) are implemented for particle-particle contact and particle-boundary interaction are present. The available integration methods for particle trajectories are Euler and Adam-Bashfort. The neighbour search is performed according to a grid-based approach. The degree of coupling between fluid and solid phase can be chosen as one-way coupling, or fully coupled. The interconnection between particle and fluid field can be calculated according to different interpolation schemes (see Figure 2.7). Different drag models are available: Syamlal-O'Brien, Beestra-van der Hoef-Kuipers , Gidaspow (Equation 2.70), Gidaspow Blend (Equation 2.71, Holloway-Yin-Sundaresan, Koch-Hill, Wen-Yu (Equation 2.65), etc.

The results are stored in ascii or binary VTK files (* .vtu for gases and *.vtp for solids). In the command line version of the code, post-processing programs are required to view the results, while the GUI offers some basic post-processing tools.

Being open-source, the software allows for great flexibility and customization. Additional models can be implemented by changing the existing subroutines or through user defined functions.

Several extensions have been developed by the Unical research group and implemented in the in-house version of the code.

A non-comprehensive list of implemented modules is presented below:

- Solid timestep for Hertzian contact model as a function of contact duration (Equation 2.50);
- Polydisperse drag models (see section 2.4.1.6);
- Di Felice drag model (Equation 2.67);
- LES turbulence models (Equations 2.19, 2.20, 2.21);
- CDT rolling friction model (Equation 2.43);
- Polynomial JKR contact model (see section 2.5.1.1);
- SJKR contact model (see section 2.5.3.1)
- Saffman lift force (see section 2.4.3.2);
- Magnus lift force (see section 2.4.3.1);
- Fluid torque with 4-way coupling (see section 2.4.4);
- Coarse graining (Napolitano et al., 2022);
- Printout of forces and torques in output VTK data files;
- Modelling of triboelectric charging and electrostatic forces (Alfano et al., 2021).
- Modelling of fictitious forces.

The simulations are conducted on a hybrid computing server (multiCPU and multiGPU) supplied by the CheProDeS laboratory at Unical, which has 16 Intel Xeon CPUs (128 total cores), 16 Nvidia GPUs, 512GB RAM and high-speed InfinityBand interconnect. Parallel processing of the calculations based on the Message Passing Interface (MPI) has been extensively used by running the code on up to 64 cores.

3.1.2 Other softwares

Two other simulation software were used for some specific applications. OpenFOAM was used to carry out CFD simulations, while LIGGGHTS was used for DEM simulations.

3.1.2.1 OpenFOAM

OpenFOAM is a free, open source CFD software developed primarily by OpenCFD Ltd since 2004. It has a large user base across most areas of engineering and science, from both commercial and academic organisations. It has an extensive range of features to solve complex fluid flows. In the present work, OpenFOAM was used for CFD applications with LES turbulence, both to validate the code subsequently implemented in MFIX, and for CFD and Lagrangian tracking simulations on a capsule-based Dry Powder Inhaler.

3.1.2.2 LIGGGHTS

LIGGGHTS®is an Open Source Discrete Element Method Particle Simulation Software. It is widely used for the simulation of particulate materials, from fundamental studies to industrial problems. In the present work, the software has been used for wall-impact simulations of a single carrier particle with a single API particle adhered. It has also been used for the validation of some models that have been subsequently implemented in the MFIX software, such as SJKR cohesion model or CDT rolling friction model.

3.2 Post-processing tools

The results obtained CFD-DEM simulations with the three software considered are in VTK format. The post processing tools to visualize, process and analyze the output data will be presented below.

3.2.1 VTK files

The Visualization Toolkit (VTK) is an open-source, freely available software system for 3D computer graphics, modeling, image processing, volume rendering, scientific visualization, and information visualization (Schroeder et al., 1999). It is capable of manipulating and displaying large scientific data. VTK consists of a C++ class library and several interpreted interface layers including Java and Python. The toolkit is created and supported by the Kitware team[1]. VTK is used world-wide in commercial applications, research and development, and as the basis of many advanced visualization applications such as ParaView (Ahrens et al., 2005).

Two differents styles of file formats are available in VTK:

- Simple Legacy Formats (serial, ascii or binary);
- XML based file formats (serial or parallel, ascii or binary).

---

[1] `https://www.kitware.com`

The legacy, serial formats are easier to read and write even by hand. However, they do not offer much flexibility and advanced features.

XML formats were created to facilitate data streaming and support parallel I/O. They also support random access, portable data compression, big endian and little endian byte order, and they offer new file extensions for different VTK dataset types. On the other hand, their syntax is more complex than legacy formats.

The VTK obtained from MFIX simulations are XML formats of two types:

- UnstructuredGrid (.vtu) files - Serial vtkUnstructuredGrid(unstructured); binary format, used for Eulerian fluid cell dataM
- PolyData (.vtp) files - Serial vtkPolyData(unstructured); ascii or binary format, used for solid particles.

3.2.2 ParaView

ParaView[2] is an open-source, multi-platform scientific data analysis and visualization tool that enables analysis and visualization of extremely large datasets. It is characterized by an extensible framework with a collection of tools and libraries for various applications (Ahrens et al., 2005).

Different versions have been used in the present work, from 5.4.0 to 5.10.0, both for rendering and data analysis. It has been used to visualize and process STL and VTK data.

The GUI is designed to easily create pipelines for data processing through the pipeline browser.

The pipeline is a set up composed of sources, filters and sinks. Sources are data input, sinks are data output, while filters transform the data until they take a form in which they can be interpreted and analysed.

There are several types of filters, each performing different operations and types of processing. Most of the filters used in the present work are listed below:

- Glyph: places markers or glyphs at point locations in the input dataset. The glyphs can be oriented or scaled based on vector and scalar attributes on those points. It can be used for advanced 3D rendering of data in geometrical shapes (spheres, arrows, etc.).
- Clip: extracts a subset of data with an implicit function (plane, sphere or box). Returns 3D outputs for 3D inputs.
- Slice: slices through the input dataset with an implicit function (plane, sphere, box) and returns data elements along the implicit function boundary. Returns 2D outputs for 3D inputs.

---

[2] `https://www.paraview.org`

- Extract selection: extracts selected elements from a dataset according to a user-defined criterion.
- Transform: geometrical manipulation of data; it can arbitrarily rotate, translate and scale a dataset.
- Descriptive statistics: computes the minimum, maximum, mean, M2, M3, and M4 aggregates, standard deviation, skewness, and kurtosis for each selected array.
- Annotate time filter: prints current time for a temporal file series on an image or animation.
- Stream tracer: to obtain fluid streamlines (applied to .vtu files).
- Temporal Particles to Pathlines: to obtain particle trajectories (applied to .vtp files).
- Plot selection over time: extracts elements from the input dataset and plots selected attributes over time.
- Integrate variables: integrates a given variable in the selected domain (3D or 2D).
- Calculator: computes a new data array or new point coordinates as a function of existing input arrays, operating like a standard scientific calculator.
- Plot on Intersection Curves: intersects two surfaces (the external surface of the input dataset and a user-defined plane), yielding a curve. Data variables are plotted along the resulting curve.
- Histograms: creates histogram of a selected variable.

The output of the visualization and data analysis process in ParaView can be images or animations. Data can also be extracted and saved as text files (.csv, .txt), legacy VTK, STL.

3.2.3 MATLAB

MATLAB®(MATLAB, 2019), short for "Matrix Laboratory", is a programming language and numeric computing environment written in C and developed by MathWorks. It can be used to analyze data, develop algorithms, and create models. It allows matrix manipulations, plotting of functions and data; it provides packages and toolboxes for signal and image processing, control systems, wireless communications, computational finance, robotics, deep learning and AI and more. In the latest versions, MATLAB® supports parallel computing (through the Parallel Computing Toolbox) and graphics processing units (GPUs).

The MATLAB® application is built around the MATLAB® programming language. It is a weakly typed programming language, as types are implicitly converted. It is also an inferred typed language because variables can be assigned without declaring their type, except if they are to be treated as symbolic objects, and that their type can change. Common usage of the MATLAB® application involves using the "Command Window" as an interactive mathematical shell. Sequences of commands can be saved and stored in program files by using scripts or functions. The latter offer more flexibility, as they can receive input values and return output values. MATLAB® also supports structure data types in the form of a "structure array", where each element of the array has the same field names.

MATLAB® is optimized for operations involving matrices and vectors. Indeed, all saved variables in MATLAB® are arrays. The process of revising loop-based, scalar-oriented code to use MATLAB® matrix and vector operations is called vectorization. Vectorizing MATLAB® code is particularly convenient, as is increases the computation performance consistently (reducing computational time) and makes the code easier to understand. On the other hand, vectorized code may require more memory use if it operates on large matrixes.

In the present work, MATLAB® has been widely used for data analysis both in the post-processing phase and in the construction of the simulation. Specific tools and algorithms have been developed to reading, processing and writing VTK files. Cluster detection algorithms have also been written making use of some functions provided by the "Statistics and Machine Learning Toolbox". The initial positioning of the particles in the simulation was carried out using an algorithm written in MATLAB®, which will be illustrated in the next chapters. Finally, the integrated graph-plotting features have been used to create most of the 2D plots that will be presented later on.

3.3 Geometry and computational grid

3.3.1 Swirl-based Dry Powder Inhaler

3.3.1.1 Geometry

The multi-scale motion of the air, carrier and API powders requires detailed consideration of the particle-particle, particle-fluid and air flow inside the DPI geometry. Key elements to consider are: (i) air flow from the inlet through the dose particle bed, in the swirl chamber and through the exit duct, up until the inhalation mouthpiece; (ii) carrier particles lift-up from the dose cup, their aero-dispersion and release from the mouthpiece; (iii)

API particles lift-up, detachment from the carrier particles as a result of fluid-particle interaction, collisions or other mechanisms, and their release through the mouthpiece.

The geometry used in the present work has been designed aiming at the following goals: reproducing the three aforementioned phenomena; maintaining the characteristic geometric elements of a DPI without referring to a specific device; keeping the design as simple as possible. An analogous approach was followed by Dos Reis et al. (2021) in their experimental work. The considered domain consists of three sections: a hemi-spherical dose cup at the base of the system that houses the initial dose of drug product, a swirl chamber with two symmetrical tangential inlets and two eccentric hemicircular walls between which the air flow develops, and a cylindrical exit duct on top of it. Views from the top, side and in 3D with transparent walls are shown in Figure 3.1, along with key dimensions.

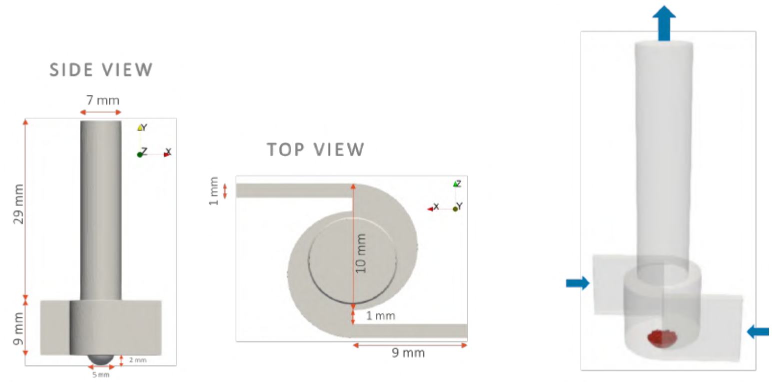

Figure 3.1: Geometry of the system. Side view, top view and 3D transparent representation. In the last one, blue arrows denote the two air inlets and the air outlet from the top of the exit duct; the red part represents the particles filling the hemispherical dose cup.

The air flow is supposed to generate a vortex in the swirl chamber, whose central low-pressure region, aligned with the dose cup, is responsible for the initial particle suction from the cup. The size and the characteristic elements selected for this geometry (e.g. swirl chamber, cylindrical duct, tangential inlets) are comparable to those of inhalers used commercially and in other similar studies (Corradi et al., 2014; Cui et al., 2014). As the inhaler is in horizontal position when used by the patient, gravity force acts in $-z$ direction, i.e., in the direction perpendicular to both the axis of the inhaler and the axis of the tangential inlets.

3.3.1.2 Mesh

In the MFIX–DEM code, complex geometries can be imported from a triangulated STL file of the device boundaries. The DEM part of the code uses directly the triangular elements of the CAD file for collision detection and force calculations; for the gas flow, in the definition of the Eulerian grid MFIX uses the Cartesian grid cut-cell technique (Dietiker et al., 2013): parallelepipedic computational cells are cut near complex surfaces to follow the boundaries, after computing the intersections of the STL with the background Cartesian mesh. For the considered device geometry, the grid resulting from setting the cell size to be slightly larger than the carrier particle maximum diameter is shown in Figure 3.2.

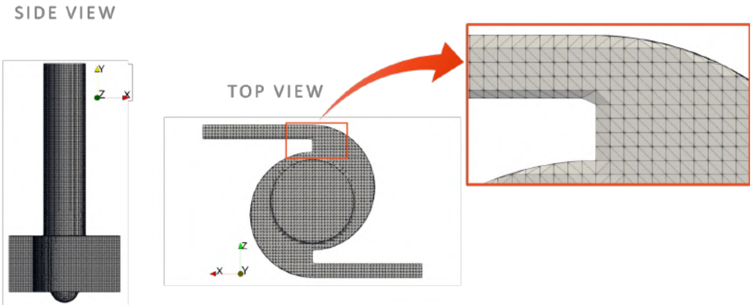

Figure 3.2: Mesh obtained with Cartesian grid cut-cell technique. The insert shows the application of the cartesian cut-cell technique to adapt the grid to the geometry, for the numerical solution of the gas flow. The grid size is 250 μm, giving rise to a total of $\sim$135k cells.

The CFD–DEM method used in this study is a 4-way coupling unresolved approach, so particular attention needs to be paid to the grid size, as a trade-off has to be found between the requirement of a sufficiently fine grid for accuracy of the simulated gas flow and the separation of scale with respect to the particle size needed to enable the local-average formulation. Moreover, as in this work also small API particles are simulated, the use of an extremely coarse grid would reduce the accuracy of the calculation of aerodynamic forces on the fine solid phase. Generally, $\Delta x/d_{p,max} > 2$ is suggested (Fullmer and Musser, 2018; Volk et al., 2018), with Δx being the characteristic cell size and $d_{p,max}$ the maximum particle diameter. However, the local-to-mesh variable interpolation method in MFIX (denoted by "GARG_2012" in the MFIX-DEM documentation(NETL Multiphase Flow Science Team, 2020)), an explicit interpolation stencil based on the distance between the CFD grid and the particle centroid, allows looser restrictions than centered volume fraction methods, as it prevents abrupt changes in the porosity (i.e. ε), avoids the possibility of ε being close to zero and it reduces the porosity standard deviation (Volk and Ghia, 2018). For this reason, a smaller $\Delta x/d_{p,max}$ ratio has been considered and a characteristic dimension of 250 μm for the cubical cells has been selected for use independently of the particle sizes (150 and 200 μm diameter for the carrier) considered, leading to a mesh composed by about 135k cells, as shown in Figure 3.2. The results obtained with the proposed grid will be later assessed against data available in the literature.

3.3.1.3 Grid independence study

As carrier particles as big as 200 μm were used in the study, there is a limitation on the minimum size of the Eulerian cells. A characteristic cell dimension (Δx) of 250 μm has been selected, leading to a maximum cell-to-particle size ratio of 1.25. A mesh sensitivity analysis has been conducted to estimate the accuracy of the solution. 50 ms of fluid-only transient simulations (60 L/min of inlet gas flowrate) were carried out on three grids: S_1, S_2 and S_3. S_1, the finest, is the grid selected for the final simulations (Δx_1 = 250 μm); S_2 and S_3 are coarser, with characteristic cell dimensions of 333 and 500 μm, respectively. The characteristic cell dimensions have been selected considering a refining ratio $r_k = \Delta x_{i+1}/\Delta x_i = \sqrt{2}$. The parameters of the selected grids are reported in Table 3.1.

	S_1 (fine)	S_2 (medium)	S_3 (coarse)
Domain division	72 x 160 x 56	56 x 120 x 42	36 x 80x28
No. of cells	135,153	61,020	18,128
Δx, μm	250	333	500

Table 3.1: Domain division, dimensions and number of cells for the three different grids (S_1, S_2, S_3).

The verification procedure proposed by Stern et al. (2006) has been used to estimate the numerical errors related to grid spacing on the finest grid, S_1. The procedure verifies the convergence of a selected parameter starting from at least three solution on different grids. The global parameter selected for the procedure is the resistance coefficient of the inhaler, R, defined as:

$$R = \frac{\sqrt{\Delta P}}{Q} \tag{3.1}$$

where $\Delta P = P_{in} - P_{out}$ is the pressure drop across the inhaler and Q is the gas flowrate. The internal resistance of the inhaler depends on the design of the device (obstructions, narrow passages, obstacles to the flow) and characterizes its method of operating: devices with high internal resistance allow a more effective deaggregation of the powder, but require a greater suction flow rate from the patient; low resistance devices, on the other hand, guarantee good performance even if the patient does not aspirate properly, but provide less energy for the lifting and deaggregation of the powder (Hoppentocht et al., 2014). The coefficient R is evaluated after 50 ms of simulation, when the flow is fully developed.

Figure 3.3 shows the resistance coefficients obtained with the three selected grids. For grid S_1, the resistance coefficient is about 0.023 kPa$^{0.5}$ L^{-1}min; this value is compatible to resistance parameters experimentally evaluated for low-medium resistance commercially available DPIs, as reported by Berkenfeld et al. (2015). The plot suggests that R monotonically increases with the number of cells and therefore with the resolution of the grid.

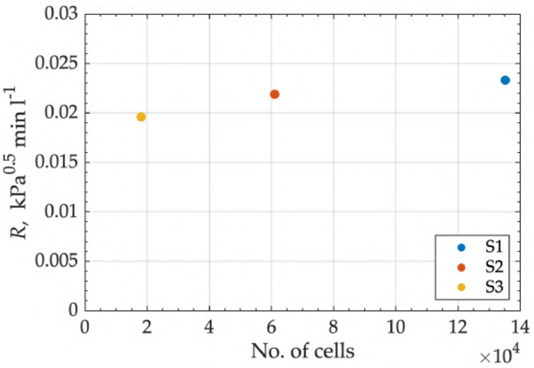

Figure 3.3: Resistance coefficient (R) obtained with grids S_1, S_2, S_3.

The results, reported in Table 3.2, show that the most grid sensitive parameter is the pressure drop, which ranges from 1.4 kPa (for the coarsest grid) to 2.0 kPa (for the finest), while the flowrate (measured at the outlet, i.e., where the boundary condition is set on pressure) does not change substantially with the grid size, respecting the continuity equation.

	S_1 (fine)	S_2 (medium)	S_3 (coarse)
ΔP [kPa]	2.0	1.7	1.4
Q [L/min]	60	60	60
R [kPa$^{0.5}$L^{-1}min]	0.023	0.022	0.020

Table 3.2: Solution obtained with the three different grids.

Evaluating R_g, i.e. the ratio between the solution changes for medium-fine, $\varepsilon_{21} = S_2 - S_1$, and coarse-medium, $\varepsilon_{32} = S_3 - S_2$, a value of $R_g = 0.38$ is found. Given that $R_g < 1$, the solution converges monotonically to the solution that would be obtained with infinitesimal cells (Stern et al., 2006). The order of accuracy, p_{RE}, the Richardson error estimate, δ^*_{RE} and the correction factor, C_k, can then computed using the Richardson extrapolation (RE) method, considering a theoretical order of accuracy $p_{k,est} = 1$:

$$p_{RE} = \frac{\ln(\varepsilon_{32}/\varepsilon_{21})}{\ln r_k} \tag{3.2}$$

$$\delta_{RE} = \frac{\varepsilon_{21}}{r^p - 1} \tag{3.3}$$

$$C_k = \frac{r_k^{p_{RE}} - 1}{r_k^{p_{k,est}} - 1} \tag{3.4}$$

The grid uncertainty can be finally be computed as:

$$U_g = |C_k \delta^*_{RE}| + |(1 - C_k)\delta^*_{RE}| \tag{3.5}$$

The results obtained from the procedure are reported in Table 3.3. The calculation gives an overall estimated uncertainty $U_{g,\%S1}$ of 20%. The parameter R is probably underestimated and the true value might be around 0.028 kPa$^{0.5}$ L^{-1} min. The underestimation of R might lead to a reduced particle emission from the inhaler.

R_g	p_{RE}	δ^*_{RE}	Ck	δ^*	U_g
0.63	1.33	-2.4E-03	1.41	$-3.4{\cdot}10^{-3}$	19%

Table 3.3: Results of the validation procedure for the resistance coefficient, R.

Iterative convergence has also been checked; the residuals fall rapidly and reach oscillatory convergence. The estimated uncertainty is about 0.2% with respect to the R value, i.e. negligible compared to the error associated to grid spacing.

The estimated error on the selected parameter is not negligible, as higher than 10%. Since using smaller cells would not allow the use of 200 μm particles, an evaluation on a more accurate grid has been conducted to test the effect of the underestimation of R on the motion of particles. A fluid only simulation and a CFD-DEM simulation with 150 μm carrier particles have been carried out on a finer grid, S_0, whose parameters are reported in Table 3.4. The characteristic dimension of the Eulerian cell size, 182 μm, has been selected considering again a refining ratio $r_k = \Delta x_{i+1}/\Delta x_i = \sqrt{2}$. The fluid only simulations have been carried out for 50 ms, while 500 ms have been simulated with both the fluid and the particles.

	Domain division	No. of cells	$\Delta x, \mu$m
S_0	99 x 220 x 77	345,657	182

Table 3.4: Parameters of grid S_0.

Figure 3.4 shows the pressure field for the simulation with grid S_0, along with the solutions for grids S_1 and S_2. As already expected from the results reported in Table 3.2, higher pressure gradients are recorded if a finer grid is used. The resistance coefficient R for grid S_0 is about 0.027 kPa$^{0.5}$L^{-1}min, compatible to the value expected for infinitesimal cells.

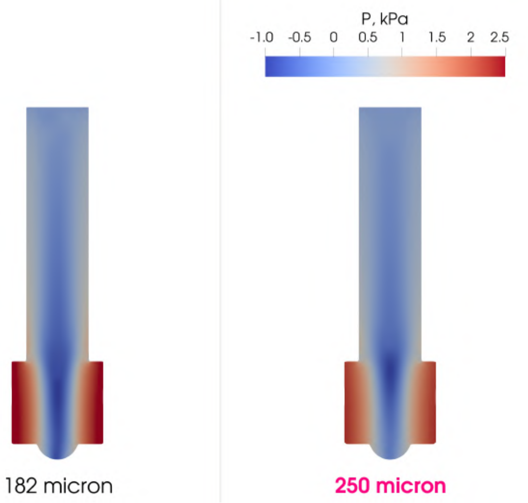

Figure 3.4: Side-view pressure field for grids S_0 (Δx=182 μm), S_1 (Δx=250 μm), S_2 (Δx=333 μm). Gas flowrate is 60 L/min.

The gas velocity magnitude is shown in Figure 3.5 for grids S_0, S_1, S_2. Higher velocities are recorded with finer grids, as also shown in the tangential velocity profiles in the mouthpiece and in the swirl chamber, reported in Figure 3.6.

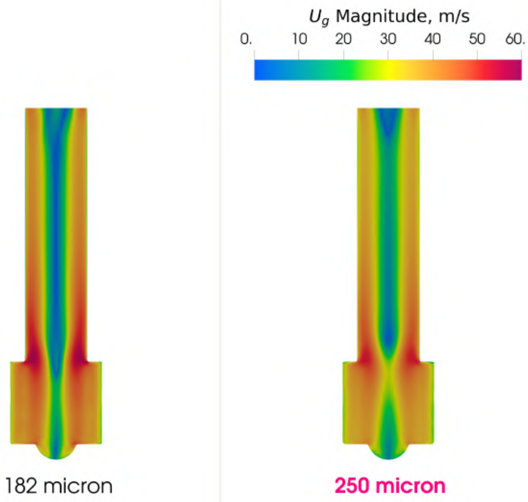

Figure 3.5: Side-view gas velocity magnitude for grids S_0 (Δx=182 μm), S_1 (Δx=250 μm), S_2 (Δx=333 μm). Gas flowrate is 60 L/min.

As mentioned above, the goal is to verify how these differences in the fluid field translate into the motion of the particles in the device. Figure

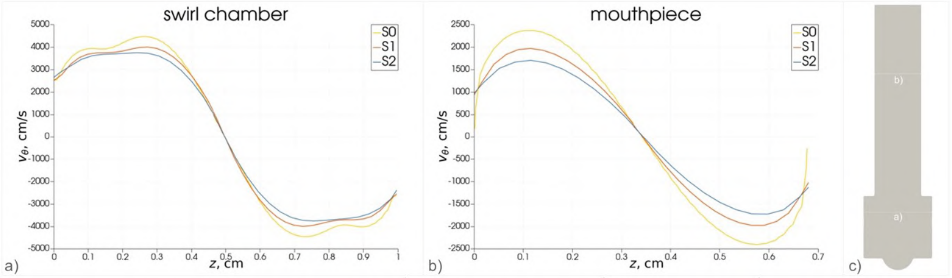

Figure 3.6: Tangential velocity profiles for grids S_0, S_1, S_2 a) in the swirl chamber and b) in the mouthpiece. c) Locations in the device from where profiles were extracted. Gas flowrate is 60 l/min.

3.7 shows the number of particles in the inhaler as a function of time for grids S_0, S_1, S_2. The three curves show the same shape. While the S_2 curve differs significantly, curves S_1 and S_0 are rather similar both in the shape and in the values: the difference in the ejected particles after 500 ms is about 5%.

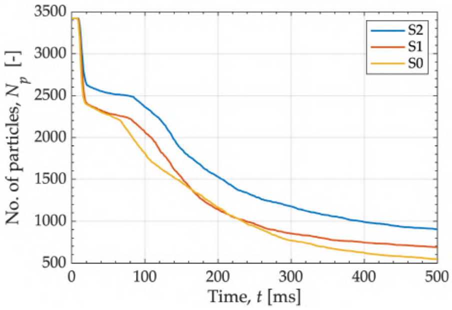

Figure 3.7: Number of carrier particles (150 μm diameter) in the device as a function of time for 500 ms of simulation. At the beginning of the simulation there are 3422 particles in the system. Gas flowrate is 60 L/min.

Figure 3.8 shows snapshots of the positions of carrier particles for the three grids at different time instants. In all cases we see: particles almost uniformly distributed along the vertical coordinate at 10 ms, accumulation both in the top and also in the bottom of the swirl chamber at 50 ms, predominant accumulation in the top of the swirl chamber from 100 ms onwards.

The dynamics of the swirling motion in the device is similar as well; Figure 3.9 shows the x-coordinate of a selected particle (ID1934) as a function of time for the three grids. The x axis is parallel to the direction of the fluid entering from the tangential inlets. This particle rotates in the swirl chamber until the end of the simulation (500 ms) in all three cases. From

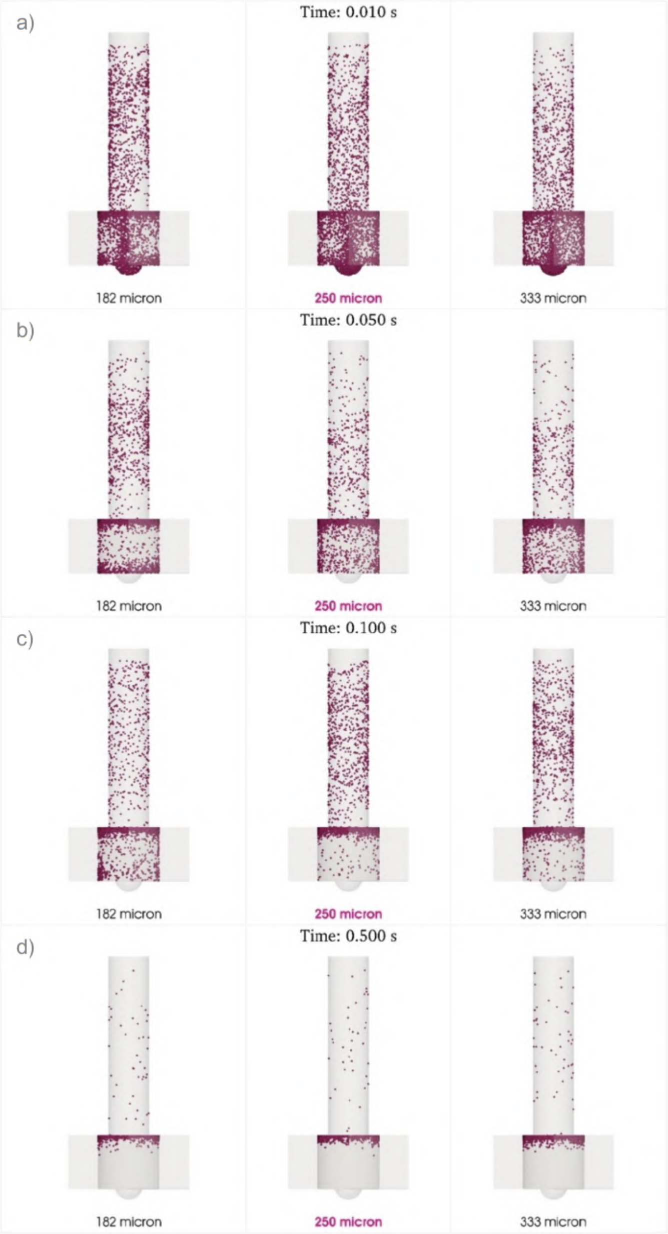

Figure 3.8: Snapshots of particle positions at 10, 50, 100, 500 ms for three grid sizes. a) 10 ms, b) 50 ms, c) 100 ms, d) 500 ms.

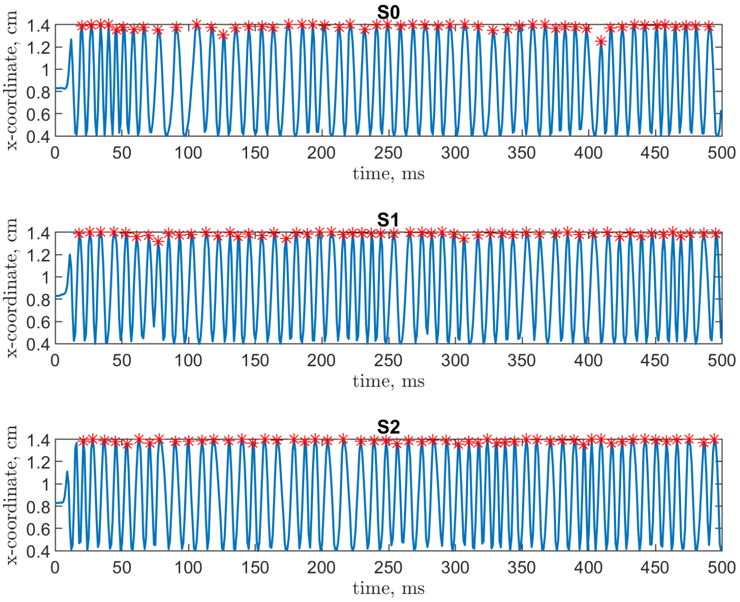

Figure 3.9: x-coordinate of particle ID1934 for grids S_0, S_1, S_2.

the plot, the average revolution period can be estimated by considering the average distance between the local maxima; the results are reported in Table 3.5. The standard error on both the number of rotations and the swirl chamber and the average rotation period is lower than 3%.

As the S_1 solution for particle flow is reasonably similar to the finer one (S_0), the grid S_1 can be judged accurate enough for the study.

	S_0	S_1	S_2	ε (%)
No. of rotations in swirl chamber, N	53	56	55	2.8
Average rotation period, T (ms)	9.0	8.7	8.8	2.2

Table 3.5: Number of rotations in the swirl chamber and average rotation period for particle ID1934.

3.3.2 Cyclohaler

A commercially available capsule-based inhaler has also be considered for some tests. The reference device is the Cyclohaler®, in which a hard gelatin capsule is utilized as a drug reservoir.

CFD simulations with LES turbulence have been carried out with the software OpenFOAM to characterize the air flow with a realistic inhalation profile. Lagrangian tracking tests have been performed as well.

The motion of particles inside the capsule has been characterized with pure DEM simulation on both carrier and API particles.

3.3.2.1 Inhaler geometry and mesh

The geometry of the inhaler is shown in Figure 3.10. It consists of a swirl chamber, a capsule reservoir, two tangential inlet sections, a mouthpiece, and a grid between the swirl chamber and the mouthpiece. The grid is used primarily to hold the capsule inside the swirl chamber. However, it has been found to be useful for two other purposes: it "straightens" the flow by consistently reducing the swirling flow in the exit pipe (mouthpiece) and induces drug detachment due to the carrier particles hitting on it (Cui et al., 2014). The inner diameter of the mouthpiece is 10.5 mm and that of the swirl chamber is 19 mm. The origin for the coordinate along the inhaler is the upper edge of the swirl chamber. The distance to the mouth piece exit is 48.1 mm and to the bottom of the reservoir is 14.3 mm (negative coordinate). The depth of the reservoir is 7.8 mm.

The mesh has been kindly provided by the "Multi-phase flow working group" - University of Magdeburg (Germany), headed by Prof. Martin Sommerfeld. It consists of about 1.4M cells and it is shown in Figure 3.11. The mesh is refined near the walls, with a cell size of approximately 16 μm. Grid independency has been checked and verified by the research group from the University of Magdeburg.

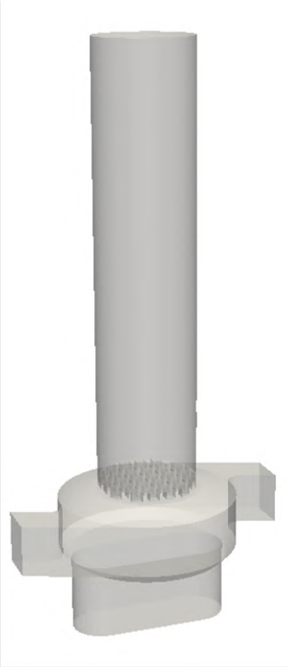

Figure 3.10: Geometry of the Cyclohaler.

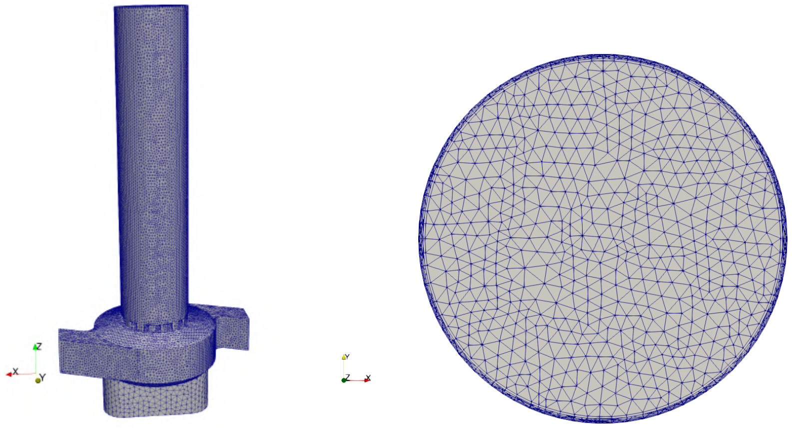

(a) (b)

Figure 3.11: Mesh used in CFD simulations: a) full inhaler, c) wall resolution near the outlet section.

3.3.2.2 Capsule geometry

A size 3 capsule has been considered (Coates et al., 2005b). The dimensions of the capsule are reported in Figure 3.12. On each side, the capsule is pierced with four holes having a diameter of 0.6 mm. In the real device, the capsule is initially placed in the capsule holder of the Cyclohaler and then pierced with apposite needles in response to pressing two buttons on the sides. The patient then brings the inhaler into a horizontal position and starts the inhalation. The air flow pushes the capsule upwards in the swirl chamber and promotes a fast-rotating motion of the capsule, which then causes the powder release from the lateral holes. The geometry of the capsule has been used as domain in the simulation and has been imported into the MFIX run as an STL file.

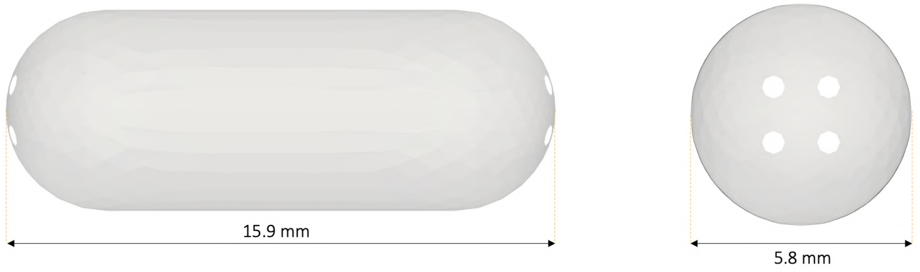

Figure 3.12: Capsule geometry.

Chapter 4

Design and modelling of a DPI

In this Chapter, the simulation work on the dispersion of carrier particles in the swirl-based DPI (section 3.3.1) will be presented.

4.1 Simulation parameters and set-up

The fluid considered in the simulations is air at 25°C. A volume flow-rate boundary condition is applied to the two tangential inlets, from which a total of 40–100 L/min of air instantly enter the system, in line with the typical flowrates generated by asthmatic patients (Buttini et al., 2016b). A constant pressure condition is used for the outlet section. The initial velocity of the fluid and its gauge pressure are zero. During breathing from DPI devices, the inhaler is typically utilized horizontally, so the gravity force in the simulations is set in z-direction, acting perpendicularly to the axis of the device. However, the overall effect of gravity is largely negligible. The properties of the fluid phase and the CFD model are reported in Table 4.1. The timestep for the simulation of the fluid phase (CFD part of the code) is adjusted during the simulation according to convergence criteria, starting from 10^{-7} s and never exceeding 10^{-5} s. The timestep for the simulation of the solid phase (DEM part of the code) is about 10^{-7} s.

In this first set of the simulations presented, only carrier particles are considered. The solid phase consists of 10 mg of free flowing, spherical particles with 150 and 200 μm diameter. The selected sizes for carrier particles are compatible to real applications directly envisaged in DPI (de Boer et al., 2012; Benassi et al., 2019).

To mimic the deposition of the carrier particles during dosing, the initial powder configuration in the hemispherical dose cup at the base of the DPI is generated by considering gravity settling of the prescribed number of particles arranged in a cubical volume above the cup with a slightly randomized

Variable	**Value**
Fluid	Air, ambient conditions
No. of grid cells	72 x 160 x 56
Inlet flowrate	40 - 100 L/min
Outlet pressure	0 Pa
Simulated time	500 ms

Table 4.1: Properties of the gas phase and the CFD model.

velocity component.

The properties of the solid particles and the DEM model are reported in Table 4.2. The physical and mechanical properties are selected to reproduce the behaviour of brittle, irregularly shaped pharmaceutical particles.

Variable	**Value**
Diameter [μm]	150; 200
Particle density [kg/m^3]	1500
Young modulus [GPa]	0.2
Poisson Ratio [-]	0.45
Restitution Coefficient [-]	0.2
Friction Coefficient [-]	0.5
Rolling Friction Coefficient [-]	0.3
Solid mass [mg]	10
Number of particles	3422; 1579

Table 4.2: Physical and DEM model properties used in simulations of carrier particles.

4.2 Single phase air flow field

As shown later, the structure of the flow turns out to be inherently anisotropic, swirling and possibly turbulent. A highly accurate solution of the flow would suggest stringent requirements on the physical model (such as Reynolds-stress turbulence models or Large Eddy Simulations) and correspondingly on the grid size in the proximity of the boundaries (Sommerfeld et al., 2019). However, this may be feasible for single phase or one-way coupled flows, in which the fine and dilute solid phase does not interfere with the gas flow. In the present CFD–DEM simulations with coarse carrier particles, the motion of the particles is expected to be governed mainly by collisions and weakly affected by the turbulent nature of the air flow (Cui et al., 2014). This is corroborated by an estimate of the generalized Stokes number (Wessel and Righi, 1988; Israel and Rosner, 1982) for the 200 μm particle system considered in this work, which yields about 750.

Different may be the case of the API solid phase, whose Stokes' number is around 5: particles are in an intermediate regime for which they do not follow fluid streamlines and the motion is not determined by their inertia either. However, the presence of the massive coarse particles is likely to change the turbulence with respect to classical approaches valid for single phase flow. In addition, using the average unresolved approach with Eulerian cells 25 times bigger than the API diameter, the model would not be able to capture turbulent vortexes and preferential paths anyway. Therefore, the description of the flow will be assessed based on the capability to represent the main features of the flow fields.

The velocity field, in terms of magnitude, resulting from a simulation without particles and constant inlet air flowrate of 60 L/min after 50 ms is reported in Figure 4.1.

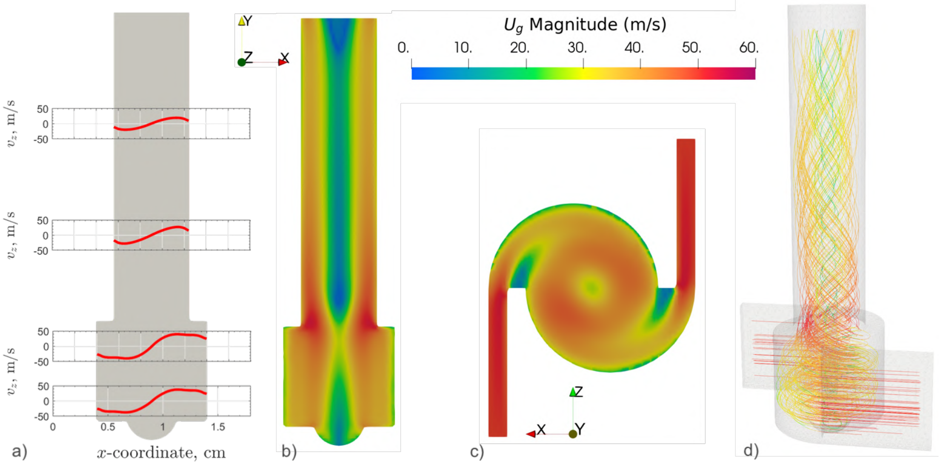

Figure 4.1: Velocity field of the fluid flow inside the device at 60 l/s inlet flowrate: a) horizontal component of velocity (v_z) profiles at different vertical coordinates, b) side view and c) top view of the gas velocity magnitude, d) streamlines.

The streamlines in the rightmost 3D representation show the horizontal inlet flow that leads to the formation of a rotational flow in the swirl chamber. The peculiar shifted half circular walls of the swirl chamber resemble those of a tangential-inlet cyclones and, due to symmetry, produce an internal circular flow with a vertical component directed upwards, as shown by the helical shape of the streamlines in the exit duct (Figure 4.1d). The cross-section in the swirl chamber shows this formation of a very symmetric circular flow centred around the axis of the device. The half-way cut plane showing in the side view reveals that the central low-velocity region is also co-axial with the flow in the exit duct. The low velocity central region penetrates the dose region down to the lower wall and its axis passes through the centre of the spherical cup. The flow appears completely developed in both the swirl chamber and the exit duct. In the transition zone, corresponding to the restriction of the vertical cross sectional area, the highest velocities are observed, reaching values above 40 m/s for an inlet flow-rate of 60 L/min. In the swirl chamber tangential velocity is found to reach higher values than in the exit duct, as shown in the x-coordinate profile (Figure 4.1a).

Development of the steady-state flow field is reached in a few millisecond time, also due to the inlet boundary condition instantaneously set to 60 L/min. The pressure drop across the inhaler, computed as the difference between the surface-averaged pressure field at inlet minus the outlet (prescribed) pressure, is about 2 kPa after 10 ms of simulation. Even in the absence of particles, the flow is never exactly fully developed, as fluctuations of a few percent points around the steady-state value of the pressure drop persist throughout the entire simulation.

As discussed earlier, the relatively coarse grid may affect the quantitative description of the gas flow in the vicinity of sharp edges. The limitations imposed by the presence of relatively coarse particles lead to the impossibility to consider the boundary layer with a very fine grid, unless by using a much more extreme smoothing of the flow around the particles rotating along the walls (see e.g. Ponzini et al. (2021)), a procedure that overcomes the practical problem but not that of the accuracy. Judging the quality of the generated flow together with the possibility offered by DEM to realistically consider particle contacts and adhesive behaviour in a fully coupled flow, the flow details obtained with the current grid will be considered acceptable. In a later subsection, the velocity profiles will be compared with higher-resolution simulations of the gas flow.

4.3 Motion of carrier particles

Two-phase flow involving carrier particles has been simulated for 500 ms to examine the trajectories of the particles inside the swirl-based device. An amount of solid corresponding to 10 mg of 150 μm carrier particles has been considered, for a total of 3422 particles. The physical and mechanical properties of the solid phase are summarized in Table 4.2. The evolution of the particle positions and velocity (in magnitude) for an inlet air flow-rate $Q = 60$ L/min is shown in Figure 4.2.

The particles are initially deposited in the dose cup and at rest (Figure 4.2a). The swirling gas acts almost immediately, even before the full development of the gas flow, on the powder. This is lifted upwards, as shown in Figure 4.2b, forming a dense central fountain of particles surrounded by a looser region, in which particles are pushed radially outwards by the inertial (i.e. centrifugal in this case) force. The particles in the central region reach

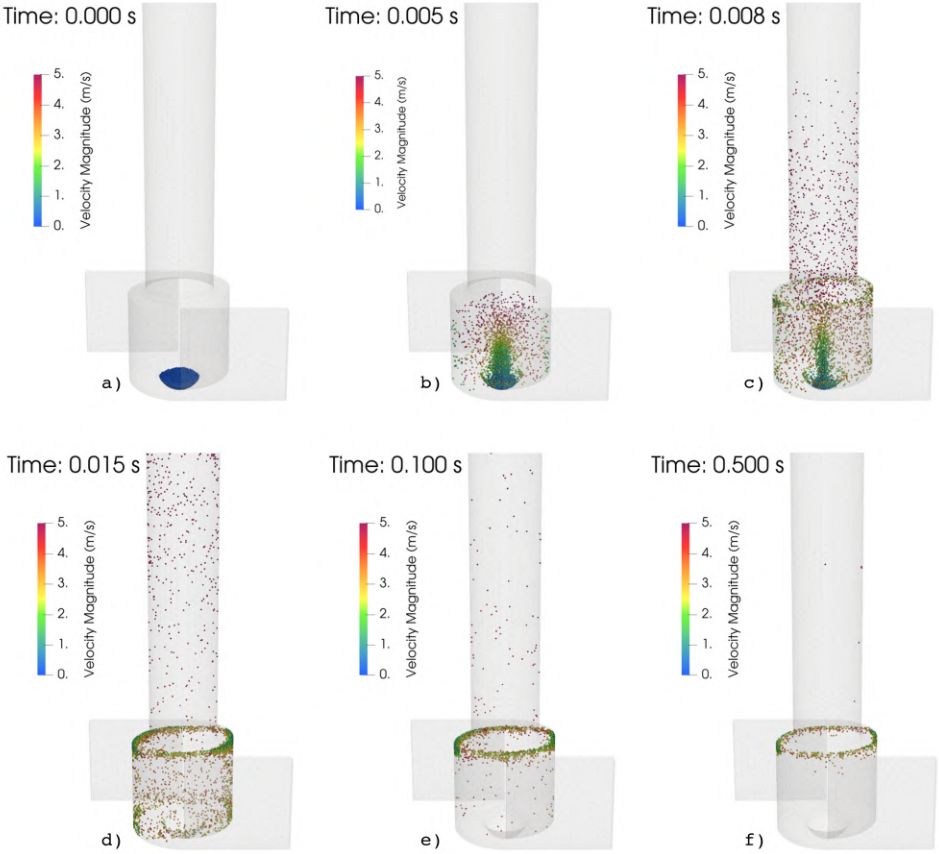

Figure 4.2: Particle positions represented by spheres coloured based on the velocity magnitude during the simulation: a) 0 ms, b) 5 ms, c) 8 ms, d) 15 ms, e) 100 ms, f) 500 ms. 60 L/min gas flowrate.

directly the exit duct (see Figure 4.2c), initially rising at a vertical velocity $v_y = 1$–2 m/s, while the other ones undergo significant horizontal acceleration reaching velocity magnitudes $|v| > 4$ m/s. When the fluid reaches the steady state, after about 14 ms of simulation, nearly all the particles have been lifted from the cup and most of them rotate in the swirl chamber (Figure 4.2d) either close to the lateral walls or below the swirl chamber ”ceiling”, just close to the beginning of the exit duct. The particle rolling over the lateral and top walls continues for relatively long. During this process, some of the particles get picked up by the air flow, enter the cylindrical duct and are then expelled through the exit surface, as the gas velocity in that region has the highest value. As a result, the solid concentration in the swirl chamber decreases gradually until the end of the simulation, as shown in Figure 4.2e and Figure 4.2f. The tendency of coarse particles to be retained in the inhaler chamber has been observed quite extensively in different swirling systems (Marshall, 2006; Han et al., 2002; Kou et al., 2016).

The images of Figure 4.2 (bottom series) show that the few carrier particles reaching the mouthpiece in the later stage are located along the walls, as the strong vortical flow initiated by the tangential air streams prevents them from reaching the core flow region. Their relatively large mass could play a role as well, since larger particles tend to move outwards as a result of the large vortical flow in the mouthpiece (shown by the gas velocity magnitude and the streamlines reported in Figure 4.1).

In quantitative terms, the exit profile of the particles can be examined as the percent of solid leaving the device in time (Figure 4.3). The first particle reaches the exit after about 9 ms. Since then, three different emission stages can be identified. A steep, linear growth is observed until 20 ms, reaching an emitted mass of about 35% of the total. Another linear, weaker trend characterizes the exit profile until 110 ms, leading to 66% of expelled solids. After that, the number of particles leaving the system follows a gently increasing trend until, at the end of the simulation (500 ms), the percentage of delivered particles reaches about 84%. By comparing the particles emitted with the particle trajectories shown in Figure 4.2, it can be concluded that the first steep stage corresponds to particles which exit essentially without contact with the walls; in the second stage, particles directly reach the exit duct walls and exit while rolling along the circular wall dragged by the gas swirling flow; in the third stage, the particles leaving the system come from the group of the ones rotating below the swirl chamber ceiling, whose gradual erosion yields a lower emission rate.

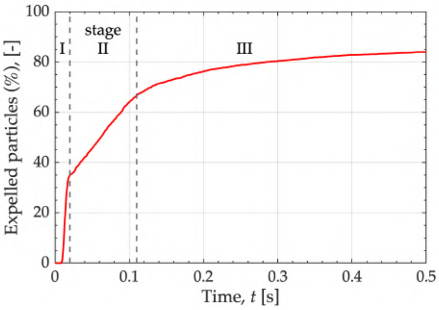

Figure 4.3: Cumulative percentage of particles that leave the device as a function of time. (60 L/min, 150 micron particles). The three stages indicated in the figure are described and commented in the accompanying text.

4.4 Model validation

Before delving into the details of the analysis of the gas and particle flows, it is useful to compare the simulated results with experimental observations and with other similar studies. In Ponzini et al. (2021) the authors investigated the detailed gas flow inside a commercial swirl-based dry powder inhaler through CFD simulations, by using a realistically complex geometric domain, body-conforming mesh, including boundary layer cells and adjusted time-varying boundary conditions to match the experimental conditions, eventually finding a good agreement with them.

Figure 4.4a shows the vertical slice plane passing through the axis of the device colored by the steady-state gas axial velocity. The chart corresponds to the analogous plot reported in Ponzini et al. (2021) and is based on the same color scale. In addition, the three heights denoted by the lines B, C and D, also corresponding to the analogous sections in Ponzini et al. (2021), are highlighted. Figure 4.4b and 4.4c show the profiles of the tangential velocity across the sections B, C and D as presented in Ponzini et al. (2021) and in the present work, respectively. They show a comparable development of the air flow in the swirl chamber and along the exit duct. The formation of the inner forced vortex and the external free vortex in the swirl chamber (sections C and D) is correctly captured, although with smaller values of the maximum tangential velocity. The main reason behind the underestimation in the tangential velocity is the use of a coarse grid, as shown in section 3.3.1.3.

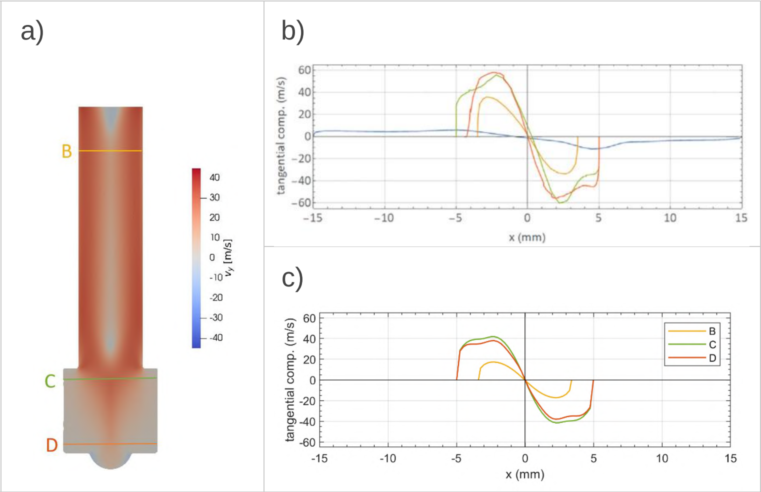

Figure 4.4: a) Map of the axial velocity in the present work and cross-section heights B, C and D corresponding to the profiles shown in parts b and c. b) Tangential velocity profiles reported in Ponzini et al. (2021) at the different cross-sections. c) Corresponding tangential velocity profiles obtained in the present work.

To check the realistic behaviour of the simulated carrier particle flow, snapshots of the carrier particles lifted by the dose cup and expelled is shown in parallel to similar experimental results obtained by laser-illuminated high-speed imaging of a commercial device presented by Pasquali et al. (2015). Figure 4.6 and Figure 4.5 show the carrier particle flow field as observed in the simulations and in the experiments at comparable times.

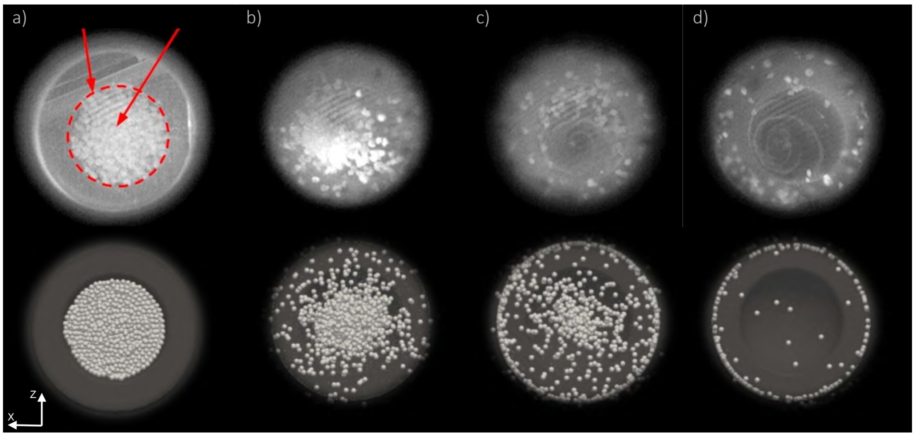

Figure 4.5: Cup emptying, top view. Flow-rate = 60 L/min, rise time 0.3 s for experimental data (top), constant flowrate profile for simulation results (bottom). The red arrows point to the cup (dashed circle) and the powder in the initial position. a) Start; b) 5 ms (after dose-protector opening); c) 10 ms; d) 15 ms. Reprinted from Pasquali et al. (2015) with permission from Elsevier.

The comparison from the top view in Figure 4.5 shows a coherent formation of a central dense region right after flow activation (Figure 4.5b), followed by a leaner phase that forms with time, which eventually leads to the formation of the circumferential flow along the exit duct. The qualitative agreement appears good, although a direct comparison is complicated by dissimilarities in the geometry, particularly near the dose cup, and the inevitable different perspective view from the camera, which is difficult to reproduce exactly.

The side view of the swirl chamber (Figure 4.6) shows the characteristic rotational flow of the carrier particle around the swirl chamber, where most of the API deaggregation is supposed to take place. In both experiments and simulations, the carrier particle develops first by covering the whole lateral walls of the swirl chamber. Then, particles in the lower region are progressively lifted giving rise to some accumulation under the chamber upper wall. Although the experimental view is not perfectly clear, also owing to inevitable reflections, the qualitative similarity of the simulated flow pattern with the observed one is rather evident. The effect of the process time-scale appears also correctly captured.

Particle image velocimetry data were collected at the exit of the device using laser illuminated high-speed imaging (Pasquali et al., 2015) and fluorescence imaging (Merusi et al., 2018). The reported mean exit velocity is around 5 m/s. The exit velocity accounts for both the gas flow pushing the particles out of the device and the particle inertia during their helical motion

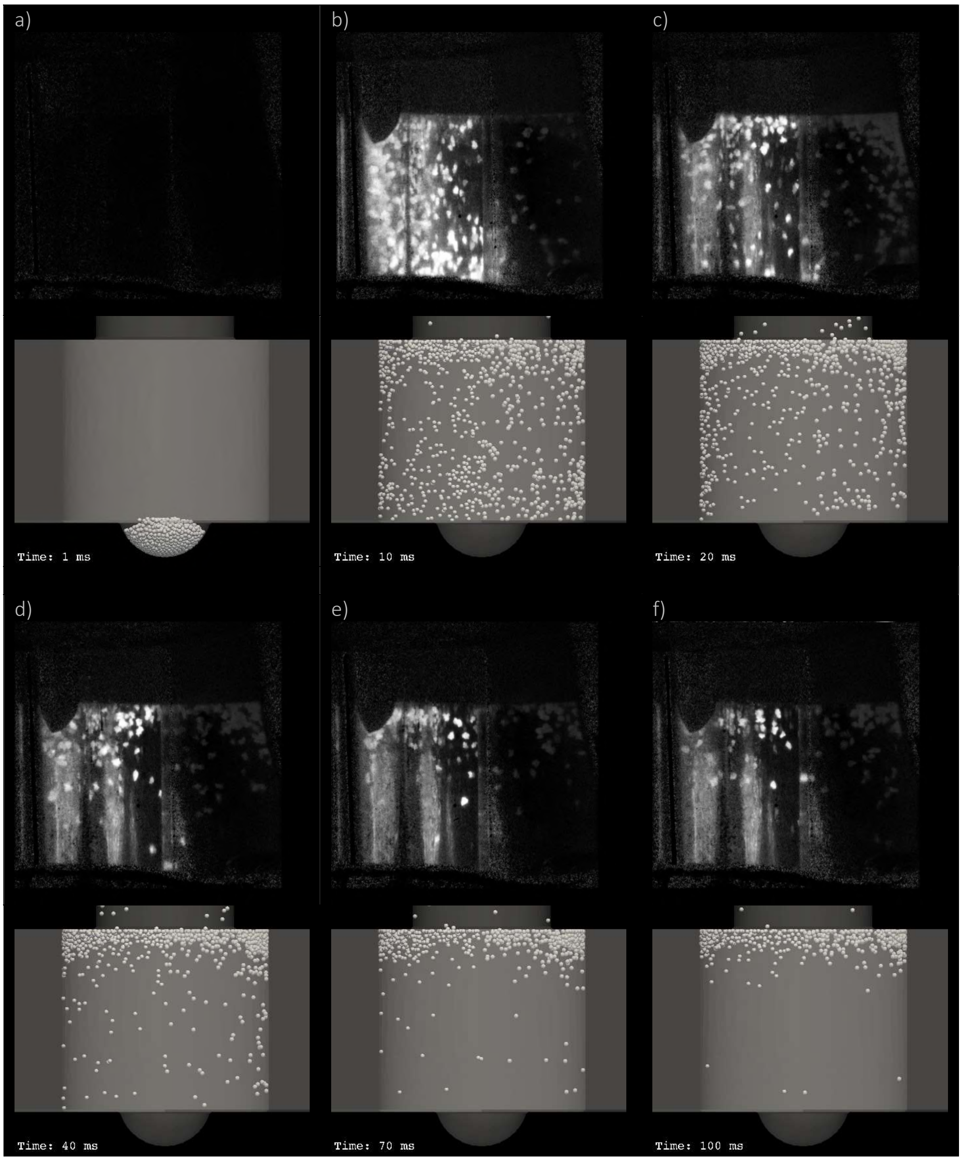

Figure 4.6: Dispersion in the swirl chamber, side view. Flow-rate = 100 L/min, square wave profile. a) 1ms; b) 10 ms; c) 20 ms; d) 40 ms; e) 70 ms; f) 100 ms.

along the walls of the exit duct. Corresponding simulated particle velocities were postprocessed to extract their value averaged over all particles close to the exit. The results are shown as a function of time in Figure 4.7. The particle expulsion occurs at velocities between 5 and 8.5 m/s during the first few milliseconds. After that, the particle velocity represented by the moving average value settles on about 4.7 m/s, in good agreement with the value reported in the experiments.

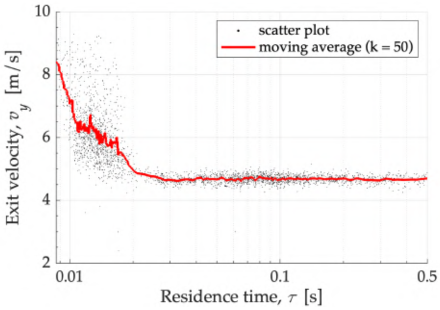

Figure 4.7: Exit velocity of carrier particles in simulations as a function of residence time. Scatter plot and smooth moving average using 50 points (LOWESS method).

4.5 Analysis of carrier particle trajectories

Individual carrier particle positions along the device are examined with the aim to distinguish between the patterns corresponding to the three emission stages (see Figure 4.3). The particles will be referred to as particle R (red), G (green), and B (blue), respectively. The lifting time (i.e. the instant when the particle reaches the swirl chamber), exit time and initial vertical coordinate of the three selected particles are reported in Table 4.3. Their trajectories are depicted in Figure 4.8.

	y_0 [cm]	t_{lift} [ms]	t_{exit} [ms]
G	0.31	1.9	9
R	0.25	7.2	101
B	0.17	12.9	>500

Table 4.3: Three particles selected from the simulation.

Particle G, whose trajectory is reported in green, is the first particle to exit (at 9 ms). Its path is almost straight: the particle goes directly from the cup to the outlet. It is lifted almost immediately, reaching the swirl chamber after 1.9 ms.

Particle B is one of the particles trapped inside the system until the end of the simulation. Its trajectory, depicted in blue in Figure 4.8a, shows that, after reaching the swirl chamber at a time $t = 12.9$ ms, it spends there the rest of the simulation time, rotating near the top walls. Its clockwise rotation is clearly visible in Figure 4.8b.

Particle R is lifted after 7.2 ms (Figure 4.8a) and then follows a helical motion with a small vertical component of velocity compared to particle B. After a few rotations in the swirl chamber, it gets dragged by the air flow in the exit duct and reaches the exit after 101 ms.

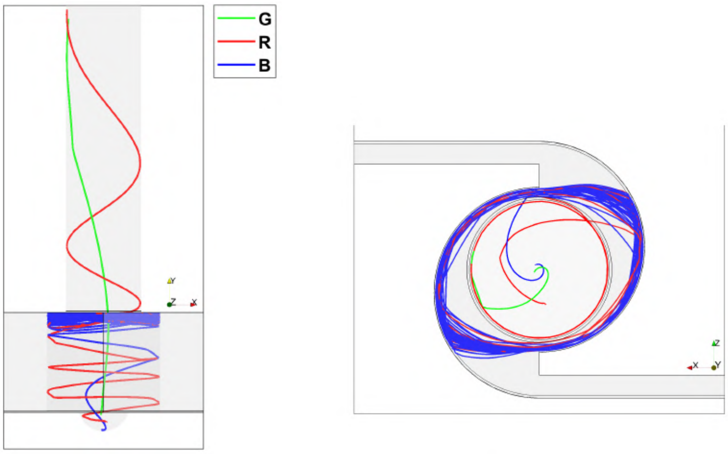

(a) Side view **(b)** Top view

Figure 4.8: Trajectories of particles G, R, B. a) Side view and b) top view.

Figure 4.9 shows the x-coordinate of the three selected particles as a function of time. From the highest and most prominent peaks in the plots (indicated with red asterisks) the number of laps in the swirl chamber can be estimated.

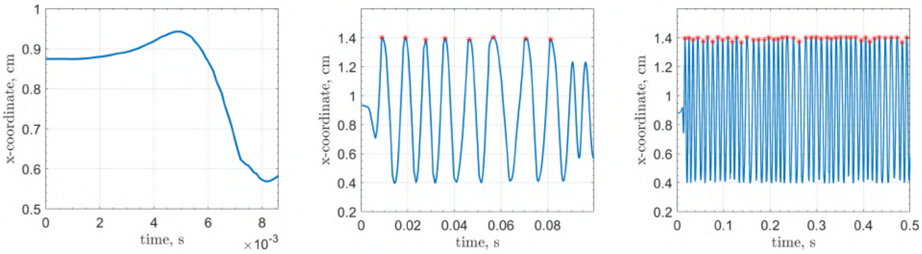

(a) G **(b)** R **(c)** B

Figure 4.9: x-coordinate as a function of time for the three selected particles: a) G, b) R, c) B.

Particle G exits without completing one full loop in the swirl chamber. Particle R completes 8 loops in the swirl chamber and 2 loops in the mouthpiece, while particle B completes 45 loops in the swirl chamber. Interestingly, the average period of revolution in the swirl chamber is about 10.5 ms for both particles R and B.

Since the three examined trajectories correspond to particles initially located differently in the cup, it may be hypothesised that a relationship exists between the initial position in the dose cup and the fate of each particle. Figure 4.10b shows the relationship between the residence time, i.e., the instant at which each particle exits the inhaler, and d_0, which is the

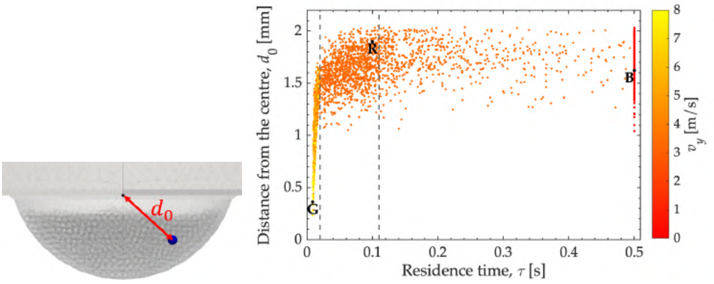

(a) Definition of d_0. **(b)** Residence time

Figure 4.10: Relationship between residence time and d_0. Particles are colored according to the final value of vertical component of velocity. The points representing particles R, G and B are marked. a) Definition of d_0, b) residence time plot.

initial distance of the center of the particle from the center of the cup (see Figure 4.10a). It can be noted that all the particles with $d_0 < 1$ mm (such as particle G) leave the device during the first peak of emission. Most of these particles are on top of the solid bulk. It can also be noted that the final value of vertical velocity, according to which the points of the plot are colored in Figure 4.10b, decreases with increasing d_0 and residence time. The general trend is that for particles with a distance $d_0 < 1$ mm the residence time is very short, above that distance there is no special relation. This may have some influence on the design of optimal cup shapes.

4.6 Carrier particle velocity field

The cartesian components of the velocity have been reprocessed in order to examine the radial (v_r), tangential (v_θ) and vertical (v_y) velocity components. v_r is directed in the line between the center of the particle and the central axis of the mouthpiece. v_θ is perpendicular to v_r, and it is defined positive in the clockwise direction.

Figure 4.11a reports the three components of velocity averaged over all the particles as a function of time.

The average vertical velocity v_y increases rapidly in the first phase, reaching almost 2 m/s. This maximum corresponds to the first stage of the powder emission profile shown in Figure 4.3. After 10 ms the tangential component v_θ becomes prominent and v_y decreases significantly. Therefore, at the end of the first emission stage (see Figure 4.3), the particle motion becomes prevalently rotational. The radial velocity v_r, after an initial decrease to a negative value, rises up to 0.4 m/s when particles leave the cup and get pushed outwards. After that, the radial component is essentially zero as particles tend to rotate around the axis of the device. After about 50 ms, the

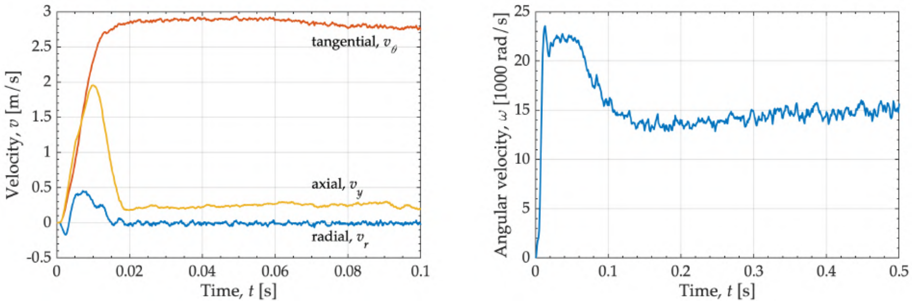

(a) **(b)**

Figure 4.11: Average value over all carrier particles of the radial (v_r), tangential (v_θ) and vertical velocity (v_y) (a) and angular velocity (b) as a function of time. Air flowrate: 60 L/min, 150 micron particles.

three velocity components fluctuate around the following values: $v_r = -0.02$ m/s, $v_\theta = 2.8$ m/s, $v_y = 0.08$ m/s.

Due to the many particle-wall impacts and the swirling nature of the fluid flow, carrier particles in DPIs experience a substantial increase of their angular velocity. The rotation of a carrier-API agglomerate may have a strong effect on fines' detachment, especially for low impact velocities, as shown by Ariane et al. (2018). Figure 4.11b shows the average magnitude of the angular velocity experienced by carrier particles in the present simulation as a function of time. Values as high as 25,000 rad/s are recorded at the beginning of the simulation. As the simulation proceeds, the average value stabilizes around 15,000 rad/s.

4.7 Effect of different parameters on powder dispersion

4.7.1 Inlet flowrate

Figure 4.12 shows the exit profile of particles, reported in terms of cumulative percentage of particles expelled from the device, for simulations with three different values of the inlet flowrate: 40 L/min, 60 L/min, 100 L/min.

After a common initial phase, it can be observed that as the inlet air flow increases, the curves are steeper in the intermediate region (from 0.1 to 0.3 seconds). On the other hand, after 0.5 s it is observed that the percentage of inhaled solid is very similar, with a variation between the curves that does not exceed 3%: after 500 ms, 81% of particles are emitted with 40 L/min, 84% with 60 L/min and 86% with 100 L/min.

The invariance of the device's emptying dynamics with the inlet flow of fluid is a positive feature, sought after as a goal by those involved in the design of DPI, as it ensures that the device can be used successfully even by patients with breathing difficulties (Buttini et al., 2016a).

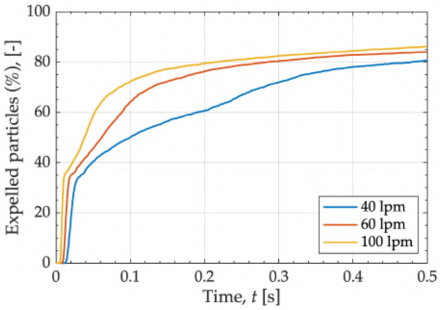

Figure 4.12: Cumulative percentage of particles that leave the device as a function of time for simulations with 3 different inlet flowrate: 40 L/min, 60 L/min, 100 L/min. 150 μm particles.

4.7.2 Particle size and rolling friction

Figure 4.13 shows the percentage of expelled particles as a function of time for simulations with two different particle diameters: 150 and 200 μm and with rolling friction active or deactivated. It can be observed that the use of the rolling friction affects the shape of the curve particularly in stage II, when the particles collide with the walls before leaving the device.

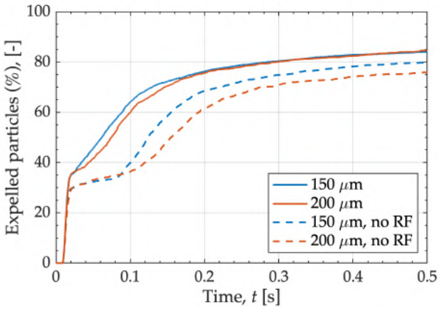

Figure 4.13: Cumulative percentage of particles that leave the device as a function of time for simulations with 2 different diameters with and without rolling friction (RF). 60 L/min gas flowrate.

Interestingly, changing the diameter of the particles does not impact sensitively on the exit profiles, particularly if the rolling friction is activated. This implies that even if the carrier particles are somewhat smaller that 200 μm or if there is size dispersion, the shape of the emission profile remains essentially unchanged. Obviously, this conclusion applies to the present analysis and it does not imply that the overall behaviour of carrier-based device will not be affected in other respects, e.g. the carrier surface exposed to contact with API would be different.

To further examine the role of the rolling friction on the tangential velocity of the carrier particles, Figure 4.14a shows the average such velocity in the swirl chamber with and without rolling friction. As a result of the limited ability of the particles to roll over the curved internal walls of the device, with rolling friction, the tangential component of the particle velocity is consistently lower. Indeed, rolling friction is generally useful to reproduce the behaviour of not spherical, rough, i.e. more realistic, particles.

Figure 4.14b shows the number of particles in the swirl chamber as a function of time for the two simulations. If the rolling friction model is activated, there are less particles in the swirl chamber from about 20 to 100 ms. This difference is compatible with the exit profiles shown in Figure 4.13. The difference in the residence time in the swirl chamber is most probably related to the difference in the tangential velocity: if rolling friction is activated, higher tangential velocities are recorded, so the stronger centrifugal forces make it harder for particles to ”escape” from the accumulation region right beyond the ceiling of the swirl chamber.

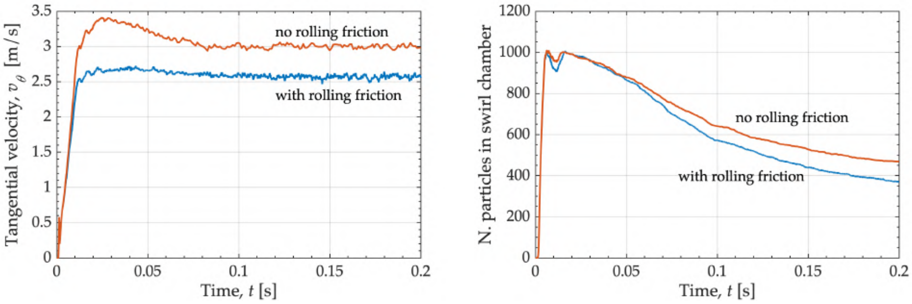

(a) **(b)**

Figure 4.14: Average tangential velocity (a) and number of particles (b) in the swirl chamber for simulations with and without rolling friction. 200 micron particles, 60 L/min inlet gas flowrate.

4.7.3 Restitution coefficient

As pointed out by Ponzini et al. (2021) and Sommerfeld and Schmalfuß (2016), the choice of the mechanical parameters of the particles, such as coefficient of friction and coefficient of restitution, has an influence on the dynamics of the particles' release. In the present work the particle parameters have been chosen with the idea of representing fragile and irregularly shaped particles. for this reason it was decided to consider, for example, a very low restitution coefficient ($e = 0.2$). To verify the effect of the choice of this parameter, a CFD-DEM simulation was conducted considering a higher restitution coefficient, $e = 0.5$. Carrier particles with a diameter of 200 μm and a gas flow rate of 60 L/min were considered.

Figure 4.15a shows the emitted fraction of carrier particles for two analogous simulations, one with $e = 0.2$ and the other with $e = 0.5$. The two curves have the same shape, but a greater amount of powder is inhaled with the lower coefficient of restitution. These results show how the mechanical properties of the carrier can have a significant influence on the emission dynamics of the powder.

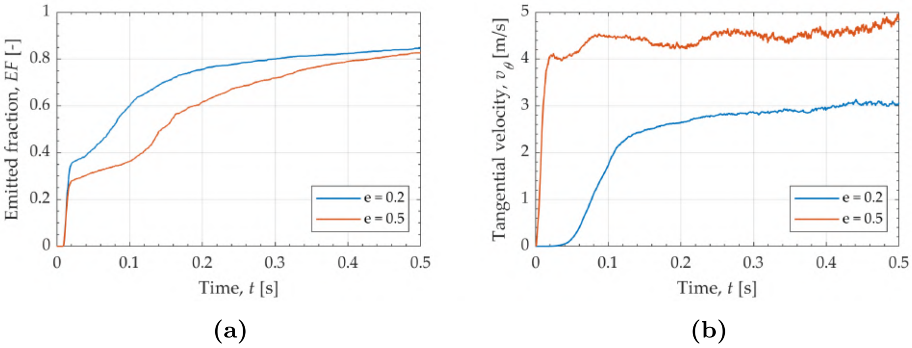

Figure 4.15: a) Cumulative percentage of particles that leave the device as a function of time and b) mean tangential velocity over time for simulations with different coefficient of restitution. 200 μm particles, 60 L/min inlet flowrate.

Similar radial and vertical mean velocity components are recorded in the two simulations, but higher tangential velocities are observed with higher restitution coefficient, as shown in Figure 4.15b. Higher mean angular velocities are observed as well: after 0.5 s, it was 25,000 rad/s with $e = 0.2$ (see Figure 4.11b), it is now around 45,000 rad/s with $e = 0.5$.

4.7.4 CFD–DEM coupling approach

As mentioned in the literature review, some authors used one-way coupled two-phase flow simulation, particularly when dealing with fine and dilute API particles transported by air (Sommerfeld et al., 2019). It would be attractive if a one-way approach yielded reasonable results, as such Lagrangian particle tracking method allows the fluid flow to be solved once and then particle trajectories to be calculated assuming developed fluid flow. Yet, it cannot be neglected that the present system involves large carrier particles and dense flow regions initially in the cup and along the axis of the device.

Using the one-way coupling scheme in MFIX, a comparative study has been carried out for the case of 60 L/min air flow, 200 μm diameter particles without rolling friction. The difference is remarkable from the first few instants of the simulation, as shown in Figure 4.16. The particles get initial lifting in the one-way coupling case; however, they are quickly spread around, without the formation of the central fountain, most of them ending one the side walls of the swirling chamber.

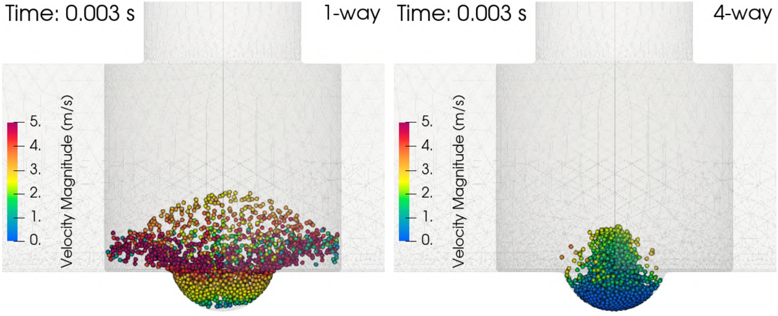

(a) 1 way, 3 ms **(b)** 4 way, 3 ms

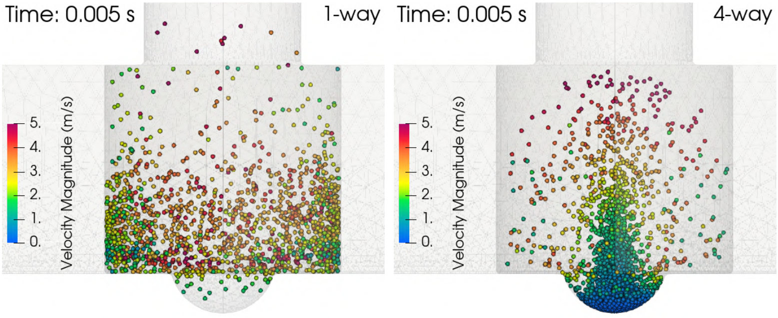

(c) 1 way, 5 ms **(d)** 4 way, 5 ms

Figure 4.16: Particle position during the simulations with 1-way and 4-way coupling.

The coupling approach influences also the development of the flow field in the first milliseconds of the simulations. Figure 4.17 shows the velocity and pressure field using the two approaches. In the area of the particles (the cup and immediately above, compare with Figure 4.16b) there are significant differences in both variables.

In the four-way coupled simulation, the gas drag force along the axis of the system is very low, owing to the low air velocity. So, the lifting action originates from the development of a low pressure region on top of the particles, leading to a suction (buoyant-like) effect in the centre of the swirling flow (see Eq. 2.75). Without the particles exerting their action on the fluid, such pressure difference between the dense particle region and the vortex core does not develop, as shown in Figure 4.17. This is confirmed by a detailed analysis of the evolution of the forces in these initial stage. The vertical components of drag force and pressure gradient force acting on particles appears significantly different, as shown in Figure 4.18.

Eventually, the different fate of the particles in one-way coupled sim-

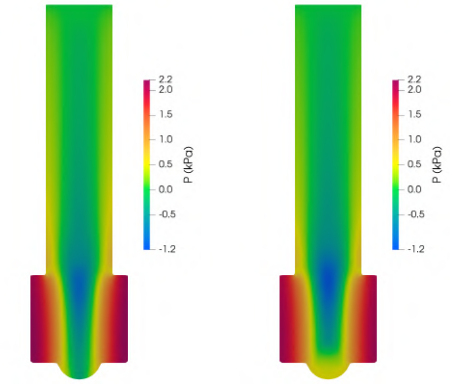

(a) P_g, 1 way **(b)** P_g, 4 way

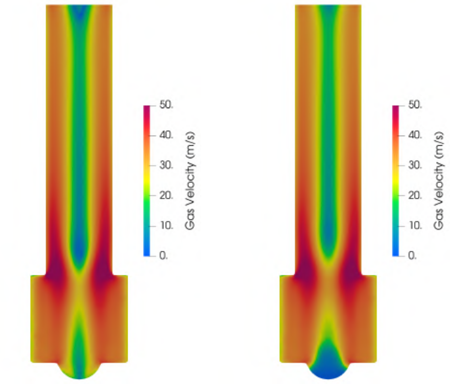

(c) U_g, 1 way **(d)** U_g, 4 way

Figure 4.17: Gas pressure (a,b) and gas velocity magnitude (c,d) at 3 ms with 1-way and 4-way coupling.

ulations strongly affects the predicted amount of emitted carrier particles, ending up with only 5% after 0.5 s, totally unrelated to the corresponding four-way coupled case of 84% of particles emitted. It can be easily concluded that in the present case of carrier-based DPI, full four-way coupled DEM-CFD is necessary.

4.7.5 Variable inhalation profile

In quantitatively describing the characteristics of DPI, it is often referred to the difference in pressure (e.g., 2-4 kPa), the volume of fluid inhaled (e.g., 4 L) or the Peak Inspiratory Flow (e.g., 40 - 100 L/min). In fact, for in vitro testing of DPI, this procedure is often followed: the flow rate is set instantaneously to a target value, dependent on the resistance of the inhaler, and is then kept constant for the time necessary to inhale a volume of up to 4 L. This method, while very useful for a standard characterization of DPI, is not

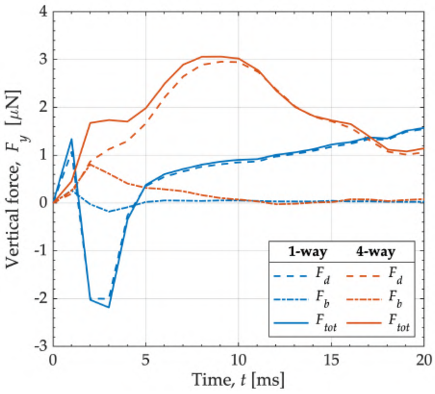

Figure 4.18: Mean y-component of the drag F_d, buoyancy F_b and total force F_{tot} acting on the particles with 1-way and 4-way coupling in the first 20 ms of simulation. 60 L/min, 200 μm particles.

representative of what happens in vivo. Buttini et al. (2016b) reported the inspiratory flow profiles obtained from asthmatic patients inhaling through the NEXThaler®, shown in Figure 4.19.

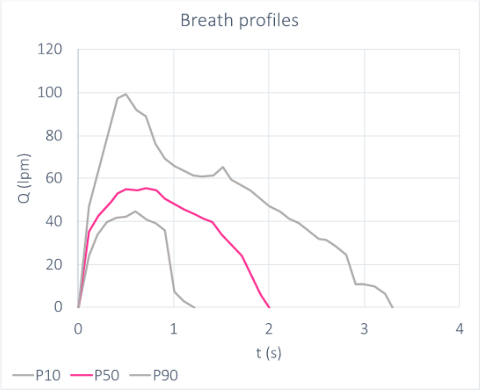

Figure 4.19: Inspiratory profiles obtained from asthmatic patients inhaling twice through the NEXThaler®. Profiles corresponding to the 10th, 50th and 90th percentile of the Peak Inspiratory Flow (PIF). Extracted from the data published in Buttini et al. (2016b).

The reported profiles (P10, P50, P90) correspond to the 10th, 50th and 90th percentile of the Peak Inspiratory Flow (PIF), respectively. The profiles develop over a period of time in the order of seconds; in the case of the P50 profile, the peak is around 60 L/min and is reached after about 0.5 s.

In the simulations presented so far, the flow rate has been considered as instantaneously equal to the peak value and constant throughout the simulation. This step increase in the inlet flowrate differs from that measured in vivo in asthmatic patients (Figure 4.19). It was therefore decided to carry out a simulation considering the realistic inhalation profile (P50) and to compare the results obtained previously with the 60 L/min constant flowrate profile (step). The P50 profile reported in Figure 4.19 was extracted from the figure and discretized in 15 linear intervals. The possibility of using variable boundary conditions for the fluid phase has been implemented in MFIX. The fluid inlet velocity value is read from a table which reports the velocity as a function of time for a certain number of intervals. The instantaneous inlet velocity is calculated by linear interpolation between the two time intervals containing the current time value. For the outlet boundary condition, the atmospheric pressure was considered throughout the whole simulation. A CFD-DEM simulation was carried out with 10 mg of 200 μm particles, by using the same particle properties as in the previous sections.

Figure 4.20 shows the positions of the carrier particles for the two simulations considered at different times: 10 ms, 40 ms, 80 ms, 200 ms.

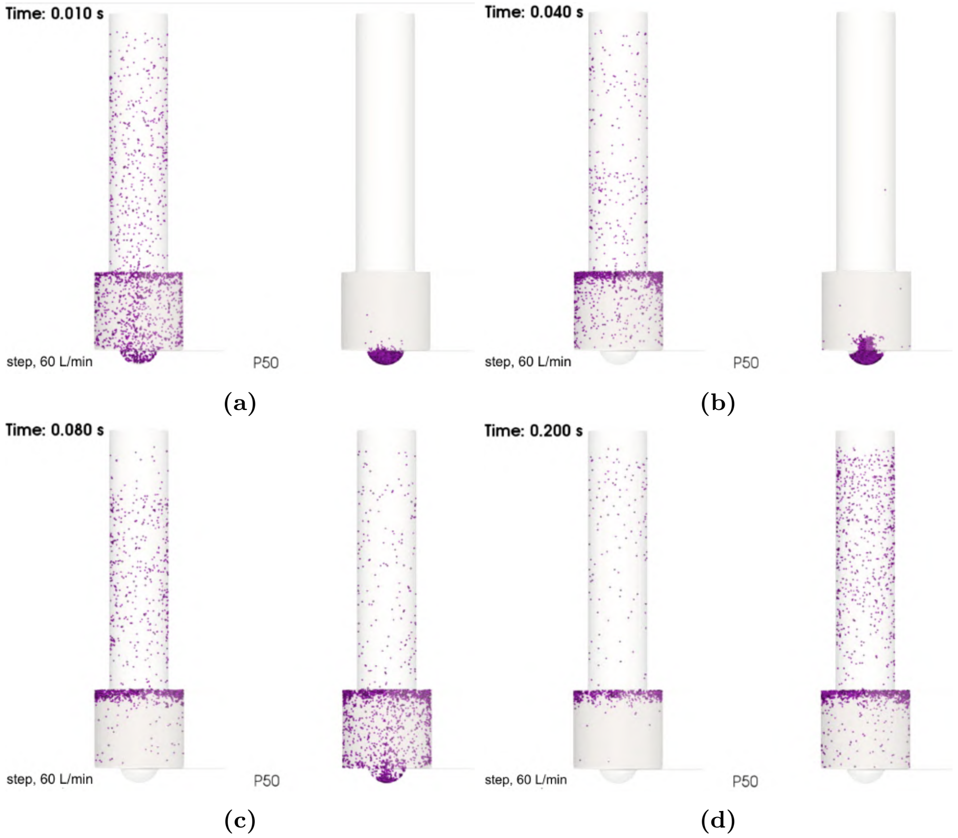

(a) (b)

(c) (d)

Figure 4.20: Particle arrangement in the inhaler with constant flowrate profile (step, 60 L/min) and realistic profile (P50): a) 10 ms, b) 40 ms, c) 80 ms, d) 200 ms.

The different timing of particle motion can be quite easily observed. With the P50 profile, the lifting of the particles from the cup takes place only after 40 ms, while with the step profile the particles are uniformly dispersed throughout the inhaler after only 10 ms.

Figure 4.21 shows the percentage of particles emitted from the system as a function of time in the two cases. The curves do have a similar shape, but their trend confirms the fact that the timing of the P50 test is extended compared to the step test.

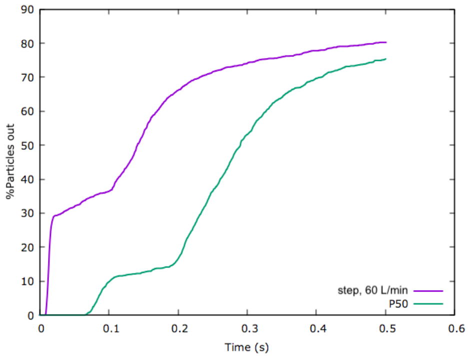

Figure 4.21: Cumulative percentage of particles that leave the device as a function of time with constant inlet flowrate (step, 60 L/min) and realistic inhalation profile (P50).

Of course, the different motion of the particles is directly related to the different motion field of the fluid in the inhaler. The velocity streamlines calculated from the results of the two simulations (step and P50) are shown in Figure 4.22, at 5 ms, 10 ms, 20 ms. If with the constant flowrate (step) the cyclonic motion is already well formed at 5 ms, with fluid velocities exceeding 40 m/s, with the realistic profile (P50), in which the flow rate increases over time, the streamlines are still mostly straight and the cyclonic motion begins to be visible only after 20 ms.

Typical powder emission profiles for different type of inhalers were shown in Figure 1.4, as reported by Clark et al. (2020). The powder emission profile obtained from the simulations with the step boundary condition is analogous to that observed in multidose inhalers with blisters or reservoirs (as already shown in Section 4.4), while the powder emission profile obtained with the P50 boundary conditions is similar to that obtained from standard, single-dose DPI. It therefore seems that mechanism used in multidose inhalers such as the BAM (Breath Actuated Mechanism), which exposes the powder bulk to the air flow only when a certain pressure gradient between inlet and outlet has been reached, ensures that the inhalation starts when the cyclonic motion of the fluid is already developed. The particles are therefore immediately exposed to a strong aerodynamic acceleration, similar to that observed in the simulations by setting the flow rate instantaneously to the value of 60 L/min.

Since the model inhaler considered in the present work was compared

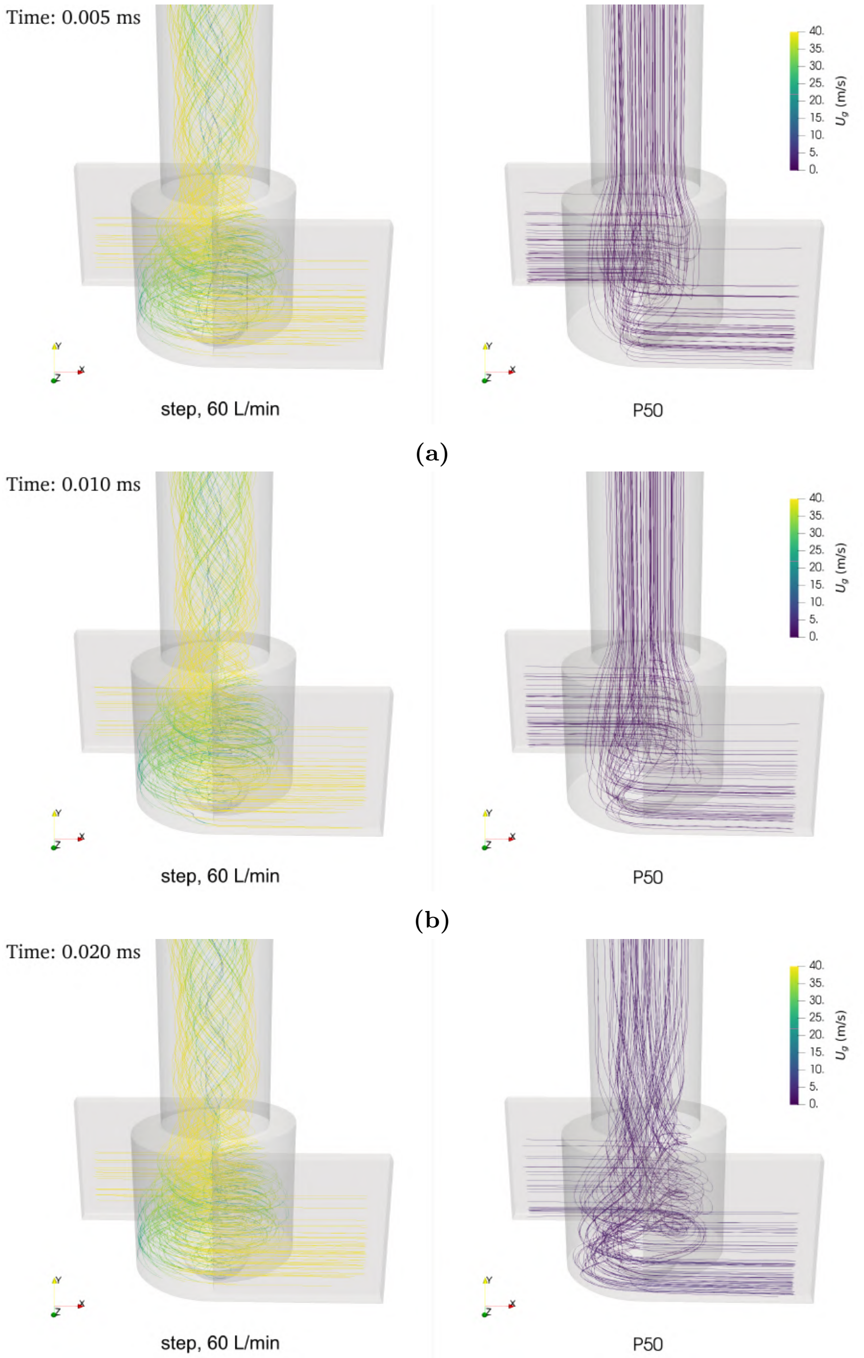

(a)

(b)

(c)

Figure 4.22: Fluid streamlines coloured according to velocity magnitude for simulation with constant flowrate (step, 60 L/min) and realistic inhalation profile (P50) at a) 5 ms, b) 10 ms, c) 20 ms.

with a commercial inhaler with BAM, it was decided to consider the constant flow rate equal to the PIF as a boundary condition for most of the simulations that will be presented. However, further evaluations will also be carried out with the time-varying inlet flow rate.

4.7.6 Cohesion

Lactose carrier particles having a diameter higher than 100 μm are classified as free-flowing (Kinnunen et al., 2014), i.e., can be easily fluidized and aerosolized. The fact that they have good flowability properties is the reason why they are used in inhalers as carriers. API particles, on the other hand, are very cohesive particles, with poor flowability properties and classified as Geldart group C powders: being very small, van Der Waals forces prevail over gravity.

It can be hypothesized that, if a high dosage formulation is considered, the carrier particles may tend to have worse flowability properties due to the large quantity of fine, sticky particles adhered.

To take this effect into account, simulations were carried out considering the introduction of cohesive forces acting both between carrier particles and between carrier particles and the walls of the inhaler and evaluating their effect on the emission of the powder from the inhaler.

The simulations presented below have been conducted considering the same physical and mechanical properties already presented (Table 4.1 and Table 4.2), with 200 μm particles and an inlet gas flow rate of 60 L/min.

4.7.6.1 Particle emission as a function of cohesiveness

To evaluate the effect that the intensity of these forces might have on powder emission, a set of simulations was carried out with the linear cohesion model, SJKR (see section 2.5.3.1) by varying the cohesion energy density, k.

Figure 4.23 shows the cohesive force (SJKR) and the elastic, repulsive normal force (Hertz) for the contact of two particles with a diameter of 200 μm as a function of the overlap. The cohesive force is normalized by dividing by the weight of the particle. Plots were obtained for three different values of the cohesion energy density, k: 50,000 J/m^3, 100,000 J/m^3, 500,000 J/m^3. As k increases, the slope of the representative line of SJKR increases.

As already observed in section 2.5.3.1, the intersection between the two curves can be calculated from:

$$\delta_{eq} = R_{eq}\left(\frac{3}{4}\pi k \frac{1}{E_{eq}}\right)^2 \tag{4.1}$$

The intersection represents the equilibrium between the two forces: if the overlap between the two bodies is greater, the repulsive force will prevail, if it is smaller, the cohesion force (attraction) will prevail. Both the equilibrium overlap and the equilibrium force increases if a higher value of k is considered. From the rightmost graph of Figure 4.23, it can be seen that the equilibrium force with $k = 500{,}000$ J/m^3 is about 6 times the weight of the particle, while it is lower than the weight in the other two cases.

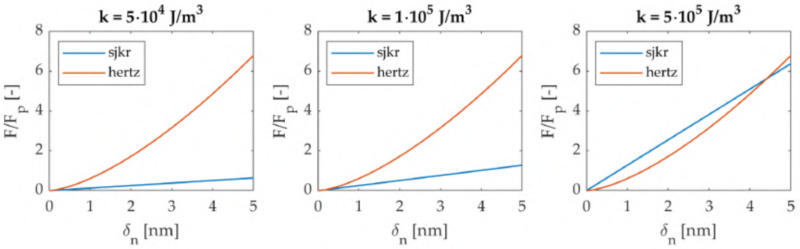

Figure 4.23: Force comparison with increasing values of the cohesion parameter, k.

Figure 4.24 shows the emitted fraction of carrier particles in the first 100 ms for the different cohesion levels considered. Powder emission does not seem to be significantly influenced by the introduction of cohesive forces. The shape of the emission curve is the same in all simulations, with the four emission stages already highlighted in Figure 4.3. However, a difference can be observed for the simulation with the highest cohesion level.

In the first 50 ms, the emission curve of the particles with the highest cohesion level (purple) is lower than the one without cohesion (blue), meaning that fewer particles come out. Subsequently, the curves reconnect, becoming practically overlapping. After 100 ms, the percentage of emitted particles with cohesive particles is 2% higher than the percentage of free flowing particles. This minimal difference (about 32 particles), however, is not significant. The cohesive forces therefore seem to slow down the first emission peak, related to the particles that are directed from the cup directly towards the mouthpiece, without rotating in the swirl chamber.

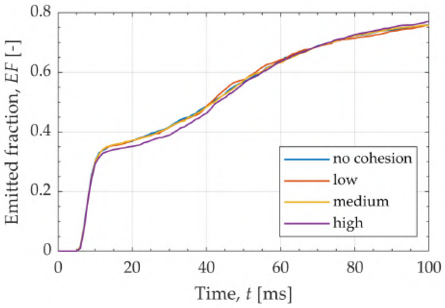

Figure 4.24: Powder emission from the inhaler for simulations increasing level of cohesive forces between carrier particles.

4.7.6.2 Comparison between SJKR and VDW cohesion models

Another model that can be applied to take into account the attractive interactions between particles in a simplified way is the VDW model (see section 2.5.3.2), available by default in the MFIX software. This model uses physical parameters, such as the Hamaker constant, that can be found in literature.

According to Marshall and Li (2014), the use of a cutoff distance $z_{in} = 0.165$ nm gives accurate results, while the Hamaker constant, A, is in the range of 10^{-19} J. Finlay (2001) reports $A = 7 \cdot 10^{-20}$ J for lactose particles used as carrier in pharmaceutical formulations. The outer cutoff (z_{out}) is 10 nm.

Using these data, the calculated surface energy is $\gamma = 0.04$ J/m^2, resulting in a pull off force of about $2{\cdot}10^{-5}$ N (Equation 2.92). This force is about 300 times the weight force for a lactose particle with a diameter of 200 μm.

The cohesion parameter of the SJKR model, k, can be calculated as a function of the pull off force, by equating the cohesive SJKR force (Equation 5.1) and the normal elastic contribution of Hertz force (Equation 2.37), giving:

$$k = \frac{1}{\pi} \sqrt[3]{F \cdot \left(\frac{4E_{eq}}{3R_{eq}}\right)^2} \tag{4.2}$$

By assuming $F = 2 \cdot 10^{-5}$ N, the calculated value of k is $2{\cdot}10^6$ J/m^3.

Figure 4.25 shows the cohesive force for both SJKR and VDW models with the selected parameters.

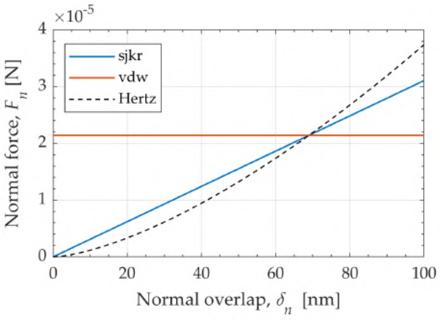

Figure 4.25: Comparison between the cohesive force calculated by SJKR and the short-range contribution of the VDW model as a function of the overlap between two particles. The dashed line shows the normal elastic force calculated with the Hertz model

It can be observed that, as the force is constant with the overlap in VDW and directly proportional to the overlap in SJKR, for overlaps lower than the equilibrium overlap (δ_{eq} about 70 nm) the force calculated by VDW is greater than that calculated by SJKR, vice versa in the case of overlap higher than that of equilibrium. Moreover, with VDW model a finite attractive force is observed when the normal overlap is approaching to zero, while with the SJKR model there is no attractive force at zero overlap.

Figure 4.26 shows the kinetics of particle escape from the system for three different simulations; one without the introduction of cohesive forces (free flowing particles, FF), one with the SJKR model and one with the VDW model.

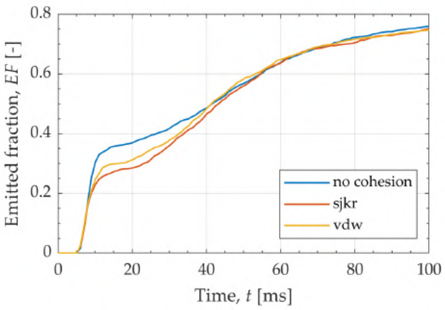

Figure 4.26: Emitted fraction as a function of the cohesion model used. The reference pull off force is $2{\cdot}10^{-5}$ N.

Also in this case, an effect of the cohesive forces is observed in the first phase of powder emission, which seems to be slowed down. Compared to the simulations presented in the previous paragraph (see Figure 4.24), this effect is even more pronounced, given that, for the SJKR model, a 4 times greater cohesion energy density has been considered. Moreover, the SJKR model appears to have a stronger effect on powder emission than the VDW model.

Finally, the effect of adhesion of the particles on the wall was evaluated considering the VDW model. The Hamaker constant for p-w interactions was taken as $3{\cdot}10^{-20}$ J, therefore lower than the p-p Hamaker constant, while the same values were considered for the inner and outer cutoff (0.165 nm and 10 nm, respectively).

The addition of the adhesion forces to the wall has a significant influence on the powder emission, modifying its release dynamics. Figure 4.27a shows the arrangement of the particles in the lower part of the device after 250 ms of simulation. In the second image it is observed that the particle-wall interactions cause adhesion phenomena to the walls (especially in the cup) and considerably interfere with the exit of the particles from the system, as can be seen in the graph in Figure 4.27b. The extent of the phenomenon, however, should be evaluated considering parameters not chosen arbitrarily but based on experimental values.

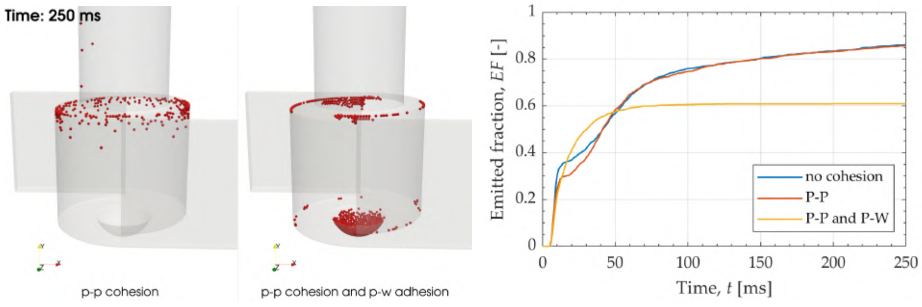

(a) (b)

Figure 4.27: a) Particle arrangement in the swirl chamber after 50 ms with and without p-w interactions, b) Percentage of particles exiting the system with free flowing particles, p-p interactions and p-p and p-w interactions.

4.8 Carrier-wall collisions

Particle-wall collisions are particularly important in carrier-based dry powder inhalers, as they are one of the main mechanism that promote the deaggregation of the API particles (Sommerfeld et al., 2019).

By making use of a version of the MFIX code specially modified to allow the tracking of each event and post-processing tools developed ad hoc, the distribution of the normal impact as a function of the collision location was reconstructed. The collision events recorded in the first 10 ms are shown in Figure 4.28.

It can be seen how the collisions on the wall trace the pattern of the formation of a helix of particles, those that first hit the initial part of the outlet duct. Following some trajectories identifiable by the corresponding aligned collisions, it is observed that the wall rotation in the swirl chamber occurs at a smaller angle than the identifiable trajectories in the outlet duct. This indicates that, in the passage from the swirl chamber to the outlet duct, between the increase of the tangential component of the velocity in the latter (linked to the greater vorticity) and the increase of the axial velocity (due to the narrowing of the section), the latter effect prevails over the particles. A significant number of collisions occur in the cup, testifying to the fact that up to that moment only a portion of the solid has been raised.

Here are some significant statistics on carrier particle collision results collected in the first 10 ms:

- maximum normal impact velocity: 4.0 m/s
- average normal impact velocity: 0.41 m/s
- total number of collisions: 3219 (about 2 impacts per carrier particle)

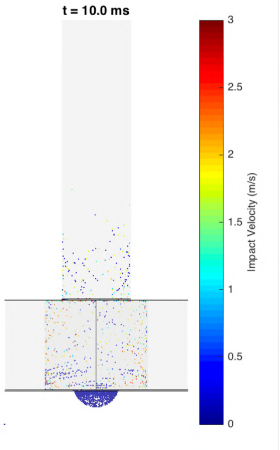

Figure 4.28: Location of carrier-wall collision events in the first 10 ms of simulation. Points are coloured according to impact velocity. 40 L/min, 200 μm particles, no rolling friction.

- average number of impacts per particle in the swirl chamber: 0.60
- average number of impacts per particle in the outlet duct: 0.13
- average number of impacts per particle in the cup: 1.40

A more detailed analysis of the collisions and for a longer period of time (50 ms) was conducted on one of the simulations previously illustrated. The impact velocity distribution along the height of the device is represented in Figure 4.29. Points are coloured according to the time at which they occurred. First of all, it is noted that the order of magnitude of the impact velocity after the first milliseconds remains almost unchanged, with maximum values that do not significantly exceed 3 m/s. The graph shows how collisions at higher normal impact velocities occur indeed in the swirl chamber. The impact velocities in this chamber appear to be homogeneously distributed, except in the first area at the bottom of the device (on the left in the graph), where evidently the particles could not reach the wall. Also, at the beginning of the outlet duct an increase in the impact velocity is observed. Finally, it is worth noting a curious but relatively clear distinction between a range of collisions which occur earlier and at a relatively low impact velocity (approximately 0.5 m/s) and collisions which occur at an appreciably higher velocity. This difference appears quite clearly both in the swirl chamber and in the outlet duct.

On average, each particle impacts with the wall 116 times in the first 50 ms. The impact average frequency is then about 2320 s^{-1}. An excellent agreement is found with the results obtained by Sommerfeld and Schmalfuß (2016), which report an impact average frequency ranging from 2000 to 3000 s^{-1} for carrier particles with diameters ranging from 100 to 500 μm. The

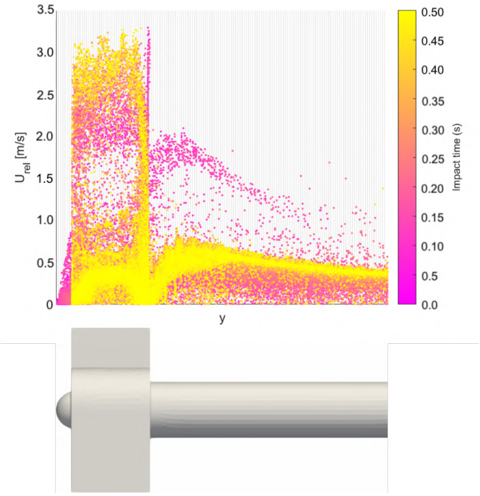

Figure 4.29: Particle-wall impact velocity as a function of y coordinate. All the impacts that occur in the first 50 ms of simulation are reported. The points are colored based on the time at which the impact occurs. 40 L/min, 200 μm particles, no rolling friction.

average impact velocity is 0.32 m/s. The number of impacts is reported in Figure 4.30. The plot confirms that the number of impacts in the swirl chamber is consistently higher than the number of impacts in the mouthpiece and it shows that the number of collisions increases after 10 ms.

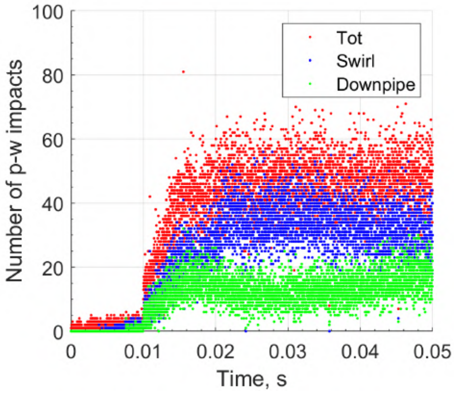

Figure 4.30: Number of particle-wall impacts as a function of time. (40 L/min, 200 μm particles, no rolling friction).

Chapter 5

Introduction of API particles

The direct addition of the API particles in the simulation is of particular interest as it allows to study the deaggregation process in detail.

Before proceeding with the addition of the second solid phase in the simulations, it was decided to carry out preliminary studies considering the behavior of a single carrier particle to which an API particle is adhered.

Carrier-wall impacts are one of the main mechanism of deagglomeration in DPI devices. The analysis of the detachment dynamics of an API particle from a carrier by normal impact with a wall will be presented, along with a discussion on the importance of models and parameter tuning.

Furthermore, the obtained results will be abstracted through the development of an analytical model to estimate the escape velocity.

5.1 Deaggregation due to particle-wall collisions

According to Sommerfeld et al. (2019), the impacts of carrier particles with the walls are one of the main mechanism responsible for deaggregation in DPI devices. It is therefore interesting to analyze under which conditions of adhesion a particle initially attached to the surface of the carrier is released following a sudden change in velocity, such as that occurring during an impact with the wall.

The detachment of API fine particles from coarse carrier particles due to carrier-wall collisions is investigated using DEM simulations.

The open source software used for the simulations mentioned in this section is LIGGGHTS (Kloss et al., 2012).

5.1.1 Simulation parameters and set-up

A carrier particle with one API particle attached in equatorial position impacts on a plane wall. If the energy of the impact overcomes the adhesion

	API	**Carrier**	**Wall**
r (μm)	5	100	-
ρ (kg/m^3)	1500	1500	-
E (MPa)	50	50	50
ν (-)	0.20	0.20	0.20
μ (-)	0.45	0.45	0.45

Table 5.1: Physical and mechanical properties used in the simulations.

energy, the API particle will detach; if not, the particle will remain attached. The configuration is shown in Figure 5.1.

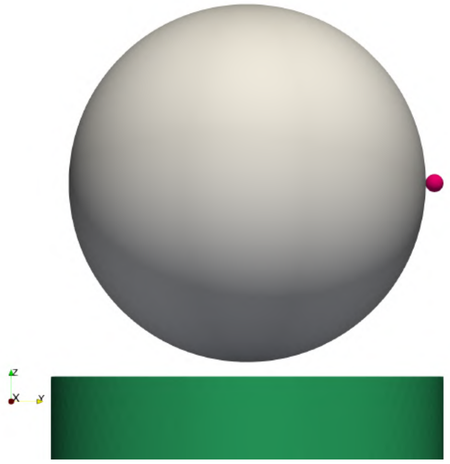

Figure 5.1: System with 2 particles and a wall used in the simulations.

Both the particles have an initial velocity perpendicular to the wall; since gravity force is deactivated, the velocity is constant before the impact.

The timestep used in the simulations is $6{\cdot}10^{-7}$ s. Restitution coefficient is set to 1 for both particle-particle and particle-wall impacts (i.e., impacts are perfectly elastic). The physical and mechanical properties are reported in Table 5.1. In some of the simulations, the CDT a rolling friction model (Equation 2.43) is activated.

The cohesion model used in the simulations is SJKR (section 2.5.3.1), available in LIGGGHTS by default. With this simple model, cohesion and adhesion are modeled through the insertion of an additional force, F_c, that is directly proportional to the overlap between the two contacting bodies:

$$F_{coh} = kA_{cont} \tag{5.1}$$

where k is the cohesion energy density (dimensionally: N/m^2), and A_{cont} is the geometric contact area between the two particles, which is a function of their radii (r_1 and r_2) and the distance between their centers (d), according to Equation 2.101.

Choosing an appropriate value for k is not a simple task, since the parameter is not a physical property, it is indeed strictly related to the SJKR cohesion model used. It can be useful to correlate it to a dimensionless parameter: the granular Bond number.

The granular Bond number, Bo, is used to describe the flowability of powders. It is defined as the ratio between the adhesive/cohesive force (F_c) and the weight (F_p) of the lightest particle (Castellanos, 2005; Siliveru et al., 2017).

The procedure to calculate k from Bo is reported below.

The reference value for the cohesive force (F_{eq}) is selected as the product between the Bond number and the weight force of the API particle:

$$F_{eq} = Bo \cdot F_{p,API} \tag{5.2}$$

As a reference value for the cohesive force, the equilibrium force is considered, i.e., the force at which the normal elastic repulsive force is balanced by the attractive cohesive force.

The overlap at which this condition occurs (equilibrium overlap, δ_{eq}), can be calculated by Hertz formula for the elastic normal force (Equation 2.37):

$$\delta_{eq} = \sqrt[3]{\frac{1}{R_{eq}} \left(\frac{3}{4} \frac{F_{eq}}{E_{eq}} \right)^2} \tag{5.3}$$

The corresponding distance (d) between the centers of the two particles is given by:

$$d = r + R - \delta_{eq} \tag{5.4}$$

from which the contact area can be calculated according to Equation 2.101.

The cohesion energy density can be finally obtained as:

$$k = \frac{F_{eq}}{A_{cont}} \tag{5.5}$$

The value of k as a function of the Bond number is shown in Figure 5.2.

In the present study, different Bond numbers, and therefore different k values, were considered to evaluate different levels of cohesion.

Since according to SJKR model no cohesion/adhesion force acts if the two particles are touching only in one point ($A_{cont} = 0$), the API and the carrier need to have an initial overlap. The initial overlap of the two particles is initially set as the equilibrium overlap (Equation 5.3).

The selected values for the Bond number are reported in Table 5.2, together with the corresponding equilibrium overlaps and cohesion energy density. The minimum Bo considered is 500, so in all cases gravity is negligible for API particles.

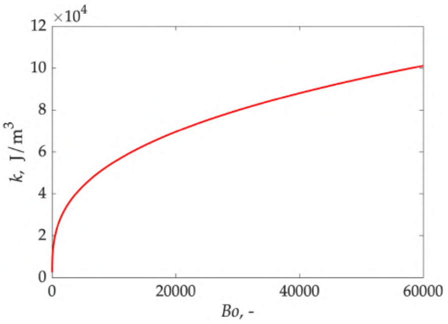

Figure 5.2: Cohesion energy density, k, as a function of the Bond number (Bo).

Bo	$\delta_{\mathbf{eq}}$ (nm)	k (J/m^3)
500	6	20,217
5,000	30	43,659
33,520	105	82,892
50,000	137	94,991

Table 5.2: Equilibrium overlap and cohesion energy density for different values of the Bond number.

5.1.2 Escape velocity

After the carrier hits the wall, the relative velocity between the two contacting particles changes abruptly. There are two possible scenarios: if the kinetic energy of the impact overcomes the work of adhesion, the API particle escapes; otherwhise, the API particles remains on the carrier. The velocity beyond which detachment occurs is referred to as *escape velocity*, v_e (Ariane et al., 2018).

The analytical determination of the escape velocity is not straightforward, so here it has been estimated through DEM simulations. For the different values of Bo that have been considered (see Table 5.2), an interval that contained the escape velocity has been found empirically through a set of DEM simulations: if particles have a "low" initial velocity, the API remains, while if the initial velocity is "high", the API escapes. The interval has then been narrowed following the bisection method. The results obtained with this procedure, reported in Table 5.3, are accurate to the second decimal place. It can be noticed that if a rolling friction model is used in the simulations, the value of the escape velocity is higher, i.e., more energy is required for API detachment.

Bo	**CDT**	**no CDT**
	v_e (m/s)	
(l)2-3 **500**	0.15	0.15
5,000	0.57	0.54
33,520	1.81	-
50,000	2.33	1.77

Table 5.3: Escape velocity as a function of Bond number with and without rolling friction.

5.1.3 Influence of DEM parameters

Several DEM simulations were carried out by varying the input parameters of the simulations, to understand which of them have a direct influence on the escape velocity. The parameters of the simulations are those shown in Table 5.1 and a Bond number of 500 was considered as a reference value for the cohesive interaction.

Table 5.4 shows the escape velocity calculated with different values for the solid phase timestep in DEM simulations. If with a time step lower than 60 ns the value of the escape velocity does not change, a small difference is observed increasing up to 600 ns. Going one order of magnitude further, up to 6000 ns, the simulation becomes unstable. Therefore, considering larger timestep in simulations, if on the one hand it speeds up the calculation, on the other hand it can cause a loss of accuracy also in the description of the detachment phenomena.

Figure 5.3 shows the escape velocity as a function of the static friction coefficient, μ_s, and the restitution coefficient, e. The results show that both parameters have an effect on the velocity at which the detachment occurs. As the static friction coefficient increases, the escape velocity increases, while it decreases as the restitution coefficient increases.

Δt (ns)	**v_e (cm/s)**
6000	unstable
600	15.2
60	15.4
6	15.4

Table 5.4: Escape velocity as a function of the DEM timestep used in the simulations.

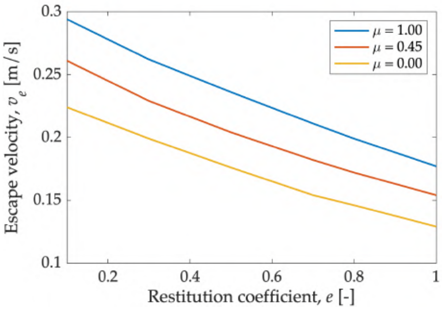

Figure 5.3: Escape velocity as a function of coefficient of restitution (e) and static friction coefficient (μ_s).

The results obtained are also useful for understanding what happens to real powders. For example, powders that tend to deform elastically will have a lower release rate than materials that dissipate during impact, while materials with a high coefficient of static friction will detach with greater difficulty.

5.1.4 The role of rolling friction

The results reported in Table 5.3 prove that the use of a rolling friction model in the DEM simulation has an influence in the detachment mechanism of the API particles. With the aim of understanding with greater detail what happens during the carrier-wall collision, four DEM simulations were carried out using a smaller timestep (60 ns) to follow closely the velocity changes during impact. The results have been saved at every timestep during integration. The reference Bond order is 33,520 in this section, a value calculated from the pull-off force between glass beads and salbutamol sulphate powder measured experimentally via AFM by (Cui et al., 2014).

In the first two simulations, the initial carrier velocity is 2.0 m/s; one is without rolling friction, the other with rolling friction. The other two simulations have a lower initial carrier velocity, 1.0 m/s and 1.8 m/s; the first one does not have rolling friction activated, the second does.

The results, in terms of vertical component of velocity profile during collision, are reported in Figure 5.4, along with snapshots of the position of particles at the end of the simulation. To directly compare the different scenarios, time and velocity have been normalized. Time, t, is divided by the carrier-wall collision duration, τ_c, while the vertical component of particle velocity, v_z, is divided by the initial velocity of the carrier, v_0. The yellow area in the plot indicates when the carrier particle is in contact with the wall.

Figure 5.4a shows the velocity profiles obtained when detachment occurs. The velocity of the carrier particle, initially directed downwards, starts de-

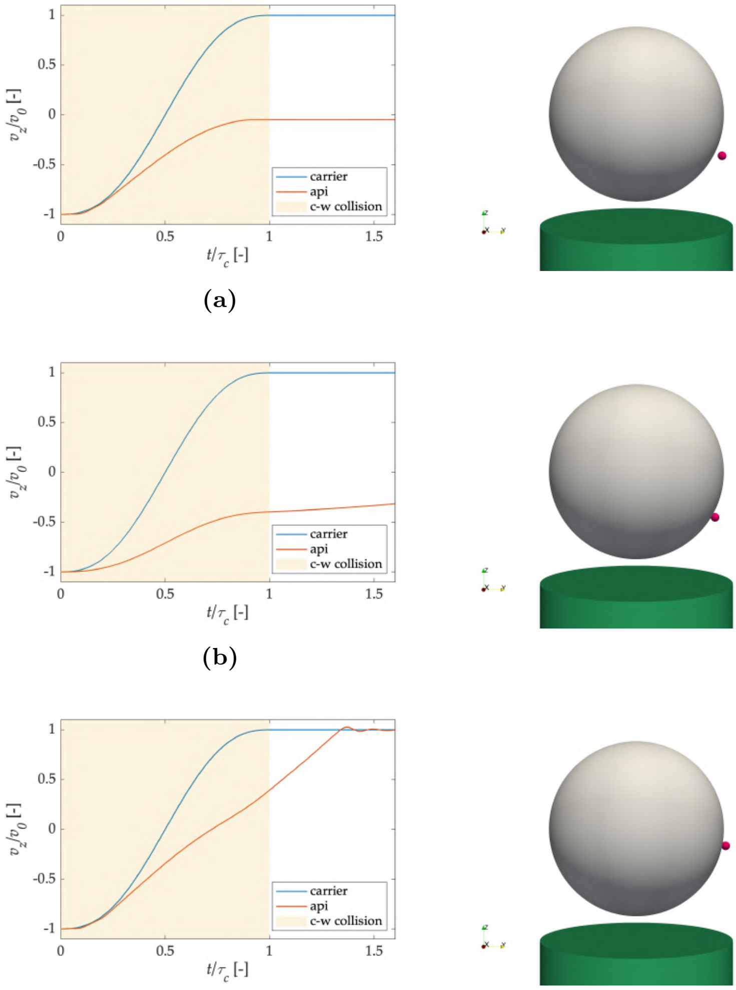

(a)

(b)

(c)

Figure 5.4: Carrier and API velocity profiles during wall collision and particle position after impact (at $t = 1.6\tau_c$) in three cases: a) detachment of API particle, b) no detachment of API particle without rolling friction, c) no detachment of API particle with rolling friction. Velocity values are normalized with the initial velocity of the carrier particle, time values are normalized with collision duration. The yellow area indicates when the carrier particle is in contact with the wall.

creasing until it gets to zero. At this point, the particle starts to rebound. Since the collision is perfectly elastic, the carrier particle will get back to its initial velocity, but headed upwards. The detached API particle will continue its movement downwards, but with a lower velocity, as part of its energy is consumed to detach from the carrier. An analogous plot is obtained whether rolling friction is activated or not, although the speed at which the detachment occurs is different.

If rolling friction is not activated and the particle does not detach (Figure 5.4b), the API particle will start rolling on the carrier surface. If rolling friction is activated, the API starts the rolling movement but stops after a few timesteps, by remaining in a fixed position when the carrier rebounds. As shown in Figure 5.4c, the velocity of the API will eventually reach the velocity of the carrier.

A comparison between the two cases where the API does not detach, with and without rolling friction (RF), is also reported in Figure 5.5.

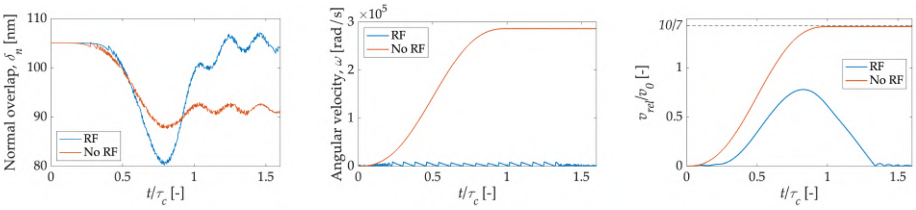

(a) **(b)** **(c)**

Figure 5.5: Evolution of a) overlap, b) angular velocity and c) relative velocity of the API particle (with respect to the carrier) during detachment with and without rolling friction (RF).

Figure 5.5a shows the normal overlap between API and carrier in the two simulations. In both cases, the two particles start from the equilibrium overlap, 105 nm, in a situation where the elastic repulsive force is perfectly balanced by the adhesive force provided by the SJKR model. During the first part of carrier-wall collision, the overlap starts decreasing. At the end of the collision, the overlap will oscillate around the initial value if rolling friction is active, while it will settle at a lower value if rolling friction is not active and therefore the API will roll on the carrier surface.

Figure 5.5b shows the angular velocity of the API particle as a function of time for the two cases considered. If RF is activated, the angular velocity oscillates throughout the simulation, with an average value that is around 4000 rad/s. If there is no rolling friction, the angular velocity increases during the impact, reaching almost 300,000 rad/s. The API will then continue to orbit on the carrier with constant angular velocity following a uniform circular motion.

Figure 5.5c shows the relative velocity (magnitude) between the API and the carrier, normalized with the initial value of the carrier velocity (1 m/s without RF, 1.81 m/s with RF). Initially, the API moves with the carrier, so its relative velocity is zero. As previously noted, if rolling friction is active, the speed of the API initially deviates from that of the carrier, and then returns to its initial value. If, on the other hand, rolling friction is not active, the trend of the relative velocity is the same as that of the angular velocity, with a progressive increase until it reaches 10/7 of the initial value. The increase in relative velocity is in fact closely related to the increase in angular velocity. The final value of the relative velocity of the API is 10/7 ·1 m/s, about 1.43 m/s. Dividing this value by the radius of the carrier particle, 5 μm, the exact final value of the angular velocity is obtained, ~286,000 rad/s.

5.1.4.1 Conversion of translational energy

Consider a spherical particle moving on a wall with an initial velocity, v_0 (Figure 5.6, left). The particle initially has a zero angular velocity ($\omega_0 = 0$).

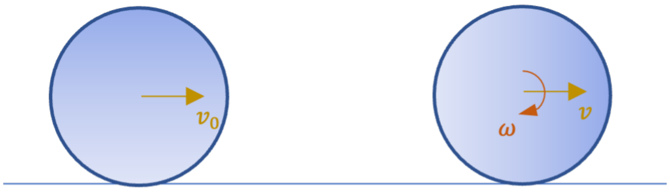

Figure 5.6: Particle on a wall.

A constant static friction force, F_A, acts between the wall and the particle and is equal to:

$$F_A = \mu_s mg \tag{5.6}$$

where μ_s is the static friction coefficient, m is the mass of the particle, g is the gravitational acceleration.

The particle, initially sliding on the wall, begins to acquire an angular velocity, ω, due to the presence of the frictional force (Figure 5.6, right). The translational energy of the particle is progressively converted into rotational energy. The translational velocity, $v(t)$, the angular velocity and the position of the particle, $x(t)$, are given by force and torque balances:

$$v\left(t\right) = v_0 - \frac{F_A}{m}t = v_0 - \mu_s g \cdot t \tag{5.7}$$

$$\omega\left(t\right) = \frac{F_A R}{I}t = \frac{5\mu_s g}{2R}t \tag{5.8}$$

$$x\left(t\right) = v_0 t - \frac{1}{2}\mu_s g t^2 \tag{5.9}$$

where $I = \frac{2}{5}mR^2$ is the moment of inertia of the spherical particle.

At a certain instant, t_{PR}, a pure rolling motion will begin, during which the particle will no longer slide on the wall. The relationship between angular velocity and translational velocity at instant t_{PR} is as follows:

$$\omega\left(t_{PR}\right) = \frac{v\left(t_{PR}\right)}{R} \tag{5.10}$$

By substituting in Equations and 5.7 and 5.8:

$$\frac{5}{2}\frac{\mu_s g}{R}t_{PR} = \frac{v_0 - \mu_s g t_{PR}}{R} \tag{5.11}$$

from which t_{PR} can be calculated:

$$t_{PR} = \frac{2}{7}\frac{v_0}{\mu_s g} \tag{5.12}$$

The distance traveled before pure rolling begins can be calculated by substituting this value in Equation 5.9:

$$L = x\left(t_{PR}\right) = \frac{2}{7}\frac{v_0^2}{\mu_s g} - \frac{1}{2}\mu_s g t_{PR}^2 = \frac{12}{49}\frac{v_0^2}{\mu_s g} \tag{5.13}$$

The sliding motion induces a dissipation. The work made by attrition (W_T) is not all dissipated though, as part is converted into rotational energy (W_R). The dissipated energy is then equal to $W_T - W_R$.

Once the distance traveled L is known, the work made by the attrition force can be calculated as:

$$W_T = F_A \cdot L = \mu_s g t_{PR} \cdot \frac{12}{49}\frac{v_0^2}{\mu_s g} = \frac{12}{49}mv_0^2 \tag{5.14}$$

The angle traveled before pure rolling begins is given by:

$$\theta = \int_0^{t_{PR}} \omega\left(t\right) dt = \frac{5}{49}\frac{1}{\mu_s g} \cdot \frac{v_0^2}{R} \tag{5.15}$$

The translational energy converted into rotational energy until time t_{PR} is given by:

$$W_R = F_A \cdot R \cdot \theta = \mu_s m g R \cdot \frac{5}{49}\frac{1}{\mu_s g} \cdot \frac{v_0^2}{R} = \frac{5}{49}mv_0^2 \tag{5.16}$$

The initial kinetic energy of the particle is:

$$E_0 = \frac{1}{2}mv_0^2 \tag{5.17}$$

while its kinetic energy at time t_{PR} is:

$$E_f = \frac{1}{2}mv_f^2 + \frac{1}{2}I\omega_f^2 = \frac{1}{2}mv_f^2 + \frac{1}{2}\cdot\frac{2}{5}mR^2\cdot\frac{v_f^2}{R^2} = \frac{7}{10}mv_f^2 \tag{5.18}$$

From the conservation of energy:

$$E_f = E_0 - (W_T - W_R) \tag{5.19}$$

$$\frac{7}{10}mv_f^2 = \frac{1}{2}mv_0^2 - \frac{12}{49}mv_0^2 + \frac{5}{49}mv_0^2 \tag{5.20}$$

$$v_f^2 = \frac{10}{7}\left(\frac{1}{2} - \frac{12}{49} + \frac{5}{49}\right)v_0^2 = \frac{10}{7} \cdot \frac{5}{14}v_0^2 = \frac{25}{49}v_0^2 \tag{5.21}$$

The velocity of the particle at time t_{PR} can finally be expressed as a function of initial velocity, v_0:

$$v_f = \frac{5}{7}v_0 \tag{5.22}$$

It is interesting to note that v_f does not depend on the static friction coefficient, although it affects the time t_{PR}. This result is independent of the nature of the normal force, provided that its value is constant. It could also be applied to the case where a normal, constant cohesive force is considered.

In Figure 5.5c it was observed that the final velocity of the API particle (no RF) rolling on the carrier's surface was equal to 10/7 of the initial one. Considering that the carrier velocity variation is $2v_0$ (the carrier goes from -1 m/s to +1 m/s), the final velocity of the API particle is in line with the analytical considerations just presented.

5.2 Analytical model for escape velocity

In the previous section, data on the escape velocity of API particles due to carrier-wall impacts were collected through DEM simulations by varying different parameters. However, the collection of these data is time-consuming, as for each calculated escape velocity value the same simulation needs to be repeated several times: first to identify an interval within which the escape velocity falls, and then to reduce the amplitude of this interval. Instead of recurring to this tedious procedure, it would be desirable to have an analytical model to estimate the value of the escape velocity as a function only of the properties of the materials involved.

With the aim of developing a simple, immediate and effective model, the system considered consists of a stationary carrier particle on which an API particle adheres with initial overlap δ_0. It is assumed that the force of gravity does not act, that the particles are in a vacuum and that there are no dissipative terms (restitution coefficient equal to 1). It is also assumed that the fine particle receives an impulse which instantly gives it a downward velocity v_0. One wonders what is the value of v_0 above which the inertia of the particle in the impact overcomes the adhesion force, causing the detachment. This value, corresponding to the escape velocity, will also depend on the position of the API particle on the carrier. Two particular positions of the API will be considered first, "south Pole" and "equator", and then the results will be generalized to any starting position.

5.2.1 South pole detachment

The first considered case is illustrated in Figure 5.7. The instantaneous initial velocity of the API particle is directed along the direction joining the two centers of the particles. The fine particle can be said to be "at the south pole" of the carrier particle.

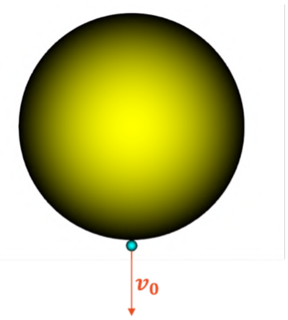

Figure 5.7: API particle in south pole position

In absence of gravity, the API particle will detach if its kinetic energy, E_k, overcomes the energy associated to cohesion:

$$E_k = \frac{1}{2} m_{API} v_0^2 \geq E_{coh} \tag{5.23}$$

in which m_{API} is the mass of the API particle and E_{coh} is the energy associated to the cohesion between the two particles.

By equating the two energy terms in Equation 5.23 the escape velocity, i.e. the critical velocity above which detachment occurs, can be calculated:

$$v_{e,sp} = \sqrt{\frac{E_{coh}}{\frac{1}{2} m_{API}}} \tag{5.24}$$

5.2.2 Equatorial detachment

The second considered case is shown in Figure 5.8, where the API particle is in an equatorial position with respect to the carrier. The force that keeps the API onto the carrier acts in the horizontal direction, while the velocity v_0 is directed vertically. The cohesive force acts therefore as a centripetal force, since it is directed towards the center of the carrier particle.

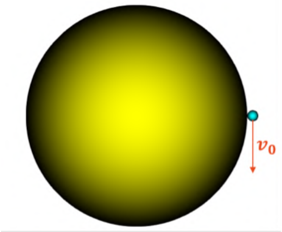

Figure 5.8: API particle in equatorial position

If the initial velocity v_0 is low, the particle begins to rotate around the carrier: part of the translational kinetic energy is converted into rotational energy (the API particle will therefore have acquired a certain angular velocity ω_f). As already shown in section 5.1.4.1, the final translational velocity of the particle (v_f) is equal to 5/7 of the initial velocity v_0.

If, on the other hand, the initial velocity v_0 is high enough to overcome the cohesive centripetal force, the API particle will be able to detach. A centrifugal force acting in tangential direction can be associated to v_0:

$$F_c = \frac{m_{API}}{R_C + R_{API}} v_0^2 \tag{5.25}$$

in which R_C and R_{API} are the radius of the carrier particle and of the API particle respectively. To detach the API from the carrier, this force must do a work L_{fc} such as to bring the initial overlap between the two particles (δ_0) to zero, overcoming the cohesion energy:

$$L_{fc} = \int_0^{\delta_0} F_c \, d\delta = \frac{m_{API}}{R_C + R_{API}} v_0^2 \delta_0 \geq E_{coh} \tag{5.26}$$

The critical escape velocity, $v_{e,eq}$ is then given by:

$$v_{e,eq} = \sqrt{\frac{E_{coh}}{\frac{m_{API}}{R_C+R_{API}} \delta_0}} \tag{5.27}$$

5.2.3 South emisphere detachment

The two discussed cases can be generalized in the event that the API position is in an intermediate position by introducing the θ angle. The velocity v_0 can be decomposed into two components, v_n and v_θ, as shown in Figure 5.9.

The v_n component comes into play in the kinetic energy, while v_θ in the work associated with the centrifugal force. Detachment occurs if:

$$L_{fc} + E_k \geq E_{coh} \tag{5.28}$$

with:

$$E_k = \frac{1}{2} m_{API} v_n^2 = \frac{1}{2} m_{API} v_o^2 \sin^2 \theta \tag{5.29}$$

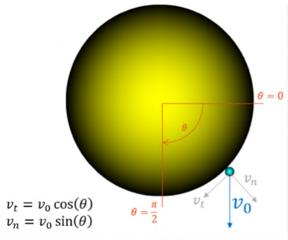

Figure 5.9: API particle attached in a generical position in the south emisphere

and:

$$L_{fc} = \frac{m_{API}}{R_C + R_{API}} v_\theta^2 \delta_0 = \frac{m_{API}}{R_C + R_{API}} \cos^2\theta v_0^2 \delta_0 \tag{5.30}$$

The escape velocity, or the critical detachment value, is given by:

$$v_e = \sqrt{\frac{E_{coh}}{m_{API}\left(\frac{\delta_0 \cos^2\theta}{R_C + R_{API}} + \frac{1}{2}\sin^2\theta\right)}} \tag{5.31}$$

If the values of critical detachment velocity from the equator ($v_{e,eq}$, Equation 5.27) and south pole ($v_{e,sp}$, Equation 5.24), the escape velocity can also be written as:

$$v_e = \sqrt{\frac{1}{\frac{1}{v_{e,eq}^2}\cos^2\theta + \frac{1}{v_{e,sp}^2}\sin^2\theta}} \tag{5.32}$$

5.2.4 Calculation of cohesion energy

The energy associated to cohesion, indicated up to now as E_{coh}, depends on the cohesion model chosen. In the present work the three cohesion models already described have been analyzed: SJKR, VDW, JKR. Assuming that at the beginning the API particle is placed on the carrier particle with an overlap equal to that of equilibrium δ_{eq}, the cohesion energy for the three models can be represented by the coloured areas in Figure 5.10 and corresponds to the work necessary to bring the particles to detach.

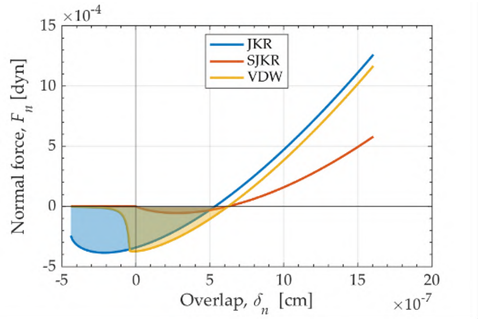

Figure 5.10: Cohesion energy with the three cohesion models VDW, JKR, SJKR.

5.2.4.1 SJKR model

The SJKR model does not provide for long-range cohesive contributions, so the detachment occurs if the overlap becomes zero. By referring to the formulation of the contact area according to the Hertz theory (see Equation 2.100), E_{coh} can be calculated as:

$$E_{coh} = \int_0^{\delta_{eq}} F_{sjkr} d\delta = \frac{k\pi R_{eq}}{2}\delta_{eq}^2 - \frac{8}{15}E_{eq}\sqrt{R_{eq}}\delta_{eq}^{2.5} \tag{5.33}$$

5.2.4.2 JKR model

With the JKR model detachment occurs at a negative overlap, so the overlap is the definite integral of the force from δ_C to δ_E (see Figure 2.17):

$$E_{coh} = \int_{\delta_C}^{\delta_E} F_{jkr}\ d\delta \tag{5.34}$$

As previously shown in section 2.5.1.1, by introducing $a^* = a/a_E$, the JKR model can be expressed in a dimensionless form:

$$\delta = \delta_E\left(3a^{*2} - 2\sqrt{a^*}\right) \tag{5.35}$$

$$F_{jkr} = 4F_p\left(-a^{*3} + a^{*1.5}\right) \tag{5.36}$$

From Equation 5.35 one can calculate:

$$d\delta = \delta_E \cdot 6a^*\ da^* - 2\delta_E \cdot \frac{1}{2\sqrt{a^*}}da^* \tag{5.37}$$

Substituting in Equation 5.34, the integral can be expressed as:

$$E_{coh} = \int_{a^*(C)}^{a^*(E)} 4F_p\left(-a^{*3} + a^{*1.5}\right)\ \left(\delta_E \cdot 6a^*\ da^* - 2\delta_E \cdot \frac{1}{2\sqrt{a^*}}da^*\right) \tag{5.38}$$

Hence, with simple algebraic passages:

$$E_{coh} = -8F_p\delta_{eq}\int_{a^*(c)}^{a^*(E)}\left(-a^{*3} + a^{*1.5}\right) \cdot \frac{1}{2\sqrt{a^*}}da^* \tag{5.39}$$

The limits of integration need to be made explicit. Point E is the point at which $F_{jkr} = 0$:

$$a^*(E) = 1 \tag{5.40}$$

Point C corresponds to the point at which $\frac{d\delta}{dF_{jkr}} = 0$:

$$a^{*}\left(C\right)=6^{-\frac{2}{3}} \tag{5.41}$$

The definite integral in Equation 5.39 can now be solved, giving:

$$E_{coh}=\frac{1}{45}\left(54+6^{\frac{2}{3}}\right)\delta_{E}F_{p} \tag{5.42}$$

5.2.4.3 VDW model

As shown in Figure 5.11, three distinct sections can be identified in the model curve of VDW cohesion model.

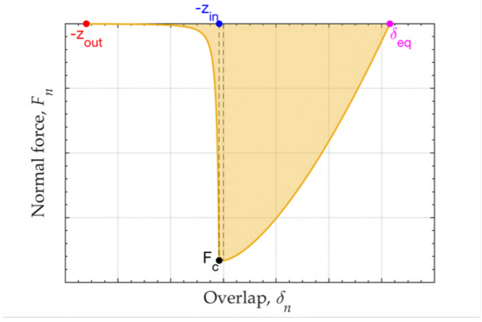

Figure 5.11: Normal force vs overlap according to VDW cohesion model.

The cohesion energy can be thus expressed as the sum of three contributions:

$$E_{coh}=E_{coh,1}+E_{coh,2}+E_{coh,3} \tag{5.43}$$

with:

$$E_{coh,1}=\int_{-z_{out}}^{-z_{in}}\frac{AR_{eq}}{6\delta^{2}}d\delta=\frac{AReq}{6}\left(\frac{1}{z_{in}}-\frac{1}{z_{out}}\right) \tag{5.44}$$

$$E_{coh,2}=\int_{-z_{in}}^{0}F_{C}d\delta=z_{in}\cdot F_{C} \tag{5.45}$$

$$E_{coh,3}=\int_{0}^{\delta_{eq}}F_{C}d\delta-\int_{0}^{\delta_{eq}}F_{Hertz}d\delta\ =F_{C}\delta_{eq}-\frac{8}{15}E_{eq}\sqrt{R_{eq}}\delta_{eq}^{2.5} \tag{5.46}$$

Adding the three terms of Equations 5.44, 5.45, 5.46 the following expression of the cohesion energy is obtained:

$$E_{coh}=A\frac{R_{eq}}{6}\left(\frac{1}{z_{in}}-\frac{1}{z_{out}}\right)+\left(z_{in}+\delta_{eq}\right)F_{c}-\frac{8}{15}E_{eq}\sqrt{R_{eq}}\delta_{eq}^{2.5} \tag{5.47}$$

5.2.5 Model validation with DEM simulations

In order to validate the developed analytical model (Equation 5.31), DEM simulations were carried out with the SJKR cohesion model, by considering a Bond order of 500. The configuration of the simulations is the same as Figure 5.9: there is a API particle adhered to a carrier particle which has a well-defined initial velocity. Nine different values of initial angle θ were considered, ranging from 0 to $\pi/2$. For each angle considered, the simulations were repeated at different initial velocity values, determining a velocity interval (truncated to two decimal points) in which the escape velocity value falls: at the upper bound the API particle detaches, while at the lower detachment does not occur. The results were compared with the values estimated by the macroscopic model and are shown in Figure 5.12. There is an excellent agreement between the values estimated by the model and the results of the simulations.

Interestingly, the escape velocity of a particle at the south pole is two orders of magnitude smaller than the escape velocity of a particle in equatorial position. In general, as the angle θ increases (and therefore as the particle moves from the equator to the south pole), the escape velocity value decreases.

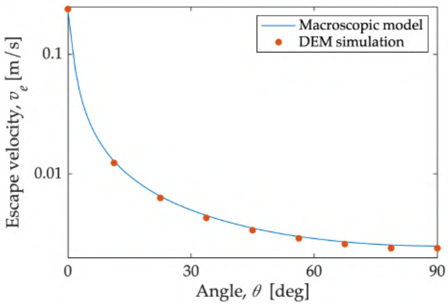

Figure 5.12: Comparison between analytical model for the escape velocity (Equation 5.31) and DEM simulations with MFIX (SJKR cohesion model).

5.2.6 Model application to carrier-wall impact

The analytical model, developed and validated, well describes the case in which the API particle, adhering to the carrier and initially stationary, instantly acquires a speed other than zero.

When a carrier particle collides with the wall, its velocity changes due to the collision. Following the collision, the carrier particle and the API particle, previously travelling together, will have a relative velocity other than zero. It is therefore a situation similar to that studied with the analytical model, although in this case the variation is not instantaneous, but occurs during the entire collision time (see Figure 5.4).

One wonders if, despite the collision dynamics is not explicitly taken into account, the analytical model can estimate with a good approximation the rate of detachment of an API particle adhering to a carrier particle hitting a wall.

The developed macroscopical model can be compared to the results presented in Table 5.3, obtained from simulations with a real impact between the carrier particle and the wall for different values of the Bond number. The cohesion model considered is SJKR and the physical and mechanical properties of the particles involved are the ones reported in Table 5.1.

Figure 5.13 shows the curve obtained with the macroscopical model (Equation 5.31) along with the points obtained with simulations with and without rolling friction.

It is observed that the curve fits well enough the results of the simulations, especially for not very high values of the Bond number. As the Bond number increases, the macroscopic model provides a good estimate of the escape velocity if there is no rolling friction; if there is rolling friction, the escape velocity calculated by the model tends to be slightly underestimated.

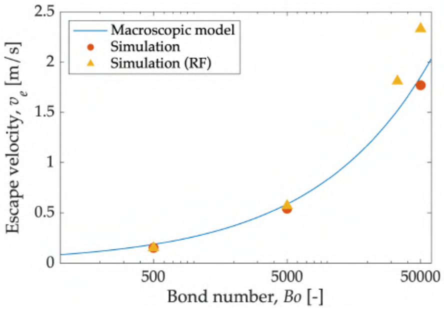

Figure 5.13: Escape velocity as a function of Bond number calculated by the macroscopic analytical model and compared to DEM simulations.

5.2.7 Effect of the cohesion model on escape velocity

The model obtained for the escape velocity can be applied to evaluate how the escape velocity varies as a function of the angle and as a function of the cohesion model. The parameters of the cohesive models have been chosen with reference to an adhesion force value equal to 500 times the weight of the API particle (Bo = 500), that is: $F = 3.8$ nN. In the case of VDW, this is the cohesive/adhesive force at zero overlap (F_c). In the case of SJKR, that value was set as the force at the equilibrium between Hertz and cohesive force. Initially the API particles are in equilibrium with the carrier. The parameters for the cohesion models are reported in Table 5.5. The curves previously shown in Figure 5.10 have been obtained starting from these same parameters.

	API	**Carrier**
γ_{vdw} (mJ/m^2)	0.062	0.062
A (J)	$7.5 \cdot 10^{-22}$	$7.5 \cdot 10^{-22}$
z_{out} (nm)	6.0	6.0
z_{in} (nm)	0.4	0.4
γ_{jkr} (mJ/m^2)	0.086	0.086

Table 5.5: Cohesion parameters for VDW and JKR model by considering $Bo = 500$.

Figure 5.14 shows the results obtained with the macroscopic model (Equation 5.32) for different angles and for the different cohesion models. Note that the ordinate axis is on a logarithmic scale.

It is observed that with the SJKR model detachment is easier than with the other two cohesion models. This result could have been predicted by observing Figure 5.10, in which it is evident that the area for SJKR is less than that for VDW which is in turn smaller than that for JKR.

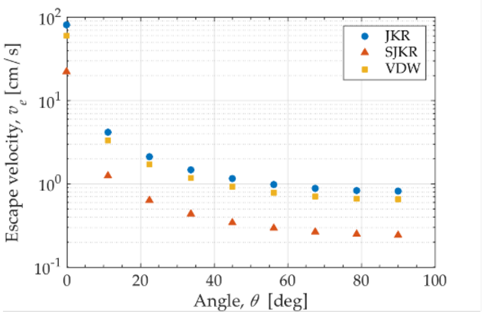

Figure 5.14: Escape velocity as a function of angle for different cohesion models.

The results obtained in these analysis suggest that the SJKR model, deviating significantly from the more accurate JKR model, is not particularly suitable for use in a system such as the one studied in the present work, as it could underestimate the impact of cohesive forces and result in an unrealistically "simple" deaggregation mechanic.

The VDW model, on the other hand, by choosing the parameters appropriately, can provide results quite similar to the JKR model, for which it can be a good alternative with a lower computational effort.

5.3 Can a single carrier-wall impact promote complete API deaggregation?

With the escape velocity model it is possible to evaluate whether the carrier-wall impact mechanism can actually be sufficient to promote the complete deaggregation of the fine ingredient.

As shown in Section 4.8, and also as reported by Sommerfeld and Schmalfuß (2016), a carrier-wall collision in the swirl chamber occurs at typical impact velocities of about 3-4 m/s. This value can be compared with the escape velocity values calculated by the analytical model; if such value is lower than the impact velocity, the particle will detach. The comparison is made considering an API particle in equatorial position (therefore more difficult to detach), the JKR model, a 100 μm carrier particle, and three different adhesion levels: low (adhesive force: 2.5 nN), medium (adhesive force: 25 nN), high (adhesive force: 250 nN). The calculated escape velocity is shown in Figure 5.15 as a function of the API diameter, along with a dashed line representing the typical carrier-wall impact velocity reported in literature and a corresponding "detachment area".

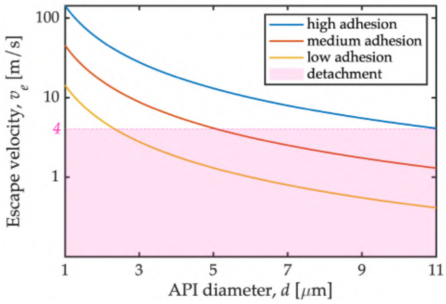

Figure 5.15: Escape velocity of particles in equatorial position as a function of API diameter and adhesion force. The dashed line shows the typical carrier-wall impact velocity in the swirl chamber.

It can be observed that the detachment of submicrometric particles the equatorial position would require impact velocities higher than 10 m/s even with the low adhesion force. In the case of a high adhesion, impact velocities higher than 4 m/s are required even for particles with a diameter greater than 5 μm; yet an adhesion force of 250 nN, a reference for the case of high adhesion, is typical of commonly used formulations such as salbutamol-lactose (Cui et al., 2014; Begat et al., 2004a).

It is therefore probable that a single carrier-wall impact cannot cause the complete detachment of the API particles, but that some API remain in the equatorial position with respect to the carrier-wall point of impact. In order for complete carrier deaggregation, other mechanisms must be involved, such as subsequent impacts or fluid dynamics effects.

Chapter 6

Simulation of carrier-API systems

In the simulations presented in this Chapter, the explicit aerodispersion of a two-component system consisting of 200 μm carrier particles coated by 10 μm API particles is considered. The size of the API is lower than 10 μm in commonly used drug formulations (Sommerfeld et al., 2019), with an average value even below 5 μm to ensure that the fines can reach the lungs. However, using such a small diameter in simulations would go beyond feasibility, as it would result in a smaller timestep and a dramatic increase of the number of particles: for example, to reach a 1% (w/w) load, more than 1 million 5-μm particles or more than 100 millions 1-μm particles would be needed.

A final size of 10 μm has been chosen in order to limit the computational load while the results still provide relevant and useful information for the actual process.

6.1 API - carrier configuration

In carrier based DPI, API particles adhere to the carrier (see Figure 6.1), which facilitates their transport. It is therefore necessary to build in the simulations an analogous configuration and characterize it.

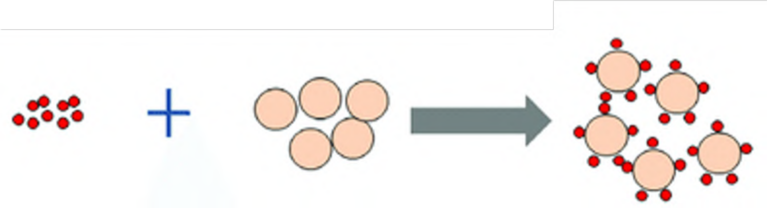

Figure 6.1: API and carrier

6.1.1 Definition of dosage

In defining the quantity of Active Pharmaceutical Ingredient in formulations of pharmaceutical interest, reference is usually made to the weight dosage. Indeed, in a simulation it is simple to know the exact number of particles in the two phases, while experimentally this is almost impossible and one thinks in terms of quantities that can be easily measured such as mass. There is therefore the need to report in the simulation in a simple way the properties that are commonly defined experimentally.

Parameters and formulas will be defined to facilitate this conversion between experimental properties and properties of interest for the simulation, assuming that the particles are spherical and that API and carrier are monodisperse solids.

The size ratio is the ratio between the size of the carrier particle, D, and the size of the API particle, d:

$$r_d = \frac{D}{d} > 1 \tag{6.1}$$

The density ratio is the ratio between the density of the carrier particle, ρ_C, and the density of the API particle, ρ_A:

$$r_\rho = \frac{\rho_C}{\rho_A} \tag{6.2}$$

The number ratio represents the mean number of API particles on a carrier particle. It is defined as the ratio between the total number of API particles, N_A, and the total number of carrier particles, N_C:

$$r_N = \frac{N_A}{N_C} \tag{6.3}$$

The weight dosage, ε_w, is the ratio between the total mass of the API, m_a, and the total mass of the powder bulk (API and carrier), $m_a + m_c$. It can be expressed as a function of the size ratio, density ratio and number ratio according to the following:

$$\varepsilon_w = \frac{m_a}{m_a + m_c} = \frac{1}{1 + \frac{r_d^3 r_\rho}{r_N}} \tag{6.4}$$

In experimental approaches such as image analysis, the API dosage is sometimes expressed in terms of surface coverage, α. Figure 6.2 shows its definition: it is the ratio between the total cross section of the API particles (in blue) and the surface area of the sphere of diameter $d + D$.

It can be calculated as:

$$\alpha = \frac{N_A \cdot \frac{\pi}{4} d^2}{\pi (d + D)^2} = \frac{r_N}{4(r_d + 1)^2} \tag{6.5}$$

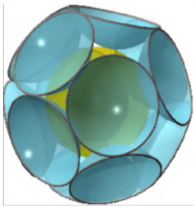

Figure 6.2: Illustration of the definition of the surface coverage.

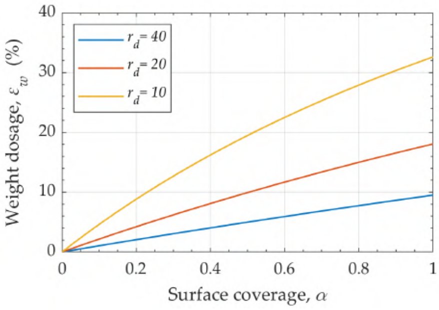

Figure 6.3: Weight dosage, ε_w, as a function of surface coverage, α, for different values of the size ratio, r_d. The considered density ratio (r_ρ) is 1.

A surface coverage equal to 1 represents, in theory, the maximum amount of API that can be arranged on the carrier considering a single layer configuration. In practice, a surface coverage of 1 cannot be achieved as there are limits regarding the packing of the spheres (Conway and Sloane, 1999).

The surface coverage can be expressed as a function of the weight dosage:

$$\alpha = \frac{\varepsilon_w}{4(\varepsilon_w - 1)} \frac{r_d^3}{(r_d + 1)^2} r_\rho \tag{6.6}$$

or viceversa:

$$\varepsilon_w = \frac{4\alpha(r_d + 1)^2}{r_d^3 r_\rho + 4\alpha(r_d + 1)^2} \tag{6.7}$$

Figure 6.3 shows the weight dosage, ε_w, as a function of surface coverage, α, for different values of the size ratio, r_d and a density ratio (r_ρ) equal to 1.

It can be observed that even considering the possibility of having a surface coverage equal to 1 (unattainable), the maximum dosage by weight that can be obtained with a single-layer configuration of monosized API particles is about 30% considering a very high size ratio, equal to 40. This value drops further considering lower size ratios, falling below 10% for $r_d = 10$.

6.1.2 Fast calculation of number of particles in each phase

In the VTK files obtained from the MFIX software all the properties of the particles present in the system at that instant are reported. In the simulations that will be presented below there are two solid phases: the carrier and the API. The two phases differ in diameter and density. To obtain average characteristics for each phase or to post-process the animations, it is first necessary to select the phase of interest, for example based on the diameter, and then process the data. This operation is quite expensive for systems for which there are many particles, whether it is done on Paraview (for rendering) or on MATLAB (for data analysis and statistics). Consider the case in which we want to know the number of particles in an instant of time for the two solid phases. In the course of the current and subsequent chapters, the analysis of the number of particles or the emitted dose for each solid phase is presented many times and for different case studies as it is an important parameter that characterizes the dynamics of the dispersion of the powder in the inhaler. In order to get this information in a fast and immediate way, an alternative has been identified to avoid the data extraction operation. In a software like Paraview it is very simple, for each instant of time, to obtain the average value of the quantities. It is sufficient to use the "Descriptive statistics" filter, which is very fast and efficient. It returns, among other properties, the following parameters:

- Cardinality: the total number of elements analyzed;
- Mean: the mean value of the selected variable;
- Maximum: the maximum value of the selected variable;
- Minimum: the mean value of the selected variable.

The application of the filter to the variable "Diameter" to the results of a simulation with only two solid phases (API and carrier) returns: the total number of particles (Cardinality, N_{tot}); the average diameter (Mean, D_{avg}); the diameter of an API particle (Minimum, D_a); the diameter of a carrier particle (Maximum, D_c).

If N_c and N_a are the number of carrier and API particles in the system, respectively, then the average diameter is given by the following:

$$D_{avg} = \frac{\sum_{i=1}^{N_a} D_{i,a} + \sum_{i=1}^{N_c} D_{i,c}}{N_{tot}} = \frac{N_a \cdot D_a + N_c \cdot D_c}{N_{tot}} \tag{6.8}$$

The number of API and carrier particles can thus be obtained as:

$$N_c = N_{tot} \frac{D_a - D_{avg}}{D_a - D_c} \tag{6.9}$$

$$N_a = N_{tot} - N_c \tag{6.10}$$

Equations 6.9 and 6.10 can be easily solved in Paraview by applying a "Calculator" filter to the results of the "Descriptive statistics" procedure.

6.2 Positioning of API particles

The production of the coated powder, which implies the adhesion of a given load of API particles on carrier particles, is obtained by assuming uniformly distributed particles attached to the surface of the carrier in a monolayer configuration. A MATLAB® algorithm calculates the positions of API particle locations in an orderly manner as a function of the assigned percent loading (w/w%) and the API particle size. The rationale behind the algorithm will be presented below.

6.2.1 Kissing number

The kissing number is defined as the maximum number of non-overlapping spheres arranged in such a way that they touch a common sphere.

In 2D, the problem is reduced to the calculation of the maximum number of circles tangent to a circle placed in the center. If the circles all have the same diameter, it is well known that the kissing number is 6. If, on the other hand, the circle placed in the center has a larger diameter than the circles around, as in Figure 6.4, the kissing number will depend on the size ratio. A formula for the calculation of the kissing number for polydisperse circles, n_k, has been derived.

Observing the configuration represented in Figure 6.4, it can be seen that the kissing number corresponds to the number of sides of the regular polygon inscribed in the circumference of side $R+r$, where r is the radius of the small circles and R is the radius of the large one.The side of the polygon is twice the radius of the small circles (r).

The apothem of such polygon, a, is given by Pythagorean theorem:

$$a = \sqrt{(R+r)^2 - r^2} \tag{6.11}$$

The ratio between the apothem and the side of the polygon, f, can be calculated from geometrical considerations as well:

$$f = \frac{a}{2r} = \frac{1}{2\tan\frac{\pi}{n_k}} \tag{6.12}$$

By combining Equations 6.11 and 6.12, n_k can be calculated as:

$$n_k = \frac{\pi}{\tan^{-1}\left(\frac{r}{\sqrt{(R+r)^2-r^2}}\right)} \tag{6.13}$$

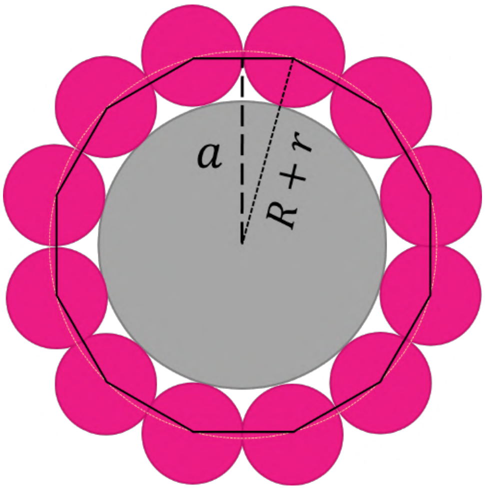

Figure 6.4: Small circles (pink) around a large circle (grey). r is the radius of the small circles, R is the radius of the large circle. a is the apothem of the regular polygon inscribed in the circumference with radius $R+r$.

Of course, n_k has to be rounded down to the smallest integer.

6.2.2 3D configuration

The calculation of the kissing number in 3D is much less trivial. The demonstration of the fact that the 3D kissing number for monodisperse spheres is 12 was derived only in the twentieth century, although the problem had already been posed in Newton's time (Conway and Sloane, 1999).

Having to build a three-dimensional configuration for the arrangement of the API on the carrier, it was decided to use the formula obtained in the 2D case (Equation 6.13), aiming at adding not the maximum possible number of tangent spheres, but the maximum number of tangent spheres that can be arranged in an orderly manner by imagining the large sphere as if it were divided into meridians.

The coordinates of the center of an API particle $(x_{API}, y_{API}, z_{API})$ tangent to a carrier particle can be expressed in spherical coordinates considering the center of the carrier particle (x_C, y_C, z_C) as the reference system:

$$x_{API} = (R+r) \cdot \sin\phi \cdot \cos\theta \tag{6.14}$$

$$y_{API} = (R+r) \cdot \cos\theta \tag{6.15}$$

$$z_{API} = (R+r) \cdot \sin\phi \cdot \sin\theta \tag{6.16}$$

where ϕ is the angular coordinate in the $x-y$ plane and θ is the angular coordinate in the $x-z$ plan.

The API particles are placed on the carrier with two nested `for` loops.

The outer loop is on the angular coordinate ϕ, ranging from 0 to π, considering a number of intervals equal to:

$$n_\phi = 0.5 \frac{\pi}{\tan^{-1}\left(\frac{r}{\sqrt{(R+r)^2 - r^2}}\right)} \tag{6.17}$$

At the i-th iteration:

$$\phi_i = \phi_{i-1} + \frac{\pi}{n_\phi - 1} \tag{6.18}$$

For each ϕ_i, an inner loop is performed to determine the angular coordinate θ, ranging from 0 to 2π.

The number of intervals for the inner loop is given by:

$$n_\theta = \frac{\pi}{\tan^{-1}\left(\frac{r}{\sqrt{[\sin\phi_i (R+r)]^2 - r^2}}\right)} \tag{6.19}$$

At the j-th iteration of the inner loop:

$$\theta_{i,j} = \theta_{i,j-1} + \frac{2\pi}{n_\theta - 1} \tag{6.20}$$

If maximum surface coverage is desired, the algorithm positions all the particles it can add; if a lower coverage is desired, the algorithm randomly chooses only some of the particles to be positioned, based on a probability defined as the ratio between the desired degree of coverage, α, and the maximum degree of coverage, α_{max}:

$$p = \frac{\alpha}{\alpha_{max}} \tag{6.21}$$

This probability can also be expressed as a function of the desired weight dosage instead of desired surface coverage, by substituting Equation 6.6 in Equation 6.21.

Due to this random element in the API positioning, each carrier particle will have a unique configuration, albeit maintaining the prescribed weight dosage.

Examples of the coated carrier particles at different degree of loading are shown in Figure 6.5 for a size ratio $r_D = 20$ and density ratio $r_\rho = 1$. The rightmost image shows the maximum surface coverage that can be obtained with the presented algorithm and for the considered size ratio and density ratio, which is $\alpha = 0.73$. The number of API particles and the surface coverage for each configuration are reported in Table 6.1.

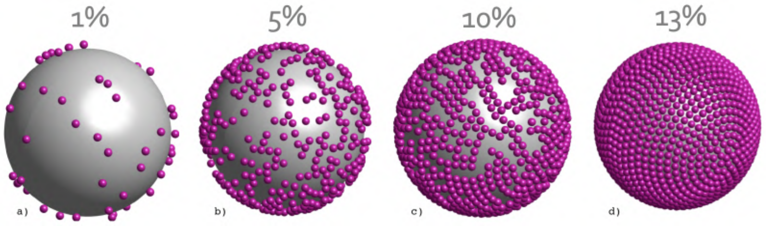

Figure 6.5: Generation of the coated carrier particles by random positioning of fine particles (purple) on the surface of coarser ones (grey) for a size ratio $r_d = 20$ and density ratio $r_\rho = 1$. API w/w loadings of 1% (a), 5% (b), 10% (c) and 13% (d).

$\varepsilon_\mathbf{w}$%	**1%**	**5%**	**10%**	**13%**
N_A	86	436	902	1297
α	0.06	0.24	0.50	0.73

Table 6.1: Weight dosage (ε_w%), number of API particles (N_A) and surface coverage (α) for the API-carrier configurations shown in Figure 6.5.

6.3 Simulation parameters and set-up

A quantity of about 10 mg of carrier particles are considered with a 1% (w/w) of API particles. Fine particles are placed on carrier particles according to a random configuration fulfilling the prescribed percent coverage. To achieve the desired dosage, each carrier is covered with about 86 API particles.

The Young modulus has been selected in order to limit the maximum normal overlap to 20 % of the API particle radius (i.e., 1 μm at a maximum impact velocity of 40 m/s). The resulting timestep for the DEM part of the code is approximately 6 ns. The other DEM parameters (restitution coefficients, static and rolling friction coefficients, Poisson coefficients) were selected to reproduce the behavior of brittle, irregularly shaped pharmaceutical particles.

As shown by Begat et al. (2004a,b), the cohesive (drug-drug) and adhesive (drug-excipient) interaction properties play a significant role in the homogeneity of the blend and the deaggregation and dispersion properties of the respirable particles. For the cohesion/adhesion model utilized (see Eq. 2.105) appropriate parameters have been used by referring to the work of Cui et al. (2014), who determined the pull-off force between untreated glass beads and spray dried salbutamol sulphate particles via AFM measurements. The reported value of the force ($2.58 \cdot 10^{-7}$ N) has been set to calculate the surface energy, γ and the Hamaker constant, A. The same adhesion/cohesion pull-off force acts for API-carrier, carrier-carrier and API-API interactions.

With such a value of force, the Bond number, i.e., the ratio between cohesive force and weight (Castellanos, 2005), for the API particle is in the order of 10^5, which is characteristic of ultra-fine, very cohesive powders categorized in the group C of Geldart's classification (Kamranian Marnani et al., 2019) for fluidized particles.

The properties of the solid particles and the DEM model are reported in Table 6.2. The same properties (Young modulus, Poisson Ratio, restitution coefficient, friction coefficients) are considered for the walls of the inhaler. Particle-wall adhesion was not included in the simulations.

	Carrier	**API**
Diameter (μm)	200	10
Particle density (kg/m^3)	1500	1400
Young modulus (GPa)	0.2	0.2
Poisson Ratio	0.45	0.45
Restitution Coefficient	0.2	0.2
Friction Coefficient	0.5	0.5
Rolling Friction Coefficient	0.3	0.3
Hamaker constant (J)	$8.85{\cdot}10^{-21}$	$8.85{\cdot}10^{-21}$
Surface energy (J/m^2)	0.004	0.004
Cohesion inner cutoff (nm)	0.165	0.165
Cohesion outer cutoff (nm)	6	6
Solid mass	10 mg	0.1 mg
Number of particles	1584	136322

Table 6.2: Physical and DEM model properties used in simulations of carrier and API particles.

A weight API dosage of 1% has been selected in the present work, which corresponds to about 140k particles with a 10 mg total mass (see Table 6.2). The surface coverage of the carrier particles is about $\alpha = 0.06$. About 1600 coated particles are regularly arranged in the hemispherical cup and a DEM gravity settling run is performed before the CFD–DEM simulation. Figure 6.6 shows the initial configuration of the coated carrier and the rearranged fine particles after the settling period, whose vibrations generated by the collisions cause the formation of API structures and agglomerates.

6.4 Dispersion of API particles

A CFD–DEM simulation has been carried out by considering the same setup for the fluid as in the previous Chapter, with an inlet flowrate of 60 L/min. At the beginning of the simulation, all carrier and API particles are positioned at their contact force equilibrium. To provide a reference, with the

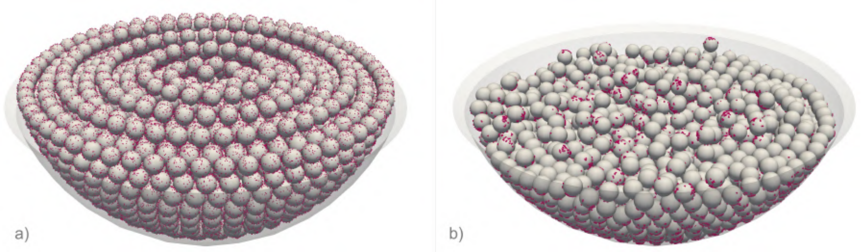

Figure 6.6: a) Initial configuration of 1585 coated carrier particles with 1% API dosage (w/w%). Each carrier particle has an average of 86 API particles stuck on the surface. b) Configuration after DEM gravity settling with the API particles repositioned.

selected cohesion and mechanical parameters, the equilibrium overlap for API-carrier contacts is approximately 8 nm. The initial configuration has been settled and relaxed with a pure DEM simulation, as already shown in Figure 6.6b.

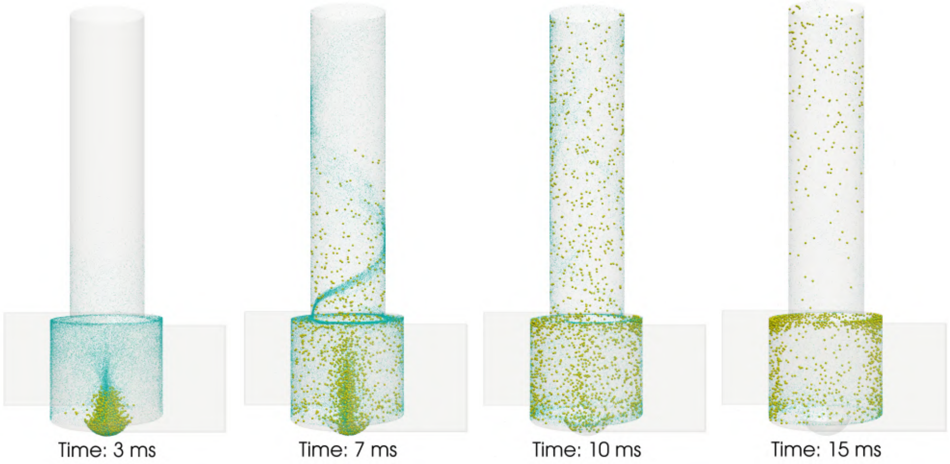

(a) **(b)** **(c)** **(d)**

Figure 6.7: Position of carrier (yellow) and API (blue) particles during the simulation: a) 3 ms, b) 7 ms, c) 10 ms, d) 15 ms. API particles are shown with an enlarged size to improve visibility. 60 L/min gas flowrate.

Figure 6.7 shows the configuration of the two solid phases during the first 15 ms of the simulation. The path followed by API particles shows that they get relatively easily deaggregated from the carrier particles by the action of the air drag force. Then they are lifted well before carrier particles, but following a similar trend as observed in simulations with just carrier particles, i.e. a central dense region, fountain-like, around the axis and the rest of particles being pushed on the swirl chamber walls (Figure

6.7a). After 3 ms, the first few API particles reach the cylindrical duct. After 7 ms the API particles have formed a helical dense flow towards the exit and the first few carrier particles enter the cylindrical duct (Figure 6.7b). After 10 ms the particles are fully dispersed throughout the device and the carrier particles show again the tendency towards accumulation near the swirl chamber ceiling (Figure 6.7c). Eventually, after 40 ms, the API particles have almost entirely left the device.

The time evolution of the release is shown in Figure 6.8 separately for API and carrier particles. Once the API particles detach from the carrier, their residence time is expectedly shorter. Carrier particles' motion follows the pattern already discussed in the previous sections. The early detachment causes a substantial release of API particles, but not all of them. As shown by the average number of attached API particles to each carrier particle, reported in the lower plot in Figure 6.8, there is an initial drop from 86 to 60 API particles attached after around 2 ms, essentially owing to the hydrodynamic interactions in the dense region. This is followed by a gradual decrease of the average number of API still in the aggregated state, which later detach likely as a result of particle-particle and particularly particle-wall impacts. After 20 ms there is, on average, only one API particle per carrier, so the carrier leaves the device totally uncoated.

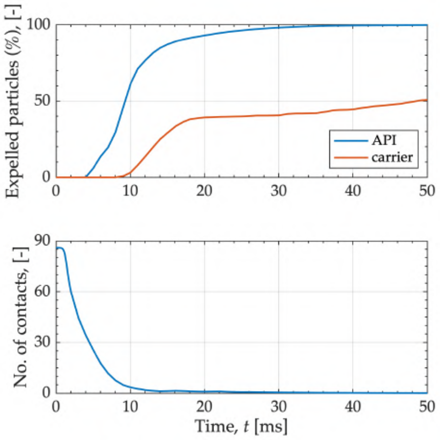

Figure 6.8: Percentage of emitted particles and average number of API particles attached to a carrier particle as a function of time (gas flowrate 60 L/min).

6.5 Comparison with experiments

The emission of API particles can be compared quantitatively with the experimental results presented by Merusi et al. (2018), who used a fluorescence imaging technique to characterize the emission of model API fines (polymer microspheres, diameter: 1.5 - 2 μm, density: 1300 kg/m^3) blended with a proprietary lactose-based carrier vehicle.

Figure 6.9a shows the fluorescent signal intensity count (Normalized Intensity, NI) of emitted API particles as a function of time for powder formulation with 1% w/w API and an inlet gas flowrate of 40 L/min. The experimental curve (in red) has been extracted from the published data in Merusi et al. (2018), while the simulation curve (in black) has been calculated with the following equation, considering the particles passing through a region (of length h) just below the outlet section:

$$NI = \frac{\sum \frac{\pi}{4} D^2 \frac{v_y}{h}}{\max(NI)} \tag{6.22}$$

where v_y is the vertical component of particle velocity, $\frac{\pi}{4}D^2$ is the particle cross section. Similar to the experimental procedure, the curve has been normalized in order to have 1 as the maximum value. The experimental curve was shifted along the time axis in order to have the maximum peak aligned with the simulation's one, as in the experiment the emission is delayed by the presence of the Breath-Actuated Mechanism (BAM, see e.g. Farkas et al. (2017); Lewis and Tweedie (2016)), a dose cover that opens up exposing the powder to the air flow when the de-pressure in the swirl chamber reaches a calibrated value.

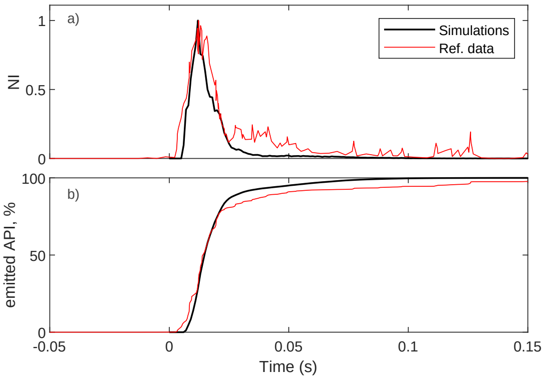

Figure 6.9: API emission in simulations and experiments with a 40 L/min inlet gas flowrate and 1% w/w API. a) Normalized fluorescence intensity, b) cumulative percentage of emitted API particles.

Figure 6.9b shows the cumulative percentage of emitted API particles as a function of time. The experimental curve has been calculated as the cumulative of the curve reported in 6.9a, while the simulation curve has been calculated with the following:

$$emitted\ api = 1 - \frac{n_a(t)}{n_{a0}} \tag{6.23}$$

where n_a is the number of API particles at time t and n_{a_0} is the initial number of API particles.

The plots in Figure 6.9 show that the timing of emission in the simulations reasonably matches the experiments: the width of the distribution is quite similar, as well as the slope of the cumulative curves. However, the simulation curve appears smoother, while the experimental one shows a tail that extends beyond 150 ms. Most of the fine powder is expelled in about 20 ms anyway.

6.6 API deaggregation

Inspection of the dose cup region during the very first few milliseconds illustrates rather clearly the early deaggregation phase in this dense region. Figure 6.10 shows snapshots of the initial phase of the simulation. As expected, the API particles exposed to the surface, i.e. to the direct action of the fluid, are lifted almost immediately. Other ones are peeled during carrier particle lift off.

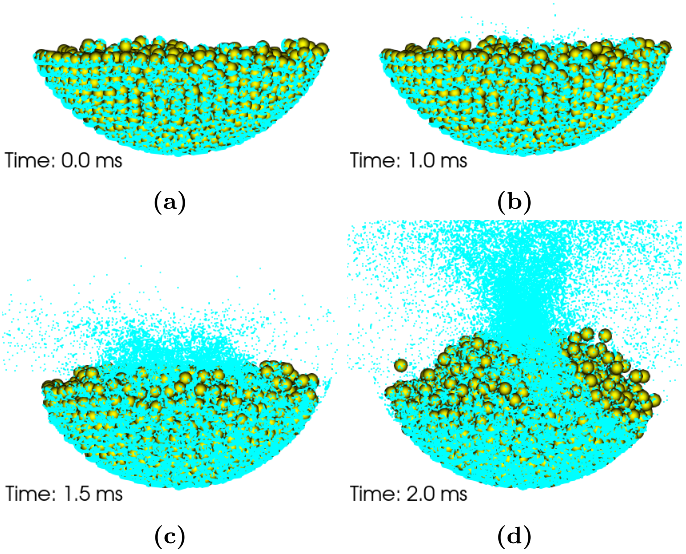

(a) (b) (c) (d)

Figure 6.10: Initial lifting of API particles. API particles are shown with an enlarged size to improve visibility.

The exact deaggregation moment results from the force equilibrium break, in which the adhesive force keeping API particles attached to the carrier is overcome either by the hydrodynamic drag, or by the inertia during impacts with the walls or with other particles. Figure 6.11 shows the evolution of average hydrodynamic force $F_d + F_b$ (drag+pressure gradient) and the contact/adhesive force F_c on API and carrier particles in the first phase of the simulation. F_c includes both elastic and adhesive forces. For the API plot

(Figure 6.11b), only the results relative to the first 3 ms of the simulation are reported since, as shown in Figure 6.10, most of the deaggregation process has already taken place by then.

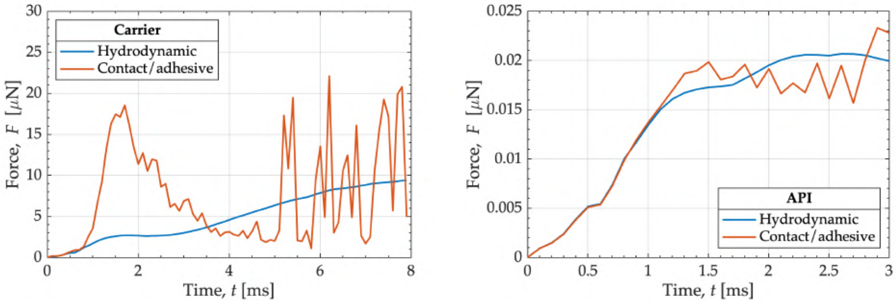

(a) **(b)**

Figure 6.11: Average forces (hydrodynamic and contact/adhesive) exerted on carrier particles in the first 8 ms (a) and on API particles during the first 3 ms of simulation (b) with an inlet gas flowrate of 60 L/min.

For the carrier particles, the evolution in time shows that the contact forces largely dominate for the very first milliseconds. Indeed, they remain static in the cup. For the API particles, the contact/adhesive force exactly balances the hydrodynamic force during the first millisecond, explaining why these fine particles move while remaining attached to the carrier.

When the two curves depart from each other (at 1 to 2 ms), as shown by the number of contacts in Figure 6.8, the API particles start detaching from the carrier and the deaggregation process takes place. By looking at the individual contributions (not shown for brevity), for the API particles F_b is negligible compared to drag and contact forces.

Both experimental and simulation works on a similar system (Ponzini et al., 2021; Pasquali et al., 2015; Merusi et al., 2018) suggest that the first mean emission peak of API particles occurs right after the start of the inhalation and is mainly due to direct aerodynamic detachment. The timing and the duration of this first emission peak are captured well by simulations, as already shown in the normalized fluorescence intensity profile reported in Figure 6.9a. However, the tail of the experimental curve suggests a second emission phase occurring around 50 ms after the start of the inhalation, meaning that more API particles could detach due to carrier-wall collisions in a later stage. A plausible cause of this dissimilarity is in the strong polydispersity of the system, for which the large ratio of cell size to API diameter causes an overestimation of the drag force. It is expected that a multigrid approach (Farzaneh et al., 2011) or a drag force model explicitly derived for polydisperse system (Cello et al., 2010) can overcome these limitations.

6.7 Effect of different parameters on deaggregation

In order to evaluate the effects of some parameters and models related to the DEM approach on the deaggregation process, further simulations were carried out with both carrier and API. Since these simulations are very long and computationally expensive, for some of them only the first 10 ms were simulated. In the results just presented it was however observed that in 10 ms the phase of deaggregation of the API from the carrier had occurred already.

6.7.1 Inlet flowrate

To evaluate the effect of the inlet air flowrate, simulations were carried out at three different flow rates: 40 L/min, 60 L/min, 80 L/min. Figure 6.12a shows the fraction of API particles exiting the inhaler in the first 50 ms for the three simulations, while Figure 6.12b shows the average number of API adhered to carrier particles.

It is observed that as the flowrate increases, both the detachment and the emission of the API are favoured. The results for a flow rate of 40 L/min show that after 50 ms approximately 7% of the API is still in the inhaler, while in the other two cases the API has practically been all expelled already.

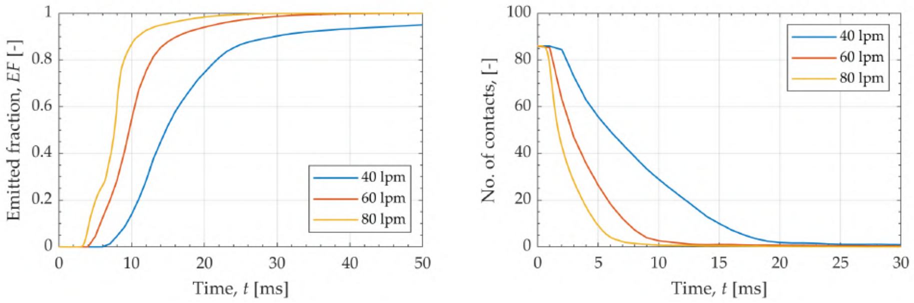

(a) (b)

Figure 6.12: Emitted fraction of API particles (a) and mean number of API particles on a carrier (b) for different inlet flowrates.

6.7.2 Cohesion model

In the simulations presented so far, the VDW model for cohesive forces has been considered. For a comparison between the simplified models for the computation of the cohesive forces, a simulation was also carried out with the SJKR model. To choose the cohesion energy parameter, k, the approach already illustrated in Section 4.7.6.2 was followed. The value considered is $k = 2.2 \cdot 10^6$ J/m^3. The inlet flowrate is 40 L/min.

The position of particles in the simulations with VDW and SJKR cohesion model at 2 ms, 4 ms and 6 ms is shown in Figure 6.13. The initial detachment of API particles from the carrier particles directly exposed to the air flow seems to occur earlier with the SJKR cohesion model (see Figure 6.13a). As a consequence, particles reach earlier both the swirl chamber (Figure 6.13b) and the mouthpiece (Figure 6.13c).

The number of emitted particles as a function of time for the first 10 ms is shown in Figure 6.14a. Figure 6.14b shows the mean number of API particles in contact with a carrier. The results prove that the deaggregation seems to be facilitated with the SJKR cohesion model, as well as the API emission. The results confirm the observations presented in Section 5.2.7; with the SJKR model, the energy associated to cohesion is lower compared to VDW model.

6.7.3 Weight dosage

It has already been noted that the use of high-dose systems in DPI inhalers is of particular interest for various applications (see Section 1.2). A weight dosage of 1%, considered in the simulations already presented, is typical of commercially available asthma and COPD products. To evaluate in an exploratory way the effects of introducing a higher dosage on the initial phase of aerodispersion, a CFD–DEM simulation has been carried out with a higher API dosage, 5%. The particle diameters are 200 μm for the carrier and 10 μm for the API. The total number of API particles with this configuration is 716,976, with about 452 API particles adhered on each carrier. The total mass of the API is about 500 μg. A fluid flow rate of 40 L/min and the cohesive model SJKR (with $k = 2.2 \cdot 10^6$ J/m^3) are considered. The simulated time is 10 ms. The initial configuration is shown in Figure 6.15.

Figure 6.16 shows snapshots of the simulation at 2 ms, 4 ms, 6 ms. On the left side, the results the analogous simulation (SJKR model, 60 L/min inlet flowrate) but with a lower dosage (ε_w =1%) at the same time instants are shown for comparison.

The difference in terms of API concentration between the two simulations is immediately noticeable, with the API almost entirely covering the walls of the swirl chamber in the higher dosage system (Figure 6.16c, right). The characteristic times are similar in both simulations: the detachment of the API which is located on the upper carrier occurs in the first 2 ms, the dispersion in the swirl chamber occurs in about 4 ms.

A consistent difference is however observed in the emitted fraction of API particles (FPF); the FPF after 10 ms with 5% dosage is about 30% lower than the simulation with 1% dosage. Although the results are related only to the very early stages of powder emission and it is not known whether

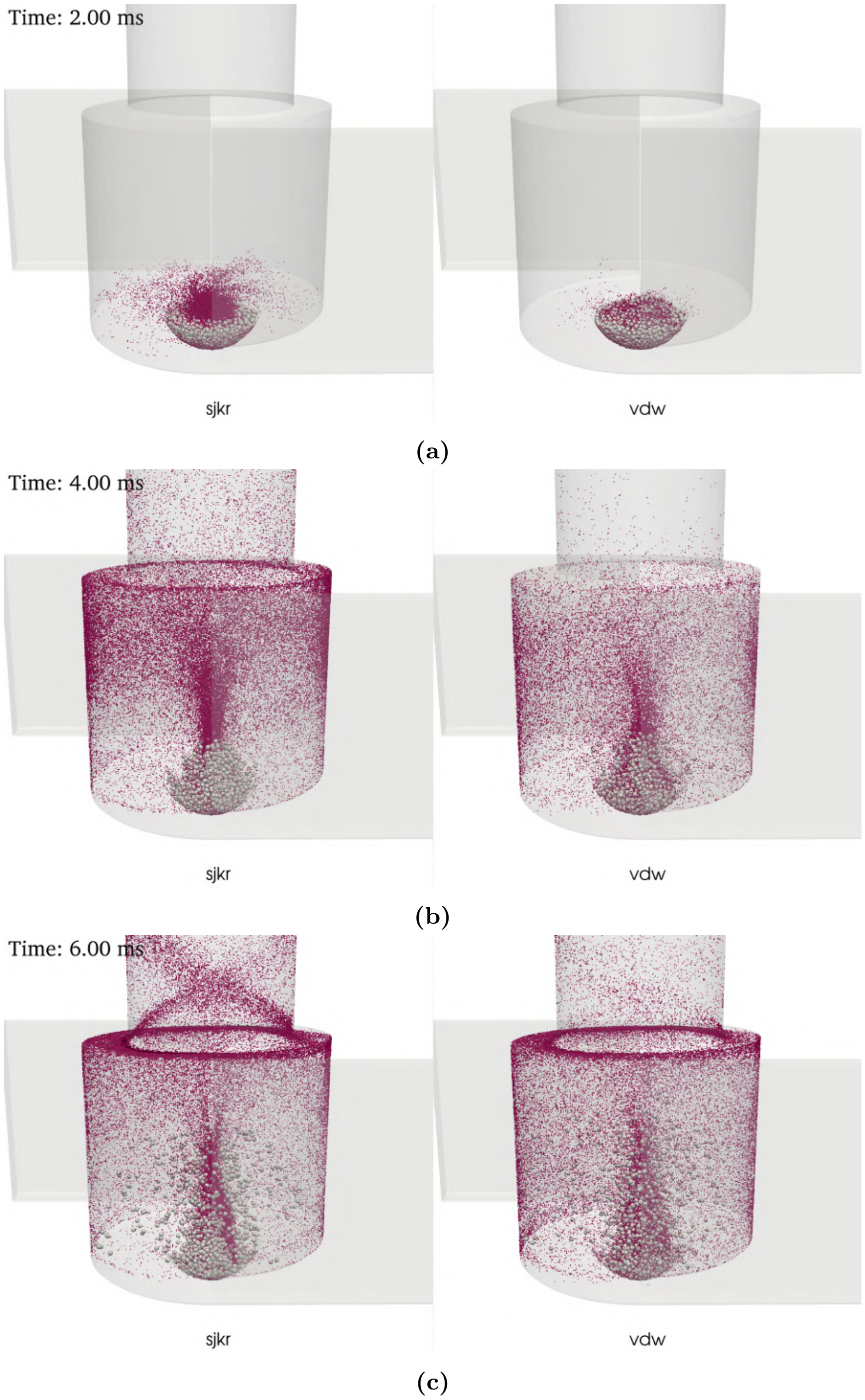

Figure 6.13: Position of particles in the simulations with VDW and SJKR cohesion model at a) 2 ms, b) 4 ms, c) 6 ms. Inlet gas flowrate is 40 L/min. API particles enlarged 4 times to improve visibility.

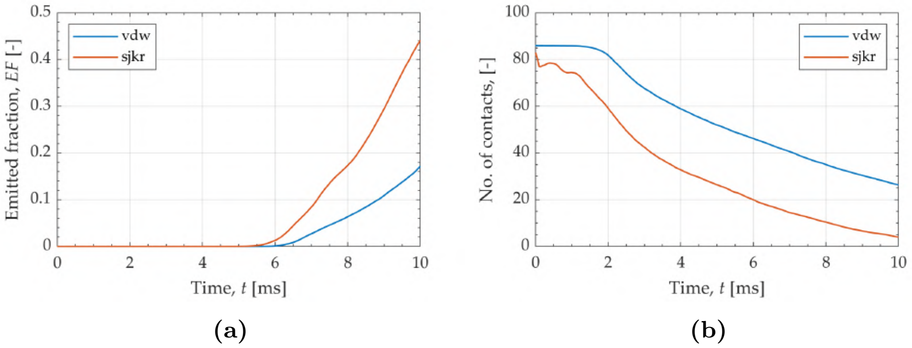

(a) **(b)**

Figure 6.14: a) Particles exiting the system and b) number of API particles in contact with a carrier for simulations with VDW and SJKR cohesion model. Inlet gas flowrate is 40 L/min.

Figure 6.15: Initial position of particles in the simulation with 5% API dosage (w/w).

this trend could reverse later, it is still an indication of the greater difficulty in fine powder emission that is observed when the dosage is higher.

To evaluate in what form the active ingredient is emitted in this first phase, a clustering algorithm has been applied to the particles located near the outlet section (up to 0.5 cm below the outlet section). Figure 6.17a shows the percentage of API particles near the outlet section that are fully deaggregated (i.e., not in contact with any other particle). Although most of the API particles emitted in this first phase are in deaggregated form, a clear decreasing trend is observed in the 5% dosage simulation, meaning that some of the API exits as an agglomerate. Figure 6.17b shows the number of API particles detected near the outlet section in aggregated form, i.e., in contact with other particles. The plot shows the ratio between the number of aggregated particles in the two simulations (1:80 at 10 ms) is far greater than the ratio between the weight dosages (1:5).

The simulation with the 5 % dosage was particularly expensive from the point of view of the computational load. The simulation of 10 ms on 64 cores took about 20 days. The post-processing phase also required special

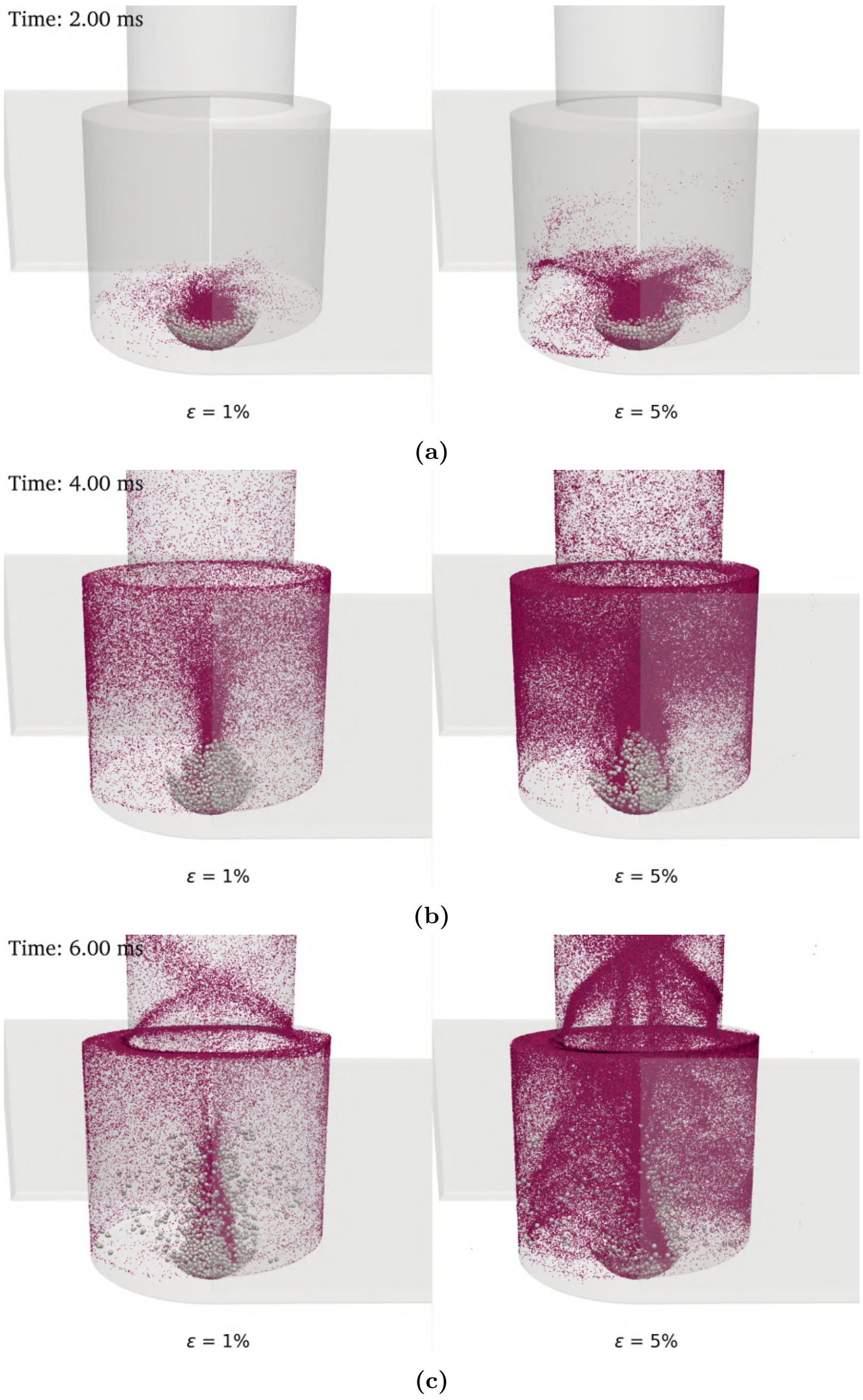

Figure 6.16: Position of particles in the simulations with 1% and 5% weight dosage of API particles at a) 2 ms, b) 4 ms, c) 6 ms. Inlet gas flowrate is 40 L/min, cohesion model is SJKR. API particles enlarged 4 times to improve visibility.

attention and significant computing resources, given the larger number of particles. For this reason, no further simulations have been performed with this configuration.

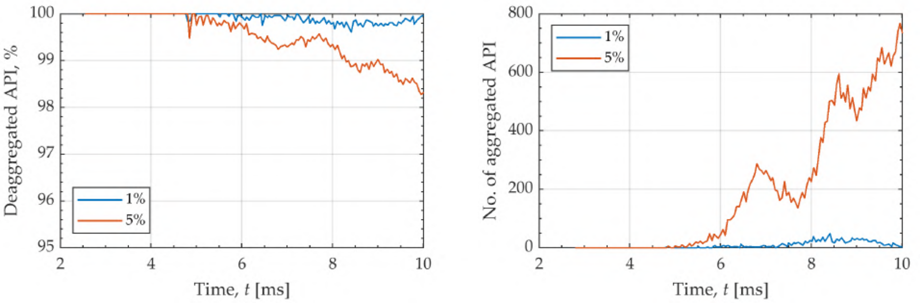

(a) **(b)**

Figure 6.17: Application of agglomerate detection algorithm near the outlet section. a) Percentage of API particle fully deaggregated (i.e., not in contact with any other particle), b) number of API particles in aggregate form. Inlet gas flowrate is 40 L/min.

6.7.4 Drag model

The drag model used in the simulations presented so far is Gidaspow blend, already presented in Section 2.4.1.5. In this drag model, polydispersion is not taken into account, i.e., the fact that the powder is composed of particles of different diameters. Given that the mixtures used in carrier-based DPI consist of powders of very different diameters (in the case considered, the carrier is 20 times larger than the API), it was decided to carry out a test with the CDD drag model (see Section 2.4.1.6), suitable for polydisperse systems as it takes into account the polydisperse correction factor (PCF). The model has been implemented in the in-house version of the MFiX code.

The tests are related to the system already illustrated, with 10 mg of powder of which 1% by weight is API. The particle diameters are 200 μm for the carrier and 10 μm for the API and the flow rate is 60 L/min. The cohesion model is VDW.

Figure 6.18 shows the comparison between two critical frames of the detachment phase (deaggregation) of the API from the carrier obtained by only changing the drag force model.

The use of the polydisperse model influences the detachment process and therefore the deaggregation of the fine powder from the carrier surface. This is due to the fact that in the presence of solids with significantly different diameters, as in this case, the surface area per unit of volume perceived by fine particles is less than that which they would have if they were in a monodisperse bed with the same porosity. On the other hand, due to the

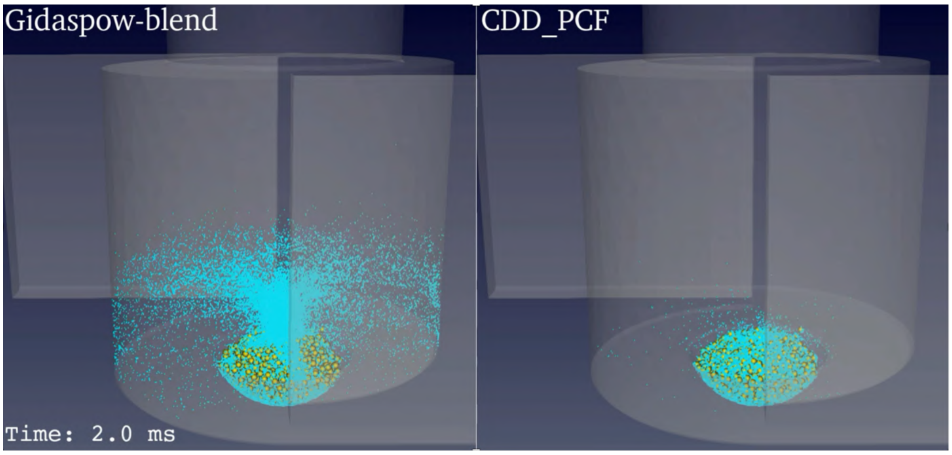

Figure 6.18: Comparison between the positions of the particles after 2 ms from the activation of the air flow obtained with the monodisperse (Gidaspow-blend) and polydisperse (PCF) drag model.

presence of the fine solid, the surface area per unit of volume perceived by the coarse solid is greater. These differences result in a reduction (compared to the monodisperse case) of the effective force on the fine particles and an increase on the coarse ones, as shown in Figure 6.19, where the mean value of the drag force on API (Figure 6.19a) and carrier (Figure 6.19b) particles during the two simulations is reported.

As a consequence, the amount of API expelled from the device is slowed down (Figure 6.20a), while the coordination number of the carrier (number of API particles attached to any carrier particle) is higher (Figure 6.20b),confirming that a greater proportion of API is not easily detached from the carrier surface.

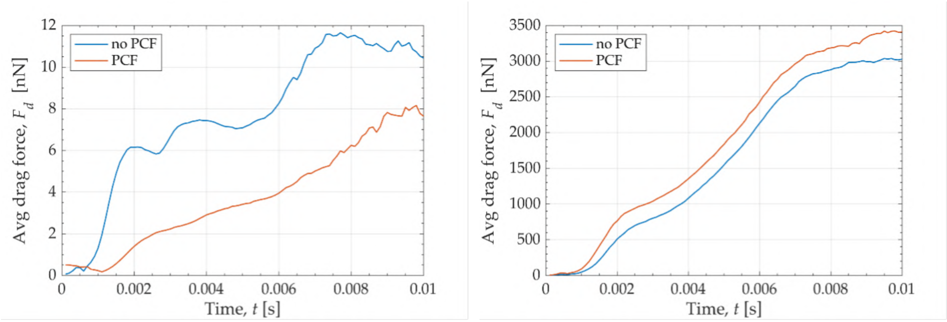

(a) **(b)**

Figure 6.19: Time evolution of the average drag force acting on API (a) and carrier (b) particles using the polydisperse (PCF) or monodisperse (no PCF) model.

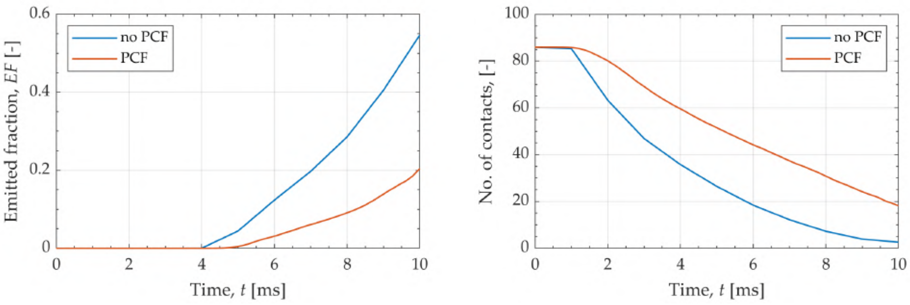

(a) **(b)**

Figure 6.20: Percentage of emitted API particles (a) and average number of API particles adhering to the carrier as a function of time as the drag model varies, polydisperse (PCF) and monodisperse (no PCF).

6.8 Variable inhalation profile

In Section 4.7.5, the release of carrier particles was analyzed considering a realistic inhalation profile instead of a step, costant flowrate inlet gas profile. The P50 realistic inhalation profile (Figure 4.19) has also been used as a boundary condition in a simulation with both API and carrier solid phases.

Figure 6.21 shows the positions of the API (purple) and carrier (white) particles at different instants of time in the simulation with the P50 profile. As already observed in the simulation with carrier only, with the realistic aspirometric profile the times are dilated and it was necessary to extend the simulation up to 250 ms to be able to visualize the different phases of the powder dispersion.

The images in Figure 6.21 are placed horizontally, in the sense in which the patient inhales. The force of gravity is directed vertically, downwards. It can be observed how, at the beginning, the particles indeed tend to move downwards, due to gravity. In the simulations with constant flow rate (step), the weight force was irrelevant, as the powder lifting by the air flow took place instantaneously. With the P50 profile, however, the drag force is very low at the beginning of the simulation (see the fluid streamlines shown in Figure 4.22), so the weight force prevails (Figure 6.21a and Figure 6.21b). A consistent effect of the airflow on powder motion is visible only after about 40 ms (Figure 6.21c). It can also be noticed how, unlike the simulation with the step profile (Figure 6.10), after carrier lifting from the cup, the API is still mostly adhered to the carrier particles. The detachment from the carrier seems to occur later (Figure 6.21d), probably due to carrier-wall and shear drag, as the cyclonic motion is developed at 50 ms. After 100 ms (Figure 6.21f), a consistent amount of powder is still rotating in the swirl chamber.

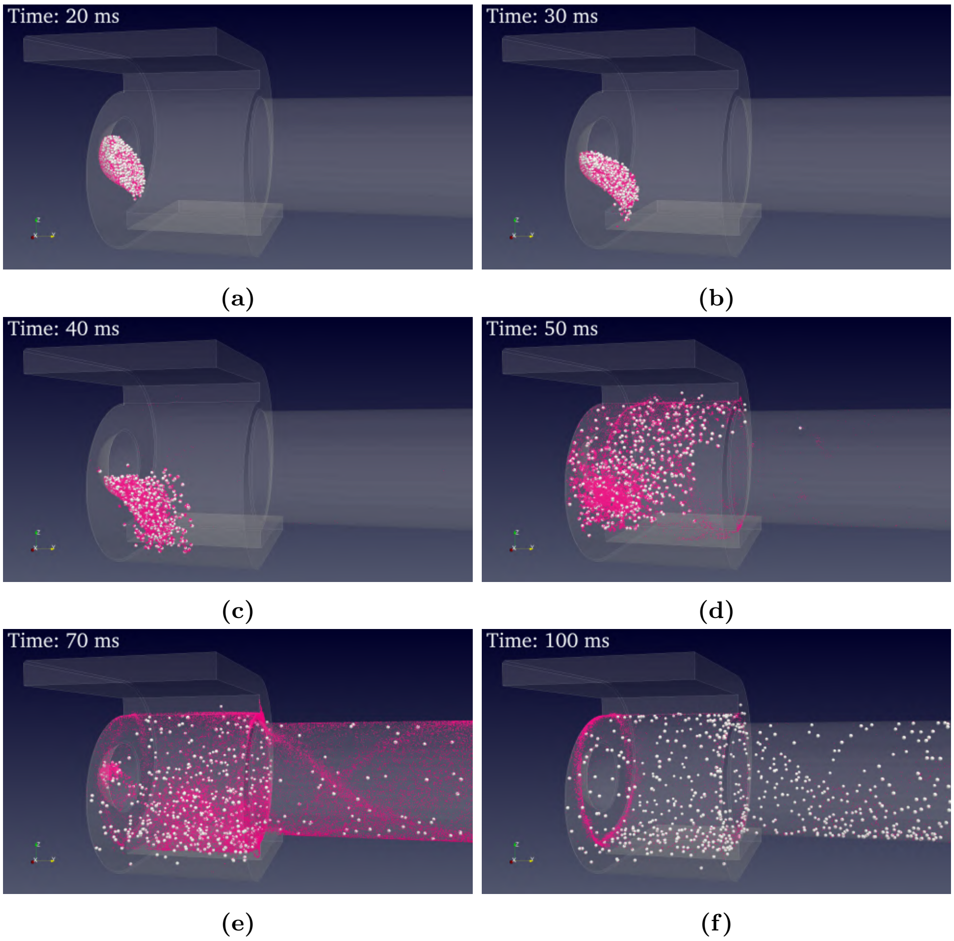

Figure 6.21: Snapshots of particle position at different times: a) 20 ms, b) 30 ms, c) 40 ms, d) 50 ms, e) 70 ms, f) 100 ms. Enlarged API to improve visibility. Gravity is directed in $-z$ axis.

Table 6.3 shows the instants of time at which a certain percentage of API particles has been emitted, from 10% (t_{10}) up to 99.9% (t_{100}). The release of API particles occurs more slowly with the P50 profile. The first API particle leaves the system after 49 ms and the 10 % of released particles is reached only after 70 ms, while in the simulation with step profile this had already happened at 6 ms.

As already noted looking at Figure 6.21, the deaggregation dynamics also occur in a different way. Figure 6.22a reports, for the two simulations step and P50, the average number of API particles adhered to the carrier, while Figure 6.22b reports the mean Bond number (i.e. the ratio between cohesive force and weight force) as a function of time. In the P50 test, the average number of API adhered to carrier begins to decrease consistently only after 50 ms, falling below 10 no earlier than 100 ms. The trend of the

	step	**P50**
t_{10}	5.7	70.8
t_{20}	7.0	73.6
t_{30}	8.1	76.2
t_{40}	9.0	78.0
t_{50}	9.7	79.9
t_{60}	10.4	82.1
t_{70}	11.3	84.6
t_{80}	12.8	89.1
t_{90}	16.2	100.5
t_{100}	45.4	210.0

Table 6.3: Exit percentiles of API particles with step and P50 inhalation profiles. t_x = time at which the emitted fraction of the API particles is $x\%$. All times are expressed in milliseconds (ms).

cohesive forces, represented by the Bond number, confirms the path. It is interesting to note that, unlike the average number of APIs adhered to the carrier, the trend of the Bond number shows a subsequent increase in both simulations. This could be due to the formation of API agglomerates or to the emission of a large part of the API which is in a completely deaggregated form.

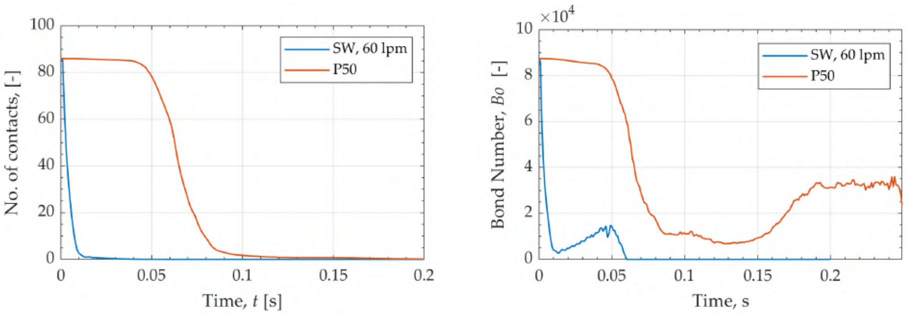

(a) **(b)**

Figure 6.22: Mean number of API particles adhered on a carrier a) and mean Bond number (ratio between cohesive force and weight) for simulations with step (60 L/min) and P50 inhalation profiles.

It is therefore interesting to see what happens near the outlet section. Figure 6.23 shows snapshots near mouthpiece exit for step and P50 simulations at times t_{25}, t_{50}, t_{75}, t_{100}. As in Table 8.6, t_x represents the time at which the emitted fraction of the API particles is $x\%$. The snapshots are therefore not presented at the same instants of time, but with the same percentage of emitted API.

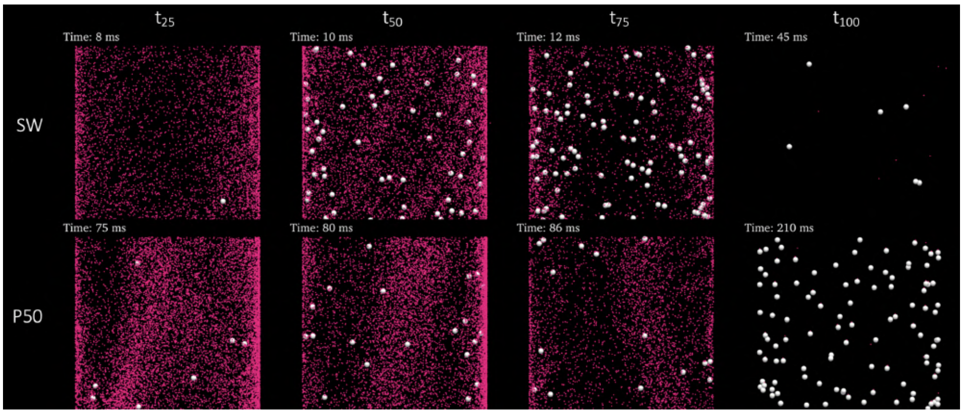

Figure 6.23: Snapshots near mouthpiece exit for simulations with constant flowrate profile, 60 L/min (step) and variable inhalation profile (P50) at times t_{25}, t_{50}, t_{75}, t_{100}. t_x = time at which the emitted fraction of the API particles is x%.

To quantify how much of the API leaves the system in a completely deaggregated form (i.e., as a single particle, not in contact with other API particles), a clustering algorithm was used, applied just below the output section, in the area represented in the snapshots of Figure 6.23.

The graph in Figure 6.24 shows the percentage of API that exit in deaggregated form for the two simulations step and P50 as a function of time.

The step curve shows that part of the API exits as an agglomerate during the first emission peak (at about 10 ms); otherwise, the API comes out almost completely in deaggregated form. Completely different situation that of the P50 simulation, in which a completely deaggregated API percentage of 100 % is never observed and for most of the simulation the percentage is around 40 %

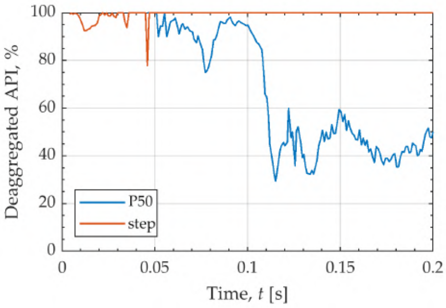

Figure 6.24: Percentage of API particles near the outlet section fully deaggregated.

The results obtained show once again how a strong initial acceleration of the fluid can play a decisive role not only in particle release, but also in the deaggregation process.

In these explorative simulations, a number of aspects still remained rather simplified, such as the size and shape distribution of the particles, the unresolved flow field in the proximity of the carrier-API interface, the boundary conditions corresponding to inhalation profiles. Together with adhesion/cohesion parameters, these may be partly responsible for a deaggregation process that appears too quick and complete than observed in real devices, for example compared to the known limited efficiency of DPIs. Further investigation will be presented later on.

Chapter 7

Capsule-based DPI

In this Chapter, the simulation work on a capsule-based Dry Powder Inhaler, Cyclohaler (Section 3.3.2) will be presented.

The presented work was done in collaboration with the University of Magdeburg, as part of a research period abroad carried out through the Erasmus+ project.

7.1 CFD modelling of the Cyclohaler

CFD simulation have been carried out on the inhaler using the open source software OpenFOAM.

7.1.1 Simulation setup

The motion of particles inside the inhaler is directly correlated to the inlet gas flowrate generated by the inhalation of the patient (Coates et al., 2005b; Lindert et al., 2014), so it is important to select a realistic inhalation profile as a reference.

A generalized curve for the inhalation profiles, tested for different dry powder inhalers, has been reported by Byron et al. (2014). The inspiratory flowrate, Q, as a function of time, t, can be expressed by the following:

$$Q\left(t\right)=\begin{cases} PIFR\cdot\sin\left(\frac{\pi}{2}\frac{t}{T_{PIFR}}\right), & 0\leq t<T_{PIFR} \\ PIFR\cdot\cos\left[\frac{\pi}{2}\frac{(t-T_{PIFR})}{(T-T_{PIFR})}\right], & T_{PIFR}\leq t<T \end{cases} \tag{7.1}$$

where T is the total inhalation time, $PIFR$ is the inspiratory peak (in L/min) and T_{PIFR} is the time at which the inspiratory peak occurs.

The inspiratory peak is inversely proportional to the resistance coefficient of the inhaler, R:

$$PIFR\left[\frac{l}{min}\right] = 1.82\left(\frac{1}{R}\right) + 21 \tag{7.2}$$

while the total inhalation time, T, depends on the inspiratory peak, $PIFR$, and the total volume of inhalation, V:

$$T\,[s] = \frac{30\pi V}{PIFR} \tag{7.3}$$

The volume of inhalation, V, and the time of the inspiration peak, T_{PIFR}, are independent on the inhaler and, for a healthy adult patient, their average values are, respectively: 2.66 L, 0.493 s (Byron et al., 2014). The resistance coefficient is a characteristic property of each inhaler and depends on its geometry (Hoppentocht et al., 2014). The resistance coefficient of the Cyclohaler is 0.022 kPa$^{0.5}$ L^{-1} min (Weuthen et al., 2002). Substituting this value of the resistance coefficient in Equation 7.2, an inspiration peak of 104 L/min can be calculated. The corresponding inhalation profile, calculated according to Equations 7.1 and 7.3, is reported in Figure 7.1.

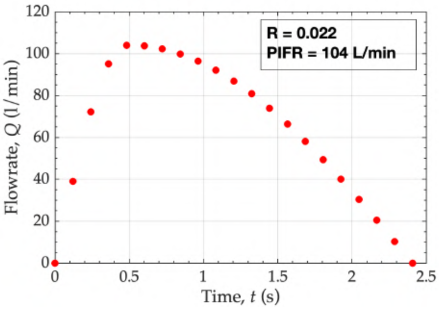

Figure 7.1: Inhalation profile for the Cyclohaler calculated according to Byron et al. (2014).

In order to have an appropriate outflow velocity profile at the exit of the mouthpiece, the mouthpiece was considered twice as long, adding to it an extension having the same diameter. A uniform velocity condition along the whole section was considered at the extension output, according to the selected time-dependent inhalation profile. In this way, at the actual height of the outlet (i.e., without considering the extension) there will be a velocity profile like that of a pipe flow. The extension of the mouthpiece was not taken into consideration in the post processing operations.

For the inlet sections, ambient pressure has been set as boundary condition. The LES-WALE model is used to model turbulence.

7.1.2 Fluid flow

Figure 7.2 shows fluid streamlines coloured according to the gas velocity magnitude for different time instants.

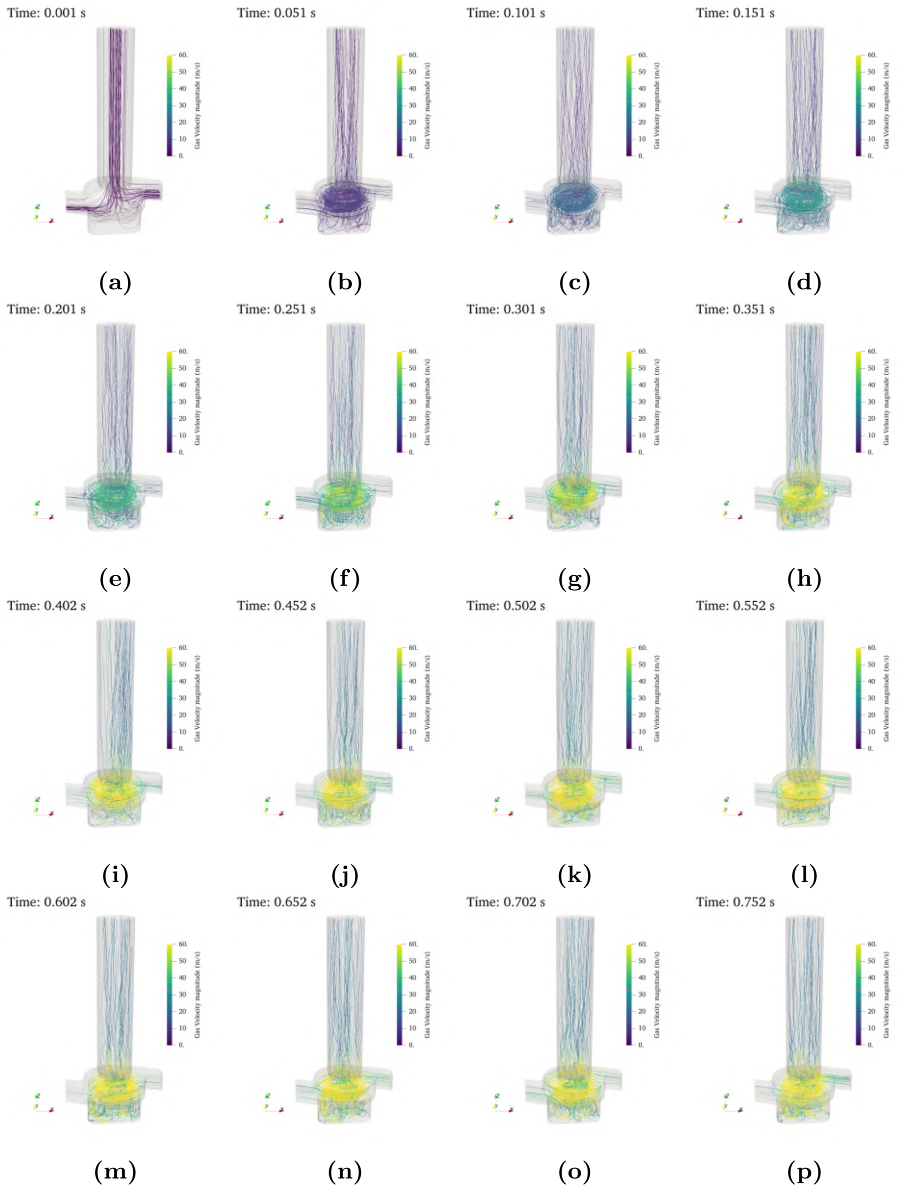

Figure 7.2: Fluid streamlines coloured according to gas velocity magnitude at different time instants.

It is observed that the formation of the vortex motion takes 50 ms, similarly to what was observed with the other geometry considered (Figure 4.22). Fluid velocities increase over time according to the increasing outlet flowrate.

7.1.3 Model validation

Measurements of velocity profile at the outlet of the Cyclohaler were carried out by Laser Doppler Anemometry (LDA) at Martin Luther University of Halle-Wittenberg (Li et al., 2015).

The results obtained from the simulation were compared with the results obtained experimentally. To make this comparison, the time average of 40 time instants from the simulation were considered, from 0.20 ms to 0.24 ms. The interval was chosen considering at what instant of time the fluid flow rate is equal to 72 L/min, which is the flow rate considered in the experiments.

The comparison is shown in Figure 7.3. A good agreement is observed between the simulation and experimental results.

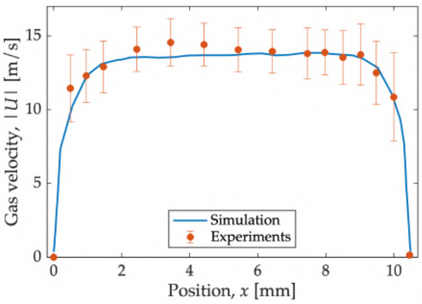

Figure 7.3: Comparison between simulation and experiments.

7.1.4 Comparison with constant flowrate

To evaluate the effect of the time-dependent inhalation profile, a transient simulation with constant flowrate (60 L/min) has been carried out. Figure 7.4 shows the calculated resistance coefficient as a function of time for variable inhalation profile and constant flowrate.

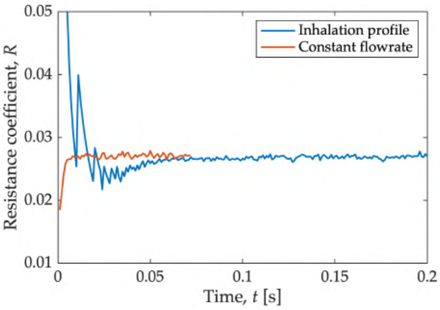

Figure 7.4: Resistance coefficient of the Cyclohaler as a function of time for variable inhalation profile and constant flowrate.

A transient phase is observed in both simulations, even though its duration is much shorter in the case of the constant flow simulation. In both cases, the final value of the R coefficient stabilizes at 0.0266 kPa$^{0.5}$ L^{-1}min, although the flow rates are different and even variable over time in the first simulation.

Interestingly, although the inhalation profile was constructed with the procedure presented in Section 7.1.1 using $R = 0.022$ kPa$^{0.5}$ L^{-1} min as a reference, a higher R coefficient is obtained from the simulation results.

7.1.5 Comparison of turbulence models

The velocity field obtained from the transient simulation with the LES turbulence model was compared with the results previously obtained with a stationary simulation (flow rate 60 L/min) carried out with the $k-\varepsilon$ turbulence model, kindly provided by the research group at the University of Magdeburg. The results were obtained considering the same geometry and mesh, as well as the same pressure boundary condition for the fluid inlet sections.

The results of the stationary simulation ($k-\varepsilon$) were compared with the results of the transient simulation (LES) at 0.19 s, when the fluid flow rate is about 60 L/min.

Comparison snapshots of the velocity field are shown in Figure 7.5 (vertical slice), Figure 7.6 (horizontal slice, near the grid), Figure 7.7 (horizontal slice, swirl chamber) and Figure 7.8 (horizontal slice, outlet section).

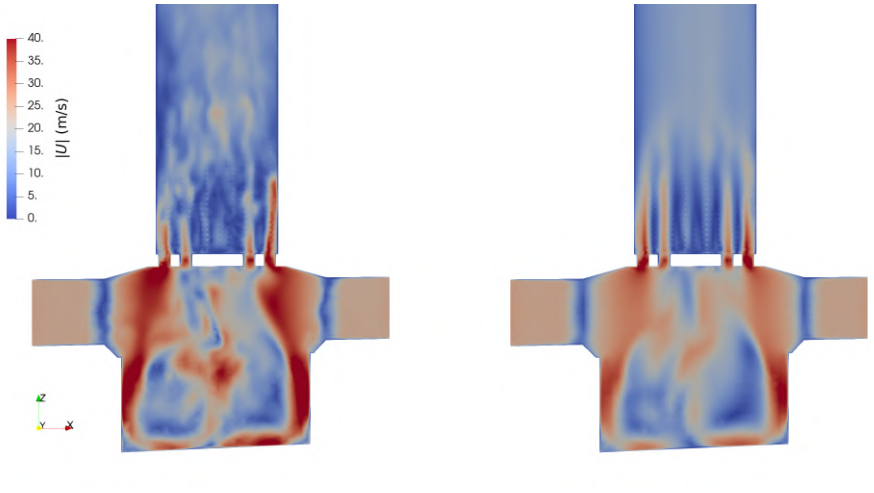

(a) (b)

Figure 7.5: Vertical slice of gas velocity for simulations with a) $LES-WALE$ turbulence model and b) $k-\varepsilon$ turbulence model. Inlet flowrate is 60 L/min.

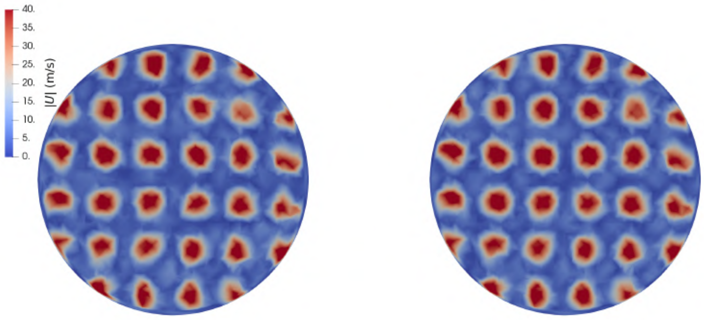

(a) (b)

Figure 7.6: Gas velocity above the grid for simulations with a) $LES - WALE$ turbulence model and b) $k - \varepsilon$ turbulence model. Inlet flowrate is 60 L/min.

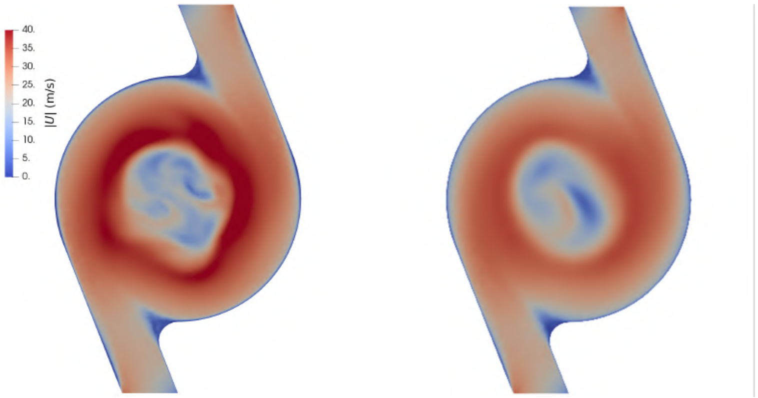

(a) (b)

Figure 7.7: Gas velocity in the swirl chamber for simulations with a) $LES - WALE$ turbulence model and b) $k - \varepsilon$ turbulence model. Inlet flowrate is 60 L/min.

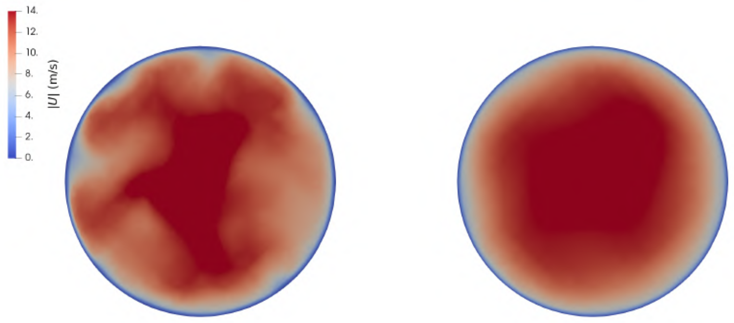

(a) **(b)**

Figure 7.8: Gas velocity near the outlet section for simulations with a) $LES-WALE$ turbulence model and b) $k-\varepsilon$ turbulence model. Inlet flowrate is 60 L/min.

The velocity fields calculated by the two simulations are very similar. However, it can be observed the greater detail that can be obtained with the LES approach, as only the smallest vortices are modeled, while larger vortexes are explicitly calculated.

Observing in particular Figure 7.5, it can be seen how the flow lines in the mouthpiece, following the passage of the fluid through the grid, are not straight as in the results obtained with the RANS approach.

7.1.6 Lagrangian tracking

Lagrangian tracking simulations were performed considering a diluted system, to evaluate the trajectories of particles moving in a turbulent flow.

In the previous chapters it has already been observed how considering a realistic inhalation profile, which takes place within seconds, leads to extended powder emission times. To avoid too long simulation times, it was decided not to consider the realistic profile, but to rely on a situation of constant flow, in order to obtain results relating to the motion of the particles in a few milliseconds of simulation. The properties of the particles and their initial position are represented in Figure 7.9.

Three Lagrangian tracking simulations were performed:

- 100 μm particles, frozen flow (F100);
- 50 μm particles, frozen flow (F50);
- 100 μm particles, transient flow (T100);

Np	1024
D (μm)	50 - 100
ρ (kg/m³)	2500
μ_s (-)	0.1
μ_r (-)	0.1
e (-)	0.9

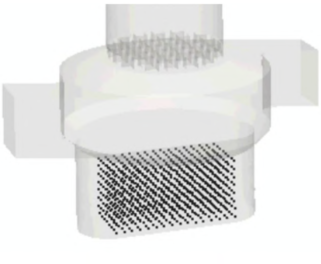

Figure 7.9: Particle properties used in Lagrangian tracking simulations and initial position of particles in the capsule holder.

The constant flow rate simulation (T100) was performed with the conditions presented in Section 7.1.4; the flow field of the fluid is transient, the fluid flowrate is instantly set to 60 L/min.

For the two frozen flow simulations (F50 and F100), on the other hand, the flow field of the fluid represented in Figures 7.5a, 7.6a, 7.7a and 7.8a is considered, and it is fixed, frozen; the fluid does not evolve in the course of the simulation, and its field of motion is static, albeit instantly swirling. Also in this case the fluid flow rate is 60 L/min.

For the Lagrangian tracking simulations, a customized version of the code provided by the research group of the University of Magdeburg was used. The following forces act on particles due to the interaction with the fluid: gravity, Wen-Yu drag force with wall correction, Saffman lift force, Magnus lift force. A turbulent dispersion model specific for LES is also used (Stochastic Langevin dispersion equation, Sommerfeld (2008)).

Only collisions between particles and walls are considered and the rebound particle velocity is calculated as:

$$U_{res} = U - (1+e)U_n n_w - \mu_s U_t \tag{7.4}$$

with U being the particle velocity before the collision, U_n the magnitude of the wall normal velocity component, U_t the velocity magnitude in direction parallel to the wall, n_w the wall normal vector, e the restitution coefficient, and μ_s the friction coefficient.

Two-way coupling, i.e., the influence of the particles on flow field and turbulence, is neglected.

7.1.6.1 Powder emission

The trajectory of a particle selected in the T100 simulation is represented in Figure 7.10. It is observed that the selected particle completes several rotations in the swirl chamber, and then exits the moutphiece with a weakly helical trajectory.

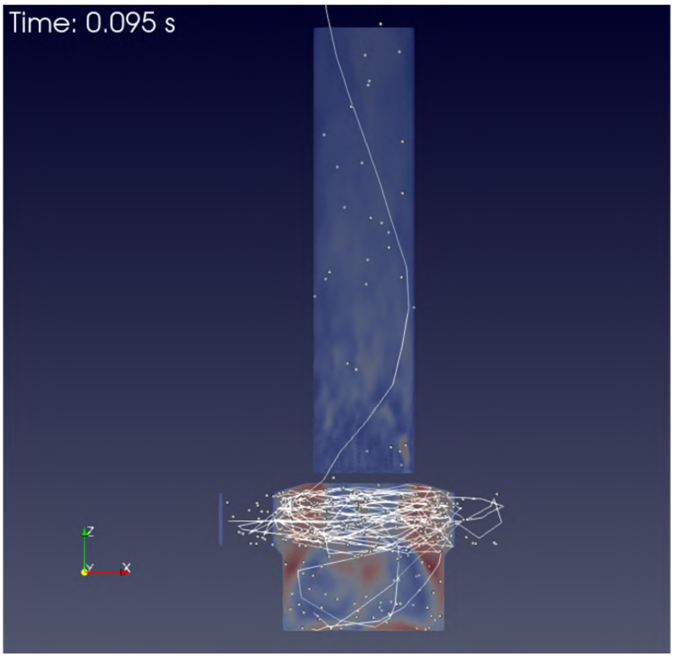

Figure 7.10: Trajectory of a particle in the first 95 ms (simulation F100).

A similar path is observed for most of the particles in all three simulations considered. However, there are some particles that come out from the two inlet sections, tangential to the swirl chamber.

The table shows the percentage of particles that come out of the inlet and outlet sections for the three simulations in 0.5 s. If for the F50 simulation the percentage of particles that come out of the inlet sections does not reach 22%, in the T100 and F100 simulations (in which the diameter of the particles is larger) this percentage rises up to almost 50%.

	F100	**F50**	**T100**
Outlet	51.3%	78.3%	59.4%
Inlet1	27.9%	11.2%	20.2%
Inlet2	22.7%	10.5%	22.6%

Table 7.1: Percentage of particles that exit the system from outlet section and inlet section for the three Lagrangian tracking simulations: 100 μm particles, frozen flow (F100); 50 μm particles, frozen flow (F50); 100 μm particles, transient flow (T100).

The motivation for this phenomenon could be the same that was observed in analyzing the results presented in Section 4.7.4, in which a 1-way coupling approach was considered in the CFD-DEM simulation of carrier particles.

Figure 7.11 shows direction of particle velocity at 6 ms in the T100 simulation. It is observed how the motion of the fluid leads the particles to quickly spread outwards, precisely in correspondence with the inlet sections. The 100 micron particles, having greater inertia, do not follow the fluid flow lines, according to which they should move towards the outlet, but continue to be pushed outwards due to the centrifugal force. The phenomenon is probably less evident in simulations with smaller particles (F50) for this very reason.

Figure 7.11: Direction of particle velocity at the beginning of the simulation (simulation T100).

The overall emission curve for the three tests, shown in Figure 7.12, is however similar in all the cases considered. The complete emptying of the inhaler occurs in about 0.5 s, with a 1st order, exponential profile curve.

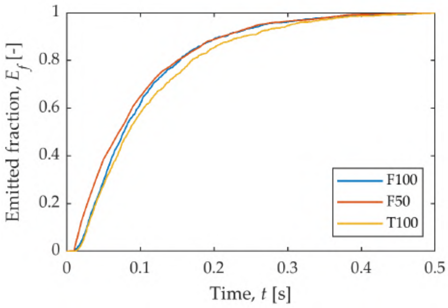

Figure 7.12: Emitted fraction of particles for the three simulations.

7.1.6.2 Collision statistics

The particle-wall collisions occurred in the three simulations were recorded and post-processed.

Figure 7.13 shows the location of all particle-wall collision events that occurred in 500 ms for F100 simulation (frozen flow, 100 μm particles). Points are coloured according to impact velocity. Most impacts and at higher velocities occur in the swirl chamber.

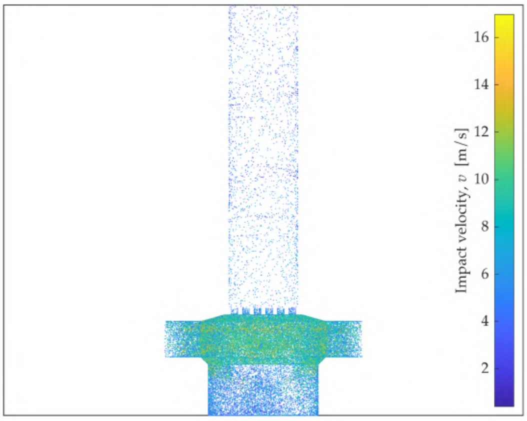

Figure 7.13: Location of all particle-wall collision events that occurred in 500 ms for F100 simulation (frozen flow, 100 μm particles). Points are coloured according to impact velocity.

A similar map is also obtained for the other two simulations. No significant differences were observed in the number of collisions and impact velocity between the T100 and F100 simulations. The F50 simulation, on the other hand, is characterized by a higher number of impacts (about 33% more) and higher impact velocities, which exceed 22 m/s.

Once the collision data is known, an approximate estimate of the dispersion phenomenon can be made, assuming that the particles studied are carrier particles covered by API.

Ariane et al. (2018) developed a simple model based on DEM to estimate how much API is detached from a carrier after a wall collision (see Figure 1.9). The model is based on the evaluation of the dispersion ratio, η, which is the ratio between the area of the carrier where API detachment occurs and the total surface area of carrier particles. η is a function of impact angle and impact velocity. It also depends on the physical and mechanical properties of the particles (radius, Young moduli, friction coefficient, cohesion energy).

The sub-scale model has been applied as follows:

- An initial surface coverage, α, is defined for all the carrier particles:

  $$\alpha = \frac{A_R}{A_{TOT}} = \frac{A_R}{N_{part} \cdot \pi D^2} \tag{7.5}$$

  where A_R is the total covered area for all carrier particle and N_{part} is the number of carrier particles;

- For each particle-wall collision, the dispersion ratio $\eta(i)$ is evaluated based on impact angle and impact velocity;
- After the i-th particle-wall collision, the total covered area and total surface coverage are updated as follows:

$$A_R(i) = A_R(i-1) - \eta(i) \cdot \pi D^2 \tag{7.6}$$

$$\alpha(i) = \frac{A_R(i)}{N_{part}(i) \cdot \pi D^2} \tag{7.7}$$

Figure 7.14 shows the result of applying the model, considering an initial surface coverage equal to 0.75. The following physical and mechanical properties were considered for the calculation of the dispersion ratio: reference adhesive force 257 nN, Young's modulus 24 GPa, density 2500 kg/m^3, static friction coefficient 0.2, Poisson coefficient 0.2.

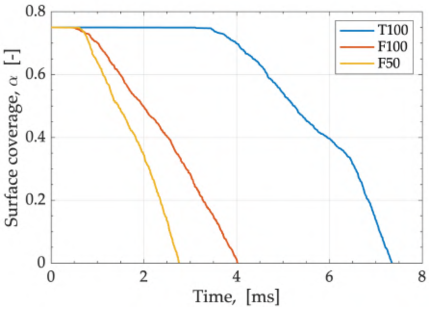

Figure 7.14: Deaggregation estimate according to the sub-scale wall collision detachment model by Ariane et al. (2018).

Although the application of the model is in a very simplified form, the results show that particle-wall collisions occur at impact velocities that cause an almost complete detachment of the API. The average value of the dispersion ratio calculated in the various tests for all impacts is in fact around 80%. Furthermore, it can be observed that in the T100 test, transient with constant flow rate, the deaggregation starts later, since there is an initial settling phase, although short.

7.2 DEM simulation of the motion of particles in the capsule

Detailed DEM simulations on the capsule of the Cyclohaler have been carried out considering a realistic loading with the aim to elucidate the role of cohesion and adhesion forces in determining the motion of the API-coated

	1	**2**
α, rad/s^2	887	-233
ω_0, rad/s	0	560
θ_0, rad	0	-140

Table 7.2: Angular acceleration, initial angular velocity and initial angle for the two traits.

carrier particles during the first instants of the process. The rotating motion of the capsule inside the inhaler is modelled in a non-inertial frame of reference through the introduction of fictitious forces generated during a reference realistic inhalation profile. Both API and carrier particles are included in the simulation, yielding useful insights on the role of the capsule in the deaggregation process.

7.2.1 Rotating motion of the capsule

The angular velocity of the capsule, ω, increases linearly with the flowrate, Q (Coates et al., 2005b). The linear dependency can be expressed by the following (Benque and Khinast, 2019):

$$\omega\,[rpm] = 42.34 \cdot Q \;\; [lpm] \tag{7.8}$$

The trend of the flowrate as a function of time (shown in Figure 7.1) can be represented with a good approximation with two linear traits: an increasing line from 0 s to 0.5 s , with the flowrate reaching the peak (104 L/min), and a subsequent decreasing one, from 0.5 s to 2.4 s. With this approximation, the profile of the angular velocity of the capsule can be estimated with a uniformly accelerated circular motion. The angular velocity is given by:

$$\omega \;= \alpha t + \omega_0 \tag{7.9}$$

Where α is the angular acceleration, ω_0 is the initial angular velocity. The capsule rotation angle, θ, is given by:

$$\theta \;= \frac{1}{2}\alpha t^2 + \omega_0 t + \theta_0 \tag{7.10}$$

The profile of angular velocity thus calculated is reported in Figure 7.15a. The parameters are reported in Table 7.2. With these parameters, the capsule completes 85 full rotations in 2.4 s, as shown in Figure 7.15b.

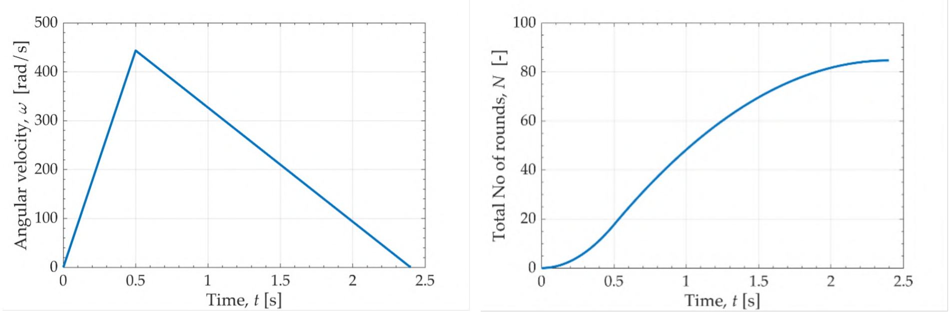

(a) **(b)**

Figure 7.15: a) Angular velocity profile assumed for the capsule, b) number of complete rotations of the capsule as a function of time.

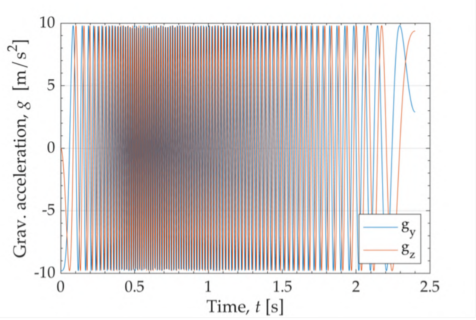

Figure 7.16: Gravitational acceleration components as a function of time

7.2.2 Modelling strategy

The phenomena has been simulated in a rotating frame of reference, by keeping the capsule in a fixed position and assuming that everything else rotates around it. With this approach the obtained results are relative to the rotating frame (i.e. particle positions are relative to a fixed position of the capsule), the highlight is on the forces related to capsule motion (centrifugal, etc.), and there is a high flexibility in the motion patterns. However, advanced post-processing tools are needed to obtain the animation from the point of view of the external, inertial observer.

As the plane of rotation ($y - z$) is parallel to gravity force, the gravity vector needs to rotate according to the angular velocity assumed for the capsule (Equation 7.8). The two components of the gravity forces that follow a periodical motion are reported in Figure 7.16. Rotation of the gravity vector around a user-defined axis of rotation has been implemented in MFIX.

In the non-inertial frame of reference, fictitious forces need to be taken into account: centrifugal force (Equation 7.11), Euler force (related to angular acceleration, Equation 7.12), and Coriolis force (Equation 7.13):

$$\vec{F}_{cen} = -m\vec{\omega} \times \left(\vec{\omega} \times \vec{r'}\right) \tag{7.11}$$

$$\vec{F}_{eul} = -m\frac{d\vec{\omega}}{dt} \times \vec{r'} \tag{7.12}$$

$$\vec{F}_{cor} = -2m\left(\vec{\omega} \times \vec{v'}\right) \tag{7.13}$$

where $\vec{\omega}$ is the angular velocity, $\vec{r'}$ and $\vec{v'}$ are, respectively, the position vector and the velocity vector of each particle in the rotating frame of reference.

These forces are calculated at each solid time step according to the instant value of the angular velocity of the capsule, $\vec{\omega}$, and applied to each particle.

The results can be analysed both in the rotating frame of reference (i.e. fixed capsule) and in the inertial frame of reference (i.e. rotating capsule) thanks to post-processing tools developed in MATLAB, with whom the coordinates and the velocities of particles can be transformed to obtain animations and data seen from an external observer.

The coordinates in the inertial frame of reference ($\vec{r}$) can be calculated from the coordinates in the rotating frame of reference ($\vec{r}'$) from the following:

$$\vec{r} = \vec{r'} \cdot R^T \tag{7.14}$$

R is the rotation matrix:

$$R = \begin{bmatrix} c + u_x^2 w & u_x u_y w - u_z s & u_x u_z w + u_y s \\ u_x u_y w + u_z s & c + u_y^2 v & u_y u_z w + u_y s \\ u_x u_z w - u_y s & u_y u_z w + u_x s & c + u_z^2 w \end{bmatrix} \tag{7.15}$$

with c, s and w functions of the current rotation angle, θ:

$$c = \cos(\theta) \tag{7.16}$$

$$s = \sin(\theta) \tag{7.17}$$

$$w = 1 - c \tag{7.18}$$

and u_x, u_y, u_z are the components of the normalized rotation axis vector.

The velocities of particles in the inertial frame of reference ($\vec{v}$) can be calculated from the velocities in the rotating frame of reference ($\vec{v}'$) as:

$$\vec{v} = \left(\vec{v'} + \vec{\omega} \times \vec{r'}\right) \cdot R^T \tag{7.19}$$

$\mathbf{t_{start}}$ (ms)	$\mathbf{t_{end}}$ (ms)	f_s (Hz)
0	67	30
67	133	60
133	200	120
200	500	180

Table 7.3: Capsule-wall collision frequency considered in the simulations

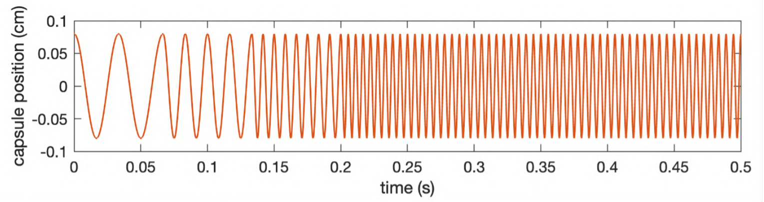

Figure 7.17: Capsule oscillating motion

7.2.3 Collision between the capsule and the inhaler

During the inhalation process, multiple collisions occur between the capsule and the grid of the inhaler (Martinelli et al., 2015). The collision frequency increases with the flowrate following an exponential trend, with a maximum value of 176.4 Hz (Benque and Khinast, 2019).

In the present work, capsule-inhaler collisions have been modelled as vibration along the inhaler longitudinal axis, x. The position of the capsule is described by the following equation:

$$s\left(t\right)=A\sin\left(2\pi f_s t+\phi\right) \tag{7.20}$$

This movement will produce an acceleration $a_s\left(t\right)$ on particles that has been implemented in MFIX as an additional fictitious force:

$$a_s\left(t\right)=\frac{d^2s}{dt^2}=-A\cdot 4\pi^2 f_s^2\sin\left(2\pi f_s t+\phi\right) \tag{7.21}$$

The amplitude of the oscillations, A, has been chosen according to the height of the swirl chamber (A=0.8 mm), while for the frequency four different values have been chosen, in order to have a capsule-wall collision frequency that increases with the flowrate, as reported in Table 7.3. A phase displacement ϕ of 90° has been considered. The resulting motion for the capsule is shown in Figure 7.17.

7.2.4 DEM parameters

The physical and mechanical properties of the particles used in the simulations are reported in Table 7.4. The diameter of the carrier particle,

	Carrier	**Fine**
Reference material	Lactose	Salbutamol
Diameter, d [μm]	100	5
Density, ρ [kg/m^3]	1500	1200
Sliding friction coefficient, μ_s [-]	0.5	0.5
Rolling friction coefficient, μ_r [-]	0.05	0.05
Restitution coefficient, e [-]	0.85	0.85
Young modulus, E [GPa]	0.2	0.2
Poisson's ratio, ν [-]	0.35	0.35
Number of particles	30976	92877

Table 7.4: DEM simulation parameters

100 μm, has been chosen according to InhaLac230®, a lactose commonly used in DPIs[1], while for the API a diameter of 5 μm has been selected, considering the maximum size at which the medication is still considered respirable (Sommerfeld et al., 2019). The mechanical properties are selected according to typical values found in the literature (Nguyen et al., 2018; van Wachem et al., 2017). The Young modulus has been decreased from 1 GPa to 0.2 GPa to reduce the timestep required for the simulation and thus the computational time.

The surface energy values used in the simulations to take into account adhesion and cohesion phenomena are reported in Table 7.5 for each couple of materials interacting. The surface energy, γ, was calculated from pull-off force values found in literature according to the expression of the pull-off force in the JKR model. The values of adhesion force for particle-particle cohesion/adhesion reported by Begat et al. (2004a) for lactose-salbutamol systems were considered, while for particle-wall adhesion reference has been made to the work of Ibrahim et al. (2000), who measured the interaction force between micron-sized lactose particles and gelatin capsules. With the selected values, particle-wall adhesion force is about 1/3 of API-carrier adhesion force, in good agreement to what is found in literature (Ibrahim et al., 2000).

7.2.5 Rotation motion only, free flowing particles

Figure 7.18 shows the initial configuration for the DEM simulation along with the rotation motion of the capsule. The device is in horizontal position when the patient inhales, so the rotation is parallel to the gravity vector. The evolution of particle motion in the rotating capsule is shown in Figure 7.19. As the capsule starts rotating, centrifugal force pushes particles towards the

---

[1] Inhalac® Technical Brochure, Meggle GmbH & Co. KG, Germany

	F [nN]	**γ [mJ/m^2]**
API-API	11	0.93
API-carrier	180	8.02
carrier-carrier	150	0.64
particle-wall	60	2.55

Table 7.5: Cohesion parameters and reference pull-off force value

Figure 7.18: a) Initial position of the particles in the capsule and rotation direction b) position of the filled capsule inside the Cyclohaler inhaler.

holes, promoting capsule emptying.

In Figure 7.20 the cumulative mass of powder that is expelled from the capsule is reported. An initial rapid increase of the emitted mass is followed by a plateau. Almost no particles exit from 0.5 to 2.1 s. It seems that the emission occurs only when the angular velocity is not too high (also reported in the right axis of Figure 7.20); due to the strong centrifugal force, particles are stuck at the ends of the capsule, around the holes. After 2 s, when the angular velocity is lower, the last particles left (about 2 mg) can move from that position and leave the capsule (see Figure 7.19f). The results suggest that the increasing and then decreasing profile of the capsule's angular velocity plays a relevant role in capsule emptying, as also reported by Benque and Khinast (2021): if the angular velocity of the capsule was set at 4500 rpm from the beginning of the simulation, the accumulation would occur instantaneously.

Looking at the mean value of the forces acting on the particles (Figure 7.21), a very strong centrifugal acceleration is observed, that reaches values higher than 150g. The Euler and Coriolis force are in the same order of magnitude of the gravity force. For most of the simulation the centrifugal force is predominant, except for the very beginning and the very end of the simulation (Figure 7.22), when the effect of the other forces is not negligible. This corroborates the hypothesis that the angular acceleration plays a role in powder emission especially in the initial phase.

In the first phase of powder emission, up to about 0.2 s, it is observed that powder release is also controlled by the size of the capsule's holes. Interestingly, the nominal size of the orifices is 0.6 mm, which is exactly

(a) (b) (c) (d) (e) (f)

Figure 7.19: Position of particles in the capsule at a) 0.1 s, b) 0.2 s, c) 0.3 s, d) 0.5 s, e) 2.0 s, f) 2.4 s.

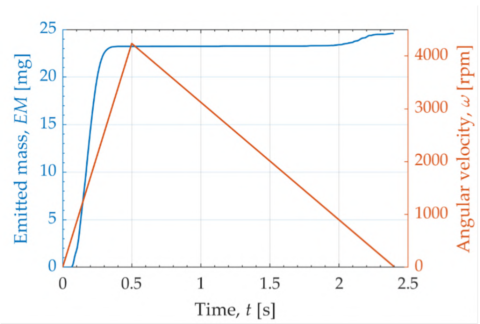

Figure 7.20: Emitted mass (left axis) along with angular velocity profile

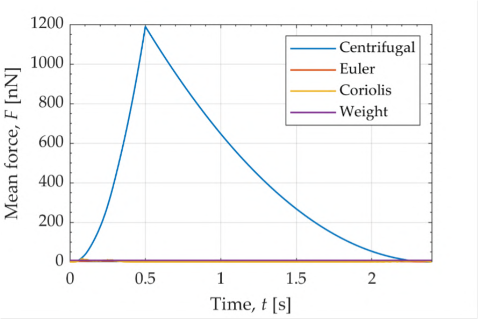

Figure 7.21: Mean fictitious forces (Centrifugal, Euler, Coriolis) acting on particles as a function of time. Weight force is reported as well.

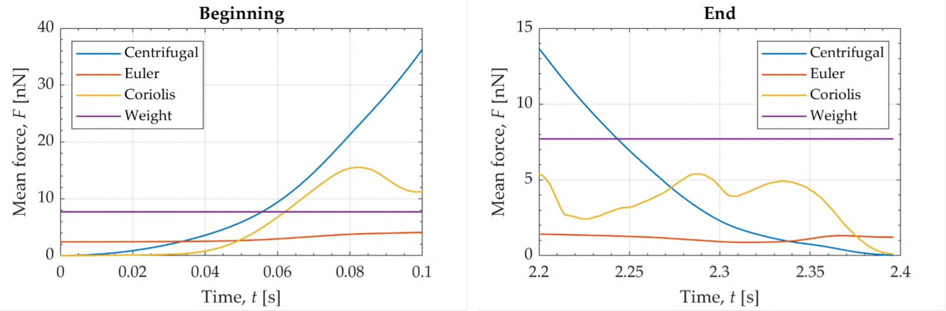

(a) **(b)**

Figure 7.22: Mean fictitious forces (centrifugal, Euler, Coriolis) and weight force at the beginning (a) and end (b) of the simulation.

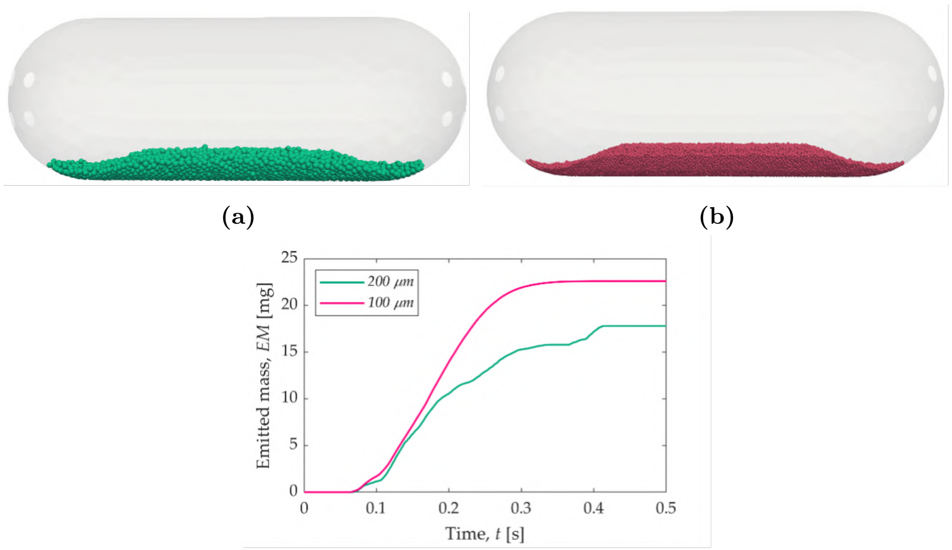

(a) **(b)**

(c)

Figure 7.23: a) Capsule filled with 25 mg of 200 micron particles, b) capsule filled with 25 mg of 100 micron particles, c) emitted mass

six times the nominal size of the carrier particles. This is considered a critical value in powder handling applications such as silos and hoppers; it is reported in literature that for orifices that are less than six particle diameters the flow is intermittent and irreproducible (Nedderman et al., 1982) and could promote obstruction phenomena such as arching (Rhodes, 2008).

A simulation with larger particles (D=200 μm) has been conducted to see if such phenomena could occur. The same mechanical properties (Table 7.4) and capsule movement have been considered, as well as the same initial mass of the powder (25 mg). Figure 7.23c shows the difference in the emitted mass for 200 μm particles (Figure 7.23a) and 100 μm particles (Figure 7.23b) for the first 0.5 s. It is observed that the holes are effectively blocked due to the reduced orifice/particle diameter ratio and the emptying of the capsule takes place with greater difficulty.

7.2.6 Rotation motion only, cohesive particles

It has been observed experimentally (Mitani et al., 2020) that after inhalation some of the powder sticks to the walls of the capsule and clustering and agglomeration phenomena occur. The DEM simulation has been repeated considering the cohesion and adhesion interactions through JKR model with the parameters reported in Table 7.5. Comparing the results thus obtained (C-R) with the free-flowing simulation (FF-R) (Figure 7.24), it can be noticed that the initial emission is slightly delayed and that the plateau in the

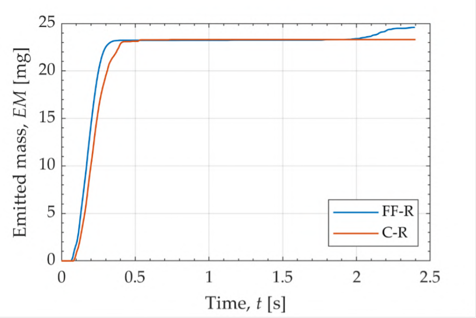

Figure 7.24: Emitted mass for free-flowing particles (FF-R) and cohesive particles (C-R).

emission profile continues until the end of the simulation, meaning that a higher residual is observed in the capsule. The evolution of particle motion in the capsule is shown in Figure 7.25. It is observed that particles start moving later compared to the free-flowing case, as the forces associated with the rotation of the capsule must overcome the particle-wall adhesion forces and particle-particle cohesion forces.

Figure 7.26 shows the accumulation in the capsule in the simulation with and without cohesive/adhesive interactions after 150 ms. The accumulation in Figure 7.26b is not only located near the holes, but also in the centre of the capsule.

7.2.7 Rotation and shaking motion, cohesive particles

As reported in subection 7.2.3, capsule - inhaler collisions are modelled as vibrations along the inhaler longitudinal axis (x). A combined motion of the capsule is considered: shaking along x axis (Figure 7.27b, down) and rotation in the $y-z$ plane (Figure 7.27b, up). Figure 7.27a shows the acceleration related to this shaking motion along with the centrifugal acceleration. The values have been divided by the gravitational acceleration. In the last interval the acceleration related to vibrations is about 100g.

The introduction of capsule vibrations made the motion of the particles more chaotic, as shown in Figure 7.28. The emission profiles (Figure 7.29) show that the capsule is almost completely empty after 0.5 seconds; the simulation could then be stopped after 0.5 s.

7.2.8 Characterization of powder emission

The emission of the powder from the capsule has been analysed for the simulation with both rotation and shaking motion and with cohesive interactions (C-RS). The emission profile (E_f), i.e., the mass fraction emitted from the capsule as a function of time, is well represented by a logistic sigmoidal

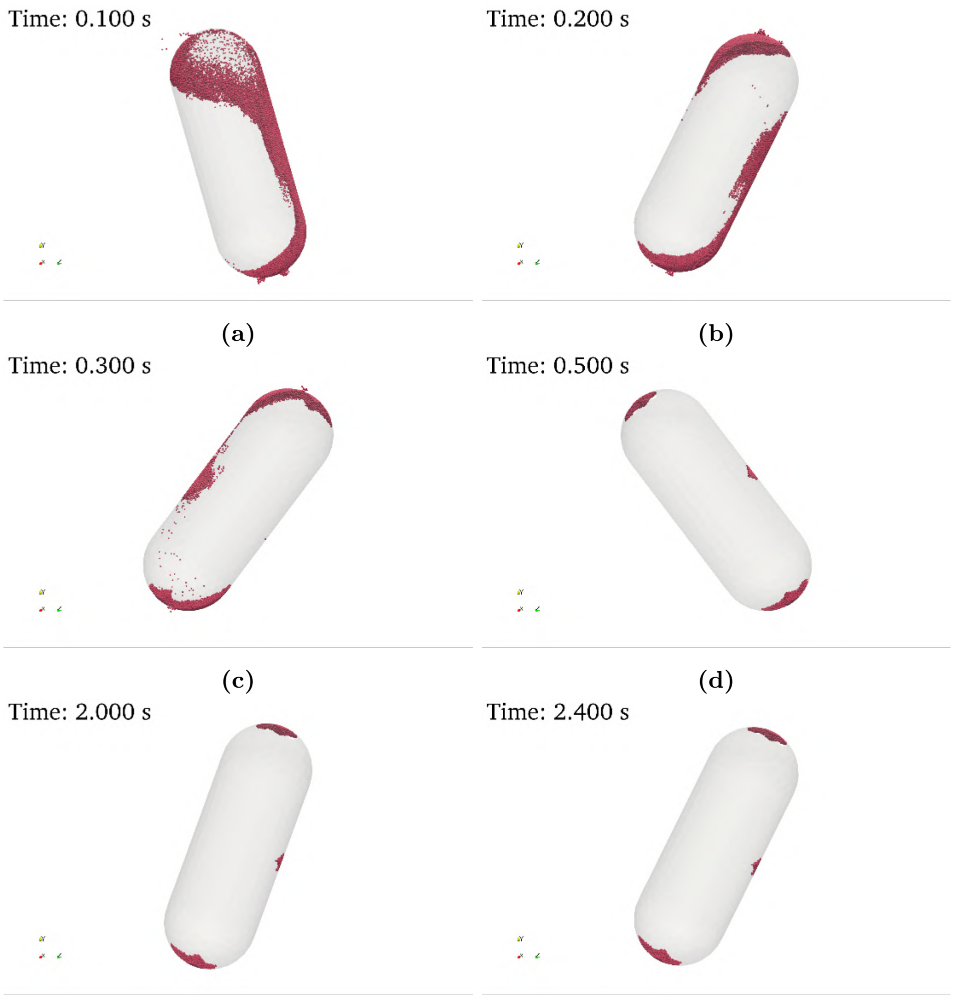

(a) **(b)** **(c)** **(d)** **(e)** **(f)**

Figure 7.25: Position of particles in the capsule at a) 0.1 s, b) 0.2 s, c) 0.3 s, d) 0.5 s, e) 2.0 s, f) 2.4 s.

(a) **(b)**

Figure 7.26: Configuration after 150 ms a) without cohesion, b) with cohesion.

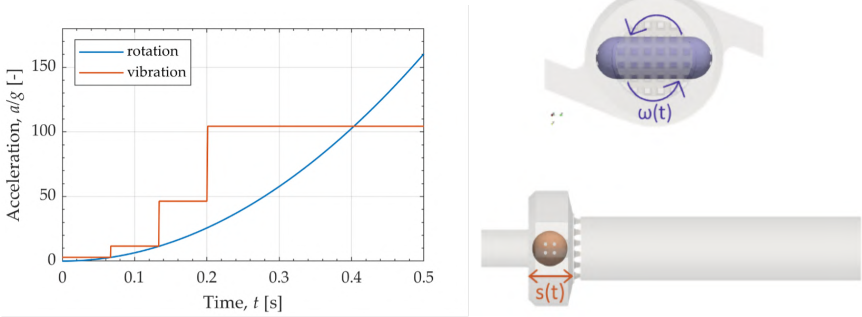

(a) **(b)**

Figure 7.27: a) Comparison between the centrifugal acceleration and the acceleration due to vibrations. Values are divided by g (gravitational acceleration); b) direction of capsule rotation (up) and capsule shaking (down).

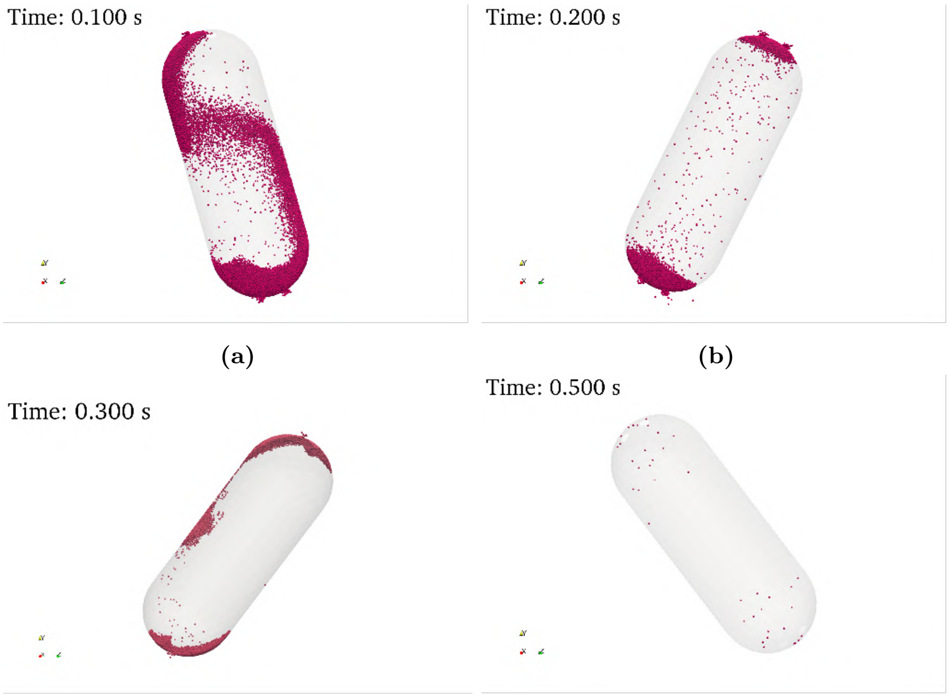

(a) **(b)**

(c) **(d)**

Figure 7.28: Position of particles in the capsule at a) 0.1 s, b) 0.2 s, c) 0.3 s, d) 0.5 s (C-RS simulation).

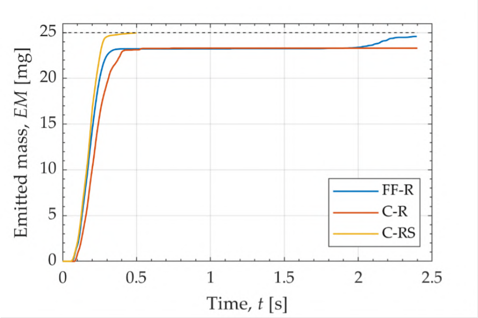

Figure 7.29: Emission profiles: free-flowing (FF-R), cohesive (C-R), cohesive and shaking (C-RS).

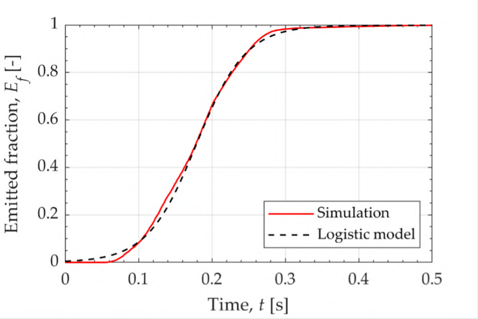

Figure 7.30: Emitted fraction in C-RS simulation and with the logistic model.

model:

$$E_f(t) = \frac{K}{1 + e^{-\frac{t - t_{50}}{t_{empty}}}} \tag{7.22}$$

where K is the saturation level, t_{50} is the median point (the time required to reach $K/2$), and t_{empty} is the characteristic emptying time, that can be calculated as:

$$t_{empty} = \frac{t_{90} - t_{10}}{\ln 81} \tag{7.23}$$

with t_{90} and t_{10} being, respectively, the time required to reach 90% and 10% of the saturation level. The parameters of the logistic model have been calculated from the simulation data; the median point, t_{50}, is 180 ms and the characteristic emptying time, t_{empty}, is around 33 ms. The saturation level, K, is 1. The comparison between the logistic model and the emission profile obtained from the DEM simulations is reported in Figure 7.30.

The emitted fraction profiles from a capsule-based carrier inhaler have been characterized experimentally by Huynh et al. (2015); Behara et al. (2011), by using a laser diffraction technique. The experiments were carried

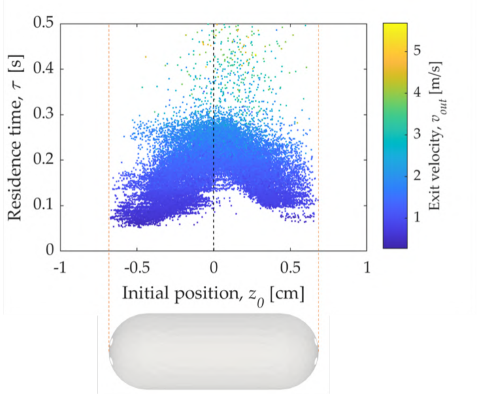

Figure 7.31: Scatter plot of residence time as a function of initial z coordinate. Points are coloured according to the magnitude of the exit velocity.

out on the whole inhaler with micronized mannitol powder. The inhaler used (low resistance RS01) was similar to the inhaler considered as a reference in the present study (Cyclohaler). Both the experimental studies observed a sigmoidal emission profile analogous with the one reported in Figure 7.30. The time required for the full emptying of the capsule (about 0.5 s) is also compatible with the emptying time measured by Coates et al. (2005b) for a 104 L/min inlet flowrate (about 0.6 s).

Figure 7.31 shows the relationship between the residence time and the initial axial position of the particles. Each point represents a particle, and the points are coloured according to the magnitude of the exit velocity. Particles that are initially placed at the centre of the capsule exit later and with a higher velocity.

From the results of the simulations, interesting details on how particles exit the capsule can be extracted. Figure 7.32a shows the locations where each particle was expelled while the arrows show the direction of the exit velocity, while Figure 7.32b shows the magnitude of the exit velocity as a function of time. The particle exit velocity vectors are tangential to the capsule and the exit velocity increases as the capsule rotates faster. These data on exit location and velocities, along with the residence time distribution, could be used as input data in a full CFD-DEM simulation of the whole inhaler, as the initial position of the particles in the swirl chamber plays a major role in powder deaggregation (Benque and Khinast, 2022).

7.2.9 Carrier-wall collisions

Particle wall collisions are extremely important in dry powder inhalers, as they are one of the mechanisms for the deaggregation of API particles (Ariane et al., 2018).

A feature that stores all particle-wall collision data (time, location, ID,

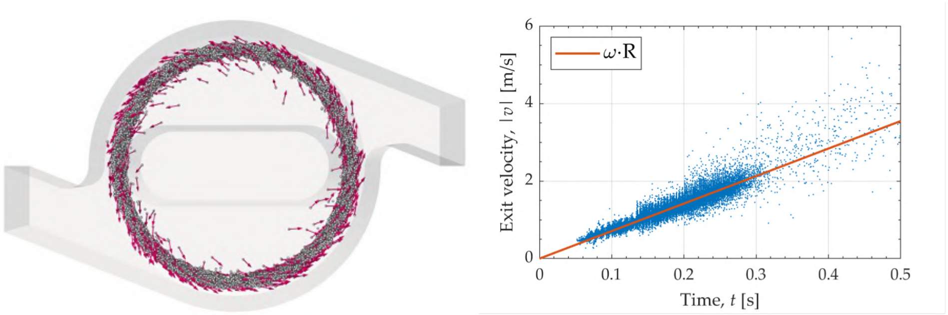

(a) **(b)**

Figure 7.32: a) Exit locations and exit velocity direction, b) exit velocity magnitude.

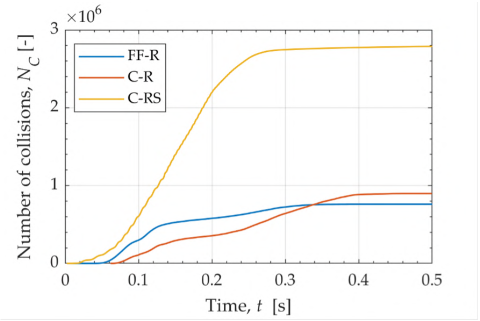

Figure 7.33: Number of carrier-wall collision as a function of time for the three simulations.

impact velocity) was implemented in MFIX to obtain useful statistics about particle-wall collisions. Figure 7.33 shows the cumulative number of collisions as a function of time for the three simulations already presented: FF-R, free flowing rotation, C-R, cohesive-rotation, and C-RS, cohesive with rotation and shaking. The curve related to the simulation with the shaking motion is consistently higher than the other two; in the rotation-shaking simulation the number of impacts is almost four times the number of impacts observed in the rotation-only simulation, as reported in Table 5. The impact energy is also greater, as higher collision velocities are recorded in the C-RS simulation.

Figure 7.34 shows a scatter plot of all the particle-wall collision events for the C-RS simulation with the points coloured according to the shaking frequency of the capsule. Velocities higher than 3 m/s only occur with the highest shaking frequency (180 Hz). These results suggest that the shaking motion related to the collisions between the capsule and the grid of the inhaler might have a crucial role in the deaggregation process.

By comparing the collision maps of the FF-R and C-RS simulations

	FF-R	**C-R**	**C-RS**
Number of collisions	0.8M	0.9M	**2.8M**
N. of collisions with v_C>1 m/s	0	796	149 483
Max impact velocity, $v_{C,max}$ [m/s]	0.4	3.0	4.8

Table 7.6: Collision statistics.

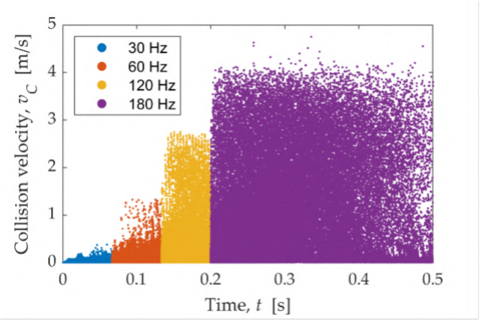

Figure 7.34: Scatter plot of impact velocity events for the C-RS simulation. Points are coloured according to the shaking frequency of the capsule.

(Figure 7.35) it can also be noted that with the shaking motion particle-wall collisions occur all around the capsule and not only at the capsule ends. Interestingly, in both cases particles tend to move and collide in the half of the capsule where they are initially placed, as proven by the colours of the collision map, where the points are coloured according to their initial axial position.

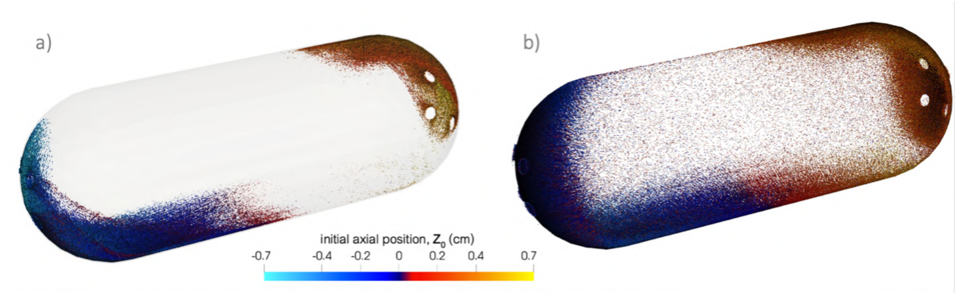

Figure 7.35: Collision map for two simulations: a) free-flowing particles, rotating motion only (FF-R) and b) cohesive particles, rotation and shaking motions (C-RS). Points are coloured according to the initial axial position (z_0) of the colliding particle.

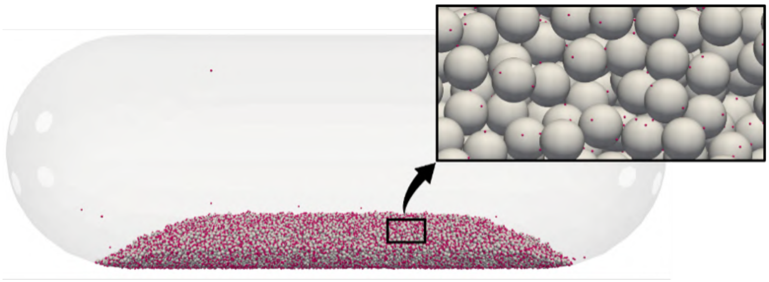

Figure 7.36: Initial position of particles inside the capsule. The magnification shows the real size of particles.

7.2.10 Simulation with both carrier and API particles

API particles have been explicitly added in the simulation to analyse the role of the capsule in the deaggregation process of carrier-based formulations. Carrier-API simulations are particularly challenging because of different factors: 1) the large carrier/API size ratio (>20/1), which has a strong impact on the neighbour search algorithm, 2) the small size of the API particles that requires a small timestep (≈1 ns) and c) the higher number of particles.

A weight dosage of 0.03% of API has been considered, in line with some commercially available products (Benhamou et al., 2001). On a total powder mass of 25 mg, there are 7.5 μg of API particles, while the rest is carrier (lactose). The mechanical properties of both solid phases are reported in Table 7.4.

API particles are initially placed on top of the carrier particles following the approach presented in Section 6.1. Fine particles strongly adhere to the surface of the carrier due to the adhesion forces modelled with the JKR model considering the parameters reported in Table 7.5. The obtained configuration has been gravity settled and it is reported in Figure 7.36. The square shows the real size of the API particles, while API particles are enlarged in the snapshot of the whole capsule to improve visibility.

300 ms have been simulated with the presented configuration. The simulation has been run in parallel on 32 processors. Both the rotation (Table 7.2) and the shaking motion (Table 7.3) have been considered, as in the C-RS simulation.

The position of carrier and API particles during the simulation is shown in Figure 7.37. The motion of the solid inside the capsule is generally similar to the case where only carrier particles are included (Figure 7.28): the particles begin to move towards the sides of the capsule as the angular velocity of the capsule increases and accumulate near the holes and leave the capsule, aided by the shaking action due to capsule-wall collisions.

The snapshots show an increasing number of API particles dispersed all around the capsule near the walls. It is interesting to characterize API-wall

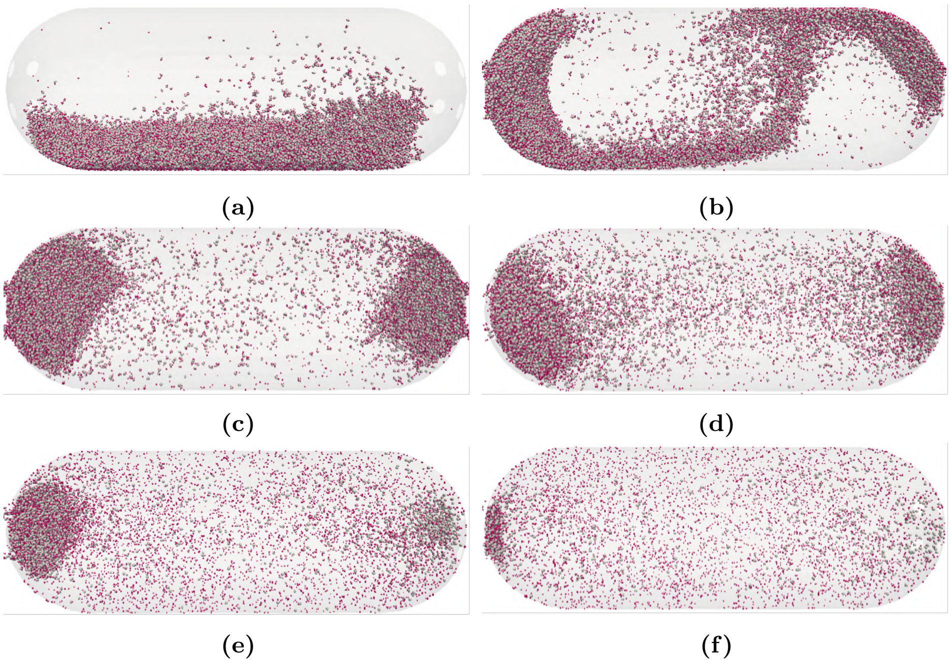

Figure 7.37: Position of carrier (grey) and API (magenta) particles in the capsule at a) 0.05 s, b) 0.10 s, c) 0.15 s, d) 0.20 s, e) 0.25 s, f) 0.3 s. API particles are enlarged 10 times to improved visibility.

adhesion phenomena. Figure 7.38 shows the total number of API particles in contact with the wall as a function of time. It can give an indication on how many particles adhere to the capsule. The plot shows that this number tends to increase with time but drops whenever the shaking frequency changes.

Figure 7.39 shows the emitted fraction of carrier and API particles as a function of time. The two curves overlap until about 0.12 s, when the emission of the API particles is slightly higher. After 0.24 s, the two curves intersect and the carrier emission becomes higher, while API emission seems to reach a lower plateau. The difference in the emission of the two solid phases is minimum anyway. After 300 ms, about 6000 of API particles and 900 carrier particles are still inside the capsule.

The similarity between the emission curves might suggest that the API leaves the capsule attached to the carrier. In Figure 7.40 particles exiting from one of the capsule's holes at different times of the simulations are reported. The snapshots visually show that the API particles seem to come out adhered to the carrier. Only towards the end of the simulation (Figure 7.40b and Figure 7.40c) some carrier particles leave fully uncovered.

The number of API adhered on carrier particles can be quantified by clustering algorithms. Figure 7.41a shows the mean number of API particles adhered on a carrier particle as a function of time. The number decreases

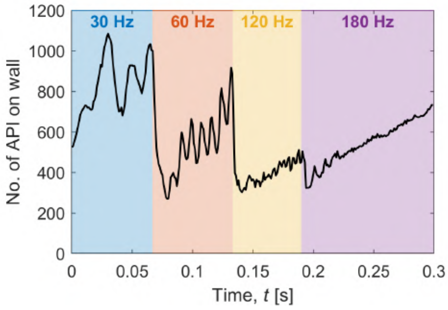

Figure 7.38: Total number of API particles in contact with the walls of the capsule. The different colours of the background indicate the different shaking frequencies.

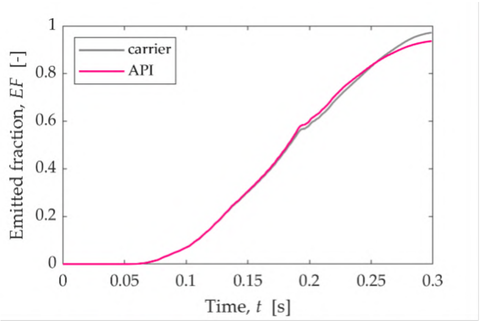

Figure 7.39: Emitted fraction of API and carrier

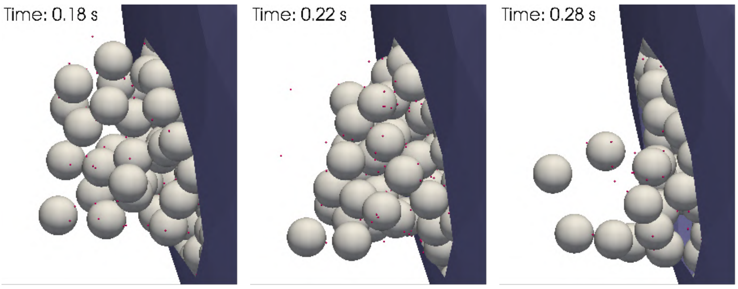

(a) **(b)** **(c)**

Figure 7.40: Particles exiting from one of the capsule's holes at a) 0.18 s, b) 0.22 s, b) 0.28 s.

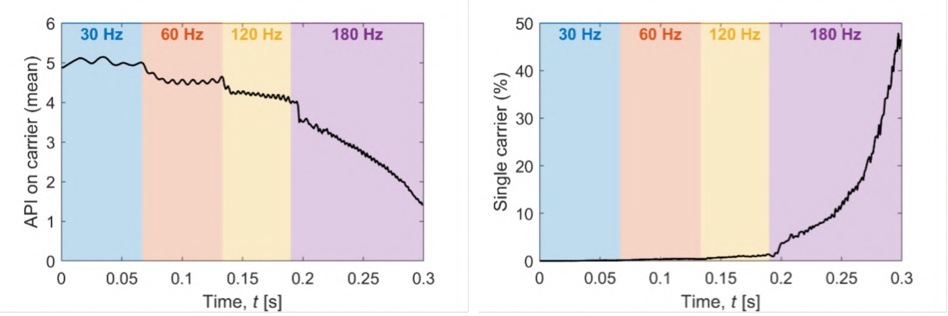

(a) (b)

Figure 7.41: a) Mean number of API adhered on a carrier particle, b) percentage of carrier particles fully deaggregated inside the capsule. The different colours of the background indicate the different shaking frequencies.

with the increasing angular velocity of the capsule and with the increasing shaking frequency. However, the decreasing trend becomes consistent only in the last part of the simulation, with a shaking frequency of 180 Hz. This observation can be confirmed by the plot in Figure 7.41b, where the percentage of fully uncovered carrier particles (i.e., without any API attached) is reported as a function of time. The percentage goes up from less than 2% to almost 50% in the last phase of the simulation alone. As already shown in Figure 7.34, high carrier-wall collision velocities are recorded when the capsule vibrates with the highest frequency. Since carrier-wall impact velocities promote powder deaggregation, the results suggest that more than the rotational movement of the capsule, it is the sudden collisions of the capsule with the swirl chamber that cause the disruption of the agglomerates.

The simulation results provide a very detailed picture of the carrier and API particle motion, elucidating the role of the rotation and shaking motion on the particle-wall collision statistics and, in turn, on the deaggregation and release process. It shall not be forgotten that the process also depends on the dry-coated particle agglomerate strength, which in turn depends on the API adhesion force and the related formulation properties. Also, particle shape may play a significant role in the way dry-coated particles roll over walls, collide with them and the way they respond to external deaggregation stimuli. Overall, the study provides insight into the dynamics of the powder deaggregation and discharge from the capsule and the results are expected to suggest directions for capsule-based inhalers' design.

Chapter 8

High dosage systems

The study on the aerodispersion of two solid phases (carrier and API) in a DPI, presented in Chapter 6, is interesting and useful to understand the dynamics of deaggregation and powder emission. However, the dosage considered (1% w/w), although in line with many products currently on the market, is not representative of a high dosage configuration (particularly desired in many applications, see e.g. Yeung et al. (2018a)), since:

- a single layer of API particles was considered on each carrier, but for high dosages the API can be found in double-triple layer;
- a diameter for API particles of 10 μm was considered, which is larger than the real active ingredients.

The number of small API particles to be simulated for high dosage systems is extremely challenging and makes a CFD-DEM simulation impractical to date. The idea is to consider a smaller system that still has the desired characteristics.

To evaluate the release dynamics of a high-dose carrier-based system, the selected system consists of one or a few carrier particles coated with a number of API particles similar to what a high-dosage formulation would contain.

8.1 Single carrier particle covered

A single 200 μm diameter carrier particle was coated with two layers of 5 and 10 μm diameter API particles. The approach used to cover the carrier is the one already illustrated in Chapter 6; all the particles that can be inserted in an orderly manner are placed in two layers. The two configurations obtained are shown in Figure 8.1. The 5 μm particle configuration contains approximately 10,000 API particles, while approximately 2,500 API particles make up the 10 μm configuration. The dosage by weight of the API

	Carrier	API
Diameter, D (μm)	200	5, 10
Density, ρ (kg/m^3)	1500	1400
Static friction coeff., μ_s (-)	0.5	0.5
Rolling friction coeff., μ_r (-)	0.3	0.3
Restitution coeff., e (-)	0.2	0.2
Young modulus, E (GPa)	0.2	0.2
Poisson coeff., ν (-)	0.45	0.45
Number of particles, N_p	1584	10438, 2654
Weight dosage, ε_w		14%, 25%

Table 8.1: Physical and mechanical properties used in the simulations.

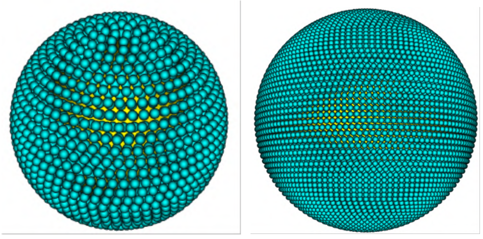
(a) (b)

Figure 8.1: Initial configurations: a) 10 μm API particles, b) 5 μm API particles.

relative to a single carrier particle is 14% for the 5 μm configuration and 25% for the 10 μm configuration.

8.1.1 Simulation parameters and setup

Table 8.1 shows the mechanical properties used in the simulation as well as the number of particles and estimated dosage.

The JKR cohesion model is used to model the adhesive/cohesive interactions between particles (particle-wall adhesion forces are not included). The budesonide-lactose system, a formulation used in various commercial inhalers (Islam and Gladki, 2008), is considered as the reference system for estimating the cohesion parameters.

Begat et al. (2004a) reported the interaction cohesive/adhesive forces between pairs of particles in the various combinations API-API, API-carrier and carrier-carrier. From these values, the surface energy density, γ, can been obtained from the relation that expresses the pull-off force, $\gamma = \frac{F}{3\pi R_{eq}}$. The parameters used and the reference values for the pull-off force are reported in Table 8.2. It can be observed that the API-API cohesive interaction is greater than the adhesion force (API-carrier interaction).

The initial condition is generated by placing the high-dose coated particle

	F, nN	γ, mJ/m^2
API-API	250	21.2
API-carrier	65	6.5
carrier-carrier	150	0.3

Table 8.2: Cohesive/adhesive interaction force and surface energy density.

right on top of the bed of 1584 carrier particles already present in the cup, as shown in Figure 8.2a. The covered carrier particle is placed in a lateral position, not in the center of the cup. A gravity settling simulation (DEM only) is then performed for about 50 ms. The initial and final position of the particles are shown in Figure 8.2b and 8.2c, respectively. After settling, a less ordered configuration is observed and some of the API particles have deposited on the lower carrier.

8.1.2 Particle dispersion

The configuration of Figure 8.2c is used as an initial simulation condition for a CFD–DEM simulation with an air flow rate of 60 L/min. The properties of the fluid phase are the same as Chapter 4. The Gidaspow-blend drag model is considered.

To follow the disaggregation process in detail, the results have been saved and processed very frequently (every 10^{-5} s).

Figure 8.3 shows the deagglomeration of 10 μm API particles during the first 2 ms of simulation.

After almost immediately detaching from the carrier, the API particles form 2 - 3 large clusters (Figure 8.3a). The action of the fluid leads to the formation of smaller agglomerates (Figure 8.3b), that move in the inhaler following the swirling motion of the fluid (Figure 8.3c). After the first collision with the wall, an almost complete deaggregation of the agglomerates occurs (Figure 8.3d).

8.1.3 Evolution of an API agglomerate

The images in Figure 8.4 show the evolution of the first API agglomerate which will impact against the wall at about 1.7 ms. The shape of the agglomerate evolves continuously and it is observed that over time new particles are added while others detach.

Figure 8.5 shows the tangential component of the particles' velocity that make up the agglomerate identified just before the impact. The mean value is $v_{\theta,mean} \approx 18$ m/s. Starting from this value, the force due to the collision of a particle with the wall can be estimated from Hertzian contact theory (see e.g. Di Renzo and Di Maio (2004)) and it is about $1.7{\cdot}10^{-4}$ N. Such

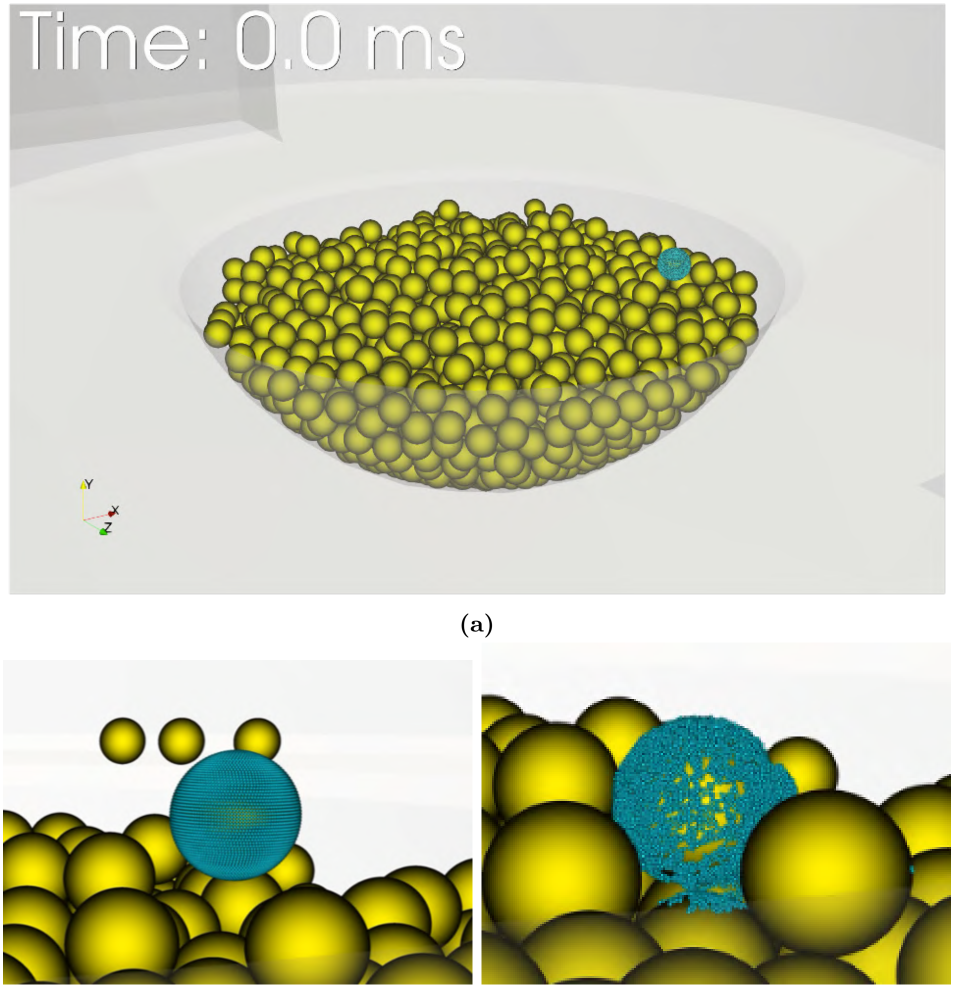

(a)

(b) **(c)**

Figure 8.2: Covered carrier particle placed on top of the filled cup (a). Configuration of the API particles before (b) and after (c) gravity settling.

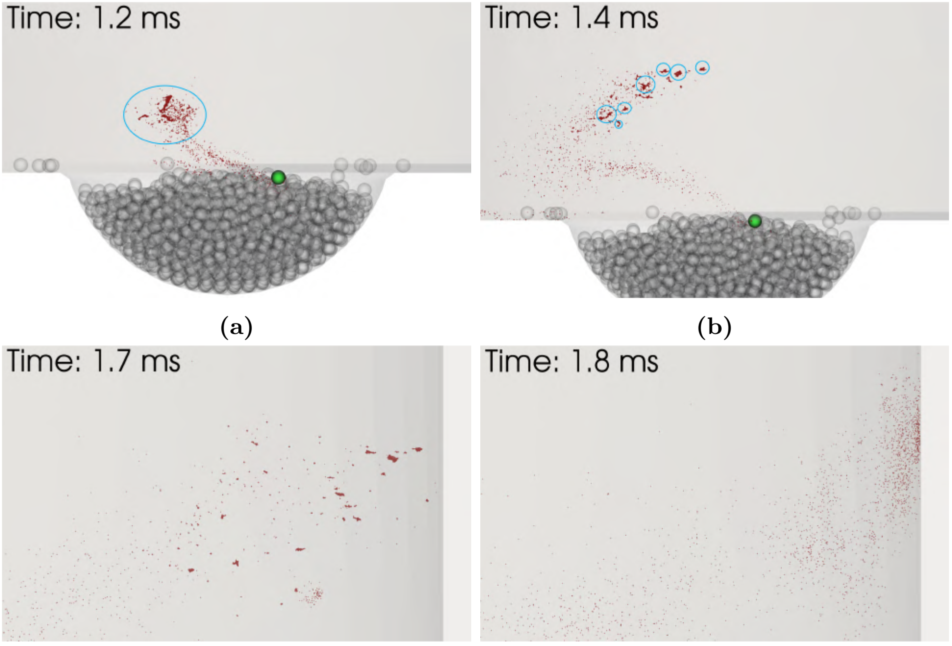

(a) **(b)**

(c) **(d)**

Figure 8.3: Deagglomeration of 10 micron API particles at a) 1.2 ms, b) 1.4 ms, c) 1.7 ms, d) 1.8 ms. 60 L/min gas flowrate.

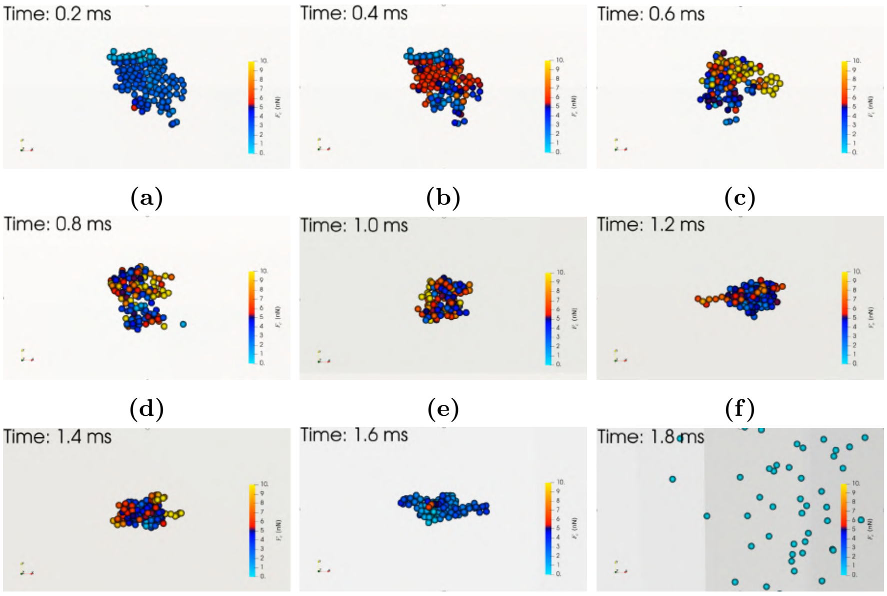

(a) **(b)** **(c)**

(d) **(e)** **(f)**

(g) **(h)** **(i)**

Figure 8.4: Dynamic evolution of the first API agglomerate hitting the wall.

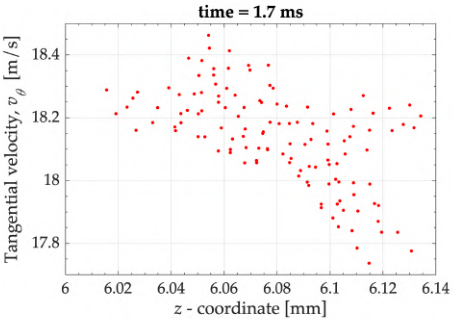

Figure 8.5: Tangential velocity of API particle in an API agglomerate

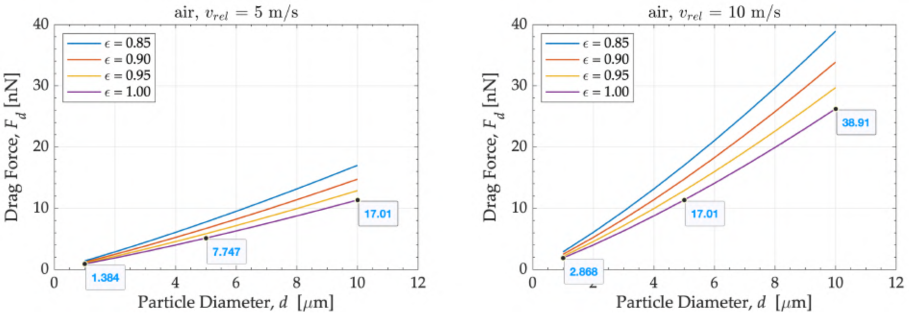

(a) **(b)**

Figure 8.6: Drag force as a function of particle diameter and voidage degree according to Gidaspow-blend drag model for a relative gas-solid velocity of a) 5 m/s, b) 10 m/s.

value of force is consistently higher than the reference value of the API-API cohesion force ($\approx 2.5{\cdot}10^{-7}$ N), so it is expected that such a strong event could cause complete fragmentation.

8.1.4 Effect of inlet flowrate and particle diameter

Figure 8.6 shows the drag force as a function of particle diameter and voidage degree according to Gidaspow-blend drag model for two different values of the relative gas-solid velocity. The value of the drag force increases with particle diameter and gas flowrate. It is therefore expected that the deaggregation process may vary by changing these two parameters.

To verify this assumption, two additional simulations were carried out: one with particles with a diameter of 10 microns and a flow rate of 40 L/min, another with particles of 5 microns and a flow rate of 60 L/min. The results were compared with the results presented in the previous section (10 micron particles, 60 L/min flow rate). The properties of the two solid phases and of the fluid phase are unchanged. The drag model considered is Gidaspow-blend.

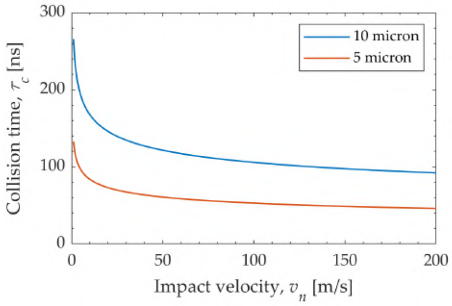

Figure 8.7: Collision duration of a particle-wall impact as a function of normal impact velocity for particles having 5 and 10 micron (mechanical properties reported in Table 8.1, Hertz contact model).

As previously noted, the use of 5 micron particles is challenging in a simulation of this type. However, thanks to the improvements made on the code, the use of parallelization and the fact that the number of particles is low compared to simulations with the entire carrier bulk covered, it was possible to complete the simulation in a reasonable time. It was necessary though to consider a lower timestep for the solid phase. Figure 8.7 shows the collision duration for a particle-wall impact for 5 and 10 μm particles. The impact duration for 5 μm particles is approximately half that of the impact duration for 10 micron particles. If with particles of 10 μm a timestep of 12 ns was sufficient to ensure numerical stability, with 5 micron particles it was necessary to go down to 9 ns.

Figure 8.8a shows that the expected trends for the drag force are confirmed. This translates into a slower fragmentation of the API agglomerates, as shown by the upper plot in Figure 8.8b, where the percentage of fully deaggregated API particles (i.e. not attached to a carrier or to other API particles) is plotted as a function of time for the three simulations. The lower flowrate has also a strong effect on the deaggregation of the API from the carrier, as shown by the percentage of API particles in contact with carrier particles (Figure 8.8b, bottom).

With the smaller diameter (5 μm), the deaggregation of API particles from the carrier occurs with a similar timing (Figure 8.8b, bottom). However, the lower drag force exerted on the particles (Figure 8.8a) leads to a higher percentage of API particles in an agglomerate form (Figure 8.8b, top): after 5 ms, the percentage of fully deaggregated 5 μm particles is 25% lower than in the analogous case with 10 μm particles. Considering larger API particles can therefore lead to an overestimation of the deaggregation phenomenon.

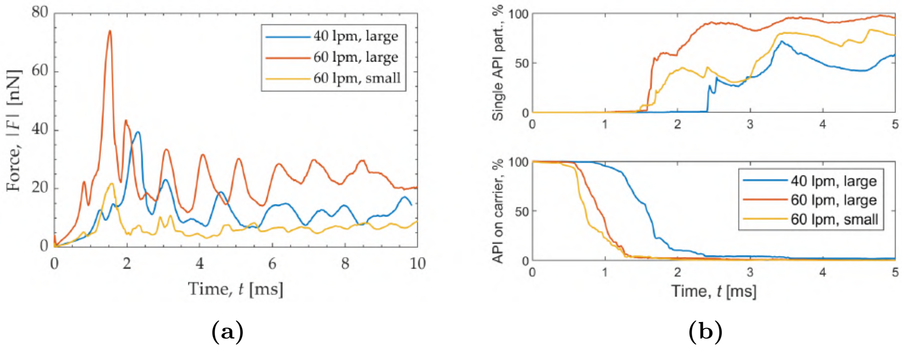

(a) **(b)**

Figure 8.8: Mean drag force (a), number of API particles on a carrier and percentage of deaggregated API particles (b) for simulations with 40 L/min and 60 L/min inlet flowrate and with 5 and 10 micron API particles.

8.1.5 Effect of lift forces and PCF drag model

The configuration with 60 L/min flowrate and 5 μm, particles, therefore with a respirable dimension, was considered as the basis for the evaluation of some models related to CFD-DEM simulations: the switch to a polydisperse drag model and the introduction of lift forces.

The following three scenarios were considered:

- Simulation with Gidaspow-blend drag model (monodisperse);
- Simulation with CDD-PCF drag model (polydisperse);
- Simulation with CDD-PCF drag model (polydisperse) and modeling of lift forces (Saffman, Magnus).

The dynamics of powder expulsion is shown in Figure 8.9 separately for the carrier and for the API. It is observed that the introduction of a drag model for polydisperse systems has a significant effect on the emission of fine particles. The addition of the lift models determines a further modification of the ejection profile, of a more limited but still appreciable extent. The addition of the lift force models also has a non-negligible effect on the expulsion rate of the carrier particles.

Without the polydisperse drag model, the API particles reach the exit duct faster, as visible in the frames of Figure 8.10, which show the position of the API particles in the different simulations after about 4 ms, and in the graphs of Figure 8.11, showing the average vertical position of the particles as a function of time. The apparently oscillatory trends of the average vertical position of the particles in Figure 8.11 are due to the exit of the particles at the top, which therefore excludes them from the average.

From the simulation with polydisperse drag and lift forces (CDD+lift) it is possible to obtain information on the different fluid-solid interaction forces.

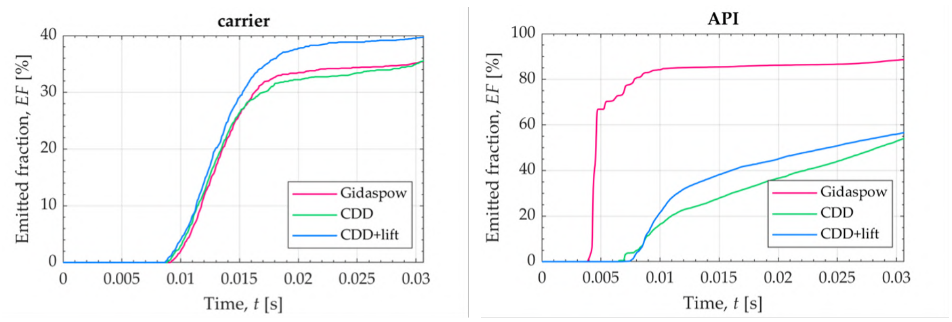

(a) **(b)**

Figure 8.9: Powder emission for a) carrier and b) API particles in the three simulations: GIdaspow, CDD, CDD+lift.

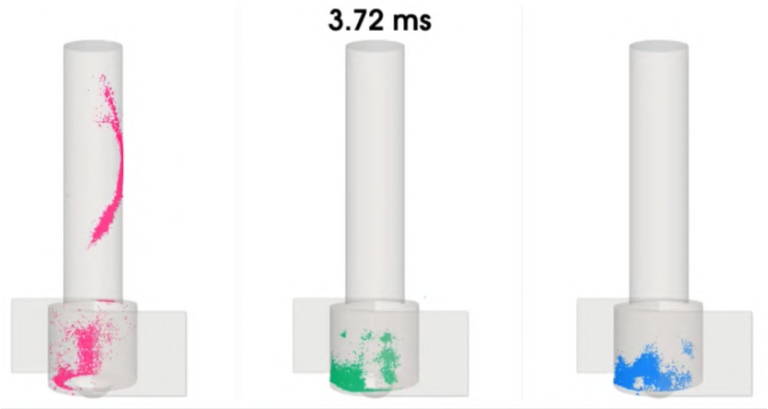

Figure 8.10: Position of the API particles in the three simulations: a) Gidaspow, b) CDD, c) CDD + lift

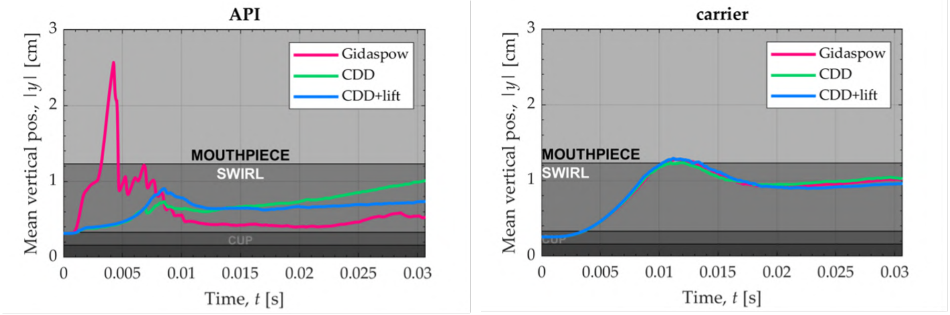

(a) **(b)**

Figure 8.11: Average vertical position of the particles over time for the three simulations. a) API, b) carrier.

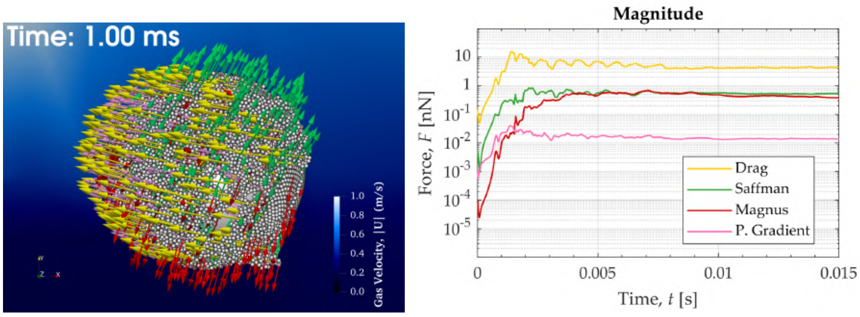

(a) **(b)**

Figure 8.12: Comparison between drag, lift, Magnus, pressure gradient forces. a) Direction of forces just before detachment from the carrier (1 ms), b) modulus of forces on API particles during the simulation. Gravity force is $\approx 10^{-3}$ nN.

A first thing to note is that the drag force often acts in a direction concordant with the force of the pressure gradient, while it is perpendicular to both lift forces. Without forgetting this important aspect linked to direction, Figure 8.12 compares the mean modulus of the different forces on the API particles. As a reference, gravity force is in the order of 10^{-3} nN. It can be noted that the least important force contribution is the pressure gradient, while both lift forces contribute in an appreciable way, reaching values equal to about 10% of the drag force, once the first 3 ms have elapsed in which the disordered evolution of the contributions of the forces reflects the delicate moment in which the air drags up the particles from the cup.

8.1.5.1 API detachment from the carrier

By analyzing the evolution of the relative position of the API particles with respect to the carrier from which they detach, it is observed that in all the simulations the detachment initially occurs in big agglomerates, due to the effect of entrainment of the air, as shown in Figure 8.13. In other words, in the first moments the API appears in the form of an agglomerate, even when detached. The timing of API detachment from the carrier is also similar in all simulations.

Wall impacts, for example carrier-wall, are also deaggregation mechanisms. Table 8.3 shows the characteristics of the first impact that occurs between the covered particle and the wall of the device. In all cases, the first impact occurs after approximately 3 ms at a normal impact speed higher than 3 m/s. In the test with a monodispersed drag model, all the fine fraction comes off well before the first impact (in fact, the wall is not visible in Figure 8.14a), while in the two simulations with CDD a part of the API is deaggregated precisely as a result of the first impact with the wall (see

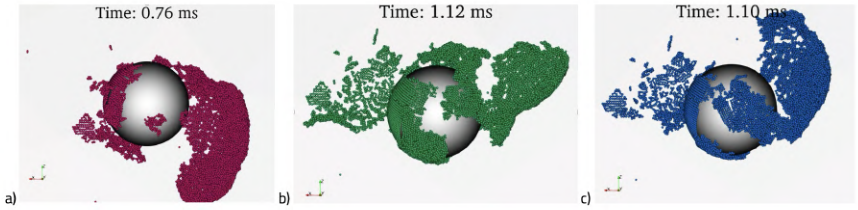

Figure 8.13: Detachment of the API from the carrier for the three simulations: a) Gidaspow, b) CDD, b) CDD + lift.

	t (ms)	vn(m/s)
Gidaspow	3.5	3.1
CDD	3.1	3.8
CDD+lift	3.1	3.9

Table 8.3: Characteristics of the first carrier-wall impact for the coated particle: instant and normal impact velocity.

Figure 8.14b and c).

As already observed with 10 μm particles, the fragmentation of the agglomerated API occurs mainly due to the impact with the wall, as shown in Figure 8.15: it is observed that the API that has already impacted with the wall is fragmented, while agglomerate of large size are still present farther from the wall. Figure 8.16 shows the average size of the API agglomerates as a function of time for the three simulations. After about 2 ms, most of the API is present as a single particle or small agglomerate (2-3 particles).

8.1.6 Effect of fluid torque

In the standard approach for CFD-DEM, the rotational particle equation (Equation 2.28) only has terms relating to contact forces or rolling friction, meaning that only contact events can affect the angular velocity of the parti-

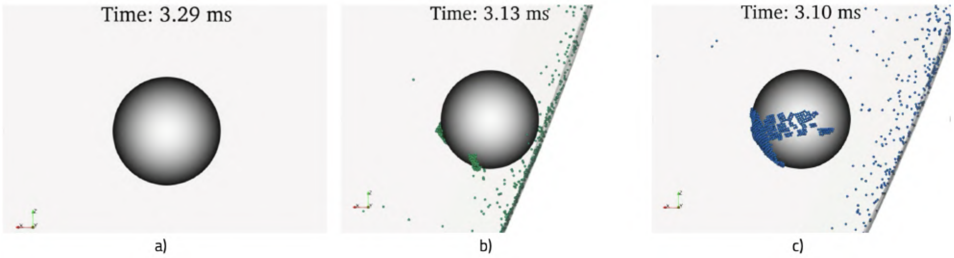

Figure 8.14: Carrier covered just before the first impact with the wall for the three simulations: a) Gidaspow, b) CDD, b) CDD + lift.

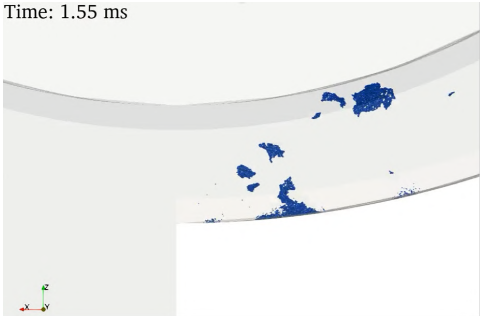

Figure 8.15: API agglomerates obtained from the simulation in the CDD + lift case. After the impact with the wall, fragmentation takes place.

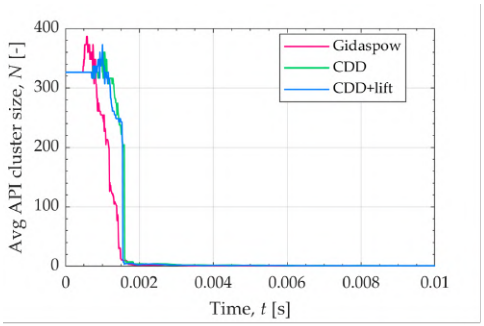

Figure 8.16: Average size of API agglomerates as a function of time in the three simulations.

cles. The introduction of a fluid torque model, already presented in Section 2.4.4, also allows the fluid to interfere in particles' angular velocity, slowing them down or accelerating them. It has been observed that in DPI the fluid motion is cyclonic and swirling, so the addition of a fluid torque model can play an important role.

The simulation with CDD drag model and Saffman and Magnus lift forces (CDD+lift) has been re-run by also including the effect of the fluid torque, modelled according to Equation 2.86. The coupling of the fluid torque (i.e., angular velocity of particles also affecting the fluid) has also been included.

By comparing the results of the simulations with and without fluid torque, a significant difference is observed in the angular velocities of the particles, reported in Figure 8.17. If carrier particles seem to be accelerated by the action of the fluid, the angular velocity of API particles is dramatically reduced: with fluid torque, the mean angular velocity never exceeds 250,000 rad/s, while without fluid torque it goes over 4,000,000 rad/s.

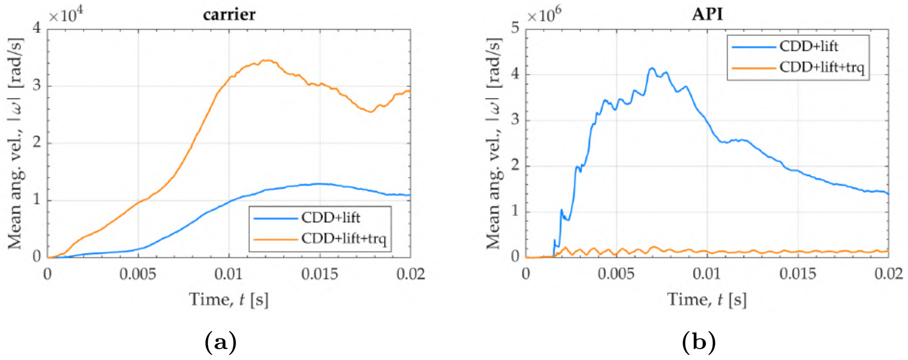

(a) (b)

Figure 8.17: Mean angular velocity with and without fluid torque on carrier (a) and API (b) particles.

To understand the reason for this contrasting effect, one can analytically estimate the effect of fluid torque on API and carrier particles in this particular system.

The action of the fluid torque (Equation 2.86) depends on the relative angular velocity, calculated as: $\omega_r = \frac{1}{2}\omega_f - \omega_i$.

ω_f is the vorticity of the fluid. Figure 8.18 shows the fluid vorticity in the upper part of the swirl chamber (at $t = 0.02s$), calculated in post-processing with Paraview. Vorticities in the order of $10^4 - 10^5$ rad/s are observed.

An analytical estimate of the angular velocity trend of one carrier and one API particle immersed in a fluid with vorticity $\omega_f = 50,000$ is shown in Figure 8.19. Angular velocities of 10,000 rad/s and 1,000,000 rad/s were used for carrier and API particles, respectively. The obtained trends confirm that the fluid has a slowing effect on the rotation of the API and an accelerating effect on the rotation of the carrier.

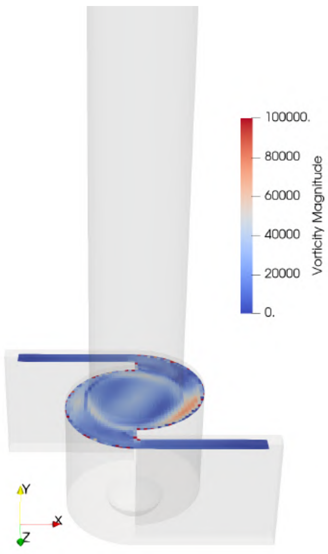

Figure 8.18: Fluid vorticity in the upper part of the swirl chamber ($t = 0.02s$).

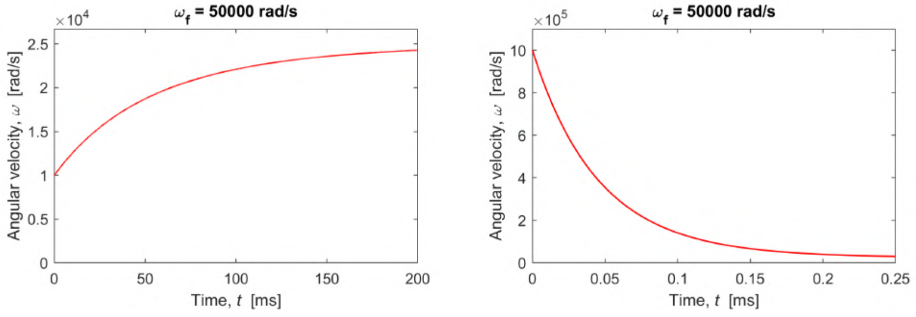

(a) **(b)**

Figure 8.19: Estimate on the effect of fluid torque on (a) a carrier particle ($D = 200\mu m$) and (b) a API particle ($D = 5\mu m$).

	t (ms)	**v (m/s)**	ω_{before} **(rad/s)**	ω_{after}**(rad/s)**
Fluid torque	1.4	27	73,000	311,000
No fluid torque	1.5	28	291,000	4,607,000

Table 8.4: Characteristics of the first API-wall impact in simulations with and without fluid torque. 5 micron, 60 L/min flowrate, CDD polydisperse drag model, Saffman and Magnus forces included.

Table 8.4 shows the characteristics of the first API-wall impact in both the simulations. It can be observed how the collision, which occurs almost in the same position and at almost the same speed, produces a different increase in angular velocity. In the event that fluid torque is added, the increment in the angular velocity due to a collision is consistently slowed down.

This difference in angular velocity results in faster API emission from the inhaler and less effective deaggregation of API fragments if the effect of fluid torque is included in the simulation. The dynamics of detachment from the carrier, on the other hand, remain almost unchanged (the API detaches as a whole and moves as an agglomerate in the swirl chamber. Progressive deagglomeration into smaller and smaller fragments by the fluid).

8.1.7 Effect of turbulence

The characteristics of the fluid certainly have an influence on the motion of the particles. In all the simulations presented, a laminar flow and a first-order discretization method were selected for the fluid phase, for the reasons already presented in Chapter 3. In this section, a preliminary test on the possibility of using a higher accuracy approach for modeling the fluid phase was carried out. A discretization order of higher accuracy (SUPERBEE) was used and the effect of turbulence was included through the LES-WALE model. The characteristics of the grid have not been modified, so the mesh is always made up of cells that are on average 250 micron in size. However, the outlet boundary condition has been changed. Instead of a pressure outlet boundary condition, the pressure profile of a developed flow in a pipe (diameter identical to the mouthpiece of the inhaler) was considered. It was indeed observed that the pressure outlet condition applied directly to the moutphiece made convergence difficult and gave unrealistic results. 20 ms of simulation were carried out with LES-WALE model and compared to the analogous simulation with laminar flow. The drag model is CDD (polydisperse drag model); fluid torque and lift forces are not taken into account.

Figure 8.20 shows the position of API (magenta) and carrier (grey) particles inside the swirl chamber for the two simulations considered at different times, while Figure 8.21 shows the whole inhaler at the end of the simulation (20 ms). The motion of the fluid is represented by streamlines.

A fairly significant difference is observed in the flow field of the fluid. With the addition of the turbulence model (and also considering a higher discretization order) the motion is more chaotic, the velocities are higher and the formation of small vortices is observed (see e.g. Figure 8.20a).

This difference does not have a significant impact on the motion of the carrier, but it does affect the motion of the API. The particles of API, being smaller, tend to be entrained by the fluid. Figure 8.22 shows the API particles at the beginning of the simulation coloured by their residence time, i.e., the time at which each of them leaves the device. As not all particles have been inhaled in 20 ms, the particles with longer residence times (> 20 ms) are coloured in grey. It can be observed that with the LES approach API particles that start from a lower position tend to be expelled later, while exit almost immediately in the laminar simulation.

An accurate and quantitative representation of the air flow field in the device requires an extremely fine grid, especially near the walls of the inhaler, to create the expected velocity profile. On the other hand, the presence of particles on the wall, where they tend to accumulate during inspiration, makes the formation of the laminar sub-layer of the air practically impossible. For reasons related to the impossibility of using a sufficiently dense grid, as well as for the presence of particles that make the convergence of turbulent flows extremely difficult, the representation of the fluid phase with the 1^{st} order upwind-laminar approach is still considered the most appropriate choice.

8.2 Multiple carrier particles covered

The results presented in the previous section showed that coating a single carrier particle with a relatively high dosage of 5 micron (therefore respirable) API particles can provide valuable information on the deaggregation process in carrier-based DPI inhalers.

In this section, the results obtained will be expanded by evaluating whether the process varies with the variation of the initial position of the coated carrier particle in the cup, and an evaluation of the effect of the initial dosage will also be carried out.

8.2.1 Simulation parameters and setup

In this system, four coated carrier particles are considered. The first particle, which will be referred to as Y, is almost in the same position as in the simulations of the previous section, i.e., above the carrier bed, to the side with respect of the inhaler axis. The positions of the other three carrier particles to be coated were selected using the results of Section 4.5:

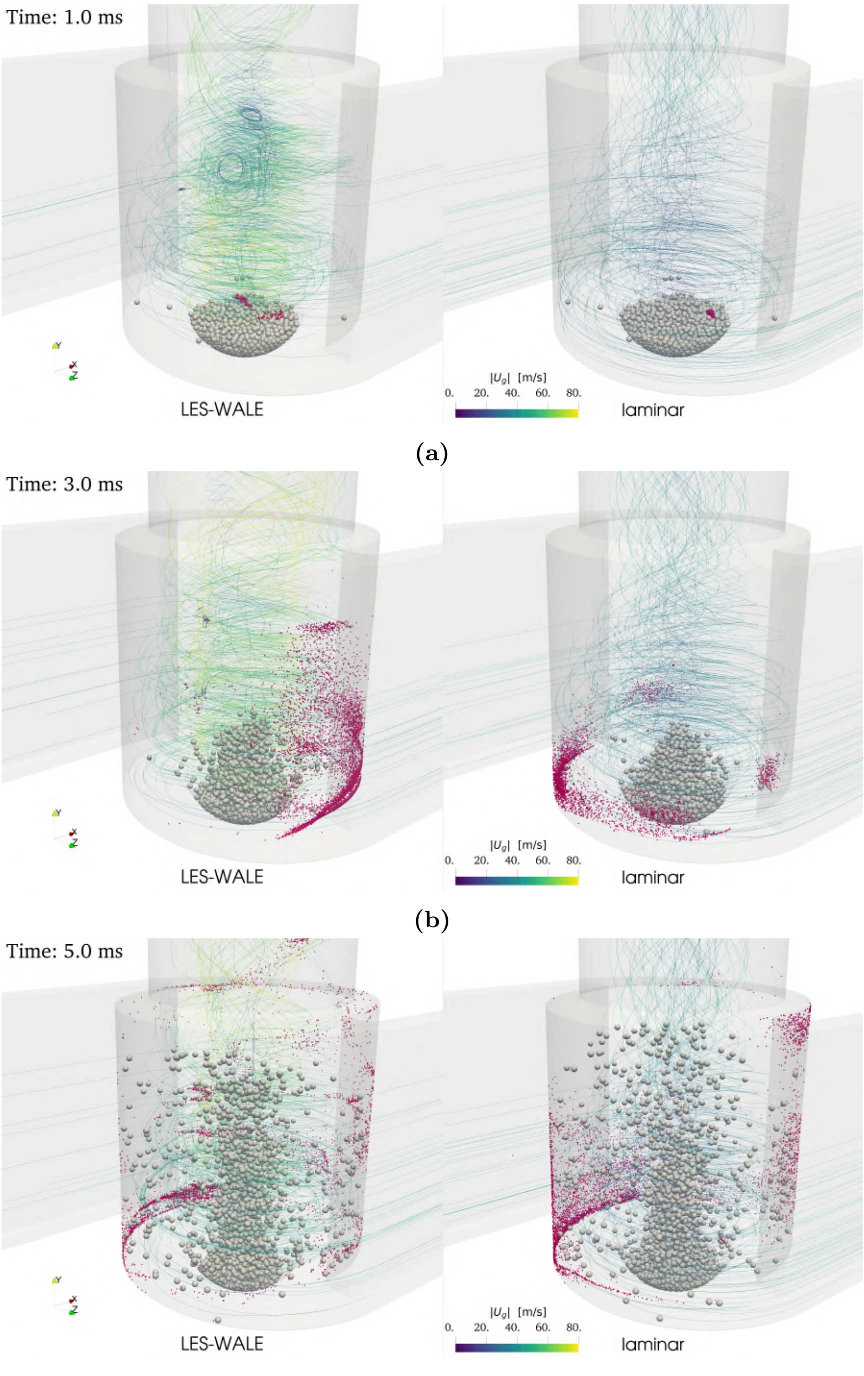

(a)

(b)

(c)

Figure 8.20: Position of carrier particles (grey), API particles (magenta) and fluid streamlines in the swirl chamber for simulations with and without LES-WALE turbulence modelling at a) 1 ms, b) 3 ms, c) 5 ms. API particles are shown with an enlarged size to improve visibility. 60 L/min gas flowrate.

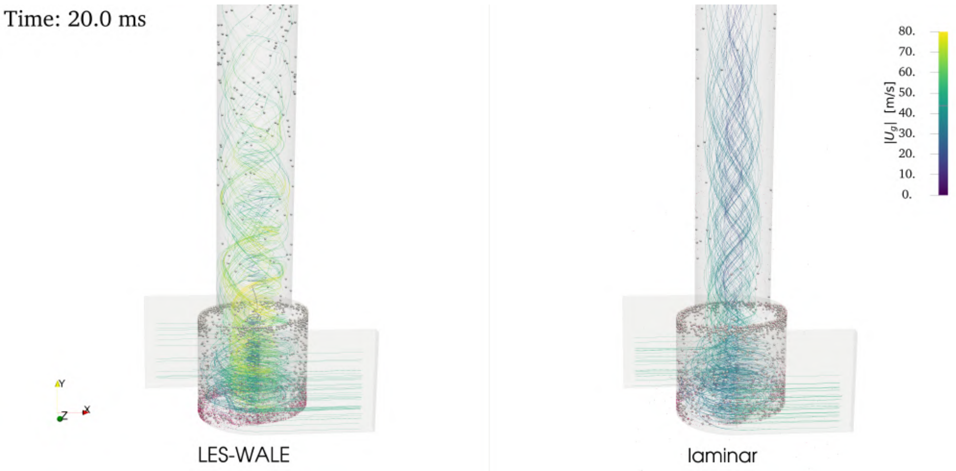

Figure 8.21: Position of carrier particles (grey), API particles (magenta) and fluid streamlines in the whole inhaler for simulations with and without LES-WALE turbulence modelling at 20 ms. API particles are shown with an enlarged size to improve visibility. 60 L/min gas flowrate

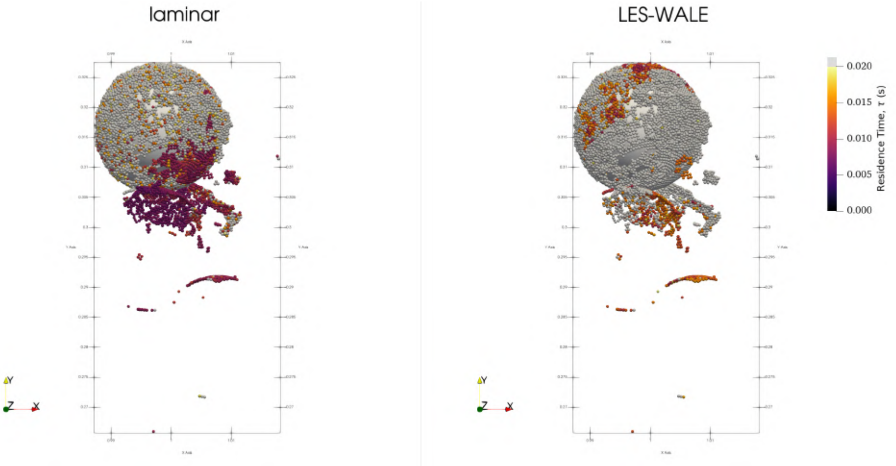

Figure 8.22: API particles in simulations with and without LES turbulence coloured according to their residence time. Particles in grey are still in the inhaler after 20 ms. 60 L/min gas flowrate.

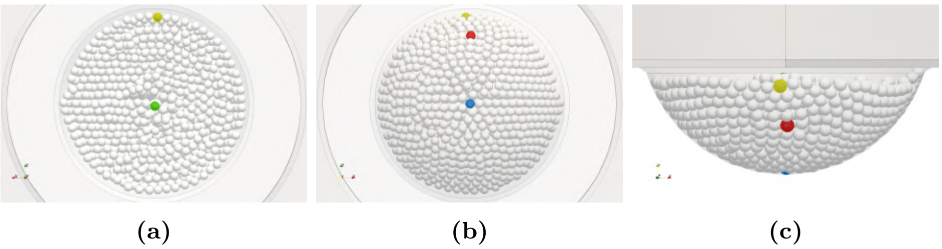

(a) (b) (c)

Figure 8.23: Initial position of API particles in the cup. a) View from the top, b) view from the bottom, c) side view.

- Particle G is placed on the top of the bulk, in a central position;
- Particle B is placed at the bottom of the bulk, in a central position;
- Particle R is placed in a median position of the bulk, laterally.

The initial position of R, G, B, Y particles is shown in Figure 8.23.

Compared to the simulations presented in the previous paragraph, a different approach was used for the setup of the initial condition. The procedure to generate the initial condition is presented below.

A full bulk of carrier particles is placed in the cup. The diameter of the carrier particles is 200 μm. For the four selected particles (R, G, B, Y), however, a larger radius is used, 220 μm. This value is the sum of the diameter of the carrier particles and twice the diameter of two API particles. The obtained configuration has been settled in the cup by gravity.

After settling, the "inflated" R, G, B, Y carrier particles are then reduced in size to 200 μm and covered with the API particles.

For the covering process of the four particles (R, G, B, Y), two layers of API particles are initially placed on the carrier in an orderly manner. All particles that can fit in the two layers are inserted, according to geometrical considerations. The obtained configuration is shown in Figure 8.24a.

Some particles are then deleted from both the second and the first layer, according to a probability defined as:

$$p = \frac{1 - 0.05}{n_{layer}} \tag{8.1}$$

where n_{layer} is the layer number: 1 for the layer closest to the carrier, 2 for the furthest. In this way there is a gradually greater probability of cancellation for the more distant layers, and the first layer will be denser than the second. The configuration after this process for a 10% dosage is shown in Figure 8.24b.

An additional short packing DEM simulation of the whole powder bulk (carrier + carrier covered with API) is finally carried out to ensure the

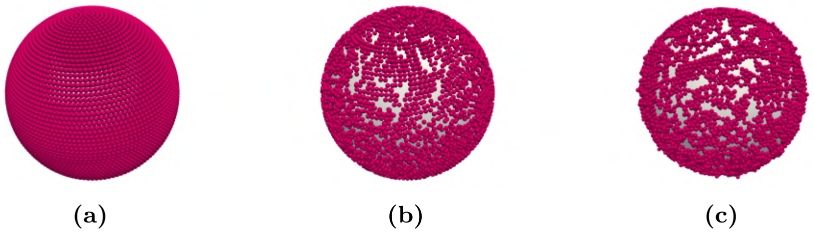

Figure 8.24: Steps to create the initial API-carrier configuration with 10% of API particles (5 μm): a) two ordered layers, b) particles deleted to reach desired dosage, c) configuration after packing.

stability of the obtained configuration. Figure 8.24c shows the change in API position after this step.

About 3200 and 6400 API particles are placed on each carrier in the 5% and 10% configuration, respectively.

From the number of API particles per carrier, the surface coverage (Ariane et al., 2018) of the carrier particle (if the API were placed in a mono-layer configuration) can be calculated as:

$$\alpha = \frac{n_{API}\frac{\pi}{4}d_{API}^2}{\pi(d_c + d_{API})^2} \tag{8.2}$$

with n_{API} the number of API particles, d_{API} and d_c the diameter of one API particle and the carrier particle, respectively. By applying Equation 8.2 to the two configurations used in the present study, a surface coverage $\alpha =$ 54% is calculated from the lower dosage (5%) , while for the higher dosage (10%) $\alpha = 113\%$. Given that $\alpha > 100\%$, the higher dosage configuration could not have been arranged in a mono-layer.

The two configurations can be compared to SEM images reported by Young et al. (2011), obtained with micron-sized salbutamol API particles ($D_{50} = 3.90$ μm) on a smooth spherical polystyrene carrier particle ($D_{50} =$ 277.5 μm), shown in Figure 8.25. The arrangement of the API on different layers is also observed in the experimental images.

Two CFD-DEM simulations have been carried out:

- 5% weight dosage, 12,786 API particles (0.32 μg);
- 10% weight dosage, 25,586 API particles (0.64 μg).

For the 5% dosage, the simulation time is 55 ms and the total number of particles is 14,370 (12,786 API, 1,584 carrier), while 27,170 is the total number of particle for the 10% dosage (25,586 API, 1584 carrier), for which 36 ms have been simulated. The physical and mechanical properties of the particles (5 μm diameter) are the same as Table 8.1. The fluid phase is air, injected with a 60 L/min flowrate. The laminar-upwind approach is

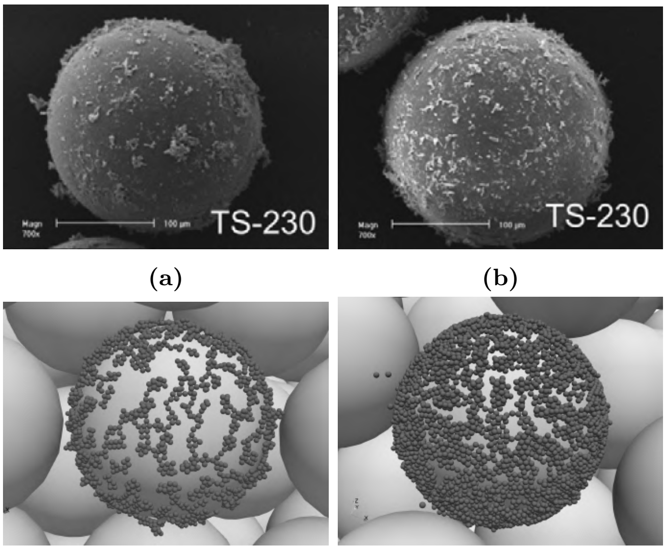

(a) (b)

(c) (d)

Figure 8.25: Scanning electron microscopy images of (a) low (carrier:drug=85:1) and (b) high (carrier:drug=5:1) dosage carrier-drug blends with a 230 μm spherical carrier particle (Young et al., 2011) compared to configuration used in the simulations: c) lower dosage (5%), d) higher dosage (10%).

used for the fluid phase. The considered drag model is CDD (polydisperse drag model). The cohesion model is JKR. The effect of lift forces (Saffman, Magnus), rolling friction and fluid torque (with 4-way coupling) is also taken into account.

8.2.2 Dispersion as a function of particle location

Figure 8.26 shows the position of API and carrier particles during the simulation. API particles are coloured according to the carrier particle they are initially placed on: API on particle R is in red, API on particle G is in green, API on particle B is in blue, API on particle Y is in yellow.

The description of the motion of the particles at different times is presented below:

- 1.5 ms (Figure 8.26a): yellow particles start to disperse. The motion is mainly tangential, similar timing to section 8.1;
- 2 ms (Figure 8.26b): yellow particles rotate at the bottom of the swirl chamber. Carrier particle G covered with green API starts to be lifted while some API gets detached in the process. The motion of particle G and relative API is prevalently vertical;

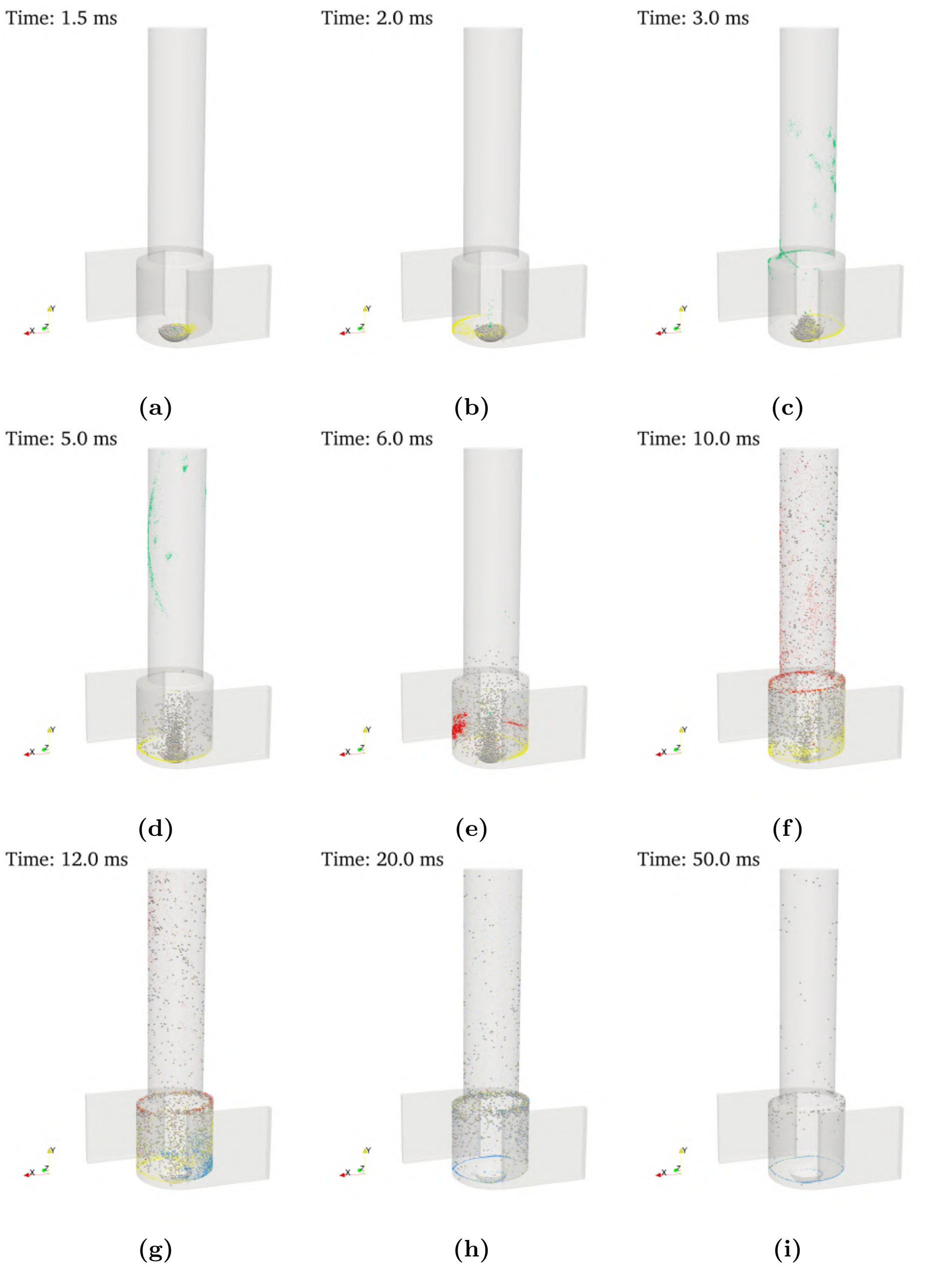

(a) (b) (c) (d) (e) (f) (g) (h) (i)

Figure 8.26: Particle position inside the inhaler during the simulation at different times: a) 1.5 ms, b) 2 ms, c) 3 ms, d) 5 ms, e) 6 ms, f) 10 ms, g) 12 ms, h) 20 ms, i) 50 ms.

- 3 ms (Figure 8.26c): yellow particles keep rotating in swirl chamber. Most green particles are now in the mouthpiece;
- 5 ms (Figure 8.26d): Almost all green particles are out of the system. First red particles start to move;
- 6 ms (Figure 8.26e): red particles dispersed in the swirl chamber;
- 10 ms (Figure 8.26f): yellow particles in the bottom of the swirl chamber, red particles in the top of the swirl chamber;
- 12 ms (Figure 8.26g): blue particles are dispersed in the lower part of the swirl chamber;
- 20 ms (Figure 8.26h): progressive dispersion of remaining carrier and API;
- 50 ms (Figure 8.26i): only few yellow and blue API particles are still in the system.

The results show that the initial position of the API particles in the bulk has a very important influence on the motion of the particles inside the inhaler.

The trajectories of selected API particles from groups B, G, Y, R are reported in Figure 8.27 at representative time instants. If the motion of the yellow particles is mainly tangential and involves numerous rotations inside the swirl chamber, the green particles leave the swirl chamber almost immediately, making only a few rotations in the mouthpiece. Red and blue particles have tangential/helical trajectories as well, but the helix of the red particles starts from higher up compared to blue and yellow particles, which tend to rotate at the bottom of the swirl chamber. However, the timing for red, yellow and blue particles are different. Blue particles, for example, being at the bottom, can only move when the entire bulk of powder has lifted.

Figure 8.28 shows the number of API particles in the system as a function of time. Green particles are the first to leave, while almost 25% of blue particles are still in the inhaler at the end of the simulation.Although the dispersion of the yellow particles occurs at the beginning of the simulation, the release occurs on average later than the release of the red particles, which instead are lifted later as they are located further down the cup.

The emission curves are slightly different between the two simulations (5% dosage, Figure 8.28a, and 10% dosage, Figure 8.28b). It is observed in particular that the yellow particles exit after the blue particles if the dosage is 10 %.

Table 8.5 shows the characteristics of API emission after 20 ms. The percentage of emitted particles is reported separately for B, R, G, Y API

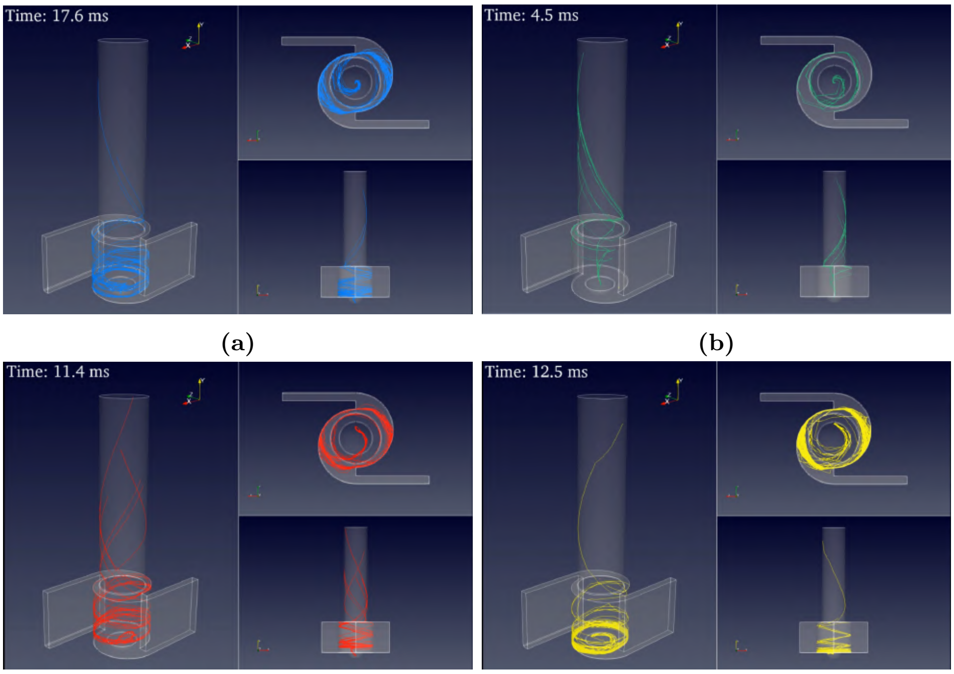

(a) **(b)**

(c) **(d)**

Figure 8.27: Trajectories of selected API particles (10 % dosage): a) B, b) G, c) R, d) Y.

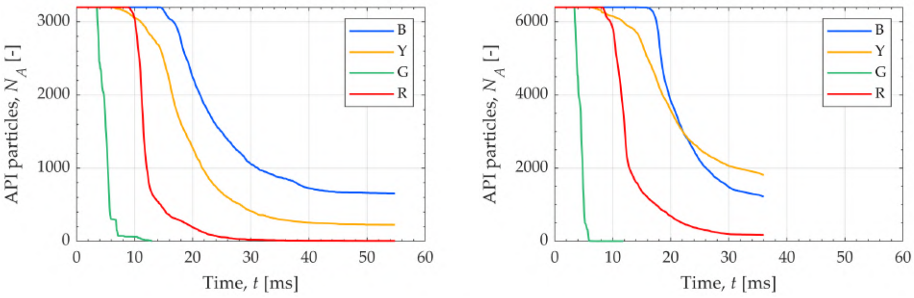

(a) **(b)**

Figure 8.28: Number of R, G, B, Y, API in the system in the simulation with a) 5% dosage and b) 10 % dosage.

	Lower dosage	Higher dosage
B	14.4%	14.2%
Y	49.8%	34.1%
R	91.3%	85.7%
G	100.0%	100.0%
FPD (μg)	0.21	0.38
FPF (%)	64	59

Table 8.5: Percentage of emitted API particles for each API phase; fine particle dose (FPD) and fine particle fraction (FPF) at 20 ms

particles. The total Fine Particle Dose (FPD) and Fine Particle Fraction (FPF) are reported as well. The first represents the mass of the API that has left the system, while the latter is the ratio between the FPD and the loaded dose, i.e., the initial mass of API loaded in the inhaler. By doubling the dosage, the FPD goes from 0.21 μg to 0.38 μg, while the FPF slightly decreases, going from 64% for the lower dosage to 59% for the higher. Young et al. (2011) found a constant FPF and a remarkably linear relationship (with zero intercept) between FPD and loaded dose for systems having carrier:drug weight ratio less than 10:1 (weight dosage $\approx$ 9%). Non-linearity is observed for higher carrier:drug ratios, with a drastic reduction in the FPF. The data in Table 8.5 show a decrease of 8% in the FPF, mainly due to R and Y particles. Since only two points are available, it is not possible to say whether this variation is still within the linearity regime.

8.2.3 API-Carrier deaggregation

The emission curves in Figure 8.28 indicate when the particles left the system, but not how they exited. The active pharmaceutical ingredient can reach the lower airways only in deaggregated form, i.e. detached from the carrier. It is therefore interesting to verify how the detachment of the active ingredient from the carrier occurs.

Figure 8.29 shows the number of API particles adhered on a carrier as a function of time for the API attached to B, G, R, Y carrier particles. Figure 8.29a for the 5% dosage simulation, while Figure 8.29b for the 10% dosage.

The detachment occurs at different times for B, G, Y, R, but in any case all the API particles detach from the carrier. It occurs almost predominantly by the aerodynamic forces. For Y it seems to be due to the strong initial acceleration of the fluid, since the fluid flow rate is set instantly to 60 L/min. This strong accelerations can mimic the effect of the Breath-Actuated Mechanism (BAM, Farkas et al. (2017); Lewis and Tweedie (2016)).Detachment from the G particle occurs when G is rotating in the mouthpiece. The detachment from R and B occurs due to the swirling motion of the fluid. In

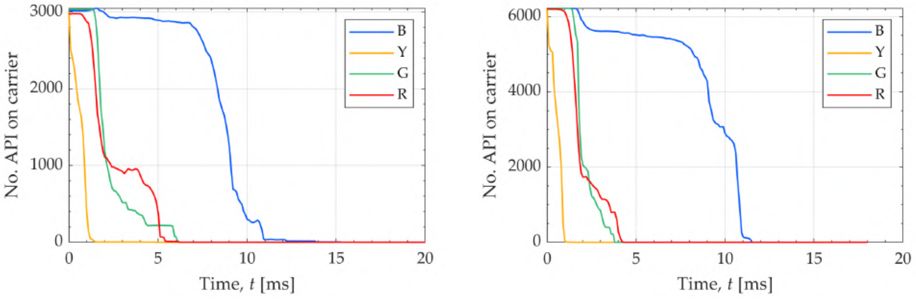

(a) **(b)**

Figure 8.29: Number of API particles adhered on a carrier particle for simulations with a) 5% dosage and b) 10 % dosage.

the case of B and R, contacts with the particles around them could also play a part.

From the curves of Figure 8.29 it is possible to extract the times at which a certain percentage of API particles is detached for each of the four particles covered in the two tests. The data is shown in Table 8.6. The times at which the detachment of 25 % of the particles (t_{25}), 50 % (t_{50}), 75 % (t_{75}), 100 % (t_{100}) occurs are reported. Interestingly, the detachment time appears to be longer in almost all cases for the low dosage simulation.

Figures 8.30, 8.31, 8.32, 8.33 show the API-carrier configuration at the times indicated in Table 8.6 for each of the coated particles (B, G, R, Y, respectively) and for the two different dosages. At high dosage, large agglomerates detach, while with low dosage the API detaches single or with small agglomerates. The detachment from the carrier in the high dosage simulation could be facilitated due to the size of the agglomerates: the flow of air that invests a large agglomerate operates on a larger surface.

The detachment of rectangularly-shaped API agglomerates from the carrier are observed experimentally by Dickhoff et al. (2005) and Yeung et al. (2018b). They both found that increasing the drug loading, large, multilayer API agglomerates attached to the carrier surface are released as a whole and not as primary fine particles. Dickhoff et al. (2003) also found that at a 60 L/min inlet flowrate, nearly all budesonide particles attached to lactose carrier particles are detached due to the strong removal aerodinamic forces. They also observed a higher API residual on the carrier with a lower API dosage.

8.2.4 Deaggregation of API clusters

It has been observed that the detachment of the API from the carrier occurs almost exclusively by the aerodynamic forces, for all the particles considered. It has also been observed that in general it is faster in the case in which the

	B		G		R		Y	
	5%	*10%*	*5%*	*10%*	*5%*	*10%*	*5%*	10%
t_{25}	8.1	8.6	1.7	1.6	1.4	1.6	0.3	0.4
t_{50}	8.8	9.7	1.9	1.8	1.7	1.8	0.8	0.6
t_{75}	9.2	10.5	2.4	2.3	4.4	2.6	0.9	0.8
t_{100}	17.4	11.6	7.8	3.8	27.1	4.4	4.9	1.4

Table 8.6: Percentiles of detachment times of API particles. t_x = time at which the detached fraction of the API particles is x%. All times are expressed in ms.

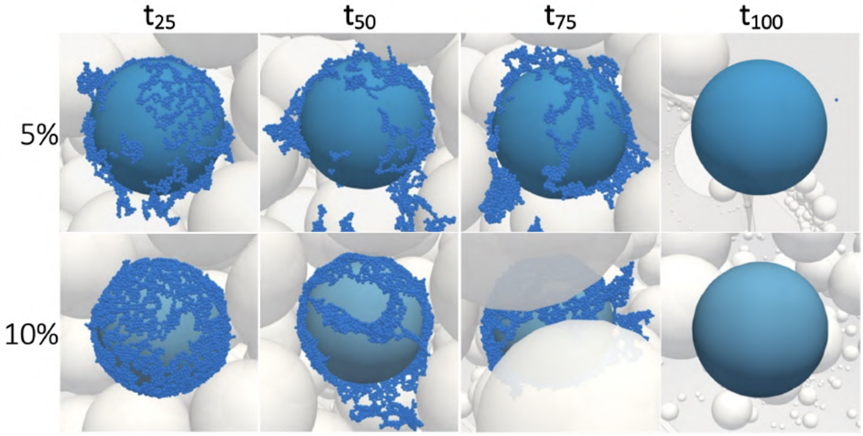

Figure 8.30: Deaggregation of carrier particle B at a) 25%, b) 50%, c) 75% and d) 100 % of deaggregated API. Simulation with 5% and 10% API dosage per carrier particle covered.

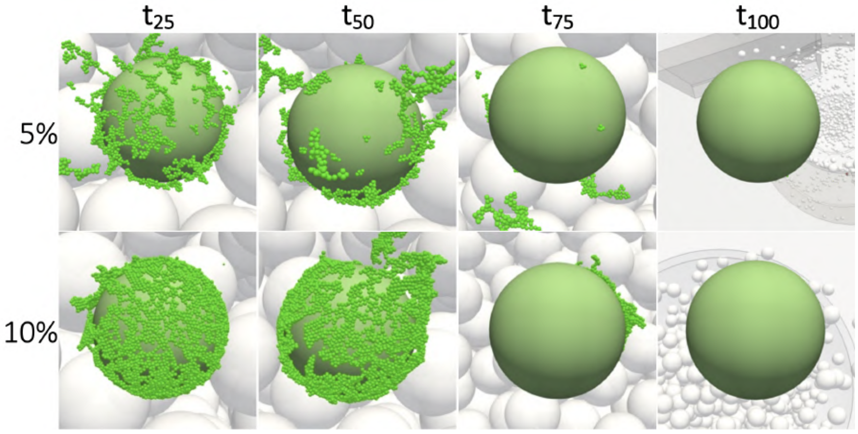

Figure 8.31: Deaggregation of carrier particle G at a) 25%, b) 50%, c) 75% and d) 100 % of deaggregated API. Simulation with 5% and 10% API dosage per carrier particle covered.

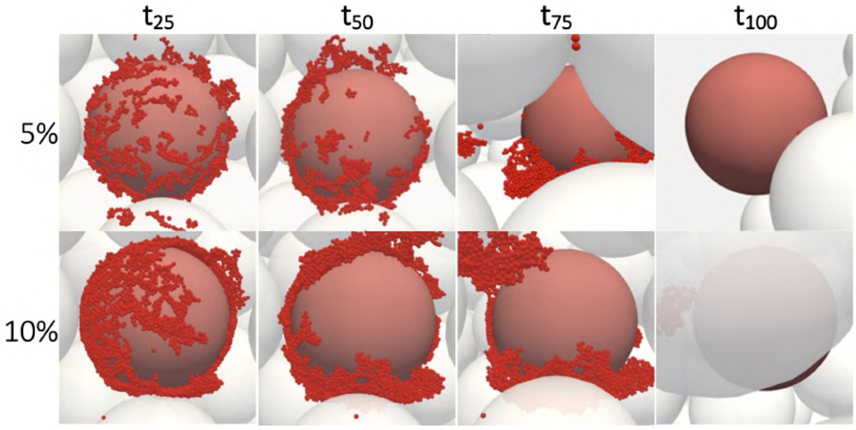

Figure 8.32: Deaggregation of carrier particle R at a) 25%, b) 50%, c) 75% and d) 100 % of deaggregated API. Simulation with 5% and 10% API dosage per carrier particle covered.

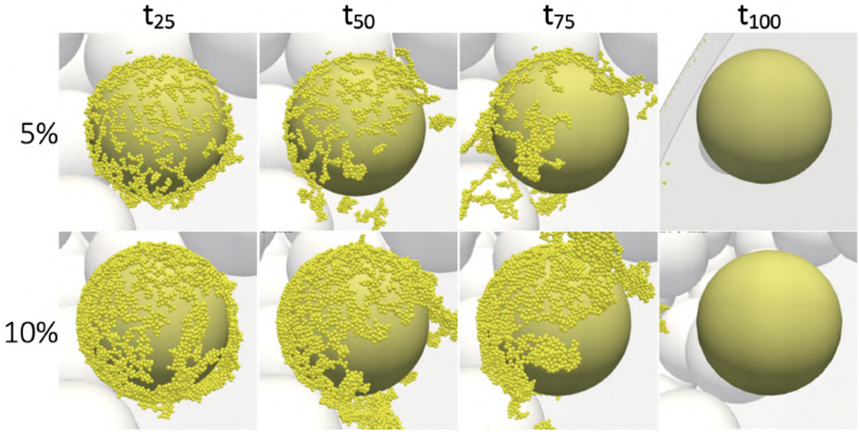

Figure 8.33: Deaggregation of carrier particle Y at a) 25%, b) 50%, c) 75% and d) 100% of deaggregated API. Simulation with 5% and 10% API dosage per carrier particle covered.

dosage is higher, since the larger agglomerates have a greater surface, which corresponds to a greater drag force.

These clusters must fragment to be inhaled, since they have to be less than 5 μm in diameter to be respirable (Sommerfeld et al., 2019). In the case considered, with 5 micron particles, only if the drug arrived with all the particles completely isolated an effective dose of 100% could be obtained. From a qualitative analysis of the results it is observed that the deaggregation of the API clusters detached from the carrier occurs by two mechanisms: 1) aerodynamic forces, 2) tangential collisions at high speed with the wall. The fact that there are larger clusters with a higher dosage could affect how easily they break down.

Figure 8.34 shows representative examples of large API clusters observed in the higher dosage simulation (10%) between 5 and 10 ms, represented in a $x-y$ plane. Most of them are the result of the "slab" detachment from the respective carrier particle and evolve dynamically in size and shape due to the shear acceleration exerted by the fluid. Some of the clusters reach sizes in the hundreds of microns.

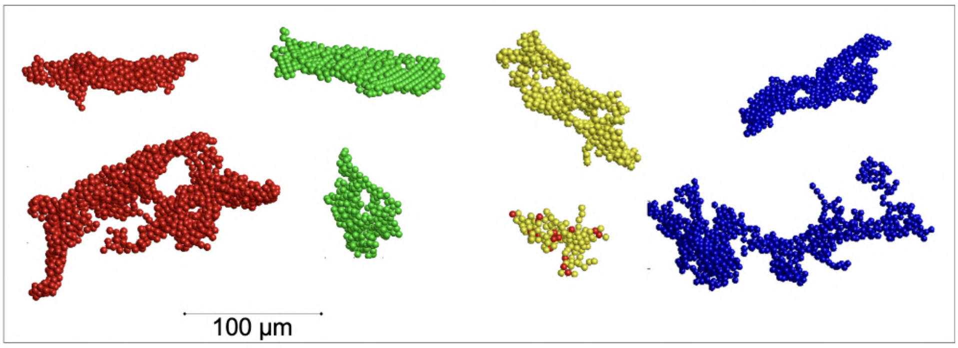

Figure 8.34: Examples of cluster observed between 5 and 10 ms. 10% dosage. Particles are coloured according to the carrier particle they were initially attached to (red, R; blue, B; green, G; yellow, Y).

Some of the clusters are more compact (e.g., top green cluster), others exhibit a chain-like morphology (e.g., bottom blue cluster).

It can be observed that one of the represented clusters (bottom yellow cluster) is made up of particles of different "colours"; this proves that the dynamic evolution of agglomerations also foresees re-aggregation phenomena.

An analysis of the coordination number of API particles allows determining the fraction of isolated particles during the dispersion process. Figure 8.35 shows the percentage of API particles that are present in the system without having any contact with other particles. It is observed that the percentage is higher with the lower dosage, so it might be thought that with a higher dosage the fragmentation of the active ingredient is more difficult.

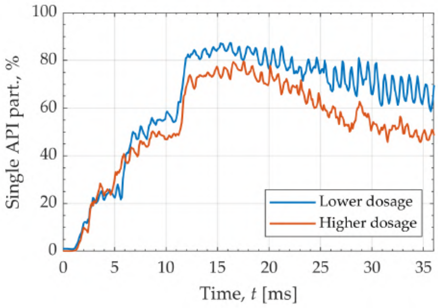

Figure 8.35: Percentage of API particles fully deaggregated for simulations with different weight dosage.

Agglomeration statistics can be obtained individually for API adhered to B, G, R, Y. Figure 8.36 shows the maximum number of API particles in a cluster. At the beginning the particles are adhered to the respective carrier, so they all belong to the same cluster. Figure 8.37 shows the number of distinct clusters. The higher the number, the more the number of particles fully deaggregated and thus respirable.

The red curve peaks at the initial number of particles in the system (Figure 8.37a), so there is a time when virtually all particles are completely deaggregated. The curve then starts decreasing in correspondence with the emission of particles from the inhaler.

Yellow particles tend to be detached immediately from the carrier (Figure 8.29a), but the API agglomerates are larger (Figure 8.36a) and last longer (Figure 8.37a).

The times of the four single curves differ somewhat between the two simulations (5% and 10%), but the dynamics are the same for both variables considered (max. number of API in a cluster and number of clusters). However, the hypothesis on the greater difficulty of fragmentation of the largest agglomerations does not seem to be confirmed. For example, look at the green curve in the two simulations. With the 5 % dosage, the number of clusters for green particles tends to be lower (Figure 8.37a) and the max. number of clusters in the system only gets to 1 when 1-2 particles are left in the inhaler, suggesting that some green API exits as an agglomerate. Looking at the results of the 10% dosage, it seems instead that the powder exits as fully deaggregated.

This could also be seen in the images on the far right in Figure 8.31. At the instant t_{100}, i.e., when all the API particles have detached from the carrier, the G particle is very close to the exit section in the case of the 5% dosage, while it is still in the middle of the mouthpiece with the 10% dosage.

Considering that the green particles have practically no contact with the other API particles, but instead go directly into the mouthpiece, it might be argued that the reason why a greater presence of single particles is observed

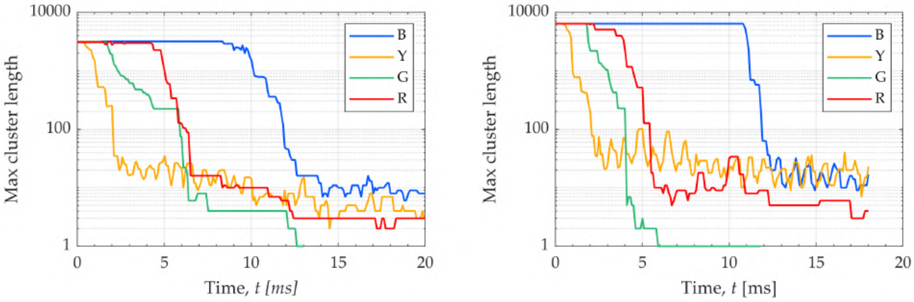

(a) (b)

Figure 8.36: Maximum number of API particles in a cluster for simulations with a) 5% dosage and b) 10 % dosage.

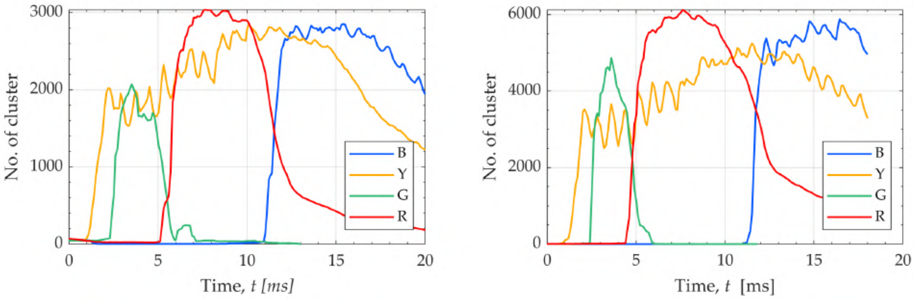

(a) (b)

Figure 8.37: Number of distinct clusters for simulations with a) 5% dosage and b) 10 % dosage.

with lower dosage is linked to phenomena of subsequent re-aggregation of the drug.

8.2.5 Re-agglomeration phenomena

To verify the presence of re-aggregation phenomena, the position of the particles at about 20 ms has been observed. During this phase most of the remaining particles rotate in the swirl chamber and are progressively dispersed.

Figure 8.38 shows two cases in which the API aggregation phenomenon occurred on carrier particles. The two snapshots were made in the 10% dosage simulation, just below the swirl chamber ceiling and the carrier R also appears among the particles. It is observed that blue and yellow APIs are present on the red carrier particle. In addition, the small agglomerates adhering to the two carrier particles are formed by particles of different colours. The agglomerates shown remain throughout the simulation, so they are stable.

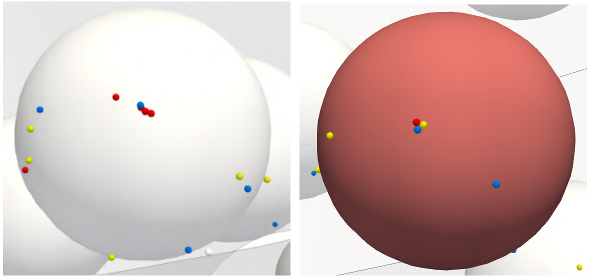

(a) (b)

Figure 8.38: Two examples of re-agglomerated API particles on carrier located near the ceiling of the swirl chamber. The weight dosage is 10%, 20 ms after the start of the simulation.

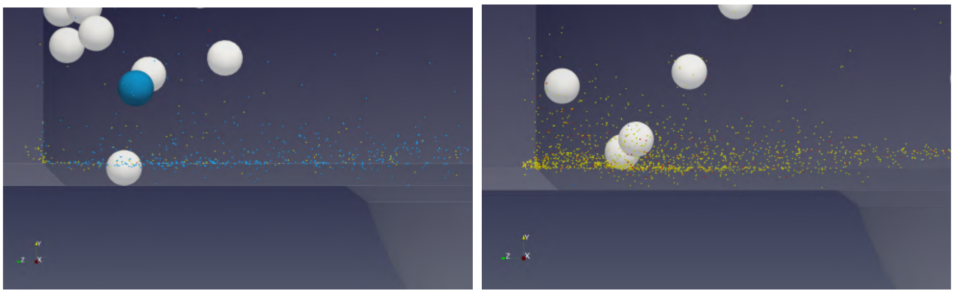

(a) (b)

Figure 8.39: API particles moving in the bottom of the swirl chamber after 20 ms. a) 5% weight dosage, b) 10 % weight dosage.

Figure 8.39 shows the bottom part of the swirl chamber, in the proximity of the cup (visible on the right), after 20 ms.

It is interesting to note that in Figure 8.39a, at 5% dosage, the blue particles prevail. In Figure 8.39b, at 10% dosage, a prevalence of yellow particles is visible. Figure 8.40 shows a close-up of the same figures. If the blue particles manifest mainly as isolated elements, the yellow particles form complex structures with relatively larger clusters. In both cases, however, the clusters observed tend to show a heterogeneous component, i.e. are formed by particles of different colours during a reagglomeration process, as already noted in Figure 8.34.

The presence of a greater number of API clusters, and with a larger size, at 10% dosage is associated with the higher number of API particles present in the simulation. This points to the fact that in reality, i.e. when the fines coat all carrier particles, API reaggregation into nonrespirable clusters is likely to be much more important, possibly affecting the DPI performance. The limited number of fine particles reasonably feasible for DEM simulations did not allow assessing the process thoroughly. However, it is already clear

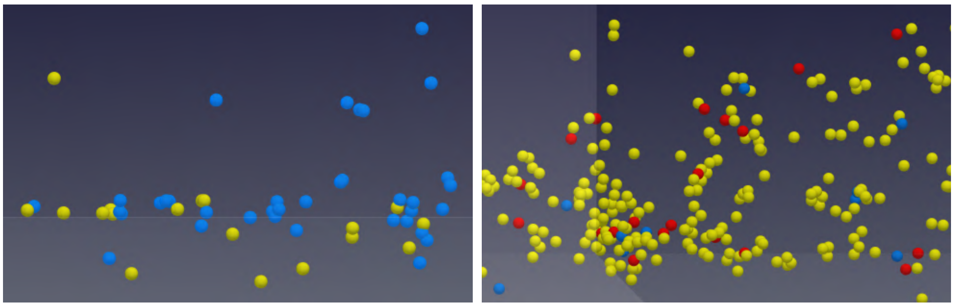

(a) (b)

Figure 8.40: Close up of API particles moving in the bottom of the swirl chamber after 20 ms. a) 5% weight dosage, b) 10 % weight dosage.

that there are chances and sufficient interaction energy, at least for the conditions investigated here, for the detached API particles to reagglomerate *after being aerosolized*, a phenomenon that may have been overlooked and deserves to be examined in more detail.

8.2.6 Comparison between two different blends

The simulations presented so far in the present system have been carried out considering the cohesive parameters of the budesonide-lactose system (Table 8.2), characterized by API-API cohesion stronger than API-carrier adhesion.

A different condition is observed when the API is salbutamol, again with lactose as carrier, where the adhesive interaction (API-carrier) is stronger than cohesive forces (API-API). The system is characterised by a different cohesive-adhesive balance (CAB, Begat et al. (2004a,b)), which is likely to influence the aerosolization process. The salbutamol-lactose system has already been considered in the thesis, while discussing the DEM simulations of the capsule of the Cyclohaler (Chapter 7).

A CFD-DEM simulation is carried out under the same loading dosage (10%) and the salbutamol-lactose cohesive properties previously reported in Table 7.5. It was necessary to repeat the settling and packing operations to avoid instability problems and to start from a ”relaxed” initial condition.

The simulation results show that the deaggregation process takes place in a notably different way compared to the previous simulation.

Figure 8.41 shows the deaggregation stages of API particles from carrier particle G. It can be observed that the initial detachment of API from the carrier due to aerodynamic forces now affects only the outermost API layer, while the fine particles in direct contact with the carrier remain adhered to it. Consequently, the detachment of large agglomerates (such as those shown in Figure 8.34) is not observed, but only of smaller clusters, formed by at most a dozen particles (see Figure 8.41a).

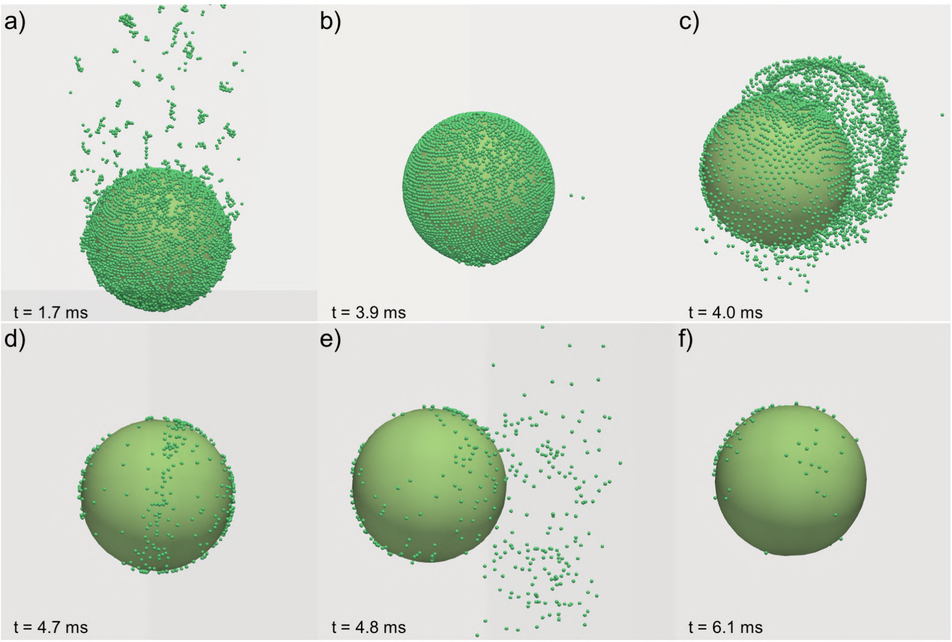

Figure 8.41: Deaggregation stages of API particles from carrier particle G in the salbutamol-lactose system. a) Detachment of the external layers due to fluid dynamic forces; b) configuration before first carrier-wall impact; c) configuration after first carrier-wall impact; d) configuration before second carrier-wall impact; e) configuration after second carrier-wall impact; f) configuration right before emission from the inhaler.

The carrier particle travels almost completely covered (Figure 8.41b) until the first impact with the wall occurs (Figure 8.41c), after which a significant part of the active principle is detached. A further detachment of particles occurs during the second (and last) impact of the carrier with the wall (Figures 8.41c and 8.41d). The carrier particle will leave the inhaler shortly thereafter (Figure 8.41e), with about 150 fine particles still adhering to it.

The importance of particle-wall collisions in the deaggregation of salbutamol particles, which tend to stay attached to the lactose carrier, was already observed in the simulation of the Cyclohaler's capsule (see e.g. Figure 7.40).

If in the case of the budesonide the carrier particles came out nearly fully uncovered of API, here we observe residual fines still attached on them. On the other hand, with the salbutamol-lactose mixture, the detachment of smaller clusters and a more limited reagglomeration leads to a lower probability of having agglomerates of the active ingredient in the inhaler.

These qualitative considerations are translated quantitatively in the bar graph of Figure 8.42, which shows:

- the FPF (i.e., percentage of API particles leaving in the inhaler as fully deaggregated, blue);
- the percentage of API particles that exit on the carrier particles (orange);
- the percentage of API particles that exit as an API aggregate (grey).

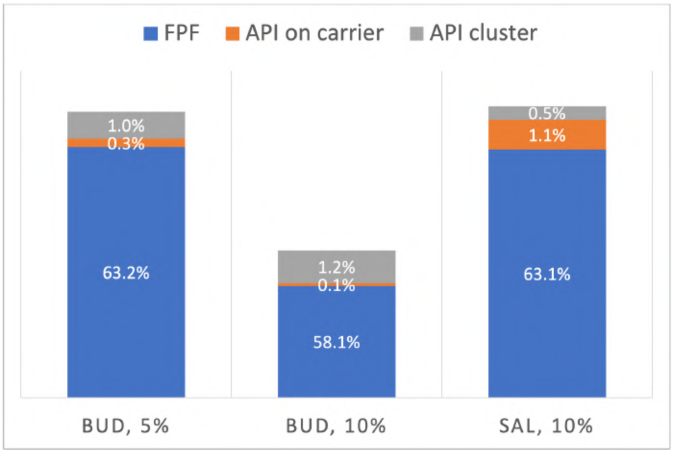

Figure 8.42: State of the API particles emitted from the inhaler in the first 20 ms for the three simulations considered: budesonide (BUD), 5% dosage; budesonide, 10% dosage; salbutamol (SAL), 10% dosage.

The different properties of the two blends ultimately translate into a different fine particle fraction (with the same dosage), which is greater in the case of salbutamol. The API leaves the device with a higher percentage still attached to the carrier and a lower tendency to form agglomerate of fines.

A lower FPF for the budesonide-lactose system compared to the salbutamol-lactose system is confirmed by the experimental work presented by Begat et al. (2004b). They found instability problems with the budesonide-lactose blend, as segregation phenomena of the API particles were observed, leading to low emission efficiency. The salbutamol-lactose blend, characterized by adhesive forces higher than cohesive forces, had better performances in terms of powder emission and deaggregation. However, the incomplete detachment of salbutamol particles from the lactose carrier lead to deposition of fine particles in the throat.

These considerations point to the importance of the cohesive/adhesive balance in determining how a given API-carrier system is delivered to the patient, possibly indicating the need for a different inhaler geometry depending on the specific drug to administer.

Overall, the results obtained prove that accurate CFD-DEM simulations are able to capture the criticalities of the two systems analyzed, allowing the microscopic mechanisms to be linked to macroscopic effects as a result of the complex aerosolisation processes in the DPI.

Chapter 9

Conclusions

The air and particle flow dynamics in swirl-based dry powder inhalers have been investigated in detail, with specific interest in the mechanisms responsible for carrier particle lift, motion and delivery and API particle deaggregation in both a representative device configuration and a commercially available DPI.

The simulations used a CFD-DEM model across all scales from the individual API-carrier contact up to the device size, considering spherical API and carrier particles with realistic contact, drag, cohesive/adhesive forces.

9.1 Design and modelling of a DPI

A DPI geometry has been designed aiming at reproducing the air flow and particle motion, without referring to a specific device and keeping the design as simple as possible.

CFD-DEM simulations have been carried out by considering a constant inlet flowrate and 10 mg of carrier particles (lactose).

The air flow analysis in the designed geometry showed that the transient air flow development is extremely quick and, without particles, steady-state is achieved in less than 10 ms, with swirling flow in the lower chamber and co-axially symmetric flow in the exit duct.

The flow of carrier particles develops following two patterns: either a fountain-like central upflow or an external region in which particles are pushed outwards to the swirl chamber walls by the centrifugal force. Particles in the latter region either leave the inhaler after a helical motion along the walls or remain trapped near the swirl chamber ceiling for at least 0.5 s.

Correspondingly, solids outflow from the device follows three stages, accounting for: up to 35% of the initial mass directly flowing out without contact with walls (stage I), up to 66% after helical flow (stage II) and a final, slower outflow after several looping in the swirling chamber, totaling about 84% of expelled solids (stage III) after 0.5 s. While the process is similar in all conditions, the percentages can vary with the inflow velocity. The occurrence of the annular motion in the swirl chamber is confirmed by experiments available in the literature.

Analysis of the individual particle trajectories showed that there is a relationship between the initial position of the solids in the dose cup and the three expulsion stages. However, such relationship is strong for stage I, which are found in the top central region of the dose, while it turns out weak for particles leaving during stage II and III.

During stage I and II the particles experience an increasing axial and tangential velocity components and a very quickly increasing angular velocity. Averaged values over all particles for 150 μm diameter are up to 2 m/s, up to 2.9 m/s and up to 24,000 rad/s, respectively.

The presence of the rolling friction in the model is shown to influence significantly expulsion during stage II. In particular, it is shown to affect the expulsion rate more than a different size of the carrier, considering 150 μm vs. 200 μm diameter particles. The restitution coefficient also plays a role in powder emission.

The coupling approach in the CFD-DEM technique affects strongly the dynamics of carrier particles' motion. By considering a one-way coupling approach (i.e., not taking into account the effect of the solid phase on the fluid motion), the emission of the powder from the inhaler is unrealistically limited, as particles spread tangentially in the swirl chamber without being able to reach the mouthpiece.

By varying the inlet flowrate from 40 L/min to 80 L/min, but still keeping it constant from the start of the simulation to the end ("step" boundary condition), the percentage of inhaled solids is very similar after 0.5 s. The invariance of the device's emptying with the inlet flow of fluid is a positive feature as it ensures that the device can be used successfully by children or patients with breathing difficulties.

However, by considering a time-evolving, realistic inlet flowrate profile, an extended timing is observed in particle motion, highlighting the predominant role of the initial acceleration of the fluid in particle lifting.

Carrier-carrier and carrier-wall cohesion has been included in the simulations. If the first does not seem to have a strong influence, the latter might change the the powder release dynamics consistently, as some particles adhere to the walls of the inhaler.

The analysis of carrier-wall collisions in the first 50 ms of simulations showed that a great number of high-velocity collisions occur in the swirl chamber.

9.2 Introduction of API particles

API particles are introduced in the simulations by considering a single API particle attached to a carrier in equatorial position. The deaggregation of API particles due to carrier-wall collisions has been investigated in detail with DEM simulations in this simple, fundamental system.

The escape velocity, i.e., the critical impact velocity of the carrier above which API deaggregation occurs, has been evaluated as a function of the granular Bond number. The escape velocity values oscillate between 0.15 and 1.77 m/s depending on the Bond number considered, respectively from 500 to 50,000. The inclusion of a rolling friction model has shown an increase in the escape velocity which goes from negligible for the minimum Bo (500) to over 30% for the maximum Bo considered (50,000).

The effect of simulation timestep, restitution coefficient and static friction coefficient on the escape velocity has been investigated as well. A larger timestep slightly facilitates detachment, as it reduces the accuracy with which the impact is described in the simulation. An increase in the escape velocity is observed by increasing the static friction or decreasing the restitution coefficient, suggesting that the mechanical properties of the powders play a significant role.

The effect of rolling friction was further analyzed, evaluating in detail the velocity, angular velocity and overlap profiles of both API and carrier during carrier-wall impact. If rolling friction is not activated, the API particle (if not detached) orbits indefinitely on the carrier with a high angular velocity and with an overlap lower than the initial one. The addition of rolling friction dampens this rolling motion, limiting the increase in angular velocity and stabilizing the fine particle.

The results of the study indicated the possibility of formulating an analytical model to estimate the escape velocity, which allows to estimate in a very simple and effective way the critical detachment velocity of the API from the carrier by considering an instantaneous variation in the velocity of the fine particle (i.e., not taking into account the dynamics of the carrier-wall impact). Through the developed model it was possible to analyze the dependence of the critical velocity on the initial angle at which the fine particle is positioned and on the cohesion model chosen. The goodness of this analytical-macroscopic model has been verified by means of specific DEM simulations, which generated results in good agreement.

Finally, the calculated values of the escape velocity have been compared to typical carrier-wall impact velocities reported in literature, concluding that a single carrier-wall collision might promote almost full deaggregation, although some particles most likely remain attached.

9.3 Simulation of carrier-API systems

The explicit aerodispersion of a two-component system consisting of 200 μm carrier particles coated by 10 μm API particles has been fully simulated, despite the extreme size difference and very small time-step required. By considering 10 mg of powder with a 1% w/w API, the system consisted of about 140,000 particles.

DEM allowed tracking all API particles during their initial lift off, some still attached to the carrier particles, other ones already deaggregated. The particle scale force balance provided valuable information on the complex interplay between adhesion/cohesion and hydrodynamics.

The results of the simulations have been compared to experimental data available in literature, showing that the first emission peak of fine particles is correctly captured, while the "tail" of the experimental emission curves is not observed.

The effect of flowrate profile, cohesion model, weight dosage and drag model have been investigated as well. An increasing flowrate promoted a faster emission and deaggregation of the active principle, while a higher API dosage (5%) proved that the deaggregation process of the API from the carrier might somehow be limited by a high fines' concentration. The cohesion model plays a role as well, as the deaggregation process seems to be unrealisticaly easy by considering the SJKR cohesion model.

The use of a polydisperse drag models allowed a more accurate estimate of the drag force acting on API particles. A test on a realistic inhalation profile showed that the initial acceleration of the fluid can play a decisive role not only in particle release, but also in the deaggregation process.

The study demonstrated the feasibility of API-carrier simulations with a size ratio of 1 to 20, although the degree of loading must be kept low to limit the number of API particles to be tracked. Through DEM it was possible to follow the motion of all the API particles during the phases of lifting, acceleration due to air, wall impacts, all allowing for a comparative analysis of the forces in play instant by instant.

9.4 Capsule-based DPI

CFD simulation have been carried on a commercially available capsule-based DPI, Cyclohaler®.

A realistic inhalation profile has been used together with LES approach to model turbulence. The results showed that the formation of the vortex alone takes about 50 ms.

The comparison between the gas flow field obtained with LES and RANS approach showed that a greater detail that can be obtained with the LES approach, as only the smallest vortices are modeled, while larger vortexes are explicitly calculated. Lagrangian tracking simulations were performed by considering 1000 particles, in order to evaluate the preferential positions of particle-wall collisions in the Cyclohaler. However, the results are limited as a 4-way approach was not considered and also the capsule was not included in the simulations, despite its fundamental role in powder motion.

Detailed DEM simulations of pharmaceutical powder discharge from the capsule of the Cyclohaler® have been carried out separately, with the aim to investigate the role of the capsule rotational and vibration motion on the dose deaggregation and release properties. The use of rotating/shaking non-inertial frame of reference simplifies the treatment as the geometry can be considered fixed, but it also requires more elaborate post-processing for result reconstruction from the viewpoint of the external observer. A variable-in-time rotational velocity of the capsule was selected in order to mimic the effect of a typical realistic inhalation profile on the capsule movement. The flow through the inhaler was however not considered. DEM simulations have been performed with carrier particles considering three combinations of particle characteristics and capsule motion: free-flowing carrier particles in a purely rotating capsule (FF-R), cohesive carrier particles in a purely rotating capsule (C-R), cohesive carrier particles in rotating and shaking capsule (C-RS).

The motion of free-flowing carrier particles subjected to uniformly accelerated rotational motion (FF-R) was considered first. The results showed that the release occurred during the initial and final stages of the process, as at high rotational velocity the remaining solids are squashed around the lateral holes. The analysis of the hole-to-particle size ratio showed that a value of 6 or higher is recommended, in order to avoid hole clogging, very similar to well-known behaviour in bulk solids gravity flow out of orifices.

The introduction of particle-particle and particle-wall cohesive forces (C-R) delays the solids outflow and may eventually cause a limited amount of solid to remain unreleased.

The shaking movement (C-RS) that occurs as a result of capsule vibration in the device is shown to appreciably improve the release of the carrier particles, particularly at frequency of the order of 180 Hz, for which the acceleration reaches 100 times the gravitational value. In this case, an analytical logistic model was found to reproduce the observed rate of emitted solid with a good approximation and parameters in fairly good agreement with experimental observations. A detailed analysis of the trajectories provided information on the typical particle-wall impact velocities and residence time, and highlighted the relevance of the initial position on the fate of the particles.

Finally, the motion of API-coated carrier particles has been investigated in the C-RS system. The flow resembles the C-RS case with only carrier particles, but the release of the API fraction is shown to occur partly as still stuck to the carrier particles and partly in deaggregated form. The key role in deaggregation is played by the shaking component of motion, which is shown to primarily determine the decrease in the degree of API coverage on the carrier.

9.5 High dosage systems

To evaluate the release dynamics of a high-dose carrier-based system, CFD-DEM simulations have been carried out in the swirl-based in-house designed DPI, considering a single carrier particle coated with a number of budesonide API particles similar to what a high-dosage formulation might contain.

Two API diameters have been considered: 10 μm and 5 μm. The carrier particle has been covered with two full layers of API particles, reaching a weight dosage of 14% for the smallest API particles (5 μm) and 25% for the largest (10 μm).

The particle dispersion has been characterized in detail by saving and processing the results very frequently (every 10^{-5} s). It has been observed that the action of the fluid leads to the formation of large API agglomerates with complex structures that evolve dynamically and tend to be destroyed only when impacting against the walls of the inhaler.

A lower inlet gas flowrate slows down the detachment of API particles from the carrier. The deaggregation process is also a function of API diameter, as smaller particle tend to aggregate with a higher extent.

The study highlighted the need for the specific gas-particle interaction models which can take into account the coexistence of solids of such different diameters. The use of a specific drag model for polydisperse systems has a significant effect on the emission of fine particles, as it tends to be slowed down. The addition of lift force models (Saffman and Magnus) also has a non-negligible effect on the expulsion rate of the carrier particles.

The introduction of a fluid torque model, which allows the fluid to interfere in particles' angular velocity, causes a significant decrement of the average API angular velocity, which results in a faster API emission from the inhaler and a less effective deaggregation of API fragments.

The use of a higher discretization order and a turbulence model with the LES approach results in a more chaotic fluid motion, in which the gas velocities are higher and the formation of small vortices is observed. This difference does not have a significant impact on the motion of the carrier, but it does affect the motion of the API. However, further investigations are required to validate and characterize the simulation with the LES approach.

The study has been extended by considering four carrier particles coated with 5% and 10% (w/w) of a 5 μm Active Pharmaceutical Ingredient (budesonide and salbutamol).

The selected coated carrier particles are placed in different, representative initial locations in the dose cup and their API deaggregation and emission stages have been characterized as a function of the initial particle position. Carrier particles placed on top of the bulk see the API detachment earlier and they follow either a straight path or a tangential, helical path depending on whether they are in the center or to the side with respect to the main axis of the inhaler. Particles that are located further down in the cup get lifted and dispersed later. The deaggregation of API particles is controlled by aerodynamic forces in any case. It prevalently occurs in tangential or in vertical direction based on the initial position of the coated carrier particles.

The emission curves differ for the two dosage considered. The fine particle fraction (FPF) after 20 ms is 63% for the lower dosage and 58% for the higher dosage, so a lower emission efficiency is somehow related to the amount of drug loaded on the carrier particle.

In the high dosage simulation, the API detach in form of relatively large clusters, which then get dragged away more easily from the carrier than the smaller agglomerates of lower dosage simulations. On the other hand, the larger agglomerates persist longer and less API appears as a single particle, i.e. in the respirable form. In addition, the higher amount of fine particles leads to an increased probability of re-agglomeration, the likely cause of a reduced FPF.

Finally, the deaggregation phenomena of the salbutamol-lactose system, characterized by high adhesion forces (API-carrier) and low cohesion forces (API-API), in the same DPI is considered. The different cohesive properties ultimately translate into a greater FPF, but also in a higher percentage of particles delivered still adhered to the carrier. The dispersion phenomenon is therefore strongly dependent on the formulation, suggesting that different inhaler geometries maybe be necessary for different drug-carrier combinations.

Overall, CFD-DEM simulations prove to be a valuable tool to link the micro-scale and macro-scale characteristics of aerosolization and dispersion processes in dry powder inhalers.

9.6 Future work

The results presented show that the potential of using full-scale DEM in the detailed analysis of the deaggregation process is huge, as the local evolution of the governing phenomena can be tracked along with the motion of the particles, providing extremely useful insight and great opportunities for improved design. In terms of feasibility, the present simulations required efforts in devising suitable schemes and computational resources. To give an indication, 10 ms of simulation including API particles at 1% load required about 1.8 days of wall clock time over 16 cores in parallel.

In these explorative simulations, a number of aspects still remained rather simplified, such as the size and shape distribution of the particles, the unresolved flow field in the proximity of the carrier-API interface, the boundary conditions corresponding to inhalation profiles. Based on the improved understanding of the fundamental mechanics inside DPI, future work still needs to be conducted to get more realistic results.

A higher number of particles might be simulated by switching to a multigrid approach or a GPU-based DEM code, which could allow the simulation of a full dosage system with respirable API particles (smaller than 5 micron).

A non-spherical shape could be used to model carrier particle. The introduction of LES turbulence, a finer CFD grid and a higher discretization order could lead to an improved understanding on the fluid-particle interaction.

From the results of the present work, useful qualitative information was obtained regarding the role of some elements of the geometry of the inhaler, such as the cup or the swirl chamber. Different inhaler geometries could be quantitatively studied based on these observation, with the aim of obtaining an optimized geometry and consequent increasing performances.

Bibliography

J. Ahrens, B. Geveci, and C. Law. Paraview: An end-user tool for large data visualization. *The visualization handbook*, 717(8), 2005.

J. Ai, J.-F. Chen, J. Rotter, and J. Ooi. Assessment of rolling resistance models in discrete element simulations. *Powder Technol.*, 206(3):269–282, 2011.

F. O. Alfano, A. Di Renzo, F. P. Di Maio, and M. Ghadiri. Computational analysis of triboelectrification due to aerodynamic powder dispersion. *Powder Technol.*, 382:491–504, 2021.

H. I. Andersson, L. Zhao, and M. Barri. Torque-coupling and particle–turbulence interactions. *J. Fluid Mech.*, 696:319–329, 2012.

M. Ariane, M. Sommerfeld, and A. Alexiadis. Wall collision and drug-carrier detachment in dry powder inhalers: using DEM to devise a sub-scale model for CFD calculations. *Powder Technol.*, 334:65–75, 2018.

G. Batchelor. *An Introduction to Fluid Dynamics*. Cambridge Mathematical Library. Cambridge University Press, 2000.

R. Beetstra, M. A. van der Hoef, and J. Kuipers. Numerical study of segregation using a new drag force correlation for polydisperse systems derived from lattice-boltzmann simulations. *Chem. Eng. Sci.*, 62(1-2):246–255, 2007.

P. Begat, D. A. Morton, J. N. Staniforth, and R. Price. The cohesive-adhesive balances in dry powder inhaler formulations I: direct quantification by atomic force microscopy. *Pharm. Res.*, 21(9):1591–1597, 2004a.

P. Begat, D. A. Morton, J. N. Staniforth, and R. Price. The cohesive-adhesive balances in dry powder inhaler formulations II: influence on fine particle delivery characteristics. *Pharm. Res.*, 21(10):1826–1833, 2004b.

S. R. B. Behara, P. Kippax, I. Larson, D. A. Morton, and P. Stewart. Kinetics of emitted mass—a study with three dry powder inhaler devices. *Chem. Eng. Sci.*, 66(21):5284–5292, 2011.

A. Benassi and C. Cottini. Numerical simulations for inhalation product development: Achievements and current limitations, 2021.

A. Benassi, I. Perazzi, R. Bosi, C. Cottini, and R. Bettini. Quantifying the loading capacity of a carrier-based DPI formulation and its dependence on the blending process. *Powder Technol.*, 356:607–617, 2019.

D. Benhamou, A. Cuvelier, J. Muir, V. Leclerc, V. Le Gros, J. Kottakis, and I. Bourdeix. Rapid onset of bronchodilation in COPD: a placebo-controlled study comparing formoterol (Foradil®Aerolizer™) with salbutamol (Ventodisk™). *Respir. med.*, 95(10):817–821, 2001.

B. Benque and J. G. Khinast. Understanding the motion of hard-shell capsules in dry powder inhalers. *Int. J. Pharm.*, 567:118481, 2019.

B. Benque and J. G. Khinast. Estimating inter-patient variability of dispersion in dry powder inhalers using cfd-dem simulations. *Eur. J. Pharm. Sci.*, 156:105574, 2021.

B. Benque and J. G. Khinast. Carrier particle emission and dispersion in transient cfd-dem simulations of a capsule-based dpi. *Eur. J. Pharm. Sci.*, 168:106073, 2022.

K. Berkenfeld, A. Lamprecht, and J. T. McConville. Devices for dry powder drug delivery to the lung. *AAPS PharmSciTech*, 16(3):479–490, 2015.

L. C. Berselli. On the large eddy simulation of the taylor–green vortex. *J. Math. Fluid Mech.*, 7(2):S164–S191, 2005.

B. Bird, W. Steward, and E. Lightfoot. *Transport Phenomena.* John Wiley & Sons, revised 2nd edition, 2007.

F. Buttini, G. Brambilla, D. Copelli, V. Sisti, A. G. Balducci, R. Bettini, and I. Pasquali. Effect of flow rate on in vitro aerodynamic performance of nexthaler® in comparison with diskus® and turbohaler® dry powder inhalers. *J. Aerosol. Med. Pulm. Drug Deliv.*, 29(2):167–178, 2016a.

F. Buttini, I. Pasquali, G. Brambilla, D. Copelli, M. Dagli Alberi, A. G. Balducci, R. Bettini, and V. Sisti. Multivariate analysis of effects of asthmatic patient respiratory profiles on the in vitro performance of a reservoir multidose and a capsule-based dry powder inhaler. *Pharm. Res.*, 33(3): 701–715, 2016b.

F. Buttini, A. G. Balducci, G. Colombo, F. Sonvico, S. Montanari, G. Pisi, A. Rossi, P. Colombo, and R. Bettini. Dose administration maneuvers and patient care in tobramycin dry powder inhalation therapy. *Int. J. Pharm.*, 548(1):182–191, 2018.

P. R. Byron, X. Wei, R. R. Delvadia, P. W. Longest, and J. Venitz. Breath profiles for testing new dpi devices in development. In *RDD*, volume 1, pages 295–302. Serentec Press Raleigh, NC, 2014.

A. Castellanos. The relationship between attractive interparticle forces and bulk behaviour in dry and uncharged fine powders. *Adv. Phys.*, 54(4): 263–376, 2005.

F. Cello, A. Di Renzo, and F. P. Di Maio. A semi-empirical model for the drag force and fluid–particle interaction in polydisperse suspensions. *Chem. Eng. Sci.*, 65(10):3128–3139, 2010.

A. R. Clark, J. G. Weers, and R. Dhand. The confusing world of dry powder inhalers: It is all about inspiratory pressures, not inspiratory flow rates. *J. Aerosol. Med. Pulm. Drug Deliv.*, 33(1):1–11, 2020.

S. Claus, C. Weiler, J. Schiewe, and W. Friess. How can we bring high drug doses to the lung? *Eur. J. Pharm. Biopharm.*, 86(1):1–6, 2014.

M. S. Coates, D. F. Fletcher, H.-K. Chan, and J. A. Raper. Effect of design on the performance of a dry powder inhaler using computational fluid dynamics. part 1: Grid structure and mouthpiece length. *J. Pharm. Sci.*, 93(11):2863–2876, 2004.

M. S. Coates, H.-K. Chan, D. F. Fletcher, and J. A. Raper. Influence of air flow on the performance of a dry powder inhaler using computational and experimental analyses. *Pharm. Res.*, 22(9):1445–1453, 2005a.

M. S. Coates, D. F. Fletcher, H.-K. Chan, and J. A. Raper. The role of capsule on the performance of a dry powder inhaler using computational and experimental analyses. *Pharm. Res.*, 22(6):923–932, 2005b.

J. H. Conway and N. J. A. Sloane. *Sphere packings, lattices and groups*, volume 290. Springer Science & Business Media, 1999.

M. Corradi, H. Chrystyn, B. G. Cosio, M. Pirozynski, S. Loukides, R. Louis, M. Spinola, and O. S. Usmani. Nexthaler, an innovative dry powder inhaler delivering an extrafine fixed combination of beclometasone and formoterol to treat large and small airways in asthma. *Expert Opin. Drug Deliv.*, 11(9):1497–1506, 2014.

Y. Cui and M. Sommerfeld. Forces on micron-sized particles randomly distributed on the surface of larger particles and possibility of detachment. *Int. J. Multiph. Flow*, 72:39–52, 2015.

Y. Cui and M. Sommerfeld. Application of lattice-boltzmann method for analysing detachment of micron-sized particles from carrier particles in turbulent flows. *Flow Turbul. Combust.*, 100(1):271–297, 2018.

Y. Cui and M. Sommerfeld. The modelling of carrier-wall collision with drug particle detachment for dry powder inhaler applications. *Powder Technol.*, 344:741–755, 2019.

Y. Cui, S. Schmalfuß, S. Zellnitz, M. Sommerfeld, and N. Urbanetz. Towards the optimisation and adaptation of dry powder inhalers. *Int. J. Pharm.*, 470(1-2):120–132, 2014.

P. A. Cundall and O. D. Strack. A discrete numerical model for granular assemblies. *Geotechnique*, 29(1):47–65, 1979.

G. DCS Computing. Liggghts(r)-public documentation, version 3.x, 2016.

A. H. de Boer, H. Chan, and R. Price. A critical view on lactose-based drug formulation and device studies for dry powder inhalation: which are relevant and what interactions to expect? *Adv. Drug Deliv. Rev.*, 64(3): 257–274, 2012.

A. H. de Boer, P. Hagedoorn, M. Hoppentocht, F. Buttini, F. Grasmeijer, and H. W. Frijlink. Dry powder inhalation: past, present and future. *Expert Opin. Drug Deliv.*, 14(4):499–512, 2017.

R. Di Felice. The voidage function for fluid-particle interaction systems. *Int. J. Multiph. Flow*, 20(1):153–159, 1994.

A. Di Renzo and F. Di Maio. Comparison of contact-force models for the simulation of collisions in DEM-based granular flow codes. *Chem. Eng. Sci.*, 59(3):525–541, 2004.

A. Di Renzo, F. P. Di Maio, R. Girimonte, and B. Formisani. DEM simulation of the mixing equilibrium in fluidized beds of two solids differing in density. *Powder Technol.*, 184(2):214–223, 2008.

A. Di Renzo, G. Picarelli, and F. P. Di Maio. Numerical investigation of funicular liquid bridge interactions between spherical particles. *Chem. Eng. Technol.*, 43(5):830–837, 2020.

A. Di Renzo, E. S. Napolitano, and F. P. Di Maio. Coarse-grain DEM modelling in fluidized bed simulation: A review. *Processes*, 9(2):279, 2021.

B. Dickhoff, A. De Boer, D. Lambregts, and H. Frijlink. The effect of carrier surface and bulk properties on drug particle detachment from crystalline lactose carrier particles during inhalation, as function of carrier payload and mixing time. *Eur. J. Pharm. Biopharm.*, 56(2):291–302, 2003.

B. Dickhoff, A. De Boer, D. Lambregts, and H. Frijlink. The interaction between carrier rugosity and carrier payload, and its effect on drug particle redispersion from adhesive mixtures during inhalation. *Eur. J. Pharm. Biopharm.*, 59(1):197–205, 2005.

J.-F. Dietiker, T. Li, R. Garg, and M. Shahnam. Cartesian grid simulations of gas–solids flow systems with complex geometry. *Powder Technol.*, 235: 696–705, 2013.

L. G. Dos Reis, V. Chaugule, D. F. Fletcher, P. M. Young, D. Traini, and J. Soria. In-vitro and particle image velocimetry studies of dry powder inhalers. *Int. J. Pharm.*, 592:119966, 2021.

S. Ergun. Fluid flow through packed columns. *Chem. Eng. Prog.*, 48:89–94, 1952.

Á. Farkas, D. Lewis, T. Church, A. Tweedie, F. Mason, A. E. Haddrell, J. P. Reid, A. Horváth, and I. Balásházy. Experimental and computational study of the effect of breath-actuated mechanism built in the nexthaler® dry powder inhaler. *Int. J. Pharm.*, 533(1):225–235, 2017.

M. Farzaneh, S. Sasic, A.-E. Almstedt, F. Johnsson, and D. Pallarès. A novel multigrid technique for lagrangian modeling of fuel mixing in fluidized beds. *Chem. Eng. Sci.*, 66(22):5628–5637, 2011.

W. H. Finlay. *The mechanics of inhaled pharmaceutical aerosols: an introduction.* Academic press, 2001.

D. F. Fletcher, V. Chaugule, L. Gomes dos Reis, P. M. Young, D. Traini, and J. Soria. On the use of computational fluid dynamics (cfd) modelling to design improved dry powder inhalers. *Pharm. Res.*, 38(2):277–288, 2021.

P. A. Flume, M. L. Aitken, D. Bilton, P. Agent, B. Charlton, E. Forster, H. G. Fox, H. Hebestreit, J. Kolbe, J. B. Zuckerman, et al. Optimising inhaled mannitol for cystic fibrosis in an adult population. *Breathe*, 11 (1):39–48, 2015.

W. D. Fullmer and J. Musser. CFD–DEM solution verification: Fixed-bed studies. *Powder Technol.*, 339:760–764, 2018.

J. E. Galvin and S. Benyahia. The effect of cohesive forces on the fluidization of aeratable powders. *AIChE J.*, 60(2):473–484, 2014.

R. Garg, J. Galvin, T. Li, and S. Pannala. Documentation of open-source MFIX–DEM software for gas-solids flows. From URL https://mfix.netl.doe.gov/documentation/dem_doc_2012-1.pdf, 2012.

M. Germano, U. Piomelli, P. Moin, and W. H. Cabot. A dynamic subgrid-scale eddy viscosity model. *Phys. Fluids A, Fluid Dyn.*, 3(7):1760–1765, 1991.

D. Gidaspow. *Multiphase flow and fluidization: continuum and kinetic theory descriptions.* Academic press, 1994.

J. Greenwood. Adhesion of elastic spheres. *Proc. R. Soc. A: Math. Phys. Eng. Sci.*, 453(1961):1277–1297, 1997.

Y. Gu, A. Ozel, and S. Sundaresan. A modified cohesion model for CFD–DEM simulations of fluidization. *Powder Technol.*, 296:17–28, 2016.

R. Han, G. Papadopoulos, and B. Greenspan. Investigation of powder dispersion inside a SPIROS® dry powder inhaler using particle image velocimetry. *Powder Technol.*, 125(2-3):266–278, 2002.

H. Hertz. Über die berührung fester elastischer körper. *Journal für die reine und angewandte Mathematik*, 92(156-171):22, 1882.

A. J. Hickey and S. R. P. da Rocha. *Pharmaceutical inhalation aerosol technology.* CRC Press, 3rd edition, 2019.

W. Holloway, X. Yin, and S. Sundaresan. Fluid-particle drag in inertial polydisperse gas–solid suspensions. *AIChE J.*, 56(8):1995–2004, 2010.

M. Hoppentocht, P. Hagedoorn, H. Frijlink, and A. De Boer. Technological and practical challenges of dry powder inhalers and formulations. *Adv. Drug Deliv. Rev.*, 75:18–31, 2014.

B. Huynh, Y. Chen, D. Fletcher, P. Young, B. Zhu, and D. Traini. An investigation into the powder release behavior from capsule-based dry powder inhalers. *Aerosol Sci. Technol.*, 49(10):902–911, 2015.

T. Ibrahim, T. Burk, F. Etzler, and R. Neuman. Direct adhesion measurements of pharmaceutical particles to gelatin capsule surfaces. *J. Adhes. Sci. Technol.*, 14(10):1225–1242, 2000.

N. Islam and E. Gladki. Dry powder inhalers (DPIs) - a review of device reliability and innovation. *Int. J. Pharm.*, 360(1-2):1–11, 2008.

R. Israel and D. E. Rosner. Use of a generalized stokes number to determine the aerodynamic capture efficiency of non-stokesian particles from a compressible gas flow. *Aerosol Sci. Technol.*, 2(1):45–51, 1982.

K. L. Johnson, K. Kendall, and a. Roberts. Surface energy and the contact of elastic solids. *Proc. R. Soc. A: Math. Phys. Eng. Sci.*, 324(1558):301–313, 1971.

W. Kaialy, M. N. Momin, M. D. Ticehurst, J. Murphy, and A. Nokhodchi. Engineered mannitol as an alternative carrier to enhance deep lung penetration of salbutamol sulphate from dry powder inhaler. *Colloids Surf. B*, 79(2):345–356, 2010.

A. Kamranian Marnani, A. Bück, S. Antonyuk, B. van Wachem, D. Thévenin, and J. Tomas. The effect of very cohesive ultra-fine particles in mixtures on compression, consolidation, and fluidization. *Processes*, 7 (7):439, 2019.

H. Kinnunen, G. Hebbink, H. Peters, J. Shur, and R. Price. An investigation into the effect of fine lactose particles on the fluidization behaviour and aerosolization performance of carrier-based dry powder inhaler formulations. *AAPS PharmSciTech*, 15(4):898–909, 2014.

C. Kloss, C. Goniva, A. Hager, S. Amberger, and S. Pirker. Models, algorithms and validation for opensource DEM and CFD–DEM. *Prog. Comput. Fluid Dyn.*, 12(2-3):140–152, 2012.

A. N. Kolmogorov. The local structure of turbulence in incompressible viscous fluid for very large reynolds numbers. *Cr Acad. Sci. URSS*, 30: 301–305, 1941.

X. Kou, S. T. Wereley, P. W. Heng, L. W. Chan, and M. T. Carvajal. Powder dispersion mechanisms within a dry powder inhaler using microscale particle image velocimetry. *Int. J. Pharm.*, 514(2):445–455, 2016.

B. L. Laube, H. M. Janssens, F. H. de Jongh, S. G. Devadason, R. Dhand, P. Diot, M. L. Everard, I. Horvath, P. Navalesi, T. Voshaar, et al. What the pulmonary specialist should know about the new inhalation therapies, 2011.

D. Lewis and A. Tweedie. Enhancing the performance of dry powder inhalers: Breath actuated mechanisms. *ONdrugDelivery Magazine*, pages 34–38, 2016.

X. Li, M. Sommerfeld, and Y. Cui. Measurements of the inlet velocity profile of the dry powder inhaler by laser doppler anemometry. University of Halle-Wittenberg, Project Report, February 2015.

S. Lindert, A. Below, and J. Breitkreutz. Performance of dry powder inhalers with single dosed capsules in preschool children and adults using improved upper airway models. *Pharmaceutics*, 6(1):36–51, 2014.

V. A. Marple, B. A. Olson, K. Santhanakrishnan, D. L. Roberts, J. P. Mitchell, and B. L. Hudson-Curtis. Next generation pharmaceutical impactor: a new impactor for pharmaceutical inhaler testing. part iii. extension of archival calibration to 15 l/min. *Journal of Aerosol Medicine*, 17 (4):335–343, 2004.

J. Marshall. Effect of particle collisions on the expulsion of heavy particles from a vortex core. *Phys. Fluids*, 18(11):113301, 2006.

J. S. Marshall and S. Li. *Adhesive particle flow.* Cambridge University Press, 2014.

F. Martinelli, A. G. Balducci, A. Rossi, F. Sonvico, P. Colombo, and F. Buttini. "Pierce and inhale" design in capsule based dry powder inhalers: Effect of capsule piercing and motion on aerodynamic performance of drugs. *Int. J. Pharm.*, 487(1-2):197–204, 2015.

MATLAB. *version 9.7 (R2019b).* The MathWorks Inc., Natick, Massachusetts, 2019.

C. Merusi, G. Brambilla, E. Long, G. Hargrave, and H. Versteeg. Optical diagnostics studies of air flow and powder fluidisation in nexthaler®. part ii: Use of fluorescent imaging to characterise transient release of fines from a dry powder inhaler. *Int. J. Pharm.*, 549(1-2):96–108, 2018.

J. Milenkovic, A. H. Alexopoulos, and C. Kiparissides. Flow and particle deposition in the Turbuhaler: A CFD simulation. *Int. J. Pharm.*, 448(1): 205–213, 2013.

J. Milenkovic, A. Alexopoulos, and C. Kiparissides. Deposition and fine particle production during dynamic flow in a dry powder inhaler: A CFD approach. *Int. J. Pharm.*, 461(1-2):129–136, 2014.

J. Milenkovic, A. H. Alexopoulos, and C. Kiparissides. Optimization of a DPI inhaler: a computational approach. *J. Pharm. Sci.*, 106(3):850–858, 2017.

R. D. Mindlin and H. Deresiewicz. Elastic spheres in contact under varying oblique forces. *J. Appl. Mech.*, 20(3):327–344, 1953.

R. Mitani, S. Ohsaki, H. Nakamura, and S. Watano. Numerical study on particle adhesion in dry powder inhaler device. *Chem. Pharm. Bull*, 68 (8):726–736, 2020.

E. S. Napolitano, A. Di Renzo, and F. P. Di Maio. Coarse-grain DEM–CFD modelling of dense particle flow in gas–solid cyclone. *Sep. Purif. Technol.*, 287:120591, 2022.

R. Nedderman, U. Tüzün, S. Savage, and G. Houlsby. Flow of granular materials-i. discharge rates from hoppers. *Chem. Eng. Sci.*, 37(11), 1982.

NETL Multiphase Flow Science Team. Documentation of open-source MFIX–DEM software for gas-solids flows. From URL https://mfix.netl.doe.gov/doc/mfix/20.1.0/, 2020.

D. Nguyen, J. Remmelgas, I. N. Björn, B. van Wachem, and K. Thalberg. Towards quantitative prediction of the performance of dry powder inhalers by multi-scale simulations and experiments. *Int. J. Pharm.*, 547(1-2):31–43, 2018.

F. Nicoud and F. Ducros. Subgrid-scale stress modelling based on the square of the velocity gradient tensor. *Flow Turbul. Combust.*, 62(3):183–200, 1999.

H. R. Norouzi, R. Zarghami, R. Sotudeh-Gharebagh, and N. Mostoufi. *Coupled CFD-DEM modeling: formulation, implementation and application to multiphase flows.* John Wiley & Sons, 2016.

M. Otsubo, C. O'Sullivan, and T. Shire. Empirical assessment of the critical time increment in explicit particulate discrete element method simulations. *Comput. Geotech.*, 86:67–79, 2017.

E. J. Parteli, J. Schmidt, C. Blümel, K.-E. Wirth, W. Peukert, and T. Pöschel. Attractive particle interaction forces and packing density of fine glass powders. *Sci. Rep.*, 4(1):1–7, 2014.

I. Pasquali, C. Merusi, G. Brambilla, E. J. Long, G. K. Hargrave, and H. K. Versteeg. Optical diagnostics study of air flow and powder fluidisation in Nexthaler® – Part I: Studies with lactose placebo formulation. *Int. J. Pharm.*, 496(2):780–791, 2015.

S. V. Patankar. A calculation procedure for two-dimensional elliptic situations. *Numer. Heat Transf.*, 4(4):409–425, 1981.

G. Pilcer and K. Amighi. Formulation strategy and use of excipients in pulmonary drug delivery. *Int. J. Pharm.*, 392(1-2):1–19, 2010.

R. Ponzini, R. Da Vià, S. Bnà, C. Cottini, and A. Benassi. Coupled CFD–DEM model for dry powder inhalers simulation: Validation and sensitivity analysis for the main model parameters. *Powder Technol.*, 385:199–226, 2021.

S. B. Pope. *Turbulent flows.* Cambridge University Press, 2000.

C. Ramírez-Aragón, J. Ordieres-Meré, F. Alba-Elías, and A. González-Marcos. Comparison of cohesive models in edem and liggghts for simulating powder compaction. *Materials*, 11(11):2341, 2018.

M. A. Rashid, S. Muneer, J. Mendhi, M. Z. R. Sabuj, Y. Alhamhoom, Y. Xiao, T. Wang, E. L. Izake, and N. Islam. Inhaled edoxaban dry powder inhaler formulations: Development, characterization and their effects on the coagulopathy associated with covid-19 infection. *Int. J. Pharm.*, 608: 121122, 2021.

M. Rhodes, editor. *Introduction to Particle Technology.* Wiley, second edition, 2008.

J. Richardson and W. Zaki. Sedimentation and fluidisation: Part i. *Chem. Eng. Res. Des.*, 75:S82–S100, 1997.

L. Rong, K. Dong, and A. Yu. Lattice-boltzmann simulation of fluid flow through packed beds of spheres: effect of particle size distribution. *Chem. Eng. Sci.*, 116:508–523, 2014.

C. A. Ruzycki, E. Javaheri, and W. H. Finlay. The use of computational fluid dynamics in inhaler design. *Expert Opin. Drug Deliv.*, 10(3):307–323, 2013.

S. Sarangi, K. Thalberg, and G. Frenning. Effect of carrier size and mechanical properties on adhesive unit stability for inhalation: A numerical study. *Powder Technol.*, 390:230–239, 2021.

R. Scherließ and C. Etschmann. Dpi formulations for high dose applications–challenges and opportunities. *Int. J. Pharm.*, 548(1):49–53, 2018.

W. Schroeder, K. Martin, L. Avila, and C. Law. *The VTK user's guide.* Kitware, 1999.

K. Siliveru, C. Jange, J. Kwek, and R. Ambrose. Granular bond number model to predict the flow of fine flour powders using particle properties. *J. Food Eng.*, 208:11–18, 2017.

J. Smagorinsky. General circulation experiments with the primitive equations: I. the basic experiment. *Mon. Weather Rev.*, 91(3):99–164, 1963.

D. Solutions. Edem. 2.6 user guide, 2014.

M. Sommerfeld. *Best practice guidelines for computational fluid dynamics of dispersed multiphase flows.* Ercoftac, 2008.

M. Sommerfeld and S. Schmalfuß. Numerical analysis of carrier particle motion in a dry powder inhaler. *J. Fluids Eng.*, 138(4):1–12, 2016.

M. Sommerfeld, Y. Cui, and S. Schmalfuß. Potential and constraints for the application of cfd combined with lagrangian particle tracking to dry powder inhalers. *Eur. J. Pharm. Sci.*, 128:299–324, 2019.

F. Stern, R. Wilson, and J. Shao. Quantitative V&V of CFD simulations and certification of CFD codes. *Int. J. Numer. Methods Fluids*, 50(11): 1335–1355, 2006.

M. Syamlal, W. Rogers, and T. J. OBrien. Mfix documentation theory guide. Technical report, USDOE Morgantown Energy Technology Center, WV (United States), 1993.

M. Syamlal et al. Mfix documentation: Numerical technique. *Rep. DOE/MC/31346*, 5824:80, 1998.

M. R. Tamadondar and A. Rasmuson. The effect of carrier surface roughness on wall collision-induced detachment of micronized pharmaceutical particles. *AIChE J.*, 66(1):e16771, 2020.

M. J. Telko and A. J. Hickey. Dry powder inhaler formulation. *Respir. Care*, 50(9):1209–1227, 2005.

Z. Tong, R. Yang, A. Yu, S. Adi, and H.-K. Chan. Numerical modelling of the breakage of loose agglomerates of fine particles. *Powder Technol.*, 196 (2):213–221, 2009.

Z. Tong, R. Yang, K. Chu, A. Yu, S. Adi, and H.-K. Chan. Numerical study of the effects of particle size and polydispersity on the agglomerate dispersion in a cyclonic flow. *Chem. Eng. J.*, 164(2-3):432–441, 2010.

Z. Tong, H. Kamiya, A. Yu, H.-K. Chan, and R. Yang. Multi-scale modelling of powder dispersion in a carrier-based inhalation system. *Pharm. Res.*, 32(6):2086–2096, 2015a.

Z. Tong, A. Yu, H.-K. Chan, and R. Yang. Discrete modelling of powder dispersion in dry powder inhalers-a brief review. *Curr. Pharm. Des.*, 21 (27):3966–3973, 2015b.

Z. Tong, W. Zhong, A. Yu, H.-K. Chan, and R. Yang. Cfd–dem investigation of the effect of agglomerate–agglomerate collision on dry powder aerosolisation. *J. Aerosol Sci.*, 92:109–121, 2016.

Z. Tong, R. Yang, and A. Yu. Cfd-dem study of the aerosolisation mechanism of carrier-based formulations with high drug loadings. *Powder Technol.*, 314:620–626, 2017.

Y. Tsuji, T. Kawaguchi, and T. Tanaka. Discrete particle simulation of two-dimensional fluidized bed. *Powder Technol.*, 77(1):79–87, 1993.

M. A. van der Hoef, M. van Sint Annaland, N. Deen, and J. Kuipers. Numerical simulation of dense gas-solid fluidized beds: a multiscale modeling strategy. *Annu. Rev. Fluid Mech.*, 40:47–70, 2008.

B. van Wachem, K. Thalberg, J. Remmelgas, and I. Niklasson-Björn. Simulation of dry powder inhalers: Combining micro-scale, meso-scale and macro-scale modeling. *AIChE J.*, 63(2):501–516, 2017.

A. Volk and U. Ghia. Theoretical analysis of CFD–DEM mathematical model solution change with varying computational cell size. In *FEDSM*, volume 51579. American Society of Mechanical Engineers, 2018.

A. Volk, U. Ghia, and G. R. Liu. Assessment of CFD–DEM solution error against computational cell size for flows through a fixed-bed of binary-sized particles. *Powder Technol.*, 325:519–529, 2018.

C. Wen and Y. Yu. A generalized method for predicting the minimum fluidization velocity. *AIChE J.*, 12(3):610–612, 1966.

C. Wensrich and A. Katterfeld. Rolling friction as a technique for modelling particle shape in dem. *Powder Technol.*, 217:409–417, 2012.

R. Wessel and J. Righi. Generalized correlations for inertial impaction of particles on a circular cylinder. *Aerosol Sci. Tech.*, 9(1):29–60, 1988.

T. Weuthen, S. Roeder, P. Brand, B. Müllinger, and G. Scheuch. In vitro testing of two formoterol dry powder inhalers at different flow rates. *Journal of Aerosol Medicine*, 15(3):297–303, 2002.

D. C. Wilcox. *Turbulence modeling for CFD.* DCW Industries, 3rd edition, 2006.

W. Wong, D. F. Fletcher, D. Traini, H.-K. Chan, and P. M. Young. The use of computational approaches in inhaler development. *Adv. Drug Deliv. Rev.*, 64(4):312–322, 2012.

J. Yang, C.-Y. Wu, and M. Adams. Dem analysis of the effect of particle–wall impact on the dispersion performance in carrier-based dry powder inhalers. *Int. J. Pharm.*, 487(1-2):32–38, 2015a.

J. Yang, C.-Y. Wu, and M. Adams. Numerical modelling of agglomeration and deagglomeration in dry powder inhalers: a review. *Curr. Pharm. Des.*, 21(40):5915–5922, 2015b.

S. Yeung, D. Traini, D. Lewis, and P. M. Young. Dosing challenges in respiratory therapies. *Int. J. Pharm.*, 548(1):659–671, 2018a.

S. Yeung, D. Traini, A. Tweedie, D. Lewis, T. Church, and P. M. Young. Limitations of high dose carrier based formulations. *Int. J. Pharm.*, 544 (1):141–152, 2018b.

P. M. Young, S. Edge, D. Traini, M. D. Jones, R. Price, D. El-Sabawi, C. Urry, and C. Smith. The influence of dose on the performance of dry powder inhalation systems. *Int. J. Pharm.*, 296(1-2):26–33, 2005.

P. M. Young, O. Wood, J. Ooi, and D. Traini. The influence of drug loading on formulation structure and aerosol performance in carrier based dry powder inhalers. *Int. J. Pharm.*, 416(1):129–135, 2011.

U. Zafar, F. Alfano, and M. Ghadiri. Evaluation of a new dispersion technique for assessing triboelectric charging of powders. *Int. J. Pharm.*, 543 (1-2):151–159, 2018.

X. Zhang, Y. Cui, R. Liang, G. Wang, X. Yue, Z. Zhao, Z. Huang, Y. Huang, J. Geng, X. Pan, et al. Novel approach for real-time monitoring of carrier-based dpis delivery process via pulmonary route based on modular modified sympatec helos. *Acta Pharm. Sin. B*, 10(7):1331–1346, 2020.

J. Zhao, A. Haghnegahdar, Y. Feng, A. Patil, N. Kulkarni, G. J. P. Singh, G. Malhotra, and R. Bharadwaj. Prediction of the carrier shape effect on particle transport, interaction and deposition in two dry powder inhalers and a mouth-to-g13 human respiratory system: A cfd-dem study. *J. Aerosol Sci.*, 160:105899, 2022.

Z. Zheng, S. S. Y. Leung, and R. Gupta. Flow and particle modelling of dry powder inhalers: Methodologies, recent development and emerging applications. *Pharmaceutics*, 13(2):189, 2021.

Q. T. Zhou, L. Qu, T. Gengenbach, I. Larson, P. J. Stewart, and D. A. Morton. Effect of surface coating with magnesium stearate via mechanical dry powder coating approach on the aerosol performance of micronized drug powders from dry powder inhalers. *AAPS PharmSciTech*, 14(1): 38–44, 2013.

D. Zillen, M. Beugeling, W. L. Hinrichs, H. W. Frijlink, and F. Grasmeijer. Natural and bioinspired excipients for dry powder inhalation formulations. *Curr. Opin. Colloid Interface Sci.*, 56:101497, 2021.